technische universität
dortmund

Exciton-phonon interactions in quantum dots and 2D materials

Dissertation

presented to the Faculty of Physics of the
TU Dortmund University, Germany,
in partial fulfillment of the requirements
for the degree of

Doktorin der Naturwissenschaften - Dr. rer. nat.

by

Janina J. Schindler

Dortmund, 30.10.2023

Accepted by the Faculty of Physics of the TU Dortmund University, Germany

Day of the oral examination: 20.12.2023

Examination board:

Prof. Dr. Marc-Alexander Aßmann
Prof. Dr. Mirko Cinchetti
Prof. Dr. Dr. Wolfgang Rhode
Dr. Bärbel Siegmann

Summary

Excitons are fundamental electronic excitations in semiconductors. They may couple to their crystal environment, namely to phonons which are elementary vibrational excitations of the crystal lattice. The coupling between excitons and phonons is essential, since it ultimately determines the radiative features of semiconducting materials and their relevance for diverse applications in optoelectronics, magneto-optics, spin- and, e.g., valleytronics. Understanding and exploiting the exciton-phonon interactions are therefore crucial for gaining insight into the physics of low-dimensional semiconductors.

The focus of this thesis lies on investigating exciton-phonon interactions in self-assembled quantum dots and uncapped and hBN-encapsulated transition metal dichalcogenide monolayers by photoluminescence and inelastic laser-light scattering spectroscopy. The first part of the thesis deals with a novel Fano-type quantum interference in InGaAs/GaAs quantum dots between the bright and dark exciton states and a continuum composed of two orthogonally linear-polarized acoustic phonons. It is sensitive to external factors such as magnetic field strength and direction and optical pumping intensity. The Fano interaction, observed between the excitonic spin transition and the acoustic phonon continuum, provides a valuable method for probing weak couplings in two-level quantum systems and offers insights into previously hidden optically inactive states in semiconductor nanostructures.
In the second part, different kinds of charge carrier-phonon interactions in van der Waals heterostructures are studied. In a WSe_2 monolayer, the interlayer electron-phonon interaction leads to a significant increase in the excitonic emission intensity which is attributed to a double resonance phenomenon. Additionally, phonon-polariton anticrossings at the neutral and negatively charged exciton resonances are revealed, as well as an upconversion of a dark intervalley exciton into a bright intravalley exciton. The energy gain associated to this upconversion is described by a cooling of the resident electrons or by an exciton scattering with Λ- or K-valley phonons. Moreover, through tuning the electron doping levels via the hBN thickness, the fine structure of excitonic complexes in MoS_2 heterostructures is explored, and remarkably enhanced g-factors are obtained in the ternary alloy $MoWSe_2$. The control and manipulation of excitonic properties and interactions, such as the excitonic g-factor and their intricate couplings to phonons, provide opportunities for further advancements in spintronics and quantum information processing. The results also highlight that the interactions between excitons and phonons must be studied thoroughly in order to exploit the full potential of these semiconductor materials and to allow for tailoring their functional and structural properties.

Zusammenfassung

Exzitonen sind fundamentale elektronische Anregungen in Halbleitern. Sie können an ihre kristalline Umgebung via Phononen koppeln, welche elementare Schwingungsanregungen des Kristallgitters sind. Die Kopplung zwischen Exzitonen und Phononen ist von grundlegender Bedeutung, da sie letztlich die Strahlungseigenschaften von Halbleitermaterialien und ihre Bedeutung für verschiedene Anwendungen in der Optoelektronik, Magnetooptik, Spin- und z. B. der Valleytronik bestimmt. Das Verständnis und die Nutzung der Exziton-Phonon-Wechselwirkungen sind daher wesentlich, um einen Einblick in die Physik niedrigdimensionaler Halbleiter zu bekommen.

Der Schwerpunkt dieser Arbeit liegt auf der Untersuchung von Exziton-Phonon-Wechselwirkungen in selbstorganisierten Quantenpunkten und nicht-ummantelten und hBN-umschlossenen Übergangsmetall-Dichalkogenid-Monolagen mittels Photolumineszenz und inelastischer Laserlichtstreuungsspektroskopie. Der erste Teil der Arbeit befasst sich mit einer neuartigen Quanteninterferenz vom Fano-Typ in InGaAs/GaAs-Quantenpunkten zwischen den hellen und dunklen Exzitonenzuständen und einem Kontinuum aus zwei orthogonal-linear polarisierten akustischen Phononen. Die Interferenz kann mittels externer Faktoren beeinflusst werden, wie Stärke und Richtung des Magnetfelds sowie der optischen Pumpintensität. Die Fano-Wechselwirkung, die zwischen dem exzitonischen Spinübergang und dem akustischen Phononenkontinuum beobachtet wird, stellt eine wertvolle Untersuchungsmethode zur Detektion schwacher Kopplungen in Zwei-Niveau-Quantensystemen dar und bietet Einblicke in bisher verborgene, optisch inaktive Zustände in Halbleiternanostrukturen.
Im zweiten Teil werden verschiedene Arten von Ladungsträger-Phonon-Wechselwirkungen in van der Waals-Heterostrukturen untersucht. In einer WSe_2-Monolage führt die Elektron-Phonon-Wechselwirkung zwischen der Monolage und hBN-Schicht zu einer signifikanten Erhöhung der exzitonischen Emissionsintensität, die auf ein Doppelresonanzphänomen zurückgeführt wird. Zusätzlich werden Phonon-Polariton-Antikreuzungen an den neutralen und negativ geladenen Exziton-Resonanzen sowie eine Aufwärtskonversion eines dunklen Intervalley-Exzitons in ein helles Intravalley-Exziton aufgedeckt. Der mit dieser Aufwärtskonversion verbundene Energiegewinn wird durch eine Abkühlung der residenten Elektronen oder durch eine Exzitonenstreuung mit Λ- oder K-valley-Phononen beschrieben. Darüber hinaus wird die Feinstruktur der exzitonischen Komplexe in MoS_2-Heterostrukturen durch die Anpassung der Elektronendotierung über die hBN-Dicke erforscht, und in der ternären Verbindung $MoWSe_2$ werden beträchtlich erhöhte g-Faktoren ermittelt. Die Kontrolle und Manipulation der exzitonischen Eigenschaften und Wechselwirkungen, wie z. B. des exzitonischen g-Faktors und der komplexen Kopplungen mit Phononen, bieten Möglichkeiten für künftige Entwicklungen in der Spintronik und der Quanteninformationsverarbeitung. Die Ergebnisse verdeutlichen auch, dass die Wechselwirkungen zwischen Exzitonen und Phononen intensiv untersucht werden müssen, um das volle Potenzial dieser Halbleitermaterialien auszuschöpfen und ihre funktionellen und strukturellen Eigenschaften maßgeschneidert gestalten zu können.

Contents

1 Introduction

The information technology of today is based on the understanding, control and manipulation of charge carriers, laying the very foundation for almost every electronic or optoelectronic device [1]. The continuously growing demand for faster data processing and transfer necessitates further progress in semiconductor technology, leading in particular to a further transistor size decrease and speed increase [2]. New approaches in semiconductor technology are hence needed to keep up progress in computational power and speed. The miniaturization of electronic devices has given rise to the usage of semiconductor nanostructures. The widespread usage of such nanomaterials in modern society may lead to a transition from the Silicon Age to a new Nano Age [3]. The reduced dimensionality of the nanostructures, such as in two-dimensional monolayers or in zero-dimensional quantum dots, changes their macroscopic properties as a result of quantum confinement [4]. Thereby, the spatial reduction modifies the carrier density of states. Moreover, such nanostructures may show strong interactions between the charge carriers and their environment, which affect the optical and electronic properties. The modified electronic structure may be examined using optical spectroscopy, a versatile tool to scrutinize and characterize semiconductors [5]. Specifically, subtle optical, spin and valley properties as well as electron-phonon interactions may be studied by optical techniques such as photoluminescence and inelastic laser-light scattering spectroscopy.

Two-dimensional (2D) materials, as the name implies, are only one atomic layer thick, about a few Ångstroms. In the bulk form, their out-of-plane atoms are typically held together by weak van der Waals bonds, while their in-plane covalent bonds are much stronger. This allows for the preparation of single atomic layers. The first systematic exfoliation and analysis of monolayers (MLs), namely graphene, took place in 2004 by Novoselov and Geim [6], and was awarded with the Nobel prize in Physics in 2010. The discovery of the direct bandgap in transition metal dichalcogenide (TMDC) MLs started their extensive study in 2010 [7]. These materials of inherent 2D character may also be seen as being pure surfaces or having a high surface sensibility. This opens up new ways of influencing and controlling charge carrier dynamics: by their direct surroundings. The combination of multiple MLs thus allows one to create robust electronic properties. In comparison to other 2D materials, TMDCs are direct-gap semiconductors with broken inversion symmetry, strong spin-orbit coupling and significantly enhanced Coulomb interaction (exciton effects) due to the strong confinement [8]. In addition to that, this class of materials hosts amazingly rich physics, such as high oscillator strengths, huge exciton binding energies, and remarkably efficient light-matter coupling [8]. These features lead to, e.g., spin-valley locking and high valley polarization, making these materials ideal candidates to observe new phenomena in transport and optics.
Quantum dots, although lower in dimensionality, have instead been known and studied since the 1980s [9, 10], for which the Nobel prize in Chemistry was awarded in 2023. They offer size-dependent properties that can be used for diverse applications such as biotechnology, energy harvesting and quantum information technology [4]. Specifically, quantum dots (QDs) offer promising properties for spin-based applications [11]. The spin,

another intrinsic property of the electron in addition to its charge, may be exploited in the field of spintronics (spin electronics), combining both the advantages of controlling the quantum mechanical spin as well as the conventional electronic charge. The control of the spin promises very fast dynamics and low power dissipation, but requires long spin lifetimes to perform a sufficient number of quantum operations and a low relaxation rate to avoid coherence loss.
One of the major disturbing phenomena introducing scattering and spin decoherence is the interaction of the charge carrier or carrier complex (besides their mutual coupling) with lattice vibrations (phonons). One effect of lattice vibrations is the modulation of the exciton wavefunction leading to changes in the energy spectrum and dynamics of excitons [12]. The absorption and emission of phonons may also result in a scattering of photogenerated excitons into spin- or momentum-dark states so that they lose their optical accessibility. The coupling of exciton or carriers to phonons furthermore significantly affects the temperature dependence of electronic transitions and, e.g., the lifetime broadening [13]. Nevertheless, the phonon interaction with carriers or excitons may also have beneficial effects. Phonons may contribute to the generation of population inversion [14] or to the upconversion of exciton emission [15]. They may realize the optical absorption in indirect-gap semiconductors [16], elliptically polarized phonons may mediate an effective exchange interaction over tens of nanometers leading to significant spin polarization of heavy holes [17], or coherent phonons may change the magnetization in semiconducting materials at ultra-fast time scales [18], underlining the importance of strain (anisotropic phonon fields) for elasto-magnetic and magneto-optical effects. Moreover, the formation of polarons (charge carriers screened by phonon clouds) due to strongly intertwining electron-phonon coupling is highly interesting for low-dimensional semiconductors, as they possess unique optoelectronic features. Besides the Coulomb interaction, the coupling to phonons is thus one of the fundamental interactions of carriers and quasi-particles in solids.
The properties of both material systems, 2D materials and QDs, are hence influenced by the interactions between charge carriers and their environment. The features of the confined carriers coined by interaction processes with, for instance, phonons may be characterized using optical techniques [19, 20]. These techniques include different types of photoluminescence (PL) spectroscopy as well as inelastic laser-light scattering spectroscopy. Thereby, PL spectroscopy provides energy-resolved information about the internal electronic structure and is sensitive to the dielectric environment, while inelastic scattering allows for detecting interaction mechanisms and for determining the involved charge carriers or carrier complexes. By combining both techniques, it is possible to characterize the electronic, vibrational, spin and valley properties of a material.

An approach towards a deeper understanding of exciton-phonon interactions in 2D materials and QDs is presented in this thesis. The thesis is organized as follows: The essential concepts and characteristics of the studied low-dimensional semiconductors are collated in chapter 2. Wherever possible, the influences of the different mechanisms on the two material systems are directly compared. They include the electronic band structure of the materials, the concept of excitons, the relevant quantum numbers and their couplings as well as phononic interactions. The second chapter 3 introduces the basics of photoluminescence and inelastic laser-light scattering as well as a thorough description of the optical setups. Therein, the different setups are contrasted according to the varying experimental requirements. The chapter concludes with details on the samples.

The following chapter 4 shows the main results of the InGaAs QD samples. Therein, the investigation of dark spins addressed optically via Fano resonance is presented. The Fano-type quantum interference between the exciton states and the continuum composed of two orthogonally linear-polarized acoustic phonons allows us to optically access the dark exciton. The interference appears under state-selective excitation and detection of the dark exciton in a QD ensemble being robust up to a temperature of 60 K and may be tuned by an external magnetic field and the optical pumping intensity. Moreover, for given light-polarization settings and detection energies, the shape of the Fano resonance is inverted, signaling the contribution of either phonon absorption or emission. Additionally, a helicity-dependent switch from a bipolar to a Gaussian-like resonance shape allows for distinguishing between the real exciton eigenstates and virtual states. The Fano interference reveals a negative exciton interaction for the QD p-shell, yielding an exciton level hierarchy in which the bright exciton is lowest in energy. This surprising finding highlights the importance of gaining access to optically hidden states exposed to external confinement in semiconductor nanostructures. Moreover, this mechanism provides a unique method to detect weak couplings of a two-level quantum system.
In chapter 5, high-quality van der Waals heterostructures consisting of hBN-encapsulated and uncapped TMDC MLs are studied. The first half of the chapter covers the optically dark material WSe_2. The interlayer electron-phonon interaction in hBN/WSe_2/hBN heterostructures leads to the observation of a strong increase in the emission intensity. This intensity gain is attributed to a double resonance, where the laser excitation and a combined Raman mode resonate with the ground and the excited states of the A exciton in the WSe_2 ML. Moreover, a pronounced effect of layer-layer interactions on the circular polarization degree is revealed. Furthermore, signatures of polaritons are observed in the photoluminescence excitation (PLE) spectra of a heterostructure consisting of a WSe_2 ML placed on hBN. An anticrossing is observed at the exciton and trion PL lines in the WSe_2 ML when crossed by the ZO (hBN) and the combined ZO (hBN) + A'$_1$ (WSe_2) phonon modes. At the exciton and trion resonance energies, the Raman line is strongly enhanced in its intensity, both line energies are shifted and the linewidths are narrowed. In addition to that, an alternative route to address the different excitonic species in TMDC MLs is used: upconversion PLE spectroscopy. This method allows us to study ways of brightening dark excitons and trions of hBN-encapsulated WSe_2. The dark intervalley exciton upconverts light into a bright intravalley exciton via electron-electron scattering, wherein the required energy gains are explained by cooling of resident electrons. This interaction process stresses the importance of dark excitons in shaping the optical behavior of TMDCs. The second half of this chapter focuses on the bright material MoS_2 and the alloy $MoWSe_2$. Therein, the fine structure of the excitonic complexes is studied in dependence of different doping levels, as obtained using uncapped MoS_2 stacked onto hBN layers of different thicknesses and of hBN-encapsulated MoS_2 MLs. Also, the effective excitonic g-factor is found to significantly vary in the different structures. In the ternary alloy $Mo_{0.7}W_{0.3}Se_2$, exciton-energy splittings are studied via polarization-resolved magneto-PL, revealing remarkably enhanced effective g-factors compared to binary TMDCs. Finally, the polarization-resolved scattering spectra demonstrate different dependences for the exciton, trion, and intervalley exciton, whereby the valley g-factor is determined by resonant intervalley cross-scattering. The latter is subject in the outlook section.

This thesis studies fundamental exciton properties in low-dimensional semiconductors

such as TMDC MLs and QDs. The exciton-phonon interactions in these materials are characterized with respect to their dependence on external perturbations using photoluminescence and inelastic laser-light scattering spectroscopy. Accordingly, new possibilities of investigating and controlling the electronic properties and interactions with the environment are revealed. The results of this research deepen our understanding for the realization of optoelectronic and magneto-optical applications using the studied materials.

2 Theoretical background

The optical study of low-dimensional semiconductor structures requires knowledge about the optical properties of the studied nanostructures and their dependencies on external parameters. This chapter provides detailed theoretical background to understand the results obtained in the experimental studies. The derivation of the electronic energy level structure in section 2.1 starts with the bulk crystal lattice and symmetry considerations. From the bulk crystal, the dimensionality is reduced to two-dimensional monolayers and further to zero-dimensional quantum dots, which leads to quantum effects due to the spatial confinement of the electronic wavefunction. The resulting consequences on the InGaAs quantum dots (section 2.1.3) and the transition metal dichalcogenide monolayers (section 2.1.4) are discussed. Thereafter, the impact of the Coulomb interaction leading to bound electron-hole pairs is investigated in section 2.2. Specifically, the characteristics of the excitons in the studied quantum dots and monolayers are presented in section 2.2.4. Switching from the electron-hole picture to the exciton picture allows for understanding the interaction of these quasi-particles with light and with other (quasi-)particles. Accordingly, the peculiarities of angular momentum coupling, spin, pseudospin and their interactions are considered in section 2.3. Moreover, the emerging magnetic moments determine the interaction between charge carriers and the magnetic field. The impact of angular momenta on the exciton fine structure of the studied structures is elucidated in section 2.3.4. Finally, phonons and their interaction mechanisms with charge carriers are studied in section 2.4. This lays the basic for an understanding of the studied exciton-phonon interactions. The optical techniques used in this thesis are explained in chapter 3.

2.1 Band structure

Understanding the optical properties of a semiconductor requires knowledge of its underlying band structure. Defined by the crystallographic order, the band structure describes the range of possible energies of the electrons in a crystal. Whereas single atoms possess discrete orbitals with a specific energy, the atoms in crystalline solids form energy bands due to their short inter-atomic distance. The orbitals are functions that describe the location of an electron in an atom. The close packing of the atoms in crystals causes the orbitals to overlap, especially the outermost valence orbitals. The electrons occupying such orbitals must not have the same quantum state (quantum number and energy level), as forbidden by Pauli's exclusion principle. Thus, each atomic orbital splits into several orbitals with a very similar, but slightly different energy. In a crystal, due to the large amount of overlapping orbitals, these split energy states are considered as continuous energy bands (see chapter 2.4.2 in [21, 22]).

2.1.1 Details on the electronic band structure

A full approach of calculating the electronic band structure is described, e.g., in chapter 2.1 in [23]. The band structure describes the relation between the possible energy eigenvalues E and the wavevector $\vec{k}$ of the electron's wavefunction Ψ in a crystal. Based on the adiabatic approximation, the dynamics of the atom cores and electrons, as heavy and light constituents of a solid, respectively, may be treated separately as independent systems. Using the simplifications explained in [23], the band structure is calculated starting from the stationary, or time-independent, **Schrödinger equation**:

$$\hat{H}\Psi(\vec{r}) = \left(-\frac{\hbar^2}{2m_{0,\mathrm{e}}}\nabla_\mathrm{e}^2 + \hat{V}(\vec{r})\right)\Psi(\vec{r}) = E\Psi(\vec{r}), \tag{2.1}$$

with the reduced Planck constant $\hbar$ and the differential Laplacian operator ∇_e^2 and mass $m_{0,\mathrm{e}}$ of the free electron. The Hamiltonian $\hat{H} = \hat{T} + \hat{V}$ of a system is a quantum operator corresponding to the total energy of that system, i.e. its' set of energy eigenvalues. It consists of a kinetic energy operator $\hat{T} = \hat{p}_\mathrm{e}^2/2m_{0,\mathrm{e}}$, with the momentum operator $\hat{p}_\mathrm{e} = -i\hbar\nabla_\mathrm{e}$. The potential energy term $V(\vec{r})$ at the position vector $\vec{r}$ results from the application of the potential energy operator $\hat{V}$ on the wavefunction $\Psi(\vec{r})$. Due to the periodicity of the ion cores in the lattice, the potential energy may be depicted as a periodic potential $V(\vec{r}) = V(\vec{r} + \vec{R})$, with lattice vector $\vec{R}$. Hence, it is determined by the underlying crystal lattice. To calculate the energy eigenvalues of the electrons in the crystal, the potential energy term is determined using **Bloch's theorem**. It exploits the translational symmetry of the crystal by stating that the electron's wavefunction $\Psi(\vec{r})$ may be regarded as a plane wave $\mathrm{e}^{i\vec{k}\vec{r}}$ modulated by a periodic function $u_{n\vec{k}}(\vec{r})$:

$$\Psi(\vec{r}) = \sum_{\vec{k}} F_n(\vec{k})\Psi_{n\vec{k}}(\vec{r}), \quad \text{with} \quad \Psi_{n\vec{k}}(\vec{r}) = \mathrm{e}^{i\vec{k}\vec{r}} \cdot u_{n\vec{k}}(\vec{r}). \tag{2.2}$$

The eigenfunctions $\Psi(\vec{r})$ of the Hamiltonian may be expressed as a sum of Bloch waves, with the amplitude $F_n(\vec{k})$ (see chapter 2.2 in [23]). The Bloch waves $\Psi_{n\vec{k}}$, indexed by the quantum number n and the wavevector $\vec{k}$ of the plane waves, show the same periodicity as the atomic structure (lattice) of the crystal. The wavefunctions are associated with the energy eigenvalues as the solutions of the Schrödinger equation for the crystal system. These energy eigenvalues of the electrons in the crystal are achieved by Fourier-transforming the real space to the momentum space, or $\vec{k}$-space. Herein, the reciprocal lattice corresponds to the direct crystal lattice. By analogy, the primitive unit cell in real space (Wigner-Seitz cell) is called first **Brillouin zone** in $\vec{k}$-space. Both cells describe the smallest repeating unit of a crystal with the full symmetry of the crystal structure. Thus, the wavevector may be restricted to values inside the first Brillouin zone without loss of information. In addition, any periodicity in real space leads to periodicity in $\vec{k}$-space. Hence, any resulting energy eigenvalues must be periodic in the reciprocal lattice: $E(\vec{k}) = E(\vec{k} + \vec{K})$, with $\vec{K}$ being a reciprocal lattice vector.
The energy levels of an electron perturbed by the periodic potential of the crystal lattice are the modified eigenenergies of a free electron in vacuum. It is described only by the plane wave part $\Psi(\vec{r}) \propto \mathrm{e}^{i\vec{k}\vec{r}}$, leading to energy levels given by the dispersion relation $E(\vec{k}) = \frac{\hbar^2\vec{k}^2}{2m_{0,\mathrm{e}}}$ [21]. The **energy eigenvalues** of a nearly free electron with fixed quantum

number n are thus given by:

$$E(\vec{k}) = \frac{\hbar^2}{2m_{\mathrm{eff,e}}}\vec{k}^2 \quad \text{with} \quad (m_{\mathrm{eff,e}}^{-1})_{ij} = \hbar^{-2}\partial^2_{k_i,k_j}E(\vec{k}). \tag{2.3}$$

Hence, the bands are approximately parabolic and isotropic close to their extrema (see also chapter 3.1 in [24]). Away from the center, the bands may be non-parabolic resulting from spin-orbit (SO) interaction of energetically higher with lower lying subbands [25], which is discussed in section 2.3.2. As indicated by equation (2.3), the free-electron dispersion is modified by its **effective mass** $m_{\mathrm{eff,e}}$ of the electron. Therein, the indices i, j denote the spatial coordinates x, y, or z. This approximation considers that the electrons are influenced by an external field generated by other charge carriers like the surrounding electrons and the ions of the lattice and, thus, do not move freely in the crystal potential. It allows for treating the electrons as free particles, only modified by an effective mass. In the scheme of the band structure, the effective mass is inversely proportional to the curvature of the dispersion relation of the bands and a smaller mass implies a larger localization energy [9]. Similarly to the dispersion, the effective mass may be anisotropic and have different values for different directions in the crystal (see chapter 1.3.2 in [26]).
The approach of calculating the band structure of a crystal assuming a free electron, whose energy is modified by an effective mass, is termed the effective mass approximation. It is useful for calculating defect energy levels and for studying electrons under any weak external perturbation [23]. Other methods of calculating the energy bands of crystals are, e.g., the empirical pseudopotential method, the tight-binding or linear combination of atomic orbitals method, and the $\vec{k}\cdot\vec{p}$ method. For example, the semiempirical $\vec{k}\cdot\vec{p}$ perturbation theory allows for calculating the shape of the energy bands in the vicinity of extremum points, while it does not require detailed knowledge about energy levels and wavefunctions throughout the Brillouin zone [27]. The term originates from the differential part of the momentum operator $\vec{p}$ in the stationary Schrödinger equation. Therein, $\vec{p}$ is a vector of operators and acts on the states of the matrix element. This approach allows for including multiple bands and the coupling between different bands (see, e.g., [22]). The wavevector $\vec{k}$ serves as the expansion parameter, with higher orders in $\vec{k}$ treated as perturbations. The $\vec{k}\cdot\vec{p}$ method is mostly used to obtain the perturbation expansion (quadratic in $\vec{k}$) of bands around high-symmetry points, specifically expressions for band dispersion and effective masses, and to find non-parabolic behavior for larger $\vec{k}$ [28].

As mentioned above, the periodicity of the crystal is represented by a periodic potential, which is modeled by an infinite periodic array of rectangular potential barriers (Kronig-Penney model). Solving the Schrödinger equation for this model leads to a broadening of the discrete energy states or levels into bands [23]. These bands are filled with electrons according to the Fermi-Dirac distribution, which gives the probability that a state with given energy is occupied by an electron. The Fermi level denotes a hypothetical state, which has a 50 % chance of being occupied. In a semiconductor, this Fermi level lies in between the evolving bands. Thereby, the **valence band** (VB) denotes the topmost band below the Fermi level, in which all possible energy states are fully filled with electrons. The next empty band above the Fermi level is the **conduction band** (CB), in which the electrons move freely and contribute to the conductivity of the material. The energy range between VB and CB is energetically forbidden for the electrons; there

are no allowed electronic states in this gap. The gap where the global maximum of the highest valence band and the global minimum of the lowest conduction band occurs it termed bandgap E_g. Its size in semiconductors is of a few eV and allows for exciting electrons optically and thermally, compared to a much larger energy gap for isolators and a negligible gap for metals. Yet, the size of the bandgap is not fixed, but varies quadratically with temperature following the Varshni formula [29].
A further important point is the difference between direct and indirect bandgaps: **direct bandgaps** are gaps where the global maximum of the valence band and the global minimum of the conduction band occur at the same point in $\vec{k}$-space. This allows for direct transitions between the extrema by absorption (or emission) of a photon. Indirect gap semiconductors obtain the maximum and minimum at different $\vec{k}$-locations, so that a further absorption (or emission) of a phonon is required to fulfill momentum conservation (see chapter 8.2 in [5]).
When an electron is excited from the VB into the CB, the empty state in the VB represents the collective response of all remaining electrons therein. This behavior may be described by considering the empty state as a particle called **hole** with positive elementary charge $+e$. The hole wavefunction is derived from the Bloch function of the empty electron state in the VB by applying the time-reversal operator; it has the opposite effective mass, electric charge, spin and wavevector of the electron [8, 26]. Thus, it enables electrical conductivity in the VB. Additionally, the VB subbands are named after the different effective hole masses, see section 2.1.3. After relaxation of the electron into the VB, the hole disappears, which is also termed electron-hole recombination.

The band structure may be visualized by plotting it in the reduced zone scheme. This scheme consists of the first Brillouin zone with restricted wavevector $\vec{k}$ and characterizes the whole crystal due to the crystal's periodicity. Often, **high-symmetry points** and planes of the unit cell are denoted in the scheme. While the Γ-point always indicates the center of the Brillouin zone at $\vec{k} = 0$, most other points depend on the concrete form of the unit cell. For example, in a hexagonal unit cell the K-point marks the middle of an edge joining two rectangular faces, while the M-point directs to the center of a rectangular face. On the contrary, the Q-point (Λ-point) denotes the point between center and edge of the Brillouin zone in the bulk (monolayer) crystal but is not a high-symmetry point [30]. In a face-centered cubic (fcc) unit cell the boundary points are, e.g., named X for the point in x-direction on the small square face or L at the center of the big hexagonal face.
The unit cell of a crystal marks its smallest unit that makes up the lattice by translation. Aside from this symmetry operation, there are often further operations under which the lattice is invariant (see chapter 3.3 in [22]). These **symmetry operations** transform the crystal lattice into itself. The eigenvalues of these operations under which a state is invariant are collected in groups. Typically, such point groups consist of lattice translations and rotations about symmetry axes, which leave one point fixed and unchanged in space. Depending on the structure of the crystals, these operations are considered as specific crystallographic point groups, labeled e.g. C_n for cyclic symmetries with n-fold rotation axes, D_n for dihedral or two-sided symmetries with additional n twofold axes perpendicular to that axis, or T_d for tetrahedral symmetries and so forth. The additional indices h, v and d indicate an additional mirror symmetry. This leads to 27 point groups for three-dimensional crystals and to 17 two-dimensional space groups [31]. Appropriate groups of the symmetry operations are important to describe the physics of semiconduc-

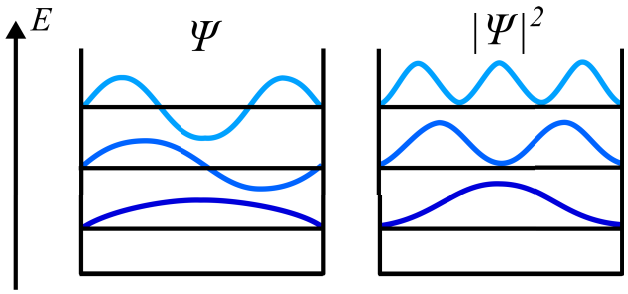

Figure 2-1: Scheme of the wavefunctions $\Psi(\vec{r},t)$ (left) and probability densities $|\Psi(\vec{r},t)|^2$ (right) of the three lowest energy levels of a confined particle. In analogy to Ref. [22].

tors. Most notably, different point group symmetries coin peculiarities of the electronic band structures [32]. A full mathematical approach via group theory goes beyond the scope of this thesis, but may be found, e.g., in chapter 2 in [23] and in [31].

The physical state of an electron is described by its wavefunction $\Psi(\vec{r},t)$, as used in the stationary wave equation (2.1). A wavefunction is a complex-valued probability amplitude, which mathematically describes the wave characteristics of a particle by relating its location to the amplitude of its wave. Likewise to atomic wavefunctions, the wavefunctions in semiconductors are classified according to their orbital angular momentum $l = 0, 1, 2, ...$ as s-, p-, d-, ... shell [24, 33]. This designation refers to the wavefunction being symmetrized according to the transformation properties under rotations, e.g., a hydrogen-like atomic s-orbital is unchanged by any rotation [23]. Due to the spherical symmetry, the electron spin splitting in the s-like bands is highly isotropic (see section 2.3.3). In addition, such s-like bands are typically narrow. Broadening of the bands is caused by atomic interaction, which is small for s-like bands that overlap only marginally between the atoms [34].
The **wavefunction probability density** or probability distribution denotes the probability of measuring a particle at a given place $\vec{r}$ at a given time t. It is determined by the squared modulus $|\Psi(\vec{r},t)|^2 = \Psi^*(\vec{r},t) \cdot \Psi(\vec{r},t)$, which is the product of the wavefunction and its complex conjugate. A scheme of the three energetically lowest wavefunctions and their probability densities is shown in figure 2-1. The wavefunction probability of the s-like ground state with $n = 1, l = 0$ is spherically symmetric, while the probability of the first excited state with $l = 1$ is modulated by a coefficient linear in the radial coordinate. Furthermore, the atomic p-like wavefunctions are triply degenerate (p_x, p_y, p_z) and obtain a dumbbell-shape. Each degenerate wavefunction obtains a main symmetry axis, while their spherical symmetry is reduced. Hence, these p-like states obtain a radial node in the center. This relates to an asymmetric electron density distribution and an anisotropic effective mass tensor in the p-like states. Due to the linear coefficient, the wavefunction probabilities of s- and p-like distributions only marginally overlap [35]. This modulation of the wavefunction is an important aspect of chapter 4, where the overlap of the spatial distribution of the wavefunction probabilities between different particles is used to estimate their interaction probability.

2.1.2 Band structure of low-dimensional nanostructures

Besides the crystal structure of the semiconducting material, the optical properties of nanostructures are also defined by the dimensionality of the structure, as **spatial confinement** constrains the movement of the electrons. Specifically, when the length scale of the nanostructure is in the range of the de Broglie-wavelength $\lambda_B = h/\sqrt{2m_{\text{eff}}E_{\text{kin}}}$ or

smaller, quantum-mechanical effects dominate the electronic and optical properties [24]. Here, $E_{\mathrm{kin}} = k_{\mathrm{B}}T$ denotes the kinetic energy in dependence of the temperature T, with the Boltzmann constant k_{B}. Therefore, the reduction of the free dimensions of a crystal changes the density of states and the energy eigenvalues as defined by the confined wavefunctions of the particles. The **density of states** is reduced from a continuous $\sqrt{E}$-dependence in three-dimensional bulk crystals, over a Heaviside step function in two-dimensional quantum wells, to quantized energy states in zero-dimensional quantum dots. Therein, the density of states is a sequence of δ-functions. Thus, quantum dots are sometimes considered as artificial atoms due to their discrete, atom-like energy levels [33].

Aside from the density of states, the wavefunctions of the particles also change due to the confinement. As mentioned in the former section, the free movement of the electrons is modified by the crystal potential, leading to the electronic band structure. For heterostructures like QWs and QDs, however, at least two different semiconductor materials with similar lattice parameters form the crystalline layer structure, resulting in a modified band structure. Hence, the single-particle wavefunction is separated into a mesoscopic envelope part $\Phi_{\mathrm{env}}(\vec{r})$ and a microscopic Bloch part $u_{n\vec{k}}(\vec{r})$ as:

$$\Psi(\vec{r}) = \sqrt{V_{ol}}\ \Phi_{\mathrm{env}}(\vec{r})\ u_{n\vec{k}}(\vec{r}), \tag{2.4}$$

with V_{ol} the volume of the crystal (corresponding to the number of primitive unit cells) [36, 37]. This approach is known as **envelope function approximation**. It is assumed that the fast-oscillating Bloch functions, which contain the microscopic details of the atom potentials, are the same in both materials due to their similar lattice constants. The slowly varying envelope functions describe the influence of the heterostructure, wherein the different material properties are included as effective parameters. Basically, the envelope functions are a modification of the plane wave part of the nearly free electron as in equation (2.2) [38]. Inserting this wavefunction into the Schrödinger equation allows for calculating the energy levels of the confined particles using the envelope function. For example, in a quantum well the in-plane motion is not confined, so the electrons may be described as nearly free particles in these directions. Their motion is thus described by an in-plane Bloch function $u_{n\vec{k}_{\perp}}(\vec{r})$ and plane waves in $\vec{x}$- and $\vec{y}$-direction, while the envelope function $\Phi_{\mathrm{env}}(\vec{z})$ reflects the confinement of the charge carriers in $\vec{z}$-direction. Moreover, in contrast to the plane waves of the nearly free electrons, the envelope functions are localized at the confining potentials [24]. The resulting confinement energies E_{conf} are explained in detail below.

The effect of the confinement on the energy levels is calculated by applying appropriate boundary conditions to the Schrödinger equation. Often, infinite potentials are chosen as boundary conditions, as they are easier to calculate. A scheme of the spatial confinements in a nanostructure and of a resulting potential are shown in figure 2-2. Under the assumption of a **quantum well** (QW) potential consisting of two infinite barriers with distance R_z in z-direction, the electron's wavevector is restricted to $k_z = n \cdot \pi / R_z$. This is due to the electron forming a standing wave within the potential. Owing to the restriction of the wavevector, the energy of the electron states, according to equation (2.3),

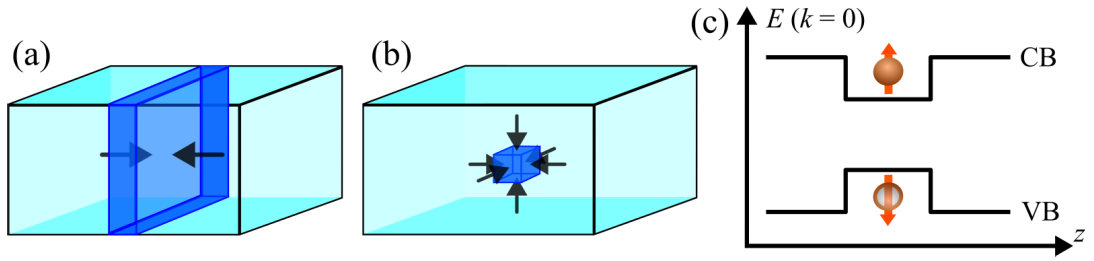

Figure 2-2: Illustration of the spatial confinement of (a) a two-dimensional quantum well in one direction and of (b) a zero-dimensional quantum dot (right) in all directions. (c) Scheme of a confined band structure with an electron (full orange sphere) in the CB and a hole (empty orange sphere) in the VB with spin directions (denoted by arrows). The charge carriers are confined in the nanostructure due to the larger bandgap of the outer material. In analogy to Ref. [24].

is increased by the confinement energy [23]:

$$E_{\mathrm{QW}} = \frac{\hbar^2}{2m_{\mathrm{eff,e}}} \frac{\pi^2}{R_z^2} n^2, \tag{2.5}$$

with n being a discrete value of the band index (principal quantum number). Hence, the spatial confinement leads to an increasing separation of the energy levels for higher n. The energy increase results from Heisenberg's uncertainty principle, as the spatial confinement along z quantizes the z-component $\hat{p}_z$ of the momentum operator and increases the uncertainty of its momentum in z-direction by $\Delta p_z \propto \hbar / R_z$. This leads to an increase of the particle's kinetic energy (see chapter 9.1 in [23]). Note that the total shift of the bandgap includes both the energy shift of the electron and of the hole states. The confinement or localization energy is inversely proportional to the well thickness: $E_{\mathrm{QW}} \propto R_z^{-2}$. Thus, the quantized energy increases for decreasing thickness, leading to an increase, or blue-shift, of the bandgap [39]. Moreover, a decreasing well thickness increases the oscillator strength for the optical transition [40]. Hence, although the studied nanostructures are small (quantum dots) or very thin (monolayers), their oscillator strengths are large, see also section 2.2.2. Note that when using finite potentials, the electron's wavefunction leaks out into the barrier and allows for electron tunneling and for electronic coupling of nanostructures (see chapter 13 in [22]). This allows for different types of exciton-phonon interactions as outlined in chapters 4 and 5.

Quantum dots (QDs) are roughly spherical semiconductor nanostructures of a few to several nanometers in size. Their dimensions are smaller than the extent of the bulk electron wavefunctions, so that the movement of the electrons is confined in all directions. Thereby, self-assembled QDs are randomly distributed and have a size distribution. As they are typically lens-shaped, their height to width-ratio is roughly 1:3 [24]. Thus, their in-plane confinement is weaker than their out-of-plane confinement. The out-of-plane confinement along the growth direction z may be treated as a narrow QW and leads to the above-described blue-shift of the bandgap energy. Additionally, the quantized subbands of such a narrow QW are split far in energy, so that only the ground state subband with $n = 1$ is discussed further (see chapter 2.3.2 in [24]). The circular in-plane confinement determines the discrete energy levels and, thus, the shell structure of the QDs. Hereby, the rotational symmetry of the confinement allows for separating the Schrödinger equation and the electron's wavefunction in azimuthal and radial coordinates. Hence, the wavefunction may be described as a product of spherical harmonics $\Psi(\theta, \phi)$ and a radial

Bessel function $R(r)$, resembling the wavefunction of an electron in a hydrogen atom. The QD potential may be approximated as a spherical potential well of diameter D for which $V(r) = -V_0$ for $r < D/2$ and zero elsewhere. The energy levels of the confined electron in such a potential read [21]:

$$E_{\mathrm{QD}} = \frac{2\hbar^2}{m_{\mathrm{eff,e}} D^2} \chi_{n,l}^2. \tag{2.6}$$

Here, $\chi_{n,l}$ are the zeros of the Bessel function, which are absolute values depending on the principal quantum numbers n and the azimuthal quantum number l. For example, $\chi_{1,0} = 2\pi$ [41]. The lowest energy level with $n = 1, l = 0$ of such a confined electron has the symmetry of a 1s orbital in a hydrogen atom. The probability density of the electron ground state in such a QD potential is described by a spherical Bessel function of first order (s-like wavefunctions). Note that the hole ground state is almost completely described by p-like wavefunctions [42]. From equation (2.6) follows directly the dependence of the eigenenergies on the diameter D of the QDs. The inverse quadratic dependence on the diameter leads to an increase of the energy level spacing for smaller QD diameters. However, in some QD types the potential in the x-y plane is rather parabolic than constant. Hence, the electron may be considered to be confined laterally by a potential $V(\vec{r}) = 1/2\, m_{\mathrm{eff,e}} \omega_0^2 r_{ad}^2$ with radius $r_{ad}^2 = x^2 + y^2$ of the QD [33]. The oscillator characteristic frequency ω_0 is the frequency that a classical particle would exhibit while oscillating in a parabolic-shaped bowl. Such a potential of a **harmonic oscillator** leads to the in-plane eigenenergies of [43]:

$$E_{n_\rho, m'} = \hbar\omega_0 (2n_\rho + |m'| + 1). \tag{2.7}$$

The quantum numbers n_ρ and m' describe the movement in two dimensions: the radial quantum number n_ρ gives the number of nodes in the wavefunction as one moves radially out from the dot center, and m' is the quantum number of the angular momentum component. It corresponds to the number of nodes ($2|m'|$) seen in moving circumferentially around the dot center [33]. The resulting energy levels, or shells, are equally spaced in energy with intershell spacing $\hbar\omega_0$ and twofold degeneracy (see chapter 2.3.2 in [43]). Hence, such a parabolic, two-dimensional potential describes well the observed equidistant shells in the photoluminescence (PL) spectrum of lens-shaped QDs (see chapter 2.3.2 in [24] and references therein). For an electron-hole pair in an anisotropic parabolic potential, equation (2.7) changes to [43]:

$$E_{n_x,n_y}^{\beta} = \hbar\omega_{\beta,x} \left(n_x + \frac{1}{2} \right) + \hbar\omega_{\beta,y} \left(n_y + \frac{1}{2} \right). \tag{2.8}$$

Herein, the quantum numbers n_x and n_y are non-negative integers enumerating the eigenstates of a one-dimensional oscillator. The frequency ω_β describes the strength of the confinement for the two carrier species, with $\beta = \mathrm{e}$ for electrons and $\beta = \mathrm{h}$ for holes. Their energy eigenvalues are described by a pair of two decoupled harmonic oscillators [44]. Moreover, such an anisotropic in-plane confinement induces mixing of the angular momentum eigenstates, such as heavy and light holes, leading to a weak level mixing of the pure states, which is not considered here [24].

Finally, the allowed optical **interband transitions** are described by the sum of funda-

mental bandgap and the confinement energy E_{conf} of both electrons and holes [21]:

$$E = E_{\text{g}} + \sum_{\beta} E_{\text{conf},\beta}. \tag{2.9}$$

Here, electron and hole energy levels are treated independently as in the strong confinement regime, where the confinement potential is larger than the Coulomb interaction between electron and hole (see section 2.2 and chapter 2.4.1 in [21]). These confinement energies depend on the specific form of the confining potential, as shown for QWs and QDs, and define the energy of the optical transitions.
The basics which are needed for further understanding the optical properties of the studied materials are described in the following sections. As explained above, the optical properties are mainly determined by the band structure. Specifically, the crystal structure, consisting of lattice and basis, and combined with symmetry operations, offers insights into the optical selection rules. In the following, the electronic band structures of group III-V zincblende QDs and group IV hexagonal transition metal dichalcogenide monolayers are discussed in detail. Furthermore, the concepts of spin and angular momentum coupling are explained, to give a more detailed insight into the band structure (details in section 2.3).

2.1.3 Band structure of InGaAs quantum dots

To determine the optical properties of zero-dimensional (0D) InGaAs quantum dots, the bulk material is considered first, hereafter the peculiarities of the quantum dots (QDs) follow. Details on the samples may be found in section 3.4.1. The QDs consist mainly of gallium arsenide (GaAs), which is a group III-V direct bandgap semiconductor. This material crystallizes in the **zincblende crystal structure**, which consists of two fcc Bravais lattices. The first Brillouin zone of the fcc-lattice has the shape of a truncated octahedron, where the reciprocal lattice is the body-centered (bcc) lattice (see chapter 2 in [45]). The crystal basis of the zincblende structure is formed by two atoms: the group III-metal (In, Ga or Al) is located at the position $(0, 0, 0)$, while the group V-nonmetal (As) is located at $a/4(1, 1, 1)$, shifted by a quarter of the lattice constant a. This crystal basis is displayed in figure 2-3 (a). The bonding between the atoms is mainly covalent and slightly ionic [5]. Due to the hybridization of the atomic s- and p-orbitals, the binding orbitals point towards the corners of a tetrahedron. This leads to tetrahedrally coordinated atoms in the zincblende structure, which means that each metal atom is bonded to four nonmetal atoms and vice versa. The fcc lattices are formed individually by both atom types, with the sublattices of the atoms shifted by a quarter of the diagonal of the cube ($a/4$) along the diagonal. Together they form a diamond lattice type where the atomic sites are occupied by alternating atoms. Due to the diatomic basis, such zincblende structures lack an inversion center, which lowers their symmetry so that they are represented by the tetragonal point group T_d [22]. The symmetry operations are further reduced for low-dimensional zincblende structures: two-dimensional QWs belong to the D_{2d} group, while lens-shaped self-assembled QDs are described by the C_{2v} group. Further elongated zincblende QDs are only symmetric regarding the identity operation and a twofold rotation about the z-axis; hence, they belong to the C_2 point group.
As depicted in figure 2-3 (b), the **direct bandgap** in zincblende structures is located **at the Γ-point** at $\vec{k} = 0$ (see also chapter 8.8 in [5]). In systems with cubic symmetry,

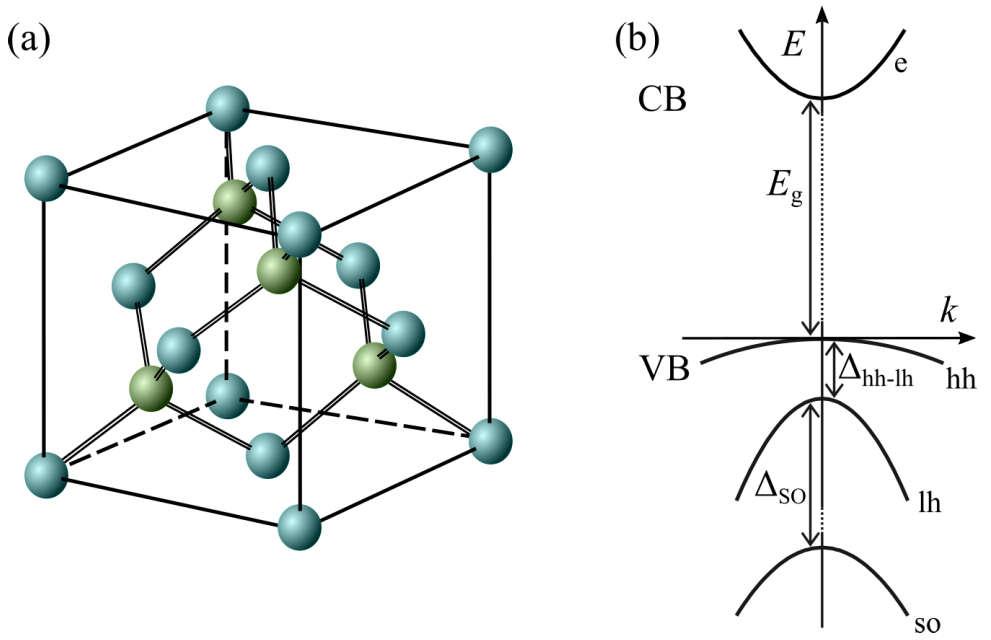

Figure 2-3: Scheme of the (a) crystal structure and (b) band structure at the Γ-point, ($\vec{k} = 0$) of a typical group III-V zincblende semiconductor. The atoms in the zincblende crystal structure are the group III-metal (In, Al, or Ga) in blue, and the group V-nonmetal (As) in green. The shown bands are the conduction band (CB) [electron (e)] and the heavy-hole (hh), light-hole (lh) and spin-orbit (SO) split-off valence bands (VB), which are separated by the respective energy splitting Δ. After Fig. 2.2 in [23] and Fig. 3.1 in [24].

the bands evolve from the hybridization of the outer, weakly bound atomic orbitals: the conduction band (CB) originates from the s-like atomic states and the valence band (VB) emerges from the p-like states. Specifically, the CB is formed by a twofold subband with orbital s-symmetry (orbital angular momentum $l = 0$). This subband is spin-degenerate ($|s| = 1/2$) aside from a negligibly small wavevector-dependent spin splitting resulting from the absence of an inversion center. Hence, the CB states allow for defining spin states, which are invariant under all symmetry transformations of the lattice (pure spin basis eigenstates). Note that a realistic modeling of the lowest electron state leads to around 90 % s-level character, and even lower pure character for higher electron and hole states [46]. On the contrary, the diatomic basis leads to eight subbands that form the top of the VB at the bandgap, arising from the atomic p-orbitals. Hence, all VB spin states obtain orbital p-symmetry (orbital angular momentum $|l| = 1$). While two subbands are rather low in energy and may be neglected directly, the six upper subbands are degenerate in energy in a first approximation. These upper subbands are split due to SO coupling into a twofold and a fourfold degenerate subband. The twofold SO split-off subband with total angular momentum $j = l + s = \pm 1/2$ is considerably lower in energy by about $\Delta_{SO} = 340\,(380)$ meV in GaAs (InAs) [47], and, thus, may also be neglected. The fourfold degenerate subband with total angular momentum $j = \pm 3/2$ is degenerate at the Γ-point, but may be distinguished into two twofold **spin-degenerate subbands** according to its total angular momentum projection j_z. For finite wavevectors, these subbands split into two branches with different curvatures. The so-called light hole (lh) band has a large curvature, a low effective mass and a total angular momentum projection $j_z = \pm 1/2$, while the **heavy hole** (hh) band has a low curvature, a high effective mass and a total **angular momentum projection** $j_z = \pm 3/2$. Their different curvatures result from the different

involved p-orbitals: a stronger overlap of the orbitals leads to a higher band dispersion and a lower effective mass according to the tight-binding model [48]. The hh states consist of both p_x- and p_y-parts, but obtain distinct spin states: $\left|hh^{\pm}\right\rangle = \mp 1/\sqrt{2}\ (p_x \pm i p_y)$ [49]. Herein, the states $p_x = -1/\sqrt{2}\ (Y_{1,1} - Y_{1,-1})$ and $p_y = i/\sqrt{2}\ (Y_{1,1} + Y_{1,-1})$ consist of the spherical harmonics $Y_{l,m}$ with $l = 1$ and $m = 0, \pm 1$ (see section 2.3.1 on quantum numbers). Contrarily, both lh states consist of all three p-type parts and of both spin orientations. This weakens the optical selection rules for the lh states, e.g., allowing for circularly and linearly polarized interband transitions (see section 3.2.2 for selection rules).

The studied **self-assembled** zincblende QDs are typically **lens-shaped and flat**, leading to a strong confinement along the growth direction z. The QDs consist mainly of GaAs with a small inflow of indium arsenide (InAs) and are surrounded by GaAs. It has a larger bandgap than the InAs-interdiffused GaAs, so that the charge carriers are confined in the potential of the QDs. Their small sizes confine the electrons' wavefunctions and lead to a reduction in the density of states yielding discrete (quantized) energy levels. The growth by molecular beam epitaxy allows for the formation of QDs due to a mismatch of the lattice constants between the materials, but this also introduces strain in the nanostructure. Hence, the electronic band structure of the dots differs from the bulk system due to the influence of confinement and strain [25]. Specifically, the fourfold degeneracy at the Γ-point is lifted.
Considering first the effect of **spatial confinement**: The energy of all states is increased by the confinement energy, as can be seen from equation (2.5). The confinement in z-direction lifts the degeneracy of the hh and lh bands at the Γ-point, as the energy shift is inversely proportional to the effective mass of the band. Since the effective mass of the lh band is lower, it shifts to higher energies and, thus, above the hh band. Moreover, the parabolic in-plane confinement leads to an increase of the level spacing. Additionally, for small dots with a size of only a few nanometers, higher-order terms of the wavevector play a more important role in the energy dispersion and the coupling to bands with different angular momenta is enhanced [24]. Specifically, strong mixing occurs at large wavevectors between the relatively closely located hh and lh subbands. This mixing leads to deviations from the parabolic dispersion relation, and the total angular momentum is no longer a good quantum number (see chapter 3.1.3 in [24]). However, these effects are neglected here, as the assumption of a small wavevector works reasonably well for the studied QDs.
Secondly, uniaxial strain along $\vec{z}$ also affects the degeneracy of the hh and lh bands at the Γ-point [25]. Thereby, the hh-lh splitting effect of the confinement is often overcompensated by a **strain**-dependent energy splitting in self-assembled QDs. The strain effects may be approximated by a uniform hydrostatic-pressure shift and a uniaxial stress-induced VB splitting [50]. Specifically, uniaxial stretch shifts the lh band to lower energies, below the hh states. The opposite ordering is achieved by uniaxial compression. As the strain effect dominates against the subband reordering due to the asymmetric spatial confinement, so that the hh band is the topmost VB in the studied QDs. The lh and hh subbands in the QDs are split by about $\Delta_{\text{hh-lh}} = 10\,\text{meV}$ at $\vec{k} = 0$ [24]. The lower-energetic lh exciton states may thus be neglected for the excitation and emission of the QDs (using a laser with a linewidth of about $4\,\mu\text{eV}$). However, a small **admixture** of the lh to the hh states, and vice versa, must be taken into account [51]. Besides, in-plane strain, e.g., due to an elliptical QD shape, leads to a symmetry reduction, slightly

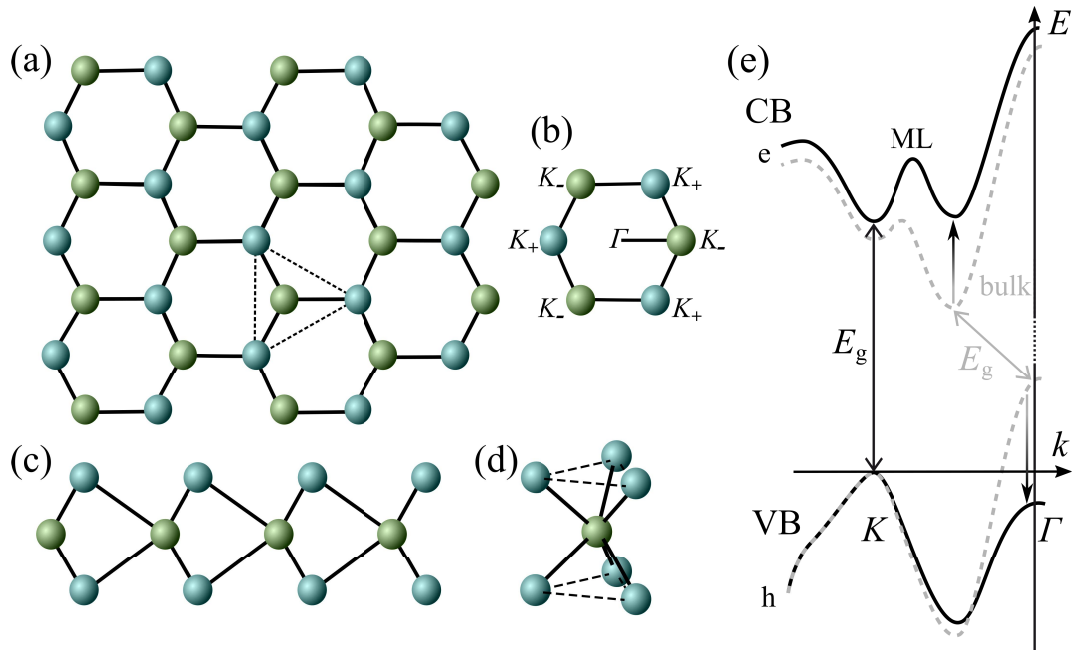

Figure 2-4: (a-d) Scheme of the crystal structure of a transition metal dichalcogenide semiconductor. The crystal structure, with the transition metal in green and the chalcogen in blue, is depicted from (a) top and (c) side view. The top view of the crystal structure includes the top view of the unit cell (dashed lines), compare (d). (b) Scheme of the in-plane Brillouin zone of a TMDC monolayer with symmetry points K_+, K_- and Γ. (d) Unit cell of a monolayer consisting of a single trigonal prism coordination unit. (e) Band structure scheme for the bulk (gray) and for a monolayer (black), whereby the bandgap shifts from indirect (Γ-Q transition) to direct (K-K transition). In analogy to Refs. [53, 54].

mixing the hh and lh states and generating non-polarized luminescence [51]. Thereby, the lh contribution increases the spin splitting of the hole and facilitates the action of the anisotropic electron-hole exchange interaction [52].

2.1.4 Band structure of 2D TMDC monolayers

The optical properties of two-dimensional (2D) transition metal dichalcogenide (TMDC, also TMD in literature) monolayers are determined starting with the bulk phase of these group VI semiconductors. The studied samples are composed of a transition metal (TM) and two chalcogen atoms, with the transition metal being either tungsten (W) or molybdenum (Mo) and the chalcogen being either sulfur (S) or selenium (Se). These semiconductors crystallize in a trigonal prismatic crystal structure, see unit cell in figure 2-4 (a) and (d). The unit cell of a monolayer consists of one trigonal prism coordination unit as depicted in figure 2-4 (d), while the unit cell of the 2H-bulk consists of two of these units. The 2H-polymorph form is the most stable layer structure of bulk TMDCs. Its unit cell consists of two single layers, where any TM atom is located on top of two chalcogen atoms of the following layer. Accordingly, the designation 2H corresponds to two layers in a unit cell with hexagonal symmetry. Seen from top, the single layers have a **honeycomb crystal structure** like graphene, with the crystal lattice consisting of a hexagonal close-packed (hcp) Bravais lattice, see figure 2-4 (a). The two-atomic crystal basis comprises one chalcogen atom and one TM atom, with neighboring hexagonal lat-

tice sites occupied with different atomic species. This breaks the inversion symmetry of the crystal for all odd layer numbers [55]. However, contrarily to graphene, a TMDC **monolayer** (ML) is composed of three hexagonally bonded sublayers of atoms: a plane of TM atoms sandwiched between two planes of chalcogen atoms, see figure 2-4 (c) and (d). Thereby, a single layer is also called triple layer or trilayer due to its three-atom thick structure X-TM-X. It may be seen as a **very thin quantum well**.
The atoms are ordered in a trigonal prismatic alignment, so that each chalcogen atom is bound to six TM atoms and each TM atom is bound to three chalcogen atoms. Very importantly, the in-plane bondings in the layers are of the rather strong covalent-ionic type, while the out-of-plane bonding between different layers is of the weak van der Waals (vdW) type. This has three important effects: firstly, the layers may be easily separated, so that MLs may be formed by peeling them off bulk materials (exfoliation). Secondly, different MLs may easily be stacked together with similar 2D materials to form vdW heterostructures. Thirdly, a direct bandgap emerges for the exfoliated MLs compared to the indirect bandgap of the bulk material. This is due to the different orbital contributions, as explained in the following paragraph. The corresponding symmetry operations of the bulk crystal are represented by the hexagonal D_{6h} point group, compared to the lower-symmetric D_{3h} group of the monolayer. The symmetry of the states at the K-points is even lower and characterized by the C_{3h} point group [8]. In reciprocal space, the lattice structure remains basically unchanged, as a Fourier transformation of the hcp lattice results in a 60° rotation but does not change any symmetries. Hence, the in-plane Brillouin zone is also of hexagonal shape, as shown in figure 2-4 (b). On the contrary to the well-known group III-V and II-VI semiconductors with a bandgap at the Γ-point, the **direct bandgap** is located **at the K-point** of the first Brillouin zone, see figure 2-4 (e). The band extrema at these points are further denoted as **valleys**.
As mentioned above, the **bandgap changes** from indirect (bulk) to direct (ML) due to a shift of the electronic band structure, leading to a huge increase of the PL. The conduction band at the Q-point shifts to higher energies and the valence band at the Γ-point shifts to lower energies for a decreasing layer number. On the contrary, the band structure at the K-point is not directly affected because of different orbital contributions to the band structure. The band structure at the Γ-point consists of p_z-orbitals from the chalcogen atoms and d_{z^2}-orbitals from the TM atoms. The p_z-orbitals of the chalcogen atoms, which lie at the outer edges of single layers, hybridize with states from neighboring layers, so that the electronic states delocalize. Hence, they are strongly affected by decreasing layer thickness. At the K-point, the electronic states are composed of the TM atoms d-orbitals, slightly mixed with the $(\mathrm{p}_x \mp i\mathrm{p}_y)$-orbitals of the chalcogen atoms. While the d-orbitals are strongly localized in the TM plane, the involved p-orbitals lie mostly in the plane of the chalcogen atoms. This prevents the hybridization with neighboring layers, so that these orbitals are insensitive to changes of the monolayer surroundings. Besides the indirect-to-direct bandgap transition, the whole band structure shifts upwards to higher energies. This shift results from the confinement effect through dimensionality reduction from bulk to 2D material, as follows from equation (2.5). The changes of the band structure from bulk to monolayer are illustrated in figure 2-4 (e).

Another important feature of TMDCs is that the SO coupling is strong. This is due to the relatively heavy elements, as compared to graphene, and the involvement of the TM d-orbitals. Details on the SO interaction are explained in section 2.3. The strong SO coupling and the absence of an inversion center have two effects: a splitting of the bands

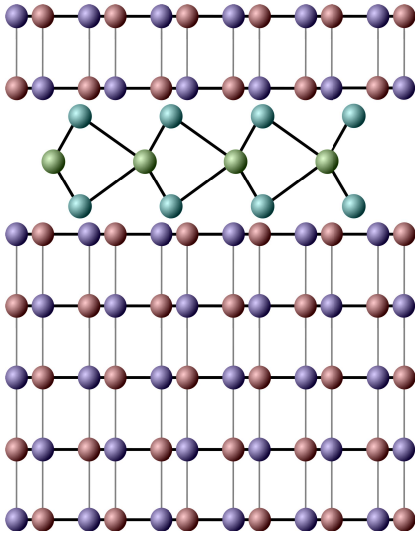

Figure 2-5: Scheme in side-view of a vdW heterostructure consisting of a TMDC monolayer encapsulated in several layers of hBN. The crystal structure of hBN, with boron in red and nitrogen in violet, is depicted, with weak interlayer vdW bonds (thin gray lines) and strong covalent bonds (black lines) within the layers. In analogy to Ref. [57].

and, therein, slightly different effective masses at the K-points for both bands. The bands of the monolayer are split at the K-point with opposite signs, resulting in a K_+ and a K_- valley. The Brillouin zone is thus separated into inequivalent corners, as shown in figure 2-4 (b). This splitting leads to a full lifting of the spin degeneracy in both valleys [56], see section 2.3.1 on spin-valley locking and valley pseudospin. Additionally, the split bands allow for the formation of two types of excitons, named **A- and B-exciton**, which involve holes from the upper and lower VB states, respectively. Yet, the B-excitons may be neglected in the following due to their large energy discrepancy, similar to the split-off and lh excitons in the QD structures. The impact of the SO splitting on the excitons are further elaborated in section 2.3.4.

The examined samples are partly encapsulated in few-layer hexagonal boron nitride (hBN) placed on a silicon substrate. hBN is chemically stable, thermally conductive, yet electrically insulating with a bandgap of around 6 eV, in the UV range [58, 59]. An **encapsulation with hBN flakes** enhances the thermal stability of the MLs [60], they get more robust towards high power densities [61] and the electron mobility increases [62]. hBN layers consist of hexagonal rings of alternating boron (B) and nitrogen (N) atoms, with strong covalent sp^2 bonds and a lattice constant similar to graphene [63]. The hexagonal crystal structure of hBN in top view is alike the one of TMDCs depicted in figure 2-4 (a). Bulk hBN has the same crystal lattice as graphite, with the hexagonal rings coincident in all layers (AB stacking, polytype 1H) [64]. The interatomic bonds between neighboring layers are very weak, compared to the strong covalent bonds with planar distribution within the layers. A joint heterostructure in side view, consisting of a TMDC ML encapsulated in hBN, is depicted in figure 2-5. The hexagonal structure allows for assembling different vdW heterostructures by stacking one on another without the need of lattice matching [57, 65]. Hereby, hBN is predominantly used to enhance the optical properties of the TMDC MLs by changing the dielectric screening [66, 67]. The top hBN layer protects the MLs from direct exposure to air, which reduces its degradation [62, 68], while the bottom hBN layer separates the MLs from the substrate, which blocks additional doping channels and suppresses defect-assisted nonradiative recombination [69]. Moreover, the atomically smooth surface of the hBN flakes without dangling bonds and charge traps reduces the number of impurities and traps for the MLs. Contrarily to other materials, the smaller lattice constant of hBN, with a mismatch of

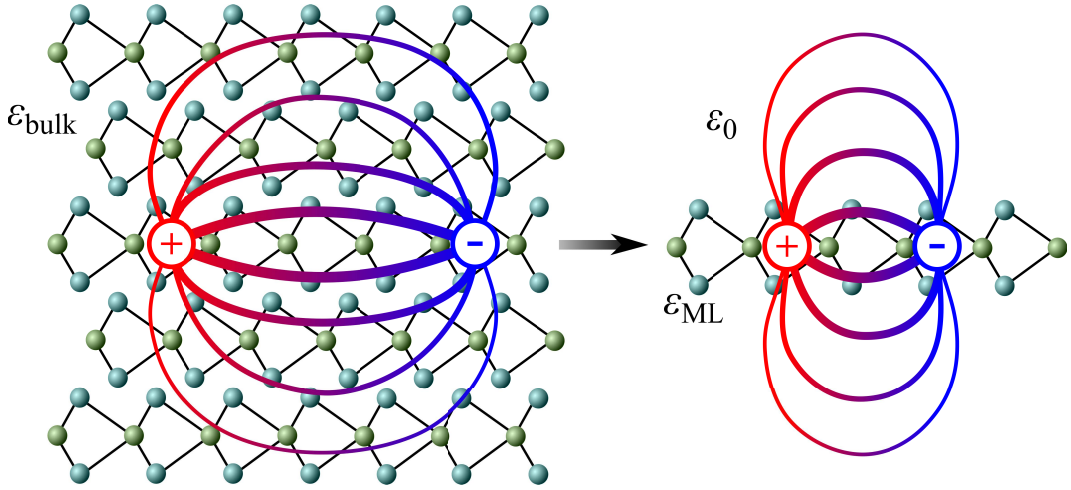

Figure 2-6: Scheme of the attractive Coulomb forces between electron and hole in TMDC structures. The relative permittivity ε of the structures is labeled by $\varepsilon_{\text{bulk}}$ for the bulk material (left) and ε_{ML} for a monolayer (right), with ε_0 for vacuum. After Fig. 1 in [75].

about $20-25\,\%$ to TMDCs, induces biaxial compressive strain in the MLs [70, 71]. This leads to red-shifts of the exciton emission and a reduction of the exciton binding energy [67]. However, the exciton transition energy stays nearly unchanged, as the reduction in exciton binding energy is practically compensated by an equivalent reduction in the free particle bandgap [67]. Furthermore, the hBN-encapsulation of the MLs leads to a narrowing of the exciton linewidth approaching 2 meV at low temperatures [72, 73] and it becomes more Gaussian [70]. Additionally, the trion intensity is lowered and the exciton luminescence strengthens due to a lower doping level of hBN compared to the substrate [70, 74]. Hereby, a high quality of the hBN is crucial, as it directly influences the minimally achievable linewidth and thus allows for observing subtle optical and spin-valley properties of the ML materials.

2.2 Excitons

The band structures of crystal electrons and holes have been described. In this section, the electromagnetic force between these charge carriers is examined, specifically, the electrostatic or electric Coulomb force. Since the charge carriers are confined in the same crystal volume, the Coulomb interaction between electron and hole leads to the formation of the so-called **exciton** (X), a **bound electron-hole pair**. It is a quasi-particle only existing in matter. The concept of an exciton is similar to a neutral hydrogen atom, consisting of an electron bound to a proton, see chapter 6.3 in [23]. Accordingly, the resulting states are quantized with principal quantum numbers n and orbital angular momentum l. However, as both particles have similar effective masses, an exciton is rather like a positronium (electron bound to its antiparticle, the positron).
Basically, there are two types of excitons: the tightly bound Frenkel exciton, that is localized at one unit cell, and the weakly bound Wannier-Mott exciton, which is larger than a unit cell. The former exciton kind typically occurs in materials with a relatively small dielectric constant and is thus neglected in the further. The latter exciton is depicted in figure 2-6 (left). The exciton as a whole may move through the crystal and

transport energy, but, as it is electrically neutral, it does not transport charge. However, charged excitons, or **trions**, which are bound states of an exciton with another free crystal electron or hole, do transport charge. They consist of either two electrons and one hole or one electron and two holes, depending on the doping of the material. Moreover, bound excitons may form higher complexes like **biexcitons**, consisting of two excitons, and higher multi-excitons. These exciton complexes become relevant specifically in chapter 5. Note that excitons are bosons with integer spin, as they consist of two fermions with half-integer spin, while trions remain fermionic quasi-particles.
The single-particle, electron-hole picture of an exciton consisting of noninteracting electron and hole wavefunctions (two-particle state) may not be accurate enough to predict exciton energies or wavefunctions. Hence, it may be necessary to use the two-particle, excitonic picture, where the exciton is represented as a single-particle eigenstate [76, 77]. Switching from the electron-hole picture to the exciton picture allows for understanding the interaction with light and other particles, as excitons and their related bound states are important in determining the optical properties of semiconductors, see chapter 6.3 in [23]. Thereby, the Coulomb interaction, treated in the following section, has different impacts depending on which type of this electron-hole interaction is regarded. It may be distinguished into long-range and short-range coupling [8]. The long-ranged part of the Coulomb force acts at large interparticle distances (small wavevectors) and are determined mainly by the envelope function of the exciton. The short-ranged part denotes the contribution from the overlap of electron and hole wavefunctions within one or a few unit cells (large wavevectors). This part is sensitive to the particular form of the Bloch waves. Usually, the short-ranged part of the direct interaction is considered together with the corresponding part of the exchange interaction. This interaction is also based on the Coulomb interaction, combined with the Pauli Exclusion Principle, see section 2.2.3. It is, however, not a true force, as it lacks a force carrier. It is rather a quantum-mechanical effect wherein identical fermions experience repulsion, while identical bosons experience attraction.

2.2.1 Direct Coulomb interaction

The **direct, long-ranged term** of the Coulomb interaction between the electron and the hole has two effects: it induces a self-energy contribution (see section 2.2.2) and leads to the **formation of excitons**. An exciton (X) is an electron-hole-pair bound together by the attractive Coulomb interaction and may be created by, e.g., optically exciting an interband transition in a semiconductor, see section 3.1. Thereby, the exciton has only a certain lifetime, until the excited electron in the CB recombines with the hole in the VB [26]. Note that to conserve energy and wavevector during photoexcitation, the process has to happen at the intersection between the radiation and the exciton dispersion curves. Thereby, the interaction between photon and exciton causes a mixed mechanical-electromagnetic wave known as an exciton-polariton, see chapter 6.3. in [23]. This interaction requires a nonzero electric dipole moment of the excitons.
The attractive Coulomb interaction between the oppositely charged electron and hole leads to an energy gain of the bound state compared to the spatially separated charge carriers. This energy gain is defined as the **binding energy** of the bound state and lowers the bandgap [78]. In literature, the binding energy is sometimes denoted as dissociation energy, as it is equal to the energy amount required to separate a particle complex.

As excitons are formed energetically below the renormalized free-particle bandgap, the lowest-energy excitonic feature is referred to as optical bandgap, whereas the energy necessary to create an unbound electron-hole pair in the continuum is known as free-particle bandgap [8]. Hence, excitons can be seen as an absorption line below the bandgap [26].

The optical properties of excitons are described by including the Coulomb interaction in the Hamiltonian of the Schrödinger equation (2.1). The Hamiltonian describes the independent motion of the charge-carrying electron and hole in the effective mass approximation and the Coulomb interaction of the electron-hole pair:

$$\hat{H} = -\frac{\hbar^2}{2m_{\mathrm{eff,e}}}\nabla_{\mathrm{e}}^2 - \frac{\hbar^2}{2m_{\mathrm{eff,h}}}\nabla_{\mathrm{h}}^2 - \frac{e^2}{\varepsilon\left(|r_{\mathrm{e}} - r_{\mathrm{h}}|\right)}. \tag{2.10}$$

The first two terms denote the kinetic energy terms of the single electron and hole, respectively, which scale with $\propto 1/R^2$ [79]. The effective masses of electron and hole are denoted via $m_{\mathrm{eff,e}}$ and $m_{\mathrm{eff,h}}$, see equation (2.3). The last term denotes the Coulomb energy, renormalized by the dielectric constant ε, where the strength of the interaction depends on the spatial distance between the two charge carriers, $\propto 1/R$. In nanostructures, the confinement potentials $V_{\mathrm{e}}(\vec{r}_{\mathrm{e}})$ of the electron and $V_{\mathrm{h}}(\vec{r}_{\mathrm{h}})$ of the hole have to be added. Additionally, the effects of inhomogeneous strain, band mixing, the piezoelectric potential, and others have to be taken into account. The confinement may be represented by either a two-dimensional angular box for a QW or a spherical potential box with diameter D for QDs with a similar confinement in all directions, see section 2.1. Accordingly, the exciton wavefunction is modulated by an envelope wavefunction, which reflects the relative electron-hole motion, and, thus, the spatial confinement which the charge carriers experience [79].
The resulting energy levels vary depending on the dimensions of the nanostructures compared to the **excitonic Bohr radius** a_{B}. The Bohr radius, originally, is a length scale which is approximately equal to the distance between the nucleus and the electron in a hydrogen atom. Likewise, the excitonic Bohr radius denotes the electron-hole separation in materials. Compared to the hydrogen atom, the separation distance is much larger due to the screening of the Coulomb force by other electrons and the smaller effective masses of electron and hole, which also lead to comparatively low binding energies. Specifically, the excitonic Bohr radius $a_{\mathrm{B}} = \hbar^2\varepsilon/\mu_{\mathrm{X}}e^2$ depends on the **reduced mass** $\mu_{\mathrm{X}} = m_{\mathrm{eff,e}}m_{\mathrm{eff,h}}/(m_{\mathrm{eff,e}} + m_{\mathrm{eff,h}})$ of the exciton and the dielectric constant (or relative permittivity) of the semiconductor ε. Hence, the excitonic size varies depending on the properties of the material. When the spatial confinement of the nanostructure is comparable to the exciton Bohr radius or smaller, the energy levels of electrons and holes are quantized independently, and the Coulomb interaction is less dominant for the excitonic properties. Thus, the different dependences on the distance R in equation (2.10) allow for differentiating between three different regimes: weak, intermediate and strong confinement [41]. In the studied nanostructures, the excitons are either strongly confined in z-direction and may be weakly confined laterally (MLs), or strongly confined in all directions (QDs), whereas the intermediate confinement regime is not relevant in this thesis.

2.2.2 Spatial confinement regimes

The carrier confinement of the nanostructures leads to a spatial overlap of the wavefunctions of the confined particles. In this way, the electron-hole Coulomb interaction is enhanced, which increases the binding energy of the particle complexes and their oscillator strength. In the **weak confinement** regime with $R > a_\mathrm{B}$, and also in the bulk, the electron and the hole form an exciton, which is characterized by a correlated motion of the electron-hole pair. This is due to the comparatively strong Coulomb interaction and the weak confinement energies of the single electrons and holes [79]. Hence, the optical spectra are determined by the quantum confinement of the exciton [41]. The **correlated motion** of the exciton may be decomposed into a center-of-mass (CM) motion, expressed by the CM coordinate $\vec{R}_\mathrm{CM} = \left(m_\mathrm{eff,e} r_\mathrm{e} + m_\mathrm{eff,h} r_\mathrm{h}\right) / \left(m_\mathrm{eff,e} + m_\mathrm{eff,h}\right)$, and by a relative motion around the center of mass, expressed by the relative coordinate $\vec{r}_\mathrm{r} = r_\mathrm{e} - r_\mathrm{h}$ (see chapter 6.3 in [23]). In bulk, the exciton CM motion has translational invariance, as the Coulomb interaction depends only on the relative coordinate of the electron and hole. Thereby, wavevector conservation applies to the exciton wavevector $\vec{K}_\mathrm{X} = \vec{k}_\mathrm{e} + \vec{k}_\mathrm{h}$, but not to the single electron and hole wavevector, $\vec{k}_\mathrm{e}$ and $\vec{k}_\mathrm{h}$, respectively. This also applies to angular momentum conservation. Also in the weak confinement regime, the electron-hole relative motion is regarded as non-confined and similar to that in the bulk. Hence, in QWs and large QDs the translational invariance in-plane is preserved, while wavevector conservation does not apply to the confined direction, here $\vec{K}_{\mathrm{X},z}$.
The exciton wavefunction $\Psi_\mathrm{X} = \Phi(\vec{r}_\mathrm{r})\Psi(\vec{R}_\mathrm{CM})$ may be represented as the product of the wavefunctions of the relative motion, corresponding to the ground or low excited state, and of the CM motion, that is subjected to the boundary conditions of the nanostructure [80]. The wavefunction of the CM motion is given by the product of the single electron and hole wavefunctions, $\Psi_\mathrm{e}(\vec{r}_\mathrm{e})$ and $\Psi_\mathrm{h}(\vec{r}_\mathrm{h})$, respectively. The relative motion of both charge carriers is expressed by an envelope wavefunction $\Phi_\mathrm{env}(\vec{r}_\mathrm{r})$, that may be considered as the bulk exciton wavefunction [79]. Thus, the exciton wavefunction may be expressed as:

$$\Psi_\mathrm{X}(\vec{K}_\mathrm{X}, \vec{r}) = \Omega^{-1/2}\ \mathrm{e}^{i\vec{K}_\mathrm{X}\vec{R}_\mathrm{CM}}\ \Phi_\mathrm{env}(\vec{r}_\mathrm{r})\ \Psi_\mathrm{e}(\vec{r}_\mathrm{e})\Psi_\mathrm{h}(\vec{r}_\mathrm{h}), \tag{2.11}$$

with the normalization factor $\Omega^{-1/2}$ corresponding to the volume of the unit cell Ω [23, 37]. Therein, the plane wave-factor describes the free propagation of the exciton through the crystal [5]. The single-particle states of the hole in the VB and of the electron in the CB may be decomposed into the respective products of Bloch wave and envelope wavefunction [81], compare equation (2.4). In spherical symmetry, the exciton envelope function is given by $\Phi_\mathrm{env}(\vec{r}, \theta, \phi) = Y_{l,m}(\theta, \phi)R(\vec{r})$, a product of spherical harmonics and a radial Bessel function [21]. Hence, the Bloch waves describe the bulk properties of the semiconductor, whereas the envelope function accounts for the spatial confinement of the nanostructure. The symmetry of the exciton wavefunction results from the direct product of the individual symmetries, which may be used to determine optical transitions [5, 21]. As, strictly speaking, the angular momentum is no longer a good quantum number in a crystal, the relative motion of the exciton has to be described by irreducible symmetry representations. However, these symmetries may be weakened by the confinement of the nanostructure. In addition, real exciton eigenstates in nanostructures never consist of pure states, but rather of a mixture of basis states with different envelopes and spin states. Yet, they are typically labeled by their corresponding spherical part [82].

The total energy of the exciton is the sum of the energy $E_{\vec{R}_{\mathrm{CM}}}$ of the CM coordinate $\vec{R}_{\mathrm{CM}}$ and the energy $E_{\vec{r}_{\mathrm{r}}}$ of the relative coordinate $\vec{r}_{\mathrm{r}}$. The energy $E_{\vec{R}_{\mathrm{CM}}}$ represents the kinetic energy of the CM motion, analogous to equation (2.3). The energy $E_{\vec{r}_{\mathrm{r}}}$ is composed of the minimum energy of the continuum states, which is the bandgap energy E_{g}, and the hydrogen-like binding energy E_{B}. Thus, the ground state energy E_{X} of an exciton is given by:

$$E_{\mathrm{X}} = E_{\vec{R}_{\mathrm{CM}}} + E_{\vec{r}_{\mathrm{r}}} = \frac{\hbar^2 \vec{K}_{\mathrm{X}}^2}{2M_{\mathrm{X}}} + E_{\mathrm{g}} - E_{\mathrm{B}}, \quad \text{with} \quad E_{\mathrm{B,bulk}} = \frac{\mu_{\mathrm{X}} e^4}{2\varepsilon^2 \hbar^2 n^2}, \tag{2.12}$$

the exciton mass $M_{\mathrm{X}} = m_{\mathrm{eff,e}} + m_{\mathrm{eff,h}}$ and the main quantum number n [23, 43]. The energy levels resemble the dispersion curve of a free electron but are determined by the total mass of the exciton. This mass is sensitive to the heavier particle mass, usually the hole. The binding energy is determined by the effective charge $e/\sqrt{\varepsilon}$, which is screened by the static charges of the semiconductor, and the reduced mass μ_{X} of the exciton. This mass is sensitive to the lighter particle mass, usually the electron [83]. For a weakly confined exciton in a nanostructure, the binding energy changes to:

$$E_{\mathrm{B,QW}} = \frac{\mu_{\mathrm{X}} e^4}{2\varepsilon^2 \hbar^2 (n - 1/2)^2} \quad \text{and} \quad E_{\mathrm{B,QD}} = \frac{\mu_{\mathrm{X}} e^4}{32\pi^2 \varepsilon^2 \hbar^2}, \tag{2.13}$$

for a 2D QW or ML [75] and for a 0D quantum dot with $n = 1$ [84], respectively. In a QW, the binding energy increases due to the **quantization** of the exciton CM motion, up to a factor of four in the 2D limit [85]. In QDs, however, the leakage of the wavefunctions into the barriers decreases the exciton binding energy [38].

In the **strong confinement** regime with $R < a_{\mathrm{B}}$, the electron and hole are only weakly correlated. The exciton energy levels may be obtained by treating the electron and hole confinement independently and the Coulomb interaction as a perturbation [79]. It can be approximated via:

$$E_{\mathrm{X}} = E_{\mathrm{e}} + E_{\mathrm{h}} - J_{\mathrm{eh}} + \delta_{\mathrm{corr,X}} \tag{2.14}$$

with the single electron (hole) confinement energy E_{e} (E_{h}), according to equation (2.3), and the energy correction $\delta_{\mathrm{corr,X}}$. The direct Coulomb integral $J_{\mathrm{eh}} \propto e^2/\varepsilon r$ lowers the exciton energy, like the binding energy in equation (2.12). The optical spectra are considered as spectra of transitions between electron and hole levels, which are slightly lowered by Coulomb interaction as a first-order perturbation. As seen in equation (2.10), the Coulomb energy increases with spatial confinement, when the wavefunctions of electron and hole obtain a larger spatial overlap. Yet, the strongly confined excitons are modified by the dielectric confinement of the surrounding. The electric field between electron and hole largely runs through the surrounding material, as depicted in figure 2-6. This **reduced screening**, or dielectric confinement effect, further enhances the binding energy and the oscillator strength [79]. The exact form of the exciton energy depends on the single-particle wavefunctions of the confined electron and hole ground states, and may be calculated using multi-band $\vec{k} \cdot \vec{p}$ theory including strain, SO interaction, band mixing, interband coupling, and piezoelectricity [42, 86, 87].
The energy correction $\delta_{\mathrm{corr,X}}$ is governed by the self-polarization energies E_{pol} of the electron and hole. The energies $E_{\mathrm{pol,e/h}} \propto e^2/\varepsilon r$) also depend on the surrounding material and further correlation effects (see section 2.2.3) [21, 88]. The self-polarization energies, or **self-energy contribution** to the absolute energies of electron and hole, relate to

the repulsive interaction between identical charges and increases the bandgap [8]. The contribution may be understood as a repulsive interaction between each particle with its own image charges and arises from the dielectric mismatch between the nanostructures with dielectric constant ε and their surroundings [38]. Moreover, the mutual interaction energy between an electron and a hole via image charges may also contribute to the surface polarization energy [79].
The **correlation effect**, or Coulomb correlation minimizes the total energy by balancing the kinetic energy of the involved single-particle states and their mutual Coulomb attraction or repulsion (see chapter 7.8 in [88]). Specifically, the single-particle orbitals change their shape and location in response to the Coulomb interaction. Thereby, the probability distribution of a charge carrier is allowed to become dependent on the positions of the other carriers. The change of shape often happens by mixing higher excited state configurations into the ground state configuration. The correlation effect is larger, the less similar electron and hole wavefunctions are and the smaller their spatial overlap is. It further depends on the spectral density of electron and hole states [88]. The correlation effect is specific for each particle type and leads to a change in the total particle energy.
For ground-state excitons, the binding energy is always positive, whereby higher complexes, like trions and biexcitons, may form anti-binding states. This is due to the repulsive electron-electron and hole-hole interactions, which may overcompensate the attractive electron-hole interaction and lead to negative binding energies. Furthermore, additional correlation and exchange effects between the exciton and the unpaired electron or hole, or of the two neutral excitons, must be considered. Generally, the binding energies of higher complexes are much smaller than the exciton binding energy, with the trion binding energy typically about 10 % of the exciton binding energy [89]. Hence, trions and higher states can be seen as absorption lines slightly below the exciton, whereby the specific arrangement in the studied nanostructures is elaborated in section 2.3.4.

The different confinement regimes further affect the transition **oscillator strength** of the exciton in the studied nanostructures and, thus, their interaction with light. In a classical model, the oscillator strength describes the fraction of oscillators that are coupled to the electromagnetic field [24]. More precisely, the oscillator strength denotes the probability of the emission or absorption of electromagnetic waves in transitions between different energy levels. Thereby, the exciton oscillator strength $f_{\mathrm{X}} \propto |\langle f|\,\hat{p}\,|i\rangle|^2$ is proportional to the square of the transition dipole moment resulting from the matrix element of the momentum operator between the initial and final states [79]. Specifically, the transition matrix element is a product of an overlap integral of the corresponding envelope functions and a momentum matrix element of the Bloch states [24]. A large oscillator strength leads to sharp excitonic transitions, indicating long exciton coherence times and well-defined polarization characteristics [79]. Yet, the oscillator strength scales inversely with the particle lifetime, so that a low oscillator strength relates to a long decay time or radiative lifetime [16]. Besides, the oscillator strength depends on the structure and symmetry of the states involved in the transition, besides the population density of the energy levels.
In the bulk, the oscillator strength is proportional to the volume in $\vec{k}$-space required to form an exciton, the excitonic Bohr radius a_{B}. This corresponds to the exciton transition probability being proportional to the probability of finding an electron and a hole in the same unit cell of the crystal [38]. In nanostructures, the oscillator strength $f_{\mathrm{fi}} \propto$

$(a_B/R)^3 f_X$ depends on the spatial confinement [38]. Therein, the transition dipole moment is determined by the momentum matrix element of the zone-center Bloch functions and the overlap integral of the envelope functions. Hence, the exciton transition probability is proportional to the spatial restriction of the carrier motion in the confined QD volume and to the overlap integral of the electron and hole eigenfunctions [90]. In the weak confinement regime, the oscillator strength of excitons is proportional to the confined volume, as the exciton acquires the sum of oscillator strengths of all lattice sites [91]. The involved transition dipole moments of the atoms add up and they form a coherent superposition, leading to a large transition dipole moment over the exciton volume [79]. This corresponds to the summation of all states contributing to the observed transition [38]. Note that the increase of the oscillator strength is only valid for the lowest transition, which typically has a larger oscillator strength than the higher excited states, and not for the whole ensemble of optical transitions.
In the strong confinement regime, the oscillator strength is proportional to the square of the electron and hole envelope function overlap [91]. Hence, the oscillator strength of the exciton increases for smaller sizes or larger spatial confinements, when the overlap between electron and hole wavefunctions is larger. A significant spatial overlap of the wavefunctions is a major condition for a large transition dipole moment, and, thus, a large polarizability, besides symmetry requirements. However, further shrinking the spatial confinement below the minimum extension of the confined particle wavefunction leads to a decrease of the oscillator strength, as the particle wavefunctions start to penetrate the barriers and the charge distribution smears out [38].

2.2.3 Exchange Coulomb interaction

In the previous section, the direct contribution of the electromagnetic Coulomb interaction has been discussed. This long-range electrostatic interaction between the electron and hole contributes dominantly to the exciton binding energy and depends on the dimensionality and dielectric properties of the semiconducting materials [8]. Adding the **Pauli exclusion principle** to the Coulomb interaction leads to the so-called exchange contribution of the Coulomb interaction. It is a consequence of the non-orthogonality of electron and hole Bloch functions within the crystal unit cell [92]. The exchange contribution accounts for about a tenth to the whole Coulomb interaction [8]. The Pauli exclusion principle denotes the fact that no more than one particle per quantum state is allowed for fermions (particles with half-integer spin), e.g., electrons. As electrons among themselves are indistinguishable, the wavefunction of the whole many-electron system has to be antisymmetrized with respect to permutations of the particles [8]. Hence, the exchange symmetry requires that two electrons in a joint state either differ in their spin orientation or the coordinate part of their wavefunction is antisymmetric. This means that the probability of finding two electrons with parallel spin very close to each other is small compared to the opposite case with antiparallel spins (symmetric wavefunction). Thus, electrons with parallel spins are better separated in space and their repulsion energy due to direct Coulomb interaction is lower [26]. A scheme of this quantum-mechanical effect is depicted in figure 2-7.
The exciton energy hence depends on the orientation of electron and hole spins, resulting in the **exciton fine structure**. By coupling the orbital part of two wavefunctions, e.g., electron-electron, hole-hole or electron-hole wavefunctions in (multi-charged) excitons,

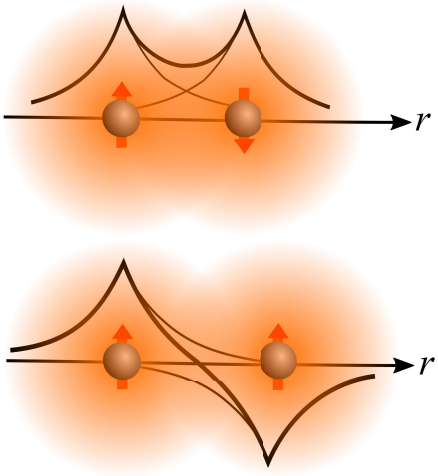

Figure 2-7: Schematic representation of two electrons (orange spheres) in a joint symmetric (top) and anti-symmetric (bottom) state. The exchange interaction leads to a repulsion between the states with same spin direction (denoted by arrows), so that their separation in space is larger, and, thus, the state is lower in energy. The black curves denote the wavefunctions in space. In analogy to Ref. [23].

their angular momenta add up and the resulting state may arrange in different forms. The effective spin interaction between the spins is described by a Heisenberg-like form [11]:

$$\hat{H}_{\mathrm{ex}} = J_{\mathrm{ex}} \hat{S}_1 \cdot \hat{S}_2. \tag{2.15}$$

The exchange splitting J_{ex} between the spins may reach up to $0.1 - 1\,\mathrm{meV}$ for two interacting electron spins $\hat{S}_1, \hat{S}_2$ in coupled QDs [93]. The interaction leads to the so-called singlet and triplet states of the excitons and trions, whereas in excitons the singlet state is spin-allowed and the triplet states are spin-forbidden. Herein, the singlet states can be reached from the ground state by an electric dipole transition, and they are thus electric-dipole allowed, optically active or bright, while the triplet states cannot be reached and are termed as electric-dipole forbidden, optically inactive or dark. Note that dark states may also be momentum-forbidden, when their CM momentum exceeds the light cone or when the electron and hole reside at different valleys of the Brillouin zone [94]. The anti-symmetric or spin singlet exciton state has total spin 0, while the symmetric or spin triplet state has total spin 1. According to its name, the triplet state has an antisymmetric orbital wavefunction and consists of three states distinguished by their total angular momentum projection $0, +1$ and -1. Likewise, trion states are denoted as symmetric or antisymmetric in accordance with the symmetry of their envelope function, dividing them into spin-singlet and -triplet states.
The general form of the electron-hole exchange interaction of a bulk exciton is formed by [95, 96]:

$$\hat{H}_{\mathrm{ex,eh}} = -\sum_{i=x,y,z} \left(a_{\mathrm{ex},i} \hat{J}_{\mathrm{h},i} \hat{S}_{\mathrm{e},i} + b_{\mathrm{ex},i} \hat{J}^3_{\mathrm{h},i} \hat{S}_{\mathrm{e},i} \right), \tag{2.16}$$

with the spin-spin coupling constants $a_{\mathrm{ex},i}$ and $b_{\mathrm{ex},i}$. Typically, the cubic terms are much smaller than the linear terms and may be neglected [95]. For lens-shaped self-assembled QDs with C_{2v} symmetry, the electron-hole exchange splitting between the optically active and inactive exciton states is also denoted by δ_{bd} and arises from the short-range electron-hole Coulomb exchange interaction, or δ_0 when it also includes long-ranged contributions [96]. The electron-hole exchange interaction may then be written as an effective spin Hamiltonian [24, 93, 97]:

$$\hat{H}_{\mathrm{ex,eh}} = 2\delta_0 \hat{J}_{\mathrm{h},z} \hat{S}_{\mathrm{e},z} + \Delta_{\mathrm{b}} (\hat{J}_{\mathrm{h},x} \hat{S}_{\mathrm{e},x} - \hat{J}_{\mathrm{h},y} \hat{S}_{\mathrm{e},y}) + \Delta_{\mathrm{d}} (\hat{J}_{\mathrm{h},x} \hat{S}_{\mathrm{e},x} + \hat{J}_{\mathrm{h},y} \hat{S}_{\mathrm{e},y}), \tag{2.17}$$

with the total angular momentum projection operator $\hat{J}_{\mathrm{h},i}$ of the hole and the spin projections $\hat{S}_{\mathrm{e},i}$ of the electron, see section 2.3.1. The in-plane anisotropy of the QDs leads to a further splitting of the optically active states with the anisotropic exchange interaction splitting δ_{b}, and a splitting δ_{d} of the optically inactive states [93]. The electron-hole exchange splitting δ_0 between the exciton states may reach up to 0.05 meV in GaAs QDs and 0.2 meV in InAs QDs [24].
Furthermore, the exchange interaction may be divided regarding its influence on the spin properties into isotropic and anisotropic parts [98]. The isotropic carrier-carrier exchange interaction conserves the spin and, e.g., provides a spin flip-flop of both carrier spins [98]. The anisotropic exchange interaction requires a symmetry reduction, e.g., resulting from spatially shifted probability densities of two spin carriers. This lifts angular momentum conservation and allows for spin non-conserving coupling. It appears in crystals and nanostructures without inversion symmetry [99, 100], where angular momentum conservation applies only to the total angular momentum due to SO interaction, see section 2.3.2. This leads to spin relaxation and polarization changes. For example, an increased anisotropic exchange, e.g., due to an elongated shape or interface fluctuations in QDs, splits the circularly polarized exciton transitions into a linearly polarized doublet [24, 101]. Although this **spin-dependent splitting** for neutral, charged, and higher exciton complexes is typically only about several tens of µeV or less [26], a thorough understanding of the fine structure is necessary to determine the excitonic eigenstates and the resulting polarization direction and amplitude of the emitted or absorbed photons. Besides, by analyzing the exciton fine structure, conclusions about the asymmetry of the nanostructures may be drawn.

The spin-dependent splitting of the energy levels is further affected by the interplay between the exchange interaction and the reduced dimensions and symmetry of the nanostructures. Like the direct Coulomb term, the exchange interaction may be divided into different parts: The long-ranged part of the Coulomb-exchange term is of electrodynamic nature and corresponds to the calculation of the Coulomb interaction up to the dipole term. It is interpreted as the interaction of an exciton, as a microscopic dipole, with its induced electromagnetic field in the process of virtual electron-hole recombination [8]. In bulk semiconductors, the long-ranged part splits the bright exciton into a longitudinal and a transverse component [102]. In low-dimensional structures, e.g., III-V quantum wells, this splitting is negligibly small. However, the effect enables efficient valley depolarization in TMDC MLs, where the long-range exchange interaction is enhanced owing to the tighter binding of the electron to the hole in the exciton [8, 56]. This enables an additional fine structure of the bright exciton into upper and lower bright branch, whereas the upper (lower) couples to light with longitudinal (transversal) polarization and the upper branch exhibits an extraordinary strong dispersion within the light cone [56, 103]. Similarly, the dark states show a splitting into truly dark and gray exciton states, which is due to the short-range exchange interaction [104]. In QDs, as a consequence of translational symmetry loss, the long-ranged part is highly dependent on the size and shape of the nanostructures and may be affected by surface and screening effects [79, 92].
At short range, the exchange interaction strongly depends on the spin (and valley) states of the particles. Both the short-ranged part of the direct interaction and the exchange interaction contribute to the total excitonic energies and the splitting between optically bright and dark exciton states [8, 105], singlet and triplet trion states [106] (see sec-

tion 2.3). Due to the strong quantization of the electron and hole states in QDs, the electron-hole exchange splitting increases and leads to linearly polarized bright exciton states at zero magnetic field [26]. However, despite the small size of self-assembled QDs, the contribution of the short-ranged parts to the exciton splitting is estimated to only about 10 %, in the µeV-range, and only about 1 % to the exciton binding energy [92]. Moreover, note that a separation into long-ranged and short-ranged parts is only valid for large crystallites, and a strict division may not be suitable in the studied nanostructures [92]. The size of the exchange splitting δ_0 may be determined using the Zeeman effect, see chapter 4, where it is also termed as zero-field offset.

2.2.4 Excitons in InGaAs quantum dots and 2D TMDC monolayers

In this section, the general properties of the excitons in III-V semiconductor QDs and in TMDC MLs are introduced. Their respective exciton fine structures are presented in detail in section 2.3.4, as they involve the concept of spin and angular momentum coupling (details in section 2.3).

Considering first the **InGaAs QDs**: the exciton Bohr radius in the corresponding bulk materials is typically much larger than the lattice constants. The exciton radius is on the order of tenth of nanometers ($a_\mathrm{B} = 37\,\mathrm{nm}$ in bulk InAs [107], $a_\mathrm{B} = 11\,\mathrm{nm}$ in bulk GaAs [24]), compared to lattice constants of $a_\mathrm{GaAs} = 0.57\,\mathrm{nm}$ in GaAs and $a_\mathrm{InAs} = 0.61\,\mathrm{nm}$ in InAs [24, 108]. Additionally, with a QD height of about 8 nm and a diameter of about 20 nm, the excitons are strongly confined in all directions. Furthermore, the translational symmetry of the III-V semiconductors is lost due to the three-dimensional confinement [102]. The excitons in these QDs may thus be seen as weakly correlated electron-hole pairs. The small dimensions give rise to fully quantized electron and hole states, and a strong spatial localization of the excitons with smeared-out wavevectors. In addition, the strong confinement of the individual wavefunctions leads to an increase of the binding energy. Yet, the low effective masses of electron and hole ($\mu_\mathrm{X} = 0.053\,m_{0,\mathrm{e}}$ in similar QDs [109], whereas $m_{\mathrm{eff,e}} = 0.026\,m_{0,\mathrm{e}}, m_{\mathrm{eff,hh}} = 0.41\,m_{0,\mathrm{e}}, m_{\mathrm{eff,lh}} = 0.026\,m_{0,\mathrm{e}}$ in InAs and $m_{\mathrm{eff,e}} = 0.067\,m_{0,\mathrm{e}}, m_{\mathrm{eff,hh}} = 0.5\,m_{0,\mathrm{e}}, m_{\mathrm{eff,lh}} = 0.082\,m_{0,\mathrm{e}}$ in GaAs [24, 110]) lead to an overall rather small binding energy of $E_\mathrm{B} = 17\,\mathrm{meV}$ [111]. This is, however, larger than the bulk binding energy of $E_\mathrm{B} = 1\,\mathrm{meV}$ in InAs [112] and $E_\mathrm{B} = 5\,\mathrm{meV}$ in GaAs [23], so that excitons in such QDs are comparatively robust against elevated temperatures. Furthermore, the low effective masses lead to a substantial leakage of the electron and hole wavefunctions outside of the QDs. As the dielectric constants of the InAs QDs and the surrounding GaAs are similar ($\varepsilon = 15.1$ in InAs to $\varepsilon = 13.2$ in GaAs [24]), the self-energy contribution is quite small, approximately 1 meV [113]. Hence, this contribution may be neglected, as exciton binding energy and self-energy contribution almost cancel each other due to their opposite signs. The effect on the single-particle energy differences is negligibly small [113].

In **TMDC MLs**, the exciton Bohr radius is on the order of a few nanometers ($a_\mathrm{B} \approx 1-3\,\mathrm{nm}$) and the correlation between an electron and a hole extends over several lattice periods (lattice constant $a_\mathrm{TMDCs} \approx 0.33\,\mathrm{nm}$) [8, 114]. Although the size difference is not large, it is mostly appropriate to describe the exciton by the Wannier-Mott description in the effective mass approximation [8]. As the ML height is on the order of 0.7 nm [53], the excitons may be treated as strongly confined in z-direction, while the lateral

ML flake size of several micrometers does not restrain the exciton wavefunction. The strong confinement and the heavy effective masses of electron and hole (e.g. in $MoSe_2$: $m_{\mathrm{eff,e}} = 0.56\, m_{0,\mathrm{e}}$, $m_{\mathrm{eff,h}} = -0.59\, m_{0,\mathrm{e}}$, in WSe_2: $m_{\mathrm{eff,e}} = 0.28\, m_{0,\mathrm{e}}$, $m_{\mathrm{eff,h}} = -0.36\, m_{0,\mathrm{e}}$, and $\mu_{\mathrm{X}} = m_{0,\mathrm{e}}/2$ [56]) lead to an enhanced Coulomb interaction [102] and a large binding energy of $E_{\mathrm{B}} = 500\,\mathrm{meV}$ [115]. The large binding energy of the excitons indicates their thermal stability at room temperature [67]. Additionally, the small Bohr radius in real space leads to a large spread of the exciton in $\vec{k}$-space, so that an accurate exciton wavefunction has to include states farther away from the K-point band extrema.
Moreover, the exciton states in the MLs deviate from the simple dependence of equation (2.13), for $n = 1, 2$, due to their inhomogeneous dielectric environment, leading to a **nonuniform dielectric screening**. The exciton radius increases with higher main quantum number n, as the electric field between electron and hole is affected by the dielectric environment, see figure 2-6 (right). The field changes with the spatial distance between electron and hole, as the ratio between the electric field flux that runs through the ML and that going through the dielectric environment varies. This changes the effective dielectric constant $\varepsilon_{\mathrm{eff}}$ of the system, gives rise to a distance dependence of the binding energy that deviates strongly from the usual $1/r$ form, and induces nonhydrogenic exciton behavior [8]. For example, the electron-hole interaction is more strongly screened by the environment for shorter ranges (lower n) and may be approximated by a weaker $\log(r)$ interaction instead of the $1/r$ Coulomb interaction at large ranges [75]. In addition, the dielectric screening changes as a function of the neighboring layers around the ML, so that the exciton behavior in MLs depends on the encapsulating layers and the substrate. Depending on the dielectric constant of the encapsulating material (typically $\varepsilon_0 < \varepsilon_{\mathrm{encaps}} < \varepsilon_{\mathrm{ML}}$), the dielectric screening increases and the binding energy decreases. Due to a smaller self-energy contribution of the encapsulating material compared to the air / vacuum case, the renormalized bandgap shows practically no shift. Additionally, the self-energy contribution in TMDC MLs is rather large, about $300 - 500\,\mathrm{meV}$ [67, 116], due to the large mismatch between the dielectric constants of the TMDCs (e.g. $\varepsilon_\perp = 6, \varepsilon_\parallel = 15$ in MoS_2 [117]) and the surrounding air / vacuum ($\varepsilon_{\mathrm{air}} \approx 1.0006$ / $\varepsilon_0 = 1$). However, the exciton binding energy is almost equal in size, but of opposite sign, and both energy contributions tend to cancel each other with respect to the absolute energies [8]. This effect also takes place for an encapsulation with hexagonal boron nitride. A smaller mismatch between the dielectric constants ($\varepsilon = 3 - 7$ in hBN [117]) leads to a smaller self-energy contribution, but also to a smaller binding energy ($E_{\mathrm{B}} \approx 220\,\mathrm{meV}$ [67]). Overall, the total bandgap energy stays nearly unchanged [73].

2.3 Quantum numbers and their couplings

Using Bloch's theorem allows for characterizing the electrons in a periodic crystal potential by a wavefunction with a set of quantum numbers for a specific band and wavevector. Each resulting electron eigenstate as solution for the eigenenergies is mainly defined by the principal, orbital, magnetic and spin quantum number. The four quantum numbers specify the complete quantum state, or wavefunction, of a single electron in an atom. The quantum numbers correspond to the (quantized) eigenvalues of operators that commute with the Hamiltonian of the system - that are conserved. These quantum-mechanical operators are vector operators, e.g., $\vec{L} = (\hat{L}_x, \hat{L}_y, \hat{L}_z)^T = \hat{L}$ for the angular momentum operator. The principal quantum number arises from the solution of the radial part

of the Schrödinger equation; it is the energy eigenvalue of the Hamilton operator $\hat{H}$. The orbital and magnetic quantum numbers directly relate to the angular momentum $\hat{L}$ as conserved quantity of the rotational-symmetric system. A further quantum number, the spin, is required to describe electromagnetic transitions measured in optical spectra. These transitions are described by optical selection rules, see section 3.2.2, which typically require a change of quantum number values. The eigenenergies, quantum numbers and optically allowed transitions are correlated with each other, and understanding the optical properties of a semiconductor requires knowledge of its quantum numbers. In the following, they are explained in detail.

2.3.1 Angular momentum, spin and pseudospin

Classical **angular momentum** consists of the orbital angular momentum and the intrinsic angular momentum of a system. In quantum mechanics, the angular momenta are quantized and underlie the uncertainty principle. Whereas the orbital angular momentum $\hat{L}$ can be understood similarly in classical and quantum mechanics, the spin angular momentum $\hat{S}$ in quantum mechanics is an intrinsic property of a particle. All elementary particles have a characteristic spin quantum number s, depending on whether they are fermions (half-integer spin) or bosons (integer spin). Quantum numbers correspond to the eigenvalues of the (angular momentum) quantum operators. The magnitude of the spin is the same for all particles of the same kind, whereas its direction may change. Thereby, the projection of the spin $\hat{S}_z$ relates to the spin projection quantum number s_z, also m_s, along the studied axis. This applies in general for operators and their projection quantum numbers. The quantization axis is typically the z-axis, corresponding to a crystallographic axis of the sample and the optical axis of the setup, see chapter 3 about experimental details.
Quantum numbers characterize the quantum state of a particle in a system, in particular the energy levels of electrons. The quantum numbers typically used are n, l, m_l and m_s. For an electron in an atom, the first three numbers specify the particular orbital of interest, the fourth specifies how many electrons occupy that orbital. The **principal quantum number** n denotes the electron shell or the energy level of an electron, ranging from 1 to the outermost electron of the system. It specifies the energy of an electron and the size of the orbital. It arises in the solution of the radial part of the Schrödinger equation, see equation (2.1), whereas the other quantum numbers are given by the solution of the spherical part. This quantum number depends on the distance R between the electron and the nucleus, with the distance increasing with n. The **orbital quantum number** l gives the magnitude of the orbital angular momentum and relates to the shape of atomic orbitals, or electron subshells, ranging from 0 to $n-1$. It is sometimes denoted as azimuthal quantum number, as it arises from the solution of the azimuthal part of the Schrödinger equation. In addition, it indicates the number of nodes of the wavefunction going through the center of the rotational-symmetric potential. The **magnetic quantum number** m_l (or l_z) describes the specific orbital within a subshell. It specifies the orientation in space of an orbital with a given energy and shape. It may be considered as the projection of the orbital angular momentum operator $\hat{L}$ along a specified axis, with values ranging from $-l$ to l in integer steps. According to its name, the magnetic quantum number affects the energy of the electron in a magnetic field, otherwise the states are degenerate. Typically, the subshells are denoted as s, p, and d for

values $l = 0, 1$ and 2 with $m_l = 0, \pm 1$, and ± 2, respectively. Similar, the spin projection or magnetic spin quantum number m_s describes the intrinsic spin angular momentum of the electron within each orbital and ranges from $-s$ to s, whereby half-integer values are allowed. For example, electrons in the p-shell obtain $n = 1, l = 1, m_l = 0, \pm 1$ and $s = \pm 1/2$, leading to six possible electron states.

As mentioned above, the **spin quantum number** is an intrinsic property of a particle. It specifies the orientation of the spin axis of an electron. The spin of a photon may be considered as the quantum-mechanical description of the polarization of light. However, for electrons, the spin has no classical analogue, but its existence has far-reaching consequences. The spin of a particle generates a **spin magnetic moment** $\vec{\mu_S} = -g_S \mu_B \vec{S}/\hbar$, where μ_B is the Bohr magneton and g_S is the spin g-factor. The term refers to the magnetic strength and orientation of a system that produces a magnetic field and may be represented by an equivalent magnetic dipole. The direction of the magnetic moment is determined by the direction of the spin, whereby the electron's magnetic moment is antiparallel to its spin as indicated by the negative sign. The spin magnetic moment helps to explain the magnetic properties of materials. For example, paramagnetic materials may obtain half-filled orbitals leading to a net magnetic moment. The unpaired spins in these materials align in the same direction as an applied field, so that such materials are attracted by magnetic fields. Furthermore, the two eigenstates of the electron spin, $s = 1/2, s_z = \pm 1/2$, lead to **spin basis eigenstates**, often denoted by spin-up $\uparrow$ ($s_z = +1/2$) and spin-down $\downarrow$ ($s_z = -1/2$) in literature. These states are the time-reversed images of each other and are distinguished by the opposite values of their magnetic moments [118]. In this context, it is convenient to use the Pauli matrices σ for the electron spin operators $\hat{S} = \hbar/2\hat{\sigma}$. The superposition of both spin states is the basis for quantum information processing, and the electron spin's natural two-state system makes it a popular candidate for a qubit. Therein, the direction of the spin, its spin projections s_z, is manipulated, while its value s is fixed [24]. Besides, the connection between spin and magnetic moment has led to the field of spintronics, which aims at exploiting the spin of charge carriers in electronics to process information [118].

A **pseudospin** denotes a (binary) quantum degree of freedom analogous to the intrinsic spin of a particle or complex. The introduction of pseudospin may be helpful in a variety of problems [26, 118]. For example, it is used in graphene: its hexagonal lattice structure with its symmetric K valleys offers chiral band eigenstates, a variable associated with its two-component wavefunction. When breaking this symmetry, the transmission of electrons becomes valley-dependent and they may be distinguished by their valley pseudospin, also named valley isospin or valley index. Note that the pseudospin in graphene is not linked with an internal magnetic moment and, thus, does not interact directly with the external magnetic field [119]. The pseudospin may be used for applications which control the valley pseudospin of the electron aside from its charge, the so-called valleytronics [120]. Generally, the pseudospin in graphene and TMDCs is very similar to the intrinsic electron spin, but behaves differently under time reversal [121], which interchanges the valleys K_+ and K_- [122].
In this thesis, the **valley pseudospin** in TMDCs is studied, which likewise arises from the degeneracy of the honeycomb lattice at the K point. In monolayer TMDCs with broken inversion symmetry, the VBs are split by SO coupling and this spin splitting is opposite at the two inequivalent valleys, see figure 2-9. Thereby, the SO coupling has the form $\hat{H}_{SO} = \lambda_{SO} \tau \hat{S}_z$, similar to equation (2.18). The valley index $\tau = \pm 1$ denotes

the degenerate band extrema [118] and the value of the pseudospin distinguishes the orbital wavefunction of the electron located in one of these valleys. Moreover, the valley pseudospin in TMDCs is associated with an intrinsic magnetic moment near the band edges [118]. This allows for coupling the pseudospin to a magnetic field and detecting (optical) valley polarization as a magnetic signal, e.g. like the valley dependence in the Hall current of graphene [123]. The valley magnetic moment $m_\tau = \alpha_i \tau \mu_\mathrm{B}$, with the valley g-factor $\alpha_i = m_{0,\mathrm{e}}/m_{\mathrm{eff},i}$ for the CB ($i = c$) and VB ($i = v$), corresponds to the lattice contribution associated with the Berry curvature [55]. It is responsible for the valley-dependent Zeeman shift of the optical resonances by $\Delta_\mathrm{Z} = \tau \Delta\alpha_{cv} \mu_\mathrm{B} \vec{B}$, with $\Delta\alpha_{cv} = \alpha_c - \alpha_v$ [124], see section 2.3.3. In addition, it gives rise to the circularly polarized optical selection rule for interband transitions: right (left)-handed circularly polarized light only couples to the K_+ (K_-) valley due to the large spin splitting of the bands. The inseparable connection between spin and valley index is termed **spin-valley locking**. Thus, the valley pseudospin may be exploited to create a spin-valley polarization using polarized light or to excite a superposition of both valleys (valley coherence).

2.3.2 Spin interactions

The discovery of novel spin effects or the modification of existent spin phenomena are mainly based on interactions between carriers themselves and between a carrier and a second system, e.g., the nuclear spin system or a lattice vibration (phonon). These spin interactions may lead to scattering processes and spin decoherence, which is often not desired. However, these interactions may also be exploited to manipulate spins and are a necessary tool for computing, communicating and sensing with spins. In this section, the spin-orbit interaction and spin-spin interactions are described, while interactions with phonons are explained in detail in section 2.4.

An important consequence of the existence of spin is the **spin-orbit** (SO) **interaction**. This interaction describes the effect that a charge carrier moving in an external electric field experiences an effective magnetic field which couples to its magnetic moment induced by its spin s (see chapter 3.1.2 in [24]). For example, in an atom where the electron orbits around the nucleus, the magnetic moment $\vec{\mu_S}$ of the electron interacts with the electric field of the nucleus via SO interaction. This leads to an energy difference between the electron energy levels by the SO splitting between former degenerate levels. The interaction increases with higher atomic order number of the anion, where the electrons are located preferentially, due to the small probability for an outer electron to approach the nucleus. In the nucleus, the electron experiences the strong electric field produced by the unscreened nuclear charge [26]. This impact on the energy levels is particularly important for the band order in 2D structures, see section 2.3.4. Specifically, the SO splitting is larger for the heavier W compounds than for the lighter Mo compounds. The main effect of the SO coupling is a splitting of degenerate bands in dependence of their total angular momentum, especially at high-symmetry points of the Brillouin zone of cubic solids [28]. The effects on the general band structure in the studied nanostructures are found in sections 2.1.3 and 2.1.4, while the effects on the fine structure are described in section 2.3.4.

The SO coupling term $\hat{H}_\mathrm{SO}$ in the presence of an electric potential V_el from the second-

order expanded Dirac equation yields

$$\hat{H}_{\mathrm{SO}} \propto \hat{S} \cdot (\nabla V_{\mathrm{el}} \times \hat{p}), \quad \text{whereby} \quad \hat{H}_{\mathrm{SO}} \approx \lambda_{\mathrm{SO}} (\hat{L} \cdot \hat{S}) \tag{2.18}$$

applies for a nearly isotropic SO coupling with the splitting constant λ_{SO}. Note that the SO interaction takes on a slightly more complicated form for an electron confined in a two-dimensional system [24]. The SO Hamiltonian in the equation above describes the effects caused by confinement or impurities. There are further Hamiltonians describing SO effects when regarding higher orders of perturbation theory, which may be divided into two groups [125]. The first group leads to SO admixture of different spin states, where the electron spin-up state acquires a small admixture of the spin-down state, and vice versa. The admixture may result from the absence of the inversion symmetry in the bulk, causing the giant SO splitting in TMDC MLs [126]. Moreover, admixture may be caused from the relativistic interaction with the electric field due to confinement or impurities. The former is typically the larger contribution, while the latter may be enhanced by band effects [125]. The second group includes mechanisms due to direct spin-phonon coupling, e.g., the SO splitting of the electron spectrum due to a strain field produced by acoustic phonons. Hence, the admixture depends on the lattice deformation, at low temperatures specifically on the contributions of piezoelectric phonons [127]. In QDs, the admixture mechanisms of the first group dominate, although SO coupling is suppressed compared to the 2D case due to the confinement of the electron wavefunctions. The contribution of the direct spin-phonon coupling to the SO coupling in QDs is comparatively very small [125, 127]. The admixture mechanisms may lead to higher levels mixed to the ground state with zero angular momentum in QDs, thereby drastically enhancing the g-factor of the ground state [128].

As both orbital and spin angular momenta are subjected to SO interaction, see equation (2.18), and hence do not commute with the Hamiltonian, it is necessary to define a combined quantum number, the **total angular momentum** $\hat{J} = \hat{L} + \hat{S}$. Thus, the conservation of angular momentum applies only to the total angular momentum. This allows for transferring angular momentum back and forth between the orbital and the spin angular momentum, while the total angular momentum remains constant. In that respect, the quantum numbers used to describe the electron levels change to the total angular momentum quantum number $j = |l \pm s|$. Its projection quantum number $j_z = m_l + m_s$, sometimes m_j, ranges from $-j$ to j, with $|m_l + m_s| \leq j$. In this way, the six possible electron states in the p-shell obtain $j = 1/2$ with $j_z = \pm 1/2$ and $j = 3/2$ with $j_z = \pm 1/2, \pm 3/2$. Thus, each electron has different quantum numbers and the Pauli exclusion principle is fulfilled. In excitons, the total angular momenta of electron and hole add up: $\hat{J}_{\mathrm{X}} = \hat{J}_{\mathrm{e}} + \hat{J}_{\mathrm{h}}$.
A further quantum number needed to describe particle wavefunctions is named parity. The operator $\hat{P}$ of parity transformation or reflection acts on the wavefunction $\hat{P}\Psi(r) = \Psi(-r)$. The eigenvalues of parity $P = (-1)^l$ classify wavefunctions into either having positive (even) or negative (odd) parity, in dependence of their orbital angular momentum [79]. Wavefunctions with odd parity may be changed by a parity transformation, they change their sign when occupied by an odd number of electrons. However, parity is not conserved in the studied low-dimensional structures. The importance of angular momentum conservation during scattering processes and its consequences are described in section 3.2.2.

Interactions between spins may happen via the dipolar interaction between electron spins, the hyperfine interaction between electron and nuclear spins, and the exchange term of the Coulomb interaction, which is effectively a spin-spin interaction (see chapter 6 in [24]). Moreover, the Pauli principle may also be seen as a spin interaction [26]. The Coulomb-exchange term, due to its importance for the exciton fine structure, has already been explained in section 2.2.3. Contrarily, the dipolar interaction, also magnetic dipole-dipole coupling, is typically too weak to be of importance in semiconductors [26]. It directly couples the magnetic moments of a pair of particles. For example, it is only about 10^{-9} meV in QDs [24]. In TMDCs, the out-of-plane dipole-dipole interaction is negligible due to the highly symmetric structure. Hence, the intralayer interaction between excitons is determined by their wavefunction overlap, while the coupling between interlayer excitons resembles a dipole-dipole interaction, as these have a permanent dipole moment [129]. Consequentially, interlayer excitons in TMDCs have a strong dipole-dipole interaction [130]. Contrastingly, hBN shows a high in-plane dipole-dipole interaction due to its highly polar structure [131].
The hyperfine interaction results from the existence of non-zero nuclear spins. Similar to SO coupling, the hyperfine interaction denotes the coupling between the total angular momentum $\hat{J}$ and the nuclear spin $\hat{I}$ and leads to a new quantum number $\hat{F}$. Likewise, the hyperfine interaction increases with higher atomic order number and induces an energy splitting between former degenerate electron states yielding the hyperfine structure [26]. Compared to electron spins, nuclear spins have much longer lifetimes as they couple only weakly to the environment. Their influence may lead to spin relaxation and decoherence processes due to mutual spin flips of electrons and nuclei. The interaction consists of different contributions: a coupling via magnetic dipole-dipole interaction and a term related to Fermi contact interaction. This interaction is enhanced by confinement and provides the dominant coupling of electron and nuclear spins in GaAs QDs, with a coupling strength of about 10^{-6} meV [24, 26]. However, the interaction only works for wavefunctions with a certain probability at the center of the atom, which is the case for s-state electrons. For p-state electrons and hole spins, the Fermi contact hyperfine interaction vanishes. This leads to a hyperfine coupling strength only via magnetic dipole-dipole interaction, which is about an order of magnitude smaller. In TMDCs, the SO splitting is about 10^4 times larger than the hyperfine interaction [132], which is on the order of 1 µeV or less [133].

2.3.3 Coupling of spins to magnetic fields

Magneto-optical measurements may be used to determine the energy levels in QDs and other nanostructures (see chapter 7.2 in [38]). Therein, a magnetic field $\vec{B}$ acts on the angular momenta and their associated magnetic moments of the electrons and other particles. This interaction may be divided into an interaction with the orbital part leading to Landau-quantization and an interaction with the spin part. These interactions are, e.g., termed Zeeman effect. Depending on the material properties and on the strength of the magnetic field compared to the quantum confinement, the orbital or Zeeman effect dominates. In the studied nanostructures with 'weak' magnetic fields up to 10 T, the interaction with the spin part is dominant. Note that in case of very strong perpendicular magnetic fields, the eigenenergies of the harmonic confinement, e.g., as in equation (2.7) with the oscillator resonance frequency ω_0, have to be modified by the

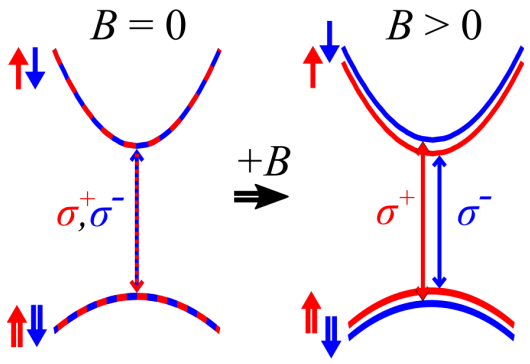

Figure 2-8: Scheme of the lowest CB and highest VB at the Γ-point of the Brillouin zone for GaAs in single-particle representation. An external magnetic field B splits the spin-degenerate bands into a spin-up (red lines and arrows) and a spin-down (blue lines and arrows) band due to the Zeeman effect (negative electron g-factor). The energetically lowest, spin-allowed optical transitions are marked by vertical arrows in the corresponding color.

cyclotron frequency ω_c, leading to Fock-Darwin eigenstates (see chapter 3.4 in [24]).

The **Zeeman effect** denotes the broadening and splitting of a spectral line into several components under a static magnetic field. It splits the former degenerate states, which are associated with different magnetic dipole moments. Specifically, the magnetic field distorts the electron orbitals and leads to energetically differently oriented states. With increasing magnetic field strength, the former degenerate energy states split and reveal their different angular momenta, as shown in figure 2-8. These new energy states may be calculated using the Zeeman term of the electron Hamiltonian given by:

$$\hat{H}_\mathrm{Z} = \frac{g\mu_\mathrm{B}}{\hbar}\vec{B}\cdot\hat{S}, \quad \text{with} \quad \hat{H}_{\mathrm{Z}_z} = \frac{1}{2}g\mu_\mathrm{B}B_z\begin{pmatrix}1 & 0\\ 0 & -1\end{pmatrix} \tag{2.19}$$

for a magnetic field applied along the z-axis, where the last term is the corresponding Pauli spin matrix σ_z [24]. A more general form is given in [96]. The total Hamiltonian of the exciton is obtained by adding the Zeeman Hamiltonian of the electron $\hat{H}_\mathrm{Z,e}$ and hole $\hat{H}_\mathrm{Z,h}$ to the exchange interaction between electron and hole $\hat{H}_\mathrm{ex,eh}$ [95, 96]. Here, the Bohr magneton $\mu_\mathrm{B} = e\hbar/2m_{0,\mathrm{e}}$ expresses the magnetic moment of an electron caused by its angular momentum. The proportionality constant g is known as the electron g-factor, or Landé factor, which characterizes the linear **splitting of electron levels** caused by the Zeeman effect. The g-factor is related to the magnetic moment resulting from the (total) angular momentum of a particle via $|\vec{\mu_J}| = \gamma|\vec{J}| = g\mu_\mathrm{B}/\hbar\cdot|\vec{J}|$. Like the total angular momentum, the electron g-factor consists of both orbital and spin contributions. The gyromagnetic ratio γ of a particle allows one to rewrite $\hat{H}_\mathrm{Z} = -\vec{\mu}\cdot\vec{B}$, with the generic magnetic moment $\vec{\mu}$ [48]. For a classical particle it may be calculated via $\gamma = gQ_c/2m$ and is equal to 1 for a uniformly distributed mass m and electric charge Q_c. This is equal to the value of the electron orbital g-factor g_L. However, the electron spin g-factor $g_{S,0}$ of the free electron in vacuum is very close to 2 [134]. Note that both spin s and magnetic quantum number m_l may lead to the splitting of the electron levels, as they both contribute to the magnetic dipole moment.
The energy of electronic CB states under application of a magnetic field may be calculated using [135]:

$$E_\mathrm{Z}(B) = E_\mathrm{g} + 2g\mu_\mathrm{B}|\vec{B}| + \alpha_\mathrm{d}^2|\vec{B}|^2 \tag{2.20}$$

wherein the effects of the magnetic field are treated as a perturbation to the ground electron states, similar to the Coulomb interaction in equation (2.10). In the Zeeman term linear in B, the g-factor may be obtained by, e.g., polarized PL measurements. The last term $\propto B^2$ describes the **diamagnetic shift**, which is an increase in energy

of both spin-split levels with magnetic field. It appears due to an opposite orientation of the induced magnetic moments in the material relative to the applied field and leads to an energy gain depending on the spatial confinement and Coulomb interaction [136]. The diamagnetic shift coefficient $\alpha_\mathrm{d} = e^2 a_\mathrm{B}^2/4\mu_\mathrm{X}$ depends on the reduced mass of the exciton and its Bohr radius [137]. In the two-dimensional limit, this coefficient changes to $\alpha_\mathrm{d,2D} = 3\alpha_\mathrm{d}/16$, with the Bohr radius $a_\mathrm{B,2D} = 2\pi\hbar^2\varepsilon/\mu_\mathrm{X}e^2$ for a hydrogenic 2D exciton [138]. For lower dimensions, the diamagnetic shift coefficient is $\alpha_\mathrm{d,QD} = 4\pi e^2 a_\mathrm{B}^2/\mu_\mathrm{X}$ [84]. The proportionality to the lateral extension of the exciton wavefunction underlines the importance of confinement effects and electron-hole Coulomb interaction [136].

The spin of the electrons and holes is effectively modified by their motion in the crystal lattice. Specifically, their ***g*-factor** is modified by SO interaction, and may even reverse its sign [139]. For example, in alloys like the studied QDs, the bulk electron g-factor of GaAs ($g = -0.44$) is slightly lowered to about $g = -0.5$ due to Indium ($g = -14.8$) admixture [24, 140]. In TMDCs, the excitonic g-factor is typically about -4 [141]. However, the spread of the measured g-factor is large, from -1.6 [73] via -2.8 [124] to -4.6 [142]. This depends on, e.g., the dielectric confinement and strain, which affect the effective masses in the bands. Hence, the different CBs also contribute differently, leading to large differences in the exciton g-factors, with the dark exciton g-factor of about -10 [143]. The effective g-factor for electrons in bulk zincblende semiconductors is given by:

$$g_\mathrm{e,bulk} = 2 - \frac{2}{3}\frac{E_\mathrm{p}\Delta_\mathrm{SO}}{E_\mathrm{g}(E_\mathrm{g} + \Delta_\mathrm{SO})}, \tag{2.21}$$

with the Kane energy E_p of the matrix element for the coupling between a p-like VB and an s-like CB [139, 144, 145]. Under the assumption of an **isotropic *g*-factor of the electron**, the g-factor increases with bandgap energy and approaches the free electron g-factor $g_{S,0} = 2$ [146]. This relation is also known as the Roth-Lax-Zwerdling equation and is based on multiband $\vec{k}\cdot\vec{p}$ theory [24, 139].
Note that this relation is only valid for electrons but not for holes, as these are far more sensitive to in-plane distortions of confinement potentials arising from, e.g., shape or strain anisotropy [147]. In nanostructures, the carrier confinement changes the bandgap and leads to considerable deviations from this relation. A decrease in size leads to an increase in the emission energy and to a decrease in the g-factor [148]. Moreover, the g-factor may rather be seen as a matrix, or a tensor, as its value for each direction may vary depending on the spatial confinement, strain, and composition in the specific direction. This reflects the external parameters lowering the symmetry of the Hamiltonian [146, 149, 150] and is specifically displayed in the **anisotropy of the hole *g*-factor**. In addition, the g-factor depends on the specific form of the wavefunctions. For example, the electron wavefunctions of s- and p-like states in QDs differ in their form: the s-like wavefunction is more localized and, thus, more sensitive to the shape of the confinement potential. On the contrary, the p-like wavefunction is more delocalized, leaks along the growth direction and has a node at the QD center. This allows one to probe the region outside or at the interfaces of a QD by analyzing the g-factor tensor components of the p-state [151]. Likewise, the anisotropy of the nanostructure may be studied by analyzing the hole instead of the electron g-factor, as it depends on the complex spin level structure of the p-like VB. Thus, it varies strongly with changing quantum confinement, e.g. height-to-diameter ratio, QD composition [146, 150] and valence band mixing [152]. These dependences of the g-factor allow for gaining information about the structural

properties of the studied nanostructures.
In systems with uniaxial symmetry, the g-factor may be described by two linearly independent components: the longitudinal $g_\parallel = g_{zz}$ and the transverse $g_\perp = g_{xx} = g_{yy}$ factors relative to the quantization axis z, with $|g_\parallel| > |g_\perp|$ [32]. The double indices denote the diagonal elements of the g-factor tensor along the corresponding axis. The energy splitting between the degenerate electron spin eigenstates proportional to the magnetic field may thus be calculated via [32, 98]

$$\Delta E_\mathrm{Z}(\theta) = g(\theta)\mu_\mathrm{B}|\vec{B}|, \quad \text{with} \quad g(\theta) = \sqrt{(g_\parallel \cos\theta)^2 + (g_\perp \sin\theta)^2}. \tag{2.22}$$

Herein, the **tilting angle** θ encloses the **magnetic field** vector $\vec{B}$ and the z-axis. Besides, note that the electron spin basis eigenstates are coupled by the off-diagonal elements of the Zeeman term in dependence of the tilting angle θ: $|\Psi_{\mathrm{e},\pm}\rangle = \cos(\theta/2)\ |\pm 1/2\rangle \ \pm \sin(\theta/2)\ |\mp 1/2\rangle$. This leads to an angular dependent mixing of the respective exciton spin states. This **state mixing** is established by the transverse electron g-factor, since the hh has zero transverse magnetic moment in high-symmetric structures [153, 154]. Yet, note that the transverse hole g-factor, $g_{\mathrm{hh},\perp}$, may deviate from zero, for example because of lh and hh states slightly mixed due to strain or shape asymmetries of the nanostructure. This mixing is typically around 10 % in the studied QD structures [46, 135]. Other effects that modify $g_{\mathrm{hh},\perp}$ are an anisotropic lateral localizing potential, leakage of the hh wavefunction into the barrier material, and admixture of higher hole states by increasing SO interaction from stronger spatial confinement [51, 128, 155]. Additionally, the magnetic coupling of a hole to a magnetic field may be described by a non-Zeeman interaction given by $\hat{H}_\mathrm{nZ} \propto \hat{J}_x^3 B_x + \hat{J}_y^3 B_y + \hat{J}_z^3 B_z$ [156], as in equation (2.16). Specifically, the hh does not couple in first and second order to a transverse magnetic field, so that the transverse hh g-factor is about zero in high-symmetric structures [153, 154]. Hence, the relatively weak third-order term plays a significant role and leads to a strongly anisotropic in-plane g-factor tensor [95].

2.3.4 Impact of angular momenta on exciton fine structure

In this section, the impact of the angular momenta on the **exciton fine structures** of the studied nanostructures are discussed. The basic properties of excitons in III-V semiconductor QDs and in TMDC MLs are found in section 2.2.4. The exciton fine structure arises from the exchange term of the Coulomb interaction, see section 2.2.3. Including interaction with the spin and orbital angular momentum, it is sensitive to the impact of an applied magnetic field on the associated magnetic moments, see section 2.3.3. Additionally, the specific selection rules resulting from the spin-valley alignment of the bands in TMDC MLs are discussed, while general selection rules and the specific rules in III-V semiconductors are explained in more detail in section 3.2.2.

In **III-V semiconductor QDs**, the large spatial confinement enhances the electron-hole exchange interaction and leads to an exciton fine structure and a polarization anisotropy [157]. This **energetic splitting of the ground exciton state** results from the coupling of the angular momenta, as the angular momenta of the neutral exciton state are no longer good quantum numbers (see chapter 6.2.1 in [24]). The single exciton states consist of a hh with $j_\mathrm{hh} = 3/2, j_{\mathrm{hh},z} = \pm 3/2$ and an electron with $j_\mathrm{e} = s_\mathrm{e} = 1/2, j_{\mathrm{e},z} = s_{\mathrm{e},z} = \pm 1/2$. Thus, there are four possible exciton states, which are characterized by

their angular momentum projections $j_z = s_{\mathrm{e},z} + j_{\mathrm{hh},z}$. Spin states with $j_z = \pm 2$ that cannot couple to the light field are named optically inactive, dark, dipole-forbidden or nonradiative. Contrarily, the optically active or bright exciton states with $j_z = \pm 1$ couple to $\sigma^{\pm}$ circularly polarized light, compare figure 2-8. The exchange interaction lifts the degeneracy between the energy levels of the exciton states, so that the bright and dark states are split by the electron-hole (or exciton) **exchange energy** δ_0, as explained in section 2.2.3 [96]. The splitting occurs mainly due to the short-ranged part of the exchange interaction [96]. The fine-structure splitting in the µeV-range may be positive or negative, depending on the QD size and piezoelectric effects [158]. Additionally, a zero-field separation between the bright and dark doublets arises from the long-ranged part of the electron-hole exchange interaction in asymmetric QDs [159]. Therein, the splitting δ_{b} between the bright doublet arises from dot-asymmetry induced exchange energy splittings in QDs with broken rotational symmetry, where the long-range interaction contributes dominantly to the splitting [96]. Contrarily, the splitting δ_{d} between the dark doublet results from the short-range exchange interaction. Yet, these splittings are typically rather small compared to δ_0, with $\delta_0 \gg \delta_{\mathrm{b}} > \delta_{\mathrm{d}}$ [96, 160]. Note that the fine structure of charged excitons, trions, reveals even more features: singlet ($s = 0$) states and triplet ($s = 0, \pm 1$) states, where the electron and hole spins are partially compensated [161].
The exciton states with the same j_z are hybridized each in case of broken rotational symmetry, e.g. an asymmetric in-plane QD shape [96]. Hence, the circularly polarized excitons transform into linearly polarized states, leading to **polarization anisotropy** [24]. Note that the bright exciton splitting vanishes in cylindrical symmetry [157]. The exciton states are split in transverse and longitudinal components due to the long-ranged part of the exchange interaction [96]. The circularly polarized exciton eigenstates are restored when applying a magnetic field, such that the Zeeman splitting is larger than the exchange splitting. Moreover, an applied **tilted magnetic field** creates a **mixing between the bright and dark exciton states** due to symmetry breaking. The mixing is established by the transverse electron g-factor, since the transverse magnetic moment of the hh is about zero [95, 155]. The tilting of the magnetic field defines how much the exciton states are mixed: from no mixing in Faraday geometry ($\vec{B} \parallel \vec{z}$) to full mixing in Voigt geometry ($\vec{B} \perp \vec{z}$). The magnetic field dependence of the exciton is determined by the exchange energies and the g-factors of the hh and electron. Contrarily, the field dependence of negatively- (positively-)charged singlet-trion is given only by the hh (e) g-factor and is characterized by the absence of exchange energy [161]. The triplet-trions correspond to excited states, which may hybridize with the singlet states in tilted magnetic fields [52].

In **TMDC MLs**, the exciton fine structure arises from the **splitting of degenerate CBs and VBs**. The splittings obtain contributions from SO splitting, short-range exchange interaction and from the difference between the exciton binding energies with slightly different CB masses [162]. As noted in section 2.1.4, the strong SO coupling and the absence of an inversion center lead to a band splitting: the bands of the monolayer are **split at the *K*-point**. This splitting divides the bands into two distinct spin orientations, spin-up and spin-down bands. The size is estimated to be around several hundred meV in the VB and of a few to tens of meV in the CB [8]. The induced splitting of the VB at the K-points is larger for the heavier W compounds ($\Delta_{\mathrm{SO,W}} \approx 400\,\mathrm{meV}$) than for the lighter Mo compounds ($\Delta_{\mathrm{SO,Mo}} \approx 200\,\mathrm{meV}$) [55, 126, 163]. Moreover, the CB splitting has a different sign depending on the TM atom: $\Delta_{\mathrm{SO,Mo}} = 3 - 20\,\mathrm{meV}$ and

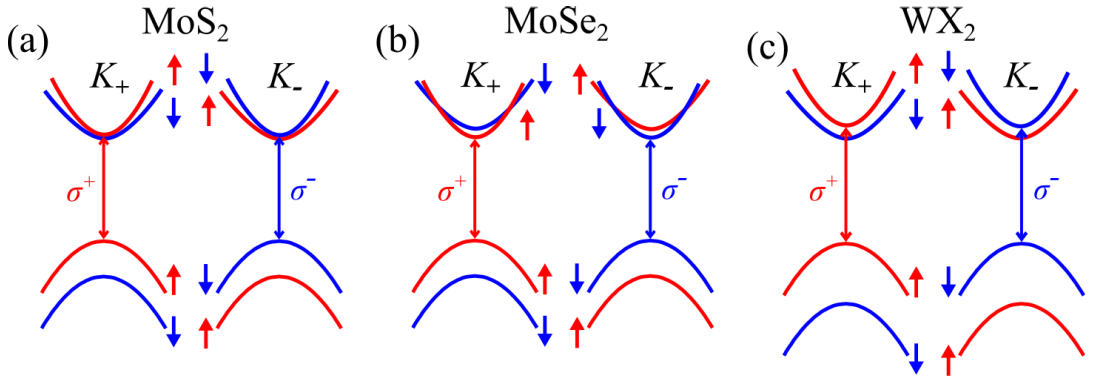

Figure 2-9: Scheme of the lowest CB and highest VB at the K_+- and K_--point of the Brillouin zone for MoS_2 (left), $MoSe_2$ (middle) and W compounds (right) in single-particle representation. The spin-orbit coupling splits each band into a spin-up (red lines and arrows) and a spin-down (blue lines and arrows) band. The energetically lowest, spin-allowed optical transitions are marked by vertical arrows in the corresponding color. After Fig. 1 in [8].

$\Delta_{\mathrm{SO,W}} \approx -30\,\mathrm{meV}$ [164, 165, 166]. Hence, the spin degeneracy in the bands is fully lifted, as can be seen in the scheme of the band structure depicted in figure 2-9. The Brillouin zone is thus separated into inequivalent corners labeled as ***K*$_+$- and *K*$_-$-points**, as shown in figure 2-4 (b). Note that in literature, these points may be denoted as K with plus and minus sign before or after the letter, as superscript, or as K and K'.
The splitting of the spin-degenerate states at the different valleys leads to a valley pseudospin, as explained in section 2.3, where also the resulting optical selection rules are discussed. These spin splittings allow one to define spin basis eigenstates for both bands [55, 118], which are linked by time-reversal symmetry, $E_\uparrow(\vec{k}) = E_\downarrow(-\vec{k})$ [8]. To change the valley, an electron either has to flip its spin or has to undergo an energetically unfavorable transition, resulting in a strong suppression of individual charge-carrier spin flips [56]. Note that the electron valley degree of freedom is only existent in MLs, as in bilayer and bulk systems the inversion symmetry is restored and the spins are degenerate at each valley [65].
Besides, the SO splitting affects the effective masses: they are slightly different for both bands at the K-points. The effective mass is heavier in the spin-up band than in the spin-down band, with around $10 - 14\,\%$ for the Mo compounds and $> 30\,\%$ for the W compounds [166, 167]. This is due to the effective mass depending on the ratio of the bandgap and the spin splittings in other bands. The spin splittings are larger for the heavier W compounds, whereas the bandgap is about the same or slightly smaller. In $MoSe_2$, the different band ordering leads to **band crossings** at the spin-split CB, as the heavier spin-up CB has a higher energy [104, 168], see figure 2-9. MoS_2 shows a similar band curvature, yet there are no band crossings. As the SO splitting is smallest in this compound, the splitting is reversed by exciton binding energies and electron-hole exchange interaction, so that the band ordering is inversed and like the W compounds [168].
The interband transitions between the different valleys allow for four **intravalley** (or direct) exciton states with $\tau_\mathrm{e} = -\tau_\mathrm{h}$ as in $|K_{+,\mathrm{e}}, K_{+,\mathrm{h}}\rangle$ and $|K_{-,\mathrm{e}}, K_{-,\mathrm{h}}\rangle$, and four **intervalley** (indirect) excitons with $\tau_\mathrm{e} = +\tau_\mathrm{h}$ as in $|K_{+,\mathrm{e}}, K_{-,\mathrm{h}}\rangle$ and $|K_{-,\mathrm{e}}, K_{+,\mathrm{h}}\rangle$. Therein, K_+ has $\tau = +1$ and K_- has $\tau = -1$, with the electron spin $s_\mathrm{e} = +1/2$ and the hole spin $s_\mathrm{h} = -1/2$ [8]. They may be divided into optically active (bright) and optically

inactive (dark) states. In the dipole approximation, e.g. in WSe_2 [169], two intravalley excitons with parallel spin, $s_e = -s_h$ as in $|K_{+,e,\uparrow}, K_{+,h,\downarrow}\rangle$ and $|K_{-,e,\downarrow}, K_{-,h,\uparrow}\rangle$, couple to the light (bright exciton states). The other two intravalley states with $s_e = +s_h$ as in $|K_{+,e,\uparrow}, K_{+,h,\uparrow}\rangle$ and $|K_{-,e,\downarrow}, K_{-,h,\downarrow}\rangle$ are spin-forbidden or dark under normal light incidence. The intervalley dark exciton states are termed accordingly as $|K_{+,e,\uparrow}, K_{-,h,\downarrow}\rangle$ and $|K_{-,e,\downarrow}, K_{+,h,\uparrow}\rangle$, while momentum-forbidden dark exciton states may be between the valleys K_+ (K_-) - Λ, Γ, Q, or else [94, 170]. The **bright-dark splitting** δ_0 between the exciton states is about +40 meV in W compounds, +14 meV in MoS_2 and −1.4 meV in $MoSe_2$ for hBN-encapsulated MLs [104]. It depends mainly on the SO splitting of the CB and on the electron-hole short-range Coulomb exchange interaction, which may change the amplitude and sign [171]. In **$MoSe_2$**, **exciton ground state** is assumed to be **bright**, composed of electron and hole with the same spin orientation ($\uparrow\uparrow$ and $\downarrow\downarrow$). On the contrary, the different sign of the splitting leads to a **dark** lowest-energy transition in the tungsten compounds **WX_2**, consisting of states with opposite spin ($\downarrow\uparrow$ and $\uparrow\downarrow$) [8]. In **MoS_2**, the SO splitting of the CB is small, but positive as in $MoSe_2$. However, the spin ordering of the conduction subbands in each valley is reversed by interactions in the exciton picture, so that the exciton ground state is dark [172]. The spin-allowed, bright transitions are depicted in figure 2-9. The distinct band ordering is the reason for the different temperature dependences of the PL. The Mo compounds show a decrease of PL intensity with increasing temperature, while the W compounds obtain a PL increase, as the lower-lying dark states quench the emission from the bright states at low temperatures [169]. Herein, MoS_2 shows a bright ground state behavior, as it has a bright single-particle arrangement of spin-polarized CBs, although the exciton ground state is dark [168]. Off-resonant excitation, where the bright excitons obtain a finite CM in-plane momentum, leads to a splitting into linearly polarized eigenstates with a dipole moment oriented parallel and perpendicular to the in-plane wavevector. This LT-splitting depends linearly on the exciton wavevector and may lead to valley decoherence by rapid intervalley transfer due to long-range exchange coupling [56].

The two spin-forbidden dark states are mixed by the short-range exchange interaction, which lifts the valley degeneracy and forms two eigenstates with spin configuration $\downarrow\uparrow \pm \uparrow\downarrow$ [104]. Basically, these states are coherent superpositions of the states in the two valleys [173]. Thereby, the higher energy component takes up the whole oscillator strength via a residual spin-flip dipole matrix element [104]. The higher energetic dark exciton ($\downarrow\uparrow + \uparrow\downarrow$) is sometimes denoted as gray exciton [104, 174]. It is observable in the cross-polarized PL spectra when using a large aperture of the microscope objective, as this exciton is only dipole allowed for z-polarized light, corresponding to its nonzero out-of-plane dipole moment [15, 103]. The splitting of the dark states scales with the exciton binding energy, typically $\delta_d < 2\,\mu eV$. The fine structure of the excitonic complexes in TMDC MLs may be revealed by trions, where the electrons and holes occupy the same or different valleys [168]. The singlet and triplet trions may be found in different intervalley and intravalley configurations. Aside from that, (charged) biexcitons may be observed in TMDC MLs and interlayer excitons may be studied in vdW heterostructures [175].

A **tilted magnetic field** orientation reveals two effects on the exciton fine structure: besides breaking the time-reversal symmetry, an out-of-plane field splits the exciton states, while an in-plane field mixes the exciton spin eigenstates and activates spin-forbidden excitons [8]. Firstly, the out-of-plane component leads to a definite Zeeman splitting of the exciton states. The Zeeman shift may be expressed as resulting from three additive terms: spin, valley and orbital contribution [176]. The orbital contribution affects

only the VBs (composed of electrons in d-orbitals with $m_l = -2$ and in p-orbitals with $m_l = -1$), but not the CBs (mainly composed of electrons in d-orbitals with $m_l = 0$). In addition, the bright and dark states split differently: the bright excitons depend linearly on the magnetic field, with the slope given by effective g-factor. Contrarily, the dark excitons are split by the exchange energy δ_d at zero field and depend nonlinearly on the field [104]. Furthermore, a diamagnetic shift may be observed, which allows one to determine the exciton radius and binding energy [67, 177, 178]. Secondly, the in-plane field **mixes the bright and dark exciton states**: while the exchange interaction mixes the two valleys, the Zeeman coupling mixes different spin subbands in the same valley [104]. Hence, a reasonably strong in-plane magnetic field brightens both dark exciton states in the molybdenum compounds MoX_2 [104]. Moreover, an in-plane field changes the valley polarization, as it transfers the in-plane oscillator strength (**brightening**) from the higher-energetic bright states to the dark-gray doublet in WX_2 [179]. The exciton state superposition leads to a **linearly polarized** luminescence **at zero field** and to a **circular** (elliptical) **polarization** at $\boldsymbol{B > 0}$ [173].

The absence of an inversion center in TMDC MLs allows for optical transitions between states of the same orbital angular momentum l via transitions with $\Delta l = 0$ [180, 181], see section 2.3.1 on angular momenta). In TMDCs, the orbital angular momentum is also termed as excitonic angular momentum (EAM), in contrast to the valley index, or (out-of-plane) valley angular momentum (VAM), which combine collinearly [181]. The angular momentum is conserved during photon (pht) absorption (or emission), when the incoming photon distributes its angular momentum to the exciton (and vice versa). However, in TMDC MLs the crystal symmetry and the valley contribution have to be included. Hence, the **selection rule** for out-of-plane **angular momentum** conservation is given by [181]:

$$\Delta l_\mathrm{pht} = \Delta\tau + \Delta l_\mathrm{X} + 3N \quad \text{with } N \in \mathbb{Z}. \tag{2.23}$$

The threefold rotational symmetry requires total angular momentum conservation including the VAM, EAM, lattice angular momentum, and photon spin angular momentum [181]. The lattice angular momentum contributes $3N$ from the crystal's threefold rotational symmetry C_{3h} at the K-points [181, 182]. It allows for transferring excess angular momentum into the crystal lattice [183]. Note that the spin of the electron does not flip during excitation, $\Delta s = 0$, although SO coupling is strong in TMDCs [56]. The exciton confined in the 2D plane possesses an angular momentum Δl_X resulting from the orbital motion of the electron relative to the hole. This is in contrast to bulk crystals, where the angular momenta of the electrons originate mainly from their atomic orbits. Besides, the valley index τ contributes angular momentum of the circulation of electrons from one atomic site to another throughout the crystal unit cell, where adjacent valleys have opposite signs [181]. Hence, for a one-photon excitation (using circular-polarized light with $\Delta l_\mathrm{pht} = \pm 1$) from the ground state to the first excitonic level ($\Delta l_\mathrm{X} = 0$), the valley angular momentum has to change according to $\Delta\tau = \pm 1$. The angular momentum is only conserved when the valley index matches with the polarization of the light. In this way, the rotational symmetry gives rise to a valley-contrasting optical circular dichroism: the interband transitions at the high symmetry points may be excited valley-selective using pure circularly polarized light [180, 184]. Right-handed (σ^+) circularly polarized light couples only to the K_+ valley with $\tau = +1$, while left-handed (σ^-) circularly polarized light couples only to the K_- valley with $\tau = -1$ [55]. The selection rule also allows one to determine the allowed transitions for nonlinear excitations with $\Delta l_\mathrm{pht} = \pm 2$ and higher,

e.g., transitions studied using second harmonic generation and two-photon luminescence. They allow to excite the dark exciton states with odd parity, while linear, one-photon absorption may only excite the bright states with even parity [115, 185]. These circularly polarized optical selection rules are also known as chiral transition rules, as the transitions are excited using chiral ($\sigma^{\pm}$ polarized) light [56]. In this way, spin-valley locking may be exploited for exciting distinct polarized exciton states and permits the optical generation and detection of the spin-valley polarization. Typically, the spin-valley locking is used either to excite and detect one of the two valleys (valley polarization) or to excite a linear and coherent superposition of both valleys (valley coherence). Yet, valley coherence is limited by rapid intervalley transfer due the long-range exchange interaction and $\vec{k} \cdot \vec{p}$ mixing [8]. It induces an intervalley transfer of the electron-hole excitation, where each electron remains in the same valley, but changes the band. This mixes the bright excitons in different valleys and enables simultaneous spin flips of an electron and a hole [56].

2.4 Phononic interactions

Phonons are the quantized quasi-particles of an elastic field. They are also considered as quantized sound waves, since long-wavelength phonons give rise to sound. Furthermore, they are denoted as lattice vibrations, as they are collective elementary excitations in the crystal lattice of solids or other condensed matter. The vibrational mode of a phonon relates to the frequency in which a lattice of atoms or molecules uniformly oscillates. The term is chosen to denote that phonons are the quanta of the vibrational field, in analogy to photons as the quanta of the electromagnetic field. The phonon wavevector is denoted by $\vec{q}$, leading to the crystal impulse $\hbar\vec{q}$ and energy $\hbar\omega_q$. In nanostructures, phonons are affected by the spatial confinement, which leads to, e.g., confined and interface modes [186]. In addition, the charge carrier-phonon interaction is increased by confinement, which affects the scattering rates and relaxation properties. The interaction of phonons and electrons is one of the fundamental interactions of (quasi-)particles in solids. It is important for the understanding of transport and thermodynamic properties in solids, like thermal and electrical conductivity. Furthermore, the electron-phonon coupling determines the temperature dependence of the electron band structure, influences the effective masses and the charge transport, and supports the formation of quasi-particles, as e.g. polarons. Besides, phonons and their interactions play a major role in the optical control of semiconductors. Hence, their study is important in determining the optical properties of semiconductor nanostructures.

2.4.1 Description of phonons

The **dynamics of a crystal lattice** are described by a model consisting of massive spheres (representing the atoms) connected by elastic springs (representing the chemical bonds) in a periodic structure. The Hamiltonian of a crystal $\hat{H}_{\mathrm{c}} = \hat{H}_{\mathrm{ion}} + \hat{H}_{\mathrm{e}}$ comprises of the Hamiltonian $\hat{H}_{\mathrm{ion}}$ of the atoms, ions or nuclei, and the Hamiltonian $\hat{H}_{\mathrm{e}}$ of the electrons (neglecting interactions) [187]. In section 2.1.1, the electronic eigenenergies of $\hat{H}_{\mathrm{e}}$ are obtained for fixed atomic core positions, making use of the so-called **adiabatic** (Born-Oppenheimer) **approximation**. It decouples the movements of electrons and

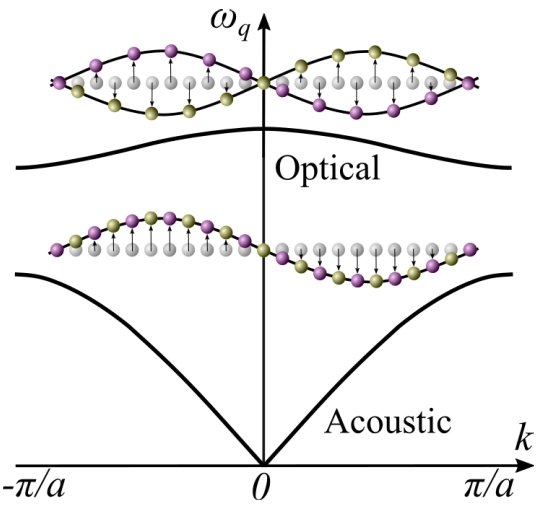

Figure 2-10: Phonon dispersion of the optical (top) and acoustic (bottom) modes in the first Brillouin zone of a linear diatomic chain, including the patterns of transversal ionic displacements. In the optical mode two neighboring atoms with different masses (pink and yellow spheres) move against each other, the vibration is out of phase. The acoustic mode results from in phase-motion of the atoms. After Fig. 2.3 in [188].

nuclei due to their different masses, which lead to movements on different timescales. Hence, the electronic eigenenergies are calculated using only the positions of the atom cores as parameters. Here, the electronic eigenenergies are treated as an effective potential for the crystal atoms, following chapter 5 in [48]. This reflects the close motion of the lattice atoms around their rest position, which are only slightly distorted by the electrons. The whole potential energy V_{eff} may be obtained by summing up the pair interaction over all atom pairs of the crystal lattice. This potential is expanded into a Taylor series up to the second order around the rest position of the atoms, wherein the first and second term may be neglected. Note that higher order terms (anharmonic corrections) are important for, e.g., the understanding of thermal expansion and thermal conduction [83]. The third term is the quadratic derivative of the displacement of the specific atom from its equilibrium position, and, thus, may be approximated by a harmonic oscillator system (**harmonic approximation**). This second-order spatial derivative of the potential is also termed as coupling or force constants. These constants allow for calculating the forces on a specific atom caused by the movement of other atoms. They have to satisfy symmetry conditions following from the isotropy of space as well as of translational invariance and of the specific point group of the lattice.

The displacement of one or more connected atoms from their equilibrium positions gives rise to **vibrational waves** propagating through the lattice. Insights into these **lattice vibrations** may be gained using the (classical) relation that the sum of the coupling forces and the inertial forces must equal zero. The resulting differential equations of the periodic crystal lattice are equations for a set of coupled harmonic oscillators. They may be solved by assuming plane waves for the movements of the atoms, leading to coupled linear equations for the displacements. These waves resemble electron Bloch waves, but, while electrons may be anywhere in the crystal, the atom positions are discrete [23]. The eigenmodes of the crystal lattice are finally obtained using Bloch's theorem and periodic boundary conditions. The resulting dependence of the mode's frequency ω_q to the wavevector is illustrated in the **phonon dispersion relation**, as displayed in figure 2-10. This dispersion is directly related to the acoustic and thermal properties of a material. Typically, only phonons near the zone center need to be considered, whereas the nonlinear part of the phonon dispersion is important for, e.g., phonons with wavelengths as short as the lattice constant and for intervalley scattering [23, 189].
The dispersion relation of the lattice vibrations consists of different branches named

acoustic and optical modes. In a three-dimensional crystal with multi-atomic basis consisting of N atoms, there a generally three acoustic branches and $3N-3$ optical branches. The acoustic branch denotes the in phase-motion of the atoms within the unit cell. The acoustic modes are zero at the center of the Brillouin zone and they follow a linear relation $\omega_q = v_\mathrm{g} q$ for small wavevectors (long wavelengths). The proportionality constant v_g, the group velocity, corresponds to the propagation speed of the acoustic mode. It corresponds to the speed of sound in the lattice in the long-wavelength limit. The optical branch denotes the modes where neighboring atoms in the unit cell vibrate with a phase difference of π. This creates a dipole moment in polar materials and allows for coupling to electromagnetic waves. At the center of the Brillouin zone, the group velocity of the optical modes is constant and depends on the different masses of the atoms in the basis.
The difference in the atomic masses also affects the gap between the modes at the boundary of the Brillouin zone. The vibration modes are further distinguished into **longitudinal and transversal modes**, depending on whether the atoms vibrate parallel or perpendicular to the propagation direction of the wave. The amount of modes depends on the dimension d_{im} of the studied structure and the number N of atoms with different masses in a unit cell, with the three acoustic branches divided into one longitudinal acoustic (LA) and $d_{im}-1$ transverse acoustic (TA) modes. The $3N-3$ optical modes are split into $N-1$ longitudinal optical (LO) and $(N-1)(d_{im}-1)$ transverse optical (TO) modes [189]. Note that the formation of purely polarized waves is only possible when the waves propagate in the direction of a symmetry axis of the crystal.
Phonons may further be separated into **polar and nonpolar modes**, depending on the symmetry and structure of the crystal [34]. Polar modes occur in crystals with covalent bondings and involve a displacement of the atoms along a direction which breaks the inversion symmetry of the crystal. These modes generate an electric dipole moment, which may interact with light and other external electric fields. In this context, homopolar refers to a mode where no first-order dipoles are induced. They appear where the atomic layers have a plane-mirror symmetry and a pair of identical atoms on each side of the plane vibrates in counter-phase, e.g. as in TMDCs [190]. Therein, the homopolar phonon mode is purely out-of-plane [191]. Note that this mode interacts via short-range deformation-potential interaction instead of long-range piezoelectric interaction for polar modes in TMDCs. In contrast, nonpolar modes do not generate an electric dipole moment. They occur mainly in nonpolar semiconductors with covalent bondings such as silicon or germanium. These modes involve a displacement of the atoms that preserves the inversion symmetry of the crystal.

The dynamics of the crystal lattice are described by a sum of harmonic oscillators with frequencies ω_q, the lattice vibration modes, with allowed wavevector $\vec{q}$ and defined polarization direction. The energies of the vibration modes may be expressed by the eigenvalues of the harmonic Hamiltonian $\hat{H}_\mathrm{harm} = \hat{T} + \hat{V}_\mathrm{harm}$, leading to the discrete eigenenergies $E_\mathrm{harm} = (n + 1/2)\hbar\omega_q$, which have to be summarized over all $3N$ modes. These collective vibration modes are not localized vibrations of individual lattice atoms, but all crystal atoms contribute to a lattice vibration. Hence, a vibration mode denotes an excited state or excitation of the whole lattice, wherein all atoms of the lattice move with the same time dependence, but phase-shifted. Making use of wave-particle duality, the collective excitation may be treated as a **quantized quasi-particle** named phonon. The concept of quasi-particles as field quanta is also used for the quanta of the electronic

spin structure (spin waves), which are termed magnons, and the quanta of the free electron gas density (plasma oscillations), which are termed plasmons. All these collective excitations behave like bosons, following Bose-Einstein statistics.
The Bose-Einstein distribution denotes the way particles occupy discrete energy states at low temperatures: all bosons may occupy the same energy state. Phonons as bosons obey the Bose-Einstein distribution, so that at low temperatures low-frequency modes have much more phonons than high-frequency modes, while the overall number of phonons reduces as the temperature goes down. Consequentially, **optical phonons freeze out at low temperatures** and optical phonon scattering is suppressed [192]. This results in an overall low scattering and a low absorption at low temperatures [34]. Moreover, high temperatures are needed for a thermal excitation of optical phonons due to their high energies (in GaAs: $E_{\mathrm{op}} \approx 36\,\mathrm{meV}$) compared to the mean acoustic phonon energy in similar QDs (of about $E_{\mathrm{ac}} \approx 1\,\mathrm{meV}$) [193, 194], and a thermal energy of $E \approx 1.7\,\mathrm{meV}$ corresponding to $T = 20\,\mathrm{K}$. Note that both Fermi-Dirac and Bose-Einstein distributions become Maxwell-Boltzmann distributions at high temperatures, so that for $T > 100\,\mathrm{K}$ inelastic scattering is dominated by optical phonons [192].

The concept of quasi-particles is helpful in determining scattering processes where (quasi-)particles collide and exchange their (quasi-)momentum. In this way, **inelastic scattering** may be used to reveal the phonon dispersion relation, using e.g. atoms, neutrons or photons (see chapter 3 in [187]). In the context of scattering, it is helpful to make use of the ladder operators: the creation operator $\hat{a}^\dagger = \sqrt{\frac{m\omega}{2\hbar}}\left(\hat{x} - \frac{i}{m\omega}\hat{p}\right)$ increases the number of particles in a given state, while the annihilation operator $\hat{a} = \sqrt{\frac{m\omega}{2\hbar}}\left(\hat{x} + \frac{i}{m\omega}\hat{p}\right)$ lowers the particle number. The operators correspond to an increase or decrease of the eigenvalue of the harmonic oscillator and change the corresponding quantum number. Here, they append or remove a single energy quantum of the oscillator. In this way, scattering may be understood as a process where the added energy is transformed into a particle state with modified energy, and of other corresponding quantum numbers, e.g., angular momentum. The corresponding Hamiltonian of the harmonic oscillator, $\hat{H}_{\mathrm{harm}} = \hat{T} + \hat{V}_{\mathrm{eff}} = \sum_q \frac{\hat{p}^2}{2m} + \frac{1}{2}m\omega_q^2\hat{x}^2$ resembling the classical harmonic oscillator, may thus be transformed to the ladder Hamiltonian $\hat{H}_{\mathrm{harm}} = \sum_q \hbar\omega_q(\hat{a}_q^\dagger\hat{a}_q + \frac{1}{2})$. It involves the phonon creation operator $\hat{a}_q^\dagger$, the phonon annihilation operator $\hat{a}_q$ and the energy $\hbar\omega_q$ of the collective lattice mode (phonon) [187].
The photons used in inelastic light scattering have an energy difference compared to the phonons of about $1 - 10\,\%$, and an equal small momentum transfer. Thus, only phonons around $\vec{q} \approx 0$ within the first Brillouin zone may be excited by optical techniques [48]. Therein, optical phonons may be examined by optical (Raman) scattering experiments as well as by optical absorption or reflection measurements. On the contrary, the most abundant acoustic phonons may only be studied optically by (Brillouin) scattering experiments [34]. Furthermore, acoustic phonons have rather low energies and require a higher energy resolution, so that their measurement is more difficult. Additionally, their linear $\omega_q \propto \vec{q}$-behavior implies that acoustic modes are sensitive to the scattering angle. In contrast, optical phonons scatter almost independently of the angle, as ω_q is about constant near $\vec{q} = 0$. Further insights into inelastic laser-light scattering are provided in section 3.2.

2.4.2 Spatial confinement of phonons

Spatial confinement affects the phonons and their scattering, e.g., by an inhomogeneous change of material properties and intrinsic strain (see chapter 8 in [88] and in [195]). In nanostructures, the lack of translational symmetry may lead to the mixing of transverse and longitudinal phononic characters [196]. In the case of strong confinement, the bulk phonon dispersion gets quantized and the resulting discrete phonon states are known as vibrons [79, 197]. The discretization of the phonon states tends to appear at QD sizes with diameters below 20 nm, noticeable typically for sizes below 20 lattice parameters [195]. Compared to bulk crystals, the interruption of the lattice periodicity in nanostructures allows for observing phonons that are not in the zone center, with $\vec{q} = n \cdot \pi / R_z$. In this case, the phonons may be treated as having a discrete energy spectrum starting at finite energy [5, 198]. The additional contribution from higher phonons results in a peak-shift and an asymmetric lineshape broadening, visible in Raman spectroscopy [195]. Thereby, the effect of the confinement depends on the difference between the phonon dispersion curves of the nanostructure compared to the host material. Such **confined modes**, as well as localized interface modes, may appear, e.g., in colloidal QDs [199] and in glass-embedded QDs [198]. Moreover, confined phonon modes appear in superlattices, where the phonon branches are backfolded within the different layers. Hence, the optical phonons cannot propagate along the growth direction, but only along their respective layers [187]. In this case, they follow the polarization-dependent selection rules, where odd confined modes are seen preferentially in off-diagonal polarization and the even ones in diagonal polarization [5].

In QDs with strong confinement, the available phonon energies typically do not match the discrete electronic energies. Hence, electron states tend to pure dephasing processes via acoustic phonons, which is termed phonon bottleneck [200]. Yet, the confinement effect is often negligible for QDs. When the elastic and acoustic mismatch between the QD and the barrier material is small, as in the studied QDs, the phonons may be considered as bulk phonons [201]. These weakly-confined phonons are represented as plane waves, where the confinement enters as a **form factor** to the coupling matrix element of the bulk phonons [195, 200, 202]. The form factor may be obtained within the envelope function formalism from the electron and hole wavefunctions in the QD. Typically, the form factor is expressed as a Gaussian envelope function [195], while it depends sensitively on the actual size of the QDs [200]. Assuming modified bulk phonons allows one to calculate the **phonon spectral density** $J_{\mathrm{ph}}(\omega) \propto \omega^3 \exp(-\omega^2/\omega_{\mathrm{co}}^2)$, with the cut-off frequency ω_{co} [200]. From this density, the coupling efficiency of the electron-phonon interaction may be estimated. For small energies, the bulk matrix element $\propto \omega^3$ dominates the coupling, while the form factor dominates at high energies and rapidly approaches zero, leading to a maximum with highest efficiency [195]. The specific coupling efficiency depends on the specific size and shape of the nanostructures.
In low-dimensional semiconductor structures, an additional coupling between electrons and phonons arises from interface motion: the so-called **ripple mechanism** [203]. It results from perturbing the electron wavefunction by interfacial motion due to acoustic phonons [204]. They cause an atomic interface to appear as a moving grating, thus changing the parameters of the system [205]. The ripple mechanism may be the dominant coupling mechanism for decreasing QD sizes less than 50 nm [203, 204, 206]. It is similar to the inelastic photon scattering by acoustic phonons in the vicinity of a free

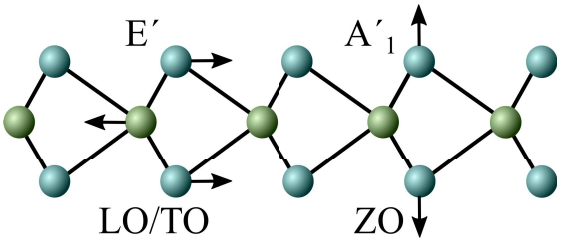

Figure 2-11: Scheme of the two first-order Raman active phonon modes in TMDCs: the in-plane, polar LO/TO mode (E', left) and the out-of-plane, homopolar ZO mode (A'$_1$, right). Black arrows indicate the vibration directions of the atoms. In analogy to Ref. [209].

surface [207].

The studied QDs consist of III-V compounds in a zincblende-type lattice. Such lattices possess two atoms per unit cell, hence the QDs obtain six phonon branches [23]. The bondings between the lattice atoms are slightly ionic rather than purely covalent, which increases the Coulomb interaction between the lattice ions. This not only enlarges the energy of the electronic bandgap, but also affects the acoustic and optical phonon modes. The TA modes obtain a much lower energy compared to the LA mode near the zone edge [23]. These acoustic modes are determined by the shear (TA modes) and the bulk elastic (LA mode) moduli, whereas the LA mode relates to compressional sound and the TA modes to shear sound. In addition, the LO modes have a higher energy compared to the TO modes (LO-TO splitting), while they are degenerate at the zone center due to the cubic symmetry of the zincblende structure [23]. This splitting is reduced due to mixing of the modes by alloy disorder and inhomogeneous strain in and around QDs [208]. Besides, the phonons in the QDs do not differ significantly from bulk phonons, as the QD confinement only weakly modifies the phonon properties via the form factor.

TMDC MLs possess three atoms per unit cell, hence they feature nine phonon branches: three acoustic and six optical branches [210, 211]. Bulk TMDCs consist of two ML units, so that these materials obtain 18 phonon branches with similar dispersion curves as in MLs [212]. Yet, these branches are split from the ML branches due to, e.g., interlayer vibrations. In MLs, the in-plane acoustic modes are the LA and TA modes, whereas the out-of-plane transversal acoustic mode is termed ZA. They have different dependences on the wavevector $\vec{q}$. Likewise, the six optical branches are two in-plane LO modes, two in-plane TO modes, and two out-of-plane transversal ZO modes [212]. The out-of-plane modes offer coupling mechanisms to the neighboring layers in vdW heterostructures. Using irreducible representations, the in-plane modes are considered as two degenerate LO/TO modes, due to the hexagonal symmetry of TMDCs. The two first-order Raman active modes which are visible in backscattering configuration are depicted in figure 2-11. In literature, the in-plane mode (left) may be denoted as E' or E^1_{2g}, and the out-of-plane mode (right) as A'$_1$ or A_{1g} [209, 213]. Similar to III-V compounds, the optical modes are affected by the LO-TO splitting, driven by the long-range Coulomb interactions from the lattice vibration coupling with the polarization field. Yet, the splitting is tiny (about $1\,\mathrm{cm}^{-1}$) at the zone center due to the lack of periodicity in the direction perpendicular to the layer [210, 214]. Besides, the slope of the LO dispersion at the zone center is influenced by the dielectric screening of the ML environment [215]. Moreover, note that the different TMDCs obtain slightly different phonon properties. For example, the large mass difference of W and S leads to a large acoustic-optical frequency gap, so that the scattering between the phonon modes is inefficient [212, 216]. This leads to a larger thermal conductivity of WS_2 compared to MoS_2.
Furthermore, chiral phonons (with helicity) may be observed in TMDC MLs. These

phonons preserve valley coherence and contribute to the exciton PL phonon replica of the spin-forbidden and of the momentum-forbidden dark excitons [175]. In chiral modes, one atom is stationary and the other rotates with a phase difference, or one atom rotates along two orthogonal in-plane directions, leading to a superposition of two orthogonal-linear vibrations of two degenerate modes [175, 217].
In vdW heterostructures, the aforedescribed intralayer modes may be accompanied by interlayer modes, resulting from the relative motion of the layers [218, 219, 220, 221]. Multiple interlayer breathing and shear modes may be found, of which some are not Raman active in the bulk. Typically, these modes have lower frequencies than other Raman modes due to the weak vdW interlayer interaction. They may be used to probe the interlayer coupling in such heterostructures [212]. Moreover, the coupling of the out-of-plane modes to the neighboring layers allows for unambiguously determining the number of layers via the energy difference between the two high-frequency modes (one degenerate in-plane mode and one homopolar out-of-plane mode) [222].

2.4.3 Electron-phonon interaction

Based on the adiabatic approximation, the dynamics of the atom cores and electrons as heavy and light constituents of a solid have been treated as independent systems. For the calculation of the electronic band structure, the positions of the atom cores are assumed to be fixed in the periodic configuration of the lattice, while the electrons contribute only to the binding forces when studying the lattice dynamics of the atom cores. Here, the **interaction of these systems by exchanging energy** with each other are studied. From the point of view of the electrons, the moving lattice perturbs the periodic potential, which may be understood as scattering between electrons and phonons, leading to three exemplary effects (after chapter 8 in [187]). Firstly, excited electrons may scatter inelastically and lose (gain) energy and momentum by emitting (absorbing) phonons. This leads to a finite lifetime of the excited electron states. Secondly, an electron system that was driven by an external field into a non-equilibrium state loses energy by emitting phonons to relax into an equilibrium state. Thereby, the crystal lattice serves as energy sink or heat reservoir. The exchange of energy alters the phase of the individual electron wavefunctions. Hence, this process termed electron-lattice relaxation is incoherent. Note that acoustic phonons relax mainly the electron momentum due to their small energies, in contrast to optical phonons which contribute to both momentum and energy relaxation [23]. Thirdly, the electron-phonon interaction in a polar lattice may lead to a new ground state of the system: a quasi-particle named polaron. Thereby, an electron creates a polarization cloud of virtual phonons around itself due to its charge, which accompanies the electron and changes its dynamic properties. A scheme of an electron in a lattice forming a polaron is depicted in figure 2-12.
Here, the coupling mechanisms leading to scattering between phonons and electrons or other particles like holes and excitons are studied, as derived from the interaction Hamiltonian $\hat{H}_{\text{e-ph}}$ of their local electron-phonon interaction potential. Their interaction may be treated as a **linear perturbation** to the unperturbed Hamiltonian $\hat{H}_0 = \hat{H}_{\text{e}} + \hat{H}_{\text{ph}}$ of the (quasi-)particles. In doing so, it is assumed that the electrons move coherently in a wave-like manner through the lattice and the electron system responds instantaneously to the ionic motion of the atom cores, the phonon system. Thus, the interaction Hamil-

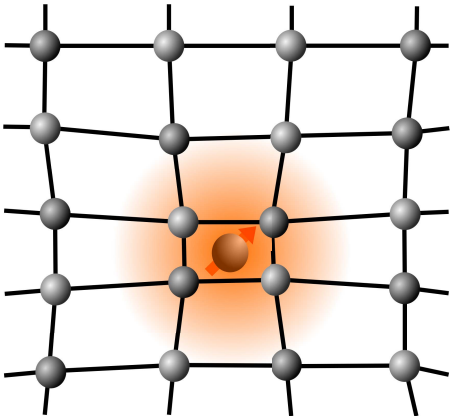

Figure 2-12: Schematic representation of the electron-phonon interaction contributing to the formation of a polaron. The electron (orange sphere) interacts with the lattice atoms (gray spheres) and forms a polaron. After Fig. 1.5 in [223].

tonian may be expressed as a Taylor series expansion of the electronic Hamiltonian (see chapter 3.3 in [23]).

The interactions of phonons with electrons vary for the different phonon types, as the atomic displacements have distinct effects depending on their type and on the structural properties of the lattice: **acoustic phonons cause local lattice compression or dilation**, **optical phonons relate to electric dipole vibrations** [23]. Specifically, the interactions of acoustic phonons (ac) may be described by acoustic deformation potentials (DP) and by piezoelectric (PE) polarization fields. These are explained below in detail. Optical phonons (op) interact via optical deformation potentials and via Fröhlich interaction (FI) [186, 210, 224]. Note that, instead of a macroscopic distortion of the lattice, optical deformation potentials alter the electronic energies by changing the bond lengths and/or the bond angles [23]. The piezoelectric and the Fröhlich interaction arise from a macroscopic polarization of the crystal lattice [225]. The dipole-like Fröhlich interaction is specific for LO phonons in polar materials, as it requires an oscillating dipole (thus excluding acoustic phonons) in which the atomic displacements run along the direction of the wavevector (thus excluding transverse phonons), see chapter 9.1.2 in [226]. It is also known as polar coupling or polarization interaction. In addition to these interactions, for semiconductors with several equivalent conduction band valleys, intervalley scattering via large-wavevector (zone-edge) phonons is another possible scattering mechanism [23], see section 3.2.
In a lattice without an inversion center, the interaction between electrons and acoustic phonons is the sum of the **acoustic deformation potential** and the **piezoelectric interactions** [227]. The piezoelectric potential results from the macroscopic electric polarization caused by an acoustic vibration, while the shift in the electronic band energies induced by static displacements of the nuclear positions is termed deformation potential [228]. In addition, the electron-phonon interaction in polar materials may be complemented by the **optical deformation potential** and the **Fröhlich interactions**. Hence, the unscreened electron-phonon interaction which couples to the carrier density is given by [23]:

$$\begin{aligned} \hat{H}_{\text{e-ph}}(\vec{r}) &= \hat{H}_{\text{DP,ac}}(\vec{r}) + \hat{H}_{\text{DP,op}}(\vec{r}) + \hat{H}_{\text{PE}}(\vec{r}) + \hat{H}_{\text{FI}}(\vec{r}) && (2.24) \\ &= E_{\text{DP,ac}}\, \nabla \cdot \boldsymbol{u}_{l,n}(\vec{r}) + E_{\text{DP,op}}(\boldsymbol{u}_{l,n}/a_0) - |e|\Phi_{\text{PE}}(\vec{r}) - |e|\Phi_{\text{LO}}(\vec{r}), && (2.25) \end{aligned}$$

with the deformation potentials E_{DP} and the displacement field $\boldsymbol{u}_{l,n}$ of the acoustic phonons. The distance between the two atoms inside a primitive unit cell is termed a_0.

Here, the acoustic deformation potential coupling is limited to the dominant term [227], which is already simplified to describe parabolic CBs, where only uniaxial coupling and no hydrostatic coupling has to be considered [201]. Note that the Hamiltonian of the acoustic deformation potential is proportional to the derivative of the atomic displacement ($\hat{H}_{\mathrm{DP,ac}} \propto \nabla \cdot \boldsymbol{u}_{l,n}$), while the optical deformation potential Hamiltonian is directly proportional to the atomic displacement ($\hat{H}_{\mathrm{DP,op}} \propto \boldsymbol{u}_{l,n}$). The Hamiltonian $\hat{H}_{\mathrm{PE}}$ of the piezoelectric coupling couples the electron with the electrostatic potential $\Phi_{\mathrm{PE}} \propto E_{\mathrm{PE}}$ from the piezoelectric polarization of the lattice. Therein, the macroscopic piezoelectric field E_{PE} induced by the acoustic phonons depends on the strain tensor, $E_{\mathrm{PE}} \propto \epsilon_{\mathrm{st}}$ [23]. The Fröhlich Hamiltonian $\hat{H}_{\mathrm{FI}}$ couples the electron with the macroscopic Coulomb potential $\Phi_{\mathrm{LO}} \propto E_{\mathrm{LO}} \propto \boldsymbol{u}_{\mathrm{LO}}$, with the electric field E_{LO} and the displacement $\boldsymbol{u}_{\mathrm{LO}}$ of the optical phonons. The exact forms of the potentials depend on the studied crystal structure, see examples in chapter 3.3 and 9.3 in [23, 79] and in [229], as they are very sensitive to the shape of the electron wavefunction [201].
The deformation potential couplings are of short-range in $\vec{q}$, while the piezoelectric and the Fröhlich interaction are of long-range in $\vec{q}$, or of short range in $\vec{r}$. These different ranges lead to the assumption that the couplings are out of phase, as they do not interfere in lowest-order perturbation theory [227]. Therefore, they may generally be treated as separate scattering mechanisms. However, when the couplings are in phase, e.g. for TA modes in TMDCs in the long-wavelength limit, the simultaneous coupling gives rise to interference [192, 225]. Note that the deformation-potential coupling is stronger in weakly or non-piezoelectric semiconductors compared to the piezoelectric coupling, while the Fröhlich coupling is typically strongest in polar materials. Besides, intervalley scattering is treated in the same way as deformation potential scattering, via an intervalley deformation potential [230].

The electron-phonon interaction depends on the kinetic energy of the involved electron and on the symmetry of the state. Likewise, the **exciton-phonon interaction** depends on the symmetry of the exciton state (type and excitation) and, hence, on the specific combination of electron and hole eigenstates [201]. The interaction Hamiltonian thus consists of both phonon interactions with electrons and holes, e.g., $\hat{H}_{\mathrm{DP,X}} = \hat{H}_{\mathrm{DP,e}} + \hat{H}_{\mathrm{DP,h}}$. The **hole-phonon interaction** may be treated similar to the electron-phonon interaction, with the hole expressed as empty electron site [231], or it may be discussed via the Bir-Pikus Hamiltonian, which includes the effects of strain from the phonons [23, 232]. Therein, the hole DP Hamiltonian mediated by the SO interaction depends on the specific hole wavefunction and is anisotropic [201, 232]. In QDs, the contribution of the holes to phonon scattering is quite small [232]. Although both electron and hole states couple to volume deformations, only the hole additionally couples to uniaxial and shear contributions. Hence, electron and hole do not contribute in a uniform manner in QDs [88]. Thereby, the properties of the created phonons and their interactions are affected by the actual QD shape, e.g., the strongest phonon emission is directed along the shortest axis of the QDs [233]. In TMDC MLs, exciton-phonon interactions are enhanced by the strong confinement and are involved in the absorption or emission by intravalley and intervalley processes at the Γ- and K-points. Moreover, chiral phonons may contribute to the interaction, e.g., they contribute to the exciton PL phonon replica of the spin-forbidden and of the momentum-forbidden dark exciton [175].

The acoustic **deformation potential coupling** scatters the electrons via the electric field produced by the strain field from acoustic phonons [34]. The long-wavelength

phonons cause a homogeneous lattice compression or dilation, and lead to a local relative volume change. This volume change creates an electric field proportional to the strain [226]. The strain tensor describes the relative volume change due to the deforming force of a stress field [34]. The electron experiences the volume change as a local change of the lattice constant, which shifts its energy [234]. Hence, mechanical deformations of the crystal lattice, as macroscopic displacements of the lattice atoms, change the energies of the electronic transitions in proportion to the strain tensor. This proportionality constant is called deformation potential, as it originates from local changes of the crystal potential. The potential is commonly assumed to be isotropic and linear in the phonon wavevector. The detailed form of the acoustic displacement field $\boldsymbol{u}_{l,n}(\vec{r}) \propto \mathrm{e}^{-i\vec{q}\vec{r}}$ depends on the specific lattice and the crystal symmetry, see e.g. [225] for TMDCs and [235, 236] for GaAs. Note that the dominant electron-phonon coupling is typically the deformation potential coupling to LA phonons [200].
The net change of the bandgap energy E_g at the Γ-point is described by $\Delta E_\mathrm{g} = (a_c - a_v)\epsilon_\mathrm{st}$, with the strain tensor $\epsilon_\mathrm{st} = \Delta V_{ol}/V_{ol}$ defined by the relative volume change [237, 238]. Therein, the deformation potential coefficients a_i of a given state in the CB ($i = c$) or VB ($i = v$) are defined as: $a_i = \Delta E_{\mathrm{st},i}/\epsilon_{\mathrm{st},i}$, with the energy shift ΔE_st under strain and assuming uniaxial absolute deformation potentials. The coefficients account for the shifts of the respective bands which form the bandgap [237]. Thereby, the absolute changes of the band energies depend on the kinetic energy of the state, which decreases when the lattice parameter of the material increases, and the type of state (bonding or antibonding), which increases or decreases the energy level when the bond length increases [237, 239]. In the case of zincblende semiconductors, the absolute deformation potential is approximated to $-8\,\mathrm{eV}$ ($-6\,\mathrm{eV}$) in GaAs (InAs) [113] and about $-7\,\mathrm{eV}$ ($-1\,\mathrm{eV}$) for the electron (hole) bands in GaAs [238]. Hence, while there is some uncertainty about the size of the absolute deformation potential, the bandgap increases for compressive strain ($\epsilon_\mathrm{st} < 0$) [238]. Typical energy shifts in QDs are on the order of 10 meV by strain amplitudes of about 10^{-3} [189, 240]. In TMDC MLs, the absolute deformation potentials are on the order of -5 to $-6\,\mathrm{eV}$, so that the bandgap in MoS_2 red-shifts by about $-50\,\mathrm{meV}$ per percent of tensile strain, with a spread of about $(45 - 70)\,\mathrm{meV}/\%$ [237]. Thereby, the CB state has antibonding character, resulting in a large negative absolute deformation potential (about $-6\,\mathrm{eV}$), with the energy of the state strongly decreasing when the material is expanded. The VB state has bonding character and, thus, obtains a small negative deformation potential ($-1\,\mathrm{eV}$), as the energy level increase of the bonding effect is partially compensated by the kinetic-energy effect [237]. In 2D materials, typically, the out-of-plane homopolar phonons contribute to the scattering via deformation potential, while the in-plane polar optical phonons interact through Fröhlich interaction [241].

The **piezoelectric coupling** scatters the electron via the electric field produced by acoustic phonons [34]. The electric field is proportional to the strain, as it results from the macroscopic polarization that accompanies an applied strain in crystals lacking an inversion center. Specifically, electric charges are accumulated in materials due to stress. The natural or induced asymmetric charge surroundings lead to oscillations of the lattice ions and the occurrence of electric dipole moments [34]. The electric dipole moments change their polarization when mechanical stress is applied. Hence, a piezoelectric potential is created from the interaction between the mechanical and electrical states in any semiconductor crystal with non-centrosymmetric structure under the generated strain.

The induced lattice compression and dilation result in an electric field parallel to the propagation direction of the acoustic phonons. The resulting polarization may be quantified by $P_i = e_{\mathrm{PE},ijk}\epsilon_{\mathrm{st},jk}$, with summation over double indices [238]. Therein, the dielectric polarization is linearly linked to the piezoelectric tensor e_{PE} and the strain tensor ϵ_{st} [187]; higher orders are neglected [242].
The piezoelectric potential $\Phi_{\mathrm{PE}}(\vec{r}) \propto \vec{q} \cdot E_{\mathrm{PE}}$, as used in equation (2.24), may be calculated by the piezoelectric field E_{PE} induced by an acoustic phonon and its wavevector $\vec{q}$. The electric field $E_{\mathrm{PE}} = e_{\mathrm{m}} iQ\,\delta R/\epsilon_{\mathrm{st}}$ consists of the strain tensor $\epsilon_{\mathrm{st}} = iQ\,\delta R$ with the atomic displacements δR and the electromechanical tensor e_{m} [23]. Due to an additional $1/Q$-term from the Coulomb interaction, the piezoelectric coupling becomes stronger for small-wavevector or long-wavelength acoustic phonons, compared to the deformation potential. This is why the piezoelectric interaction is assumed to be of long-range, while the deformation potential interaction is considered as short-range. In the long-wavelength limit, the piezoelectric interaction may be approximated by a linear behavior [192]. Thus, neither polar nor piezoelectric scattering provide a large momentum transfer and may be neglected for intervalley scattering [34]. Furthermore, the piezoelectric interaction may be positive (attenuation) or negative (gain) in terms of the electron mobility, while other electron-phonon interactions always have a positive impact on the energy loss.
In unstrained or weakly strained III-V semiconductors, the piezoelectric effect may be neglected, as it is typically much weaker than the deformation potential interaction [200, 204, 243]. This is due to the symmetry of the zincblende lattice, where only one off-diagonal piezoelectric coefficient of the tensor contributes [202, 238]. The piezoelectric contribution increases for a higher asymmetry between the electron and hole wavefunctions due to the nonvanishing electron-hole dipole moment [244]. Hence, in the case of similar electron and hole wavefunctions, the electron and hole contributions nearly cancel each other, leading to a negligible piezoelectric interaction [245].
In 2D TMDCs, the electron-phonon interactions mainly originate from the deformation potential or the Fröhlich interaction [213]. Typically, the out-of-plane homopolar phonons contribute to the scattering via deformation potential, while the in-plane polar optical phonons interact through Fröhlich interaction [241]. Specifically, the latter may be much stronger than the former for resonant exciton energy excitation. However, at low energies the piezoelectric scattering may be strongly screened, in contrast to the deformation potential scattering of the TA phonons [192]. Both interactions are highly anisotropic: the deformation potential coupling has the threefold rotational symmetry of the conduction band, while the sixfold rotational symmetry of the piezoelectric coupling stems from the hexagonal crystal lattice [192]. Note that piezoelectricity appears only in MLs and other odd layers, due to the need for broken inversion symmetry [246].

The electron-phonon interaction is very susceptible to **temperature** changes, since phonons as well as electrons are, among other (quasi-)particles, central thermal energy carriers contributing to the heat capacity of a material. Specifically, the electron-optical phonon interaction is suppressed at low temperatures [247]. At high temperatures $T > 100\,\mathrm{K}$, inelastic scattering is dominated by optical phonons [192]. Note that the interactions with optical phonons may be neglected for the scattering experiments in the studied QDs due to their large **phonon energies** (see chapter 4 and similar in [248]), while they are included in the upconversion studies of TMDCs due to the higher energy gain in the multi-phonon processes (see chapter 5 and in [15, 249]), although both materials are studied at low temperatures. Furthermore, note that phonon scattering due

to electron-phonon interactions leads to a remarkable inhomogeneous broadening of the PL lineshapes with rising temperature [250]. Therein, scattering with optical phonons contributes to phonon sidebands, while scattering with acoustic phonons induces a broad background in the spectra [202].

3 Experimental background and methods

When light interacts with a material, the incident beam is reflected, refracted, absorbed or scattered. The modified beam provides information about the internal structure and the properties of the material. Specifically, optical techniques are used to study the characteristics of low-dimensional semiconductors in order to gain information about exciton-phonon interactions (see section 2.4.3). These optical techniques stand out regarding their non-contact and non-destructive nature, little sample preparation and the facile laser beam manipulation, e.g., regarding selectable excitation energy, power density or polarization. In this thesis, the samples are examined by photoluminescence spectroscopy related to optical absorption and by inelastic light scattering.
Photoluminescence (PL) spectroscopy is widely used to characterize the optical and electronic properties stemming from excited states. PL spectroscopy differentiates from photoluminescence excitation (PLE) spectroscopy which is used to investigate the whole electronic level structure of the material. Both techniques are explained in detail in the section 3.1. The following section 3.2 deals with inelastic light scattering. Inelastic scattering is accompanied by an energy (or wavelength) change of the involved particles. It allows for directly determining the g-factor or energy splitting of electrons, holes and excitons, and for detecting spin interaction mechanisms with different scattering partners. Moreover, the challenges of measuring scattered light compared to PL(E) spectroscopy are discussed. Apart from the low probability of scattering events, the examined energy shifts in the resonant scattering process are rather weak in intensity and energetically in close proximity to the laser line [251]; thus, their measurement requires advanced techniques and devices. The setups and devices that fulfill these requirements are explained in more detail in section 3.3.
Besides the specific measurement technique, the conceptual design of the setup also depends on the size of the studied low-dimensional structures: quantum dots and monolayers. Quantum dots (QDs) as zero-dimensional structures are small in size, only about several tens of nanometers in diameter [252, 253]. Yet, the large amount of similar QDs in one sample yields accurate results when performing ensemble measurements with a spatial resolution in the millimeter range. Compared to QDs, two-dimensional monolayer materials are relatively large in lateral real space dimensions, with a size of about several micrometers [254]. However, their measurement requires micrometer resolution, as they occur as single flake due to their fabrication process and neighboring layers with higher layer numbers might disturb their signal. Hence, additional emphasis is placed on the usage of the micrometer positioner system. In the last section 3.4, details on sample fabrication are provided. The examined QDs are grown via molecular beam epitaxy as a bottom-up approach, while the examined high-quality monolayers are fabricated in a top-down approach using adhesive tape. Additionally, the post-annealing process has further impact on the sample properties. The description of these properties completes this chapter.

3.1 Photoluminescence and photoluminescence excitation spectroscopy

Photoluminescence spectroscopy and the complementary photoluminescence excitation spectroscopy are two similar spectroscopic techniques. Both processes, consisting of photoexcitation, relaxation and recombination, are shown in figure 3-1 (a) and (d) schematically, in (b) and (e) spectrally, and in (c) and (f) exemplary spectra are shown. Both spectroscopy techniques analyze the emission (light intensity) of a sample as a function of emitted and, respectively, incident photon energy (or wavelength). The resulting intensity-energy distribution, also called spectrum, contains information about, e.g., the energy levels of the semiconducting material studied.

Generally, luminescence is a radiative photon emission process caused by electronic excitation processes. In the case of **photoluminescence** (PL), the absorption of higher energetic photons leads to the spontaneous emission of photons stemming from the allowed electric dipole transitions. Specifically in semiconductors, the emitted photons result from electron-hole pair and excitonic transitions. The energy of the incident laser light is typically larger than the bandgap energy of the semiconducting material (non-resonant excitation), so that the absorption of photons within the crystal is possible. The incoming light excites electrons from the valence band into the conduction band (**photoexcitation**) and leaves photo-excited holes in the valence band. The transition of an electron between the initial and the final state is described by the matrix element of the Hamiltonian consisting of an electron interacting with the quantized electromagnetic field of a photon. The details of how the Hamiltonian for radiative transitions of QDs evolves from the interaction of an atom with electromagnetic radiation and its consequences can be found in chapter 5 in [24]. The resulting transition matrix element consists of the electron momentum operator acting on the initial and the final state, allowing for defining selection rules. In the process of photoexcitation, the ground and excited electronic states are coupled, induced by the oscillating electric field of the photon (see chapter 9.4 in [22]). This mixing can only occur when the energy difference of the coupled states corresponds to the photon energy and the transition dipole moment corresponds to the photon dipole moment. Hence, the photon's energy and momentum are transferred to a photo-excited electron-hole pair, as required by energy and momentum conservation.
After the initial photoexcitation process, as depicted in figure 3-1 (a) and (b), the excited electrons and holes relax non-radiatively into energetically lower-lying states towards the bandgap minimum. This thermalization process leads to the emission of optical and acoustic phonons, while the charge carriers cool down to lattice temperature and reach quasi-thermal equilibrium distribution (see chapter 6 in [19]). Note that this **relaxation** process may consist of intermediate steps not shown in the figure. Additionally, the mutual attraction of electrons and holes via the Coulomb force leads to exciton formation (see details on excitons in section 2.2). The excitons may be formed either by direct resonant excitation as stationary eigenstates or after band-to-band excitation with some delay under the emission of acoustic phonons (see chapter 23.3.1 in [5] and chapter 4.2 in [19]). During the relaxation process, the electrons, holes and excitons may interact with other charged particles via Coulomb scattering. This may alter their energy and momentum and lead to spatial diffusion, which decreases the PL efficiency. These interaction processes are reduced for resonant excitation of the charge carriers, which limits

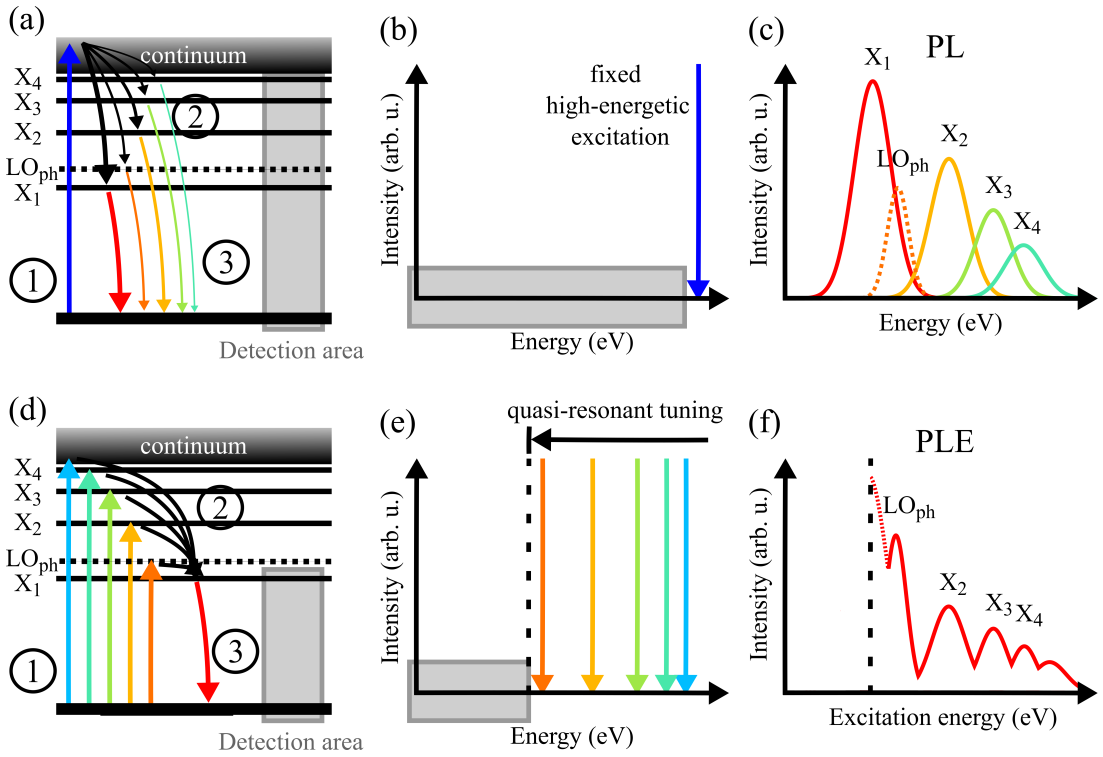

Figure 3-1: Scheme of PL (top) and PLE (bottom) spectroscopy. Numbers in the level scheme in (a) and (d) indicate the following processes: (1) excitation, (2) (non-radiative) relaxation, and (3) recombination / annihilation. The relaxation process may consist of several intermediate steps not shown here. (b) and (e) show schemes of the spectral excitation and detection, while (c) and (f) show exemplary resulting spectra. Note their different x-axes. The peaks in PLE denote specific absorption and interaction between excited states (X_1-X_4) and with phonons (LO_{ph}).

the thermalization to the confined states in the nanostructure and the diffusion to non-confined spatial directions (see chapter 3.3 in [19]). In addition, resonant excitation also bypasses the related charge carrier capture and nonradiative recombination in, e.g., a barrier layer [255].

Finally, the electron-hole pairs or excitons recombine through the emission of light (luminescence), as the last step of the thermalization process. Like the initial photoexcitation process, the finalization of PL by charge carrier **recombination** is also characterized by an individual one-photon process described by a transition matrix element of the involved states. The luminescence usually stems from a recombination of the lowest excited state confined in the nanostructure, but may also stem from higher states. However, the higher states are usually not visible due to their relatively small binding energies, vanishing oscillator strengths or due to broadening mechanisms (see chapter 15.1 in [5]). Yet, note that the oscillator strength at the second lowest transition is the strongest in many tetrahedrally coordinated semiconductors, e.g. in many zincblende structures [23, 256]. In addition, the charge carriers may recombine nonradiatively and, thus, cannot be detected optically. A requirement for radiative recombination is that the involved states are optically active with high radiative efficiency. The radiative efficiency, which covers the ratio of incident photons to photo-excited electrons (absorption efficiency) and back to outgoing photons (recombination efficiency), must at least be high enough so that the outgoing light is detectable. Optically active means that the angular momentum of the transition between the involved electronic levels matches the angular momentum of the

incoming and outgoing photons, so that a direct excitation from and recombination to the valence band is possible. The resulting selection rules from energy and momentum conservation are discussed in section 3.2.2.
As shown in figure 3-1 (c), an exemplary PL spectrum consists mostly of the lowest excited states in the nanostructure, as these are populated the most at low temperatures. Aside from the levels near the bandgap, continuum states and barrier states may be visible in the PL as well. For instance, with increasing excitation power the excited states in QDs emit light due to the level-filling effect (see chapter 2.3.2 in [24]). Thus, the emitted light contains information about the whole energy level structure (photon wavelengths), exciton number (PL intensity), polarization of the transitions and other electronic and structural properties of the material. PL studies allow for determining the inner structure of the material and effects on excitonic transitions like homogeneous broadening of the exciton recombination line. Furthermore, changes of the exciton binding energy due to enhanced charge carrier localization, e.g., due to internal strain, and carrier-carrier interactions are detectable [257]. The PL properties are also sensitive towards external parameters like temperature and applied fields, for example, electric and magnetic fields and pressure. Besides, the dielectric environment, like interface morphology, and sample quality affect the emitted light (see chapter 6 in [19]). This makes PL spectroscopy a powerful tool for material characterization.
Compared to other sample characterization methods, PL spectroscopy is advantageous since it provides energy resolved information non-destructively and is easy to use as it does not require specific sample preparation or treatment. For example, electroluminescence as electrical characterization technique requires electrical contacts placed onto the sample for applying voltage to yield luminescence [258]. However, PL spectroscopy has some drawbacks since it provides information mainly on radiative recombination processes. Moreover, optical transitions in indirect bandgap semiconductors, which require additional phonons, obtain much smaller radiative recombination probabilities [259]; hence, they are more difficult to observe in PL. Other non-radiative recombination processes may only be obtained indirectly through the analysis of the radiative recombination efficiency and its dependence on external parameters.

Complementary information may be gained via **photoluminescence excitation** (PLE) spectroscopy. Similar to absorption spectroscopy, this method provides information on absorption properties, but is a more sensitive optical method with improved signal-to-noise ratio [259]. The photoexcitation process in PLE spectroscopy is initialized using a tunable excitation source, in contrast to the fixed high-energetic laser excitation used for PL spectroscopy. Here, the excitation energy is tuned while the detection position is fixed, e.g., at a specific exciton energy, see figure 3-1 (d) and (e). The emission intensity is recorded as a function of the excitation energy keeping the incident photon density constant. Hereby, the excitation energy is typically decreased from higher energy (larger than the bandgap, but below the barrier absorption edge) towards quasi-resonant excitation close to the detection energy. Each transition is, again, described by a transition matrix element of the involved states. The peaks in the PLE spectra indicate absorption (lines), as shown exemplary in figure 3-1 (f), and an increasing peak intensity indicates the coupling of different states. In this way it is possible to detect contributions from different energy states to the luminescence of the selected level and to identify the origin of multiple emission lines. Thus, PLE spectroscopy is a powerful method to investigate the electronic level structure via the luminescence of specific emission centers including their

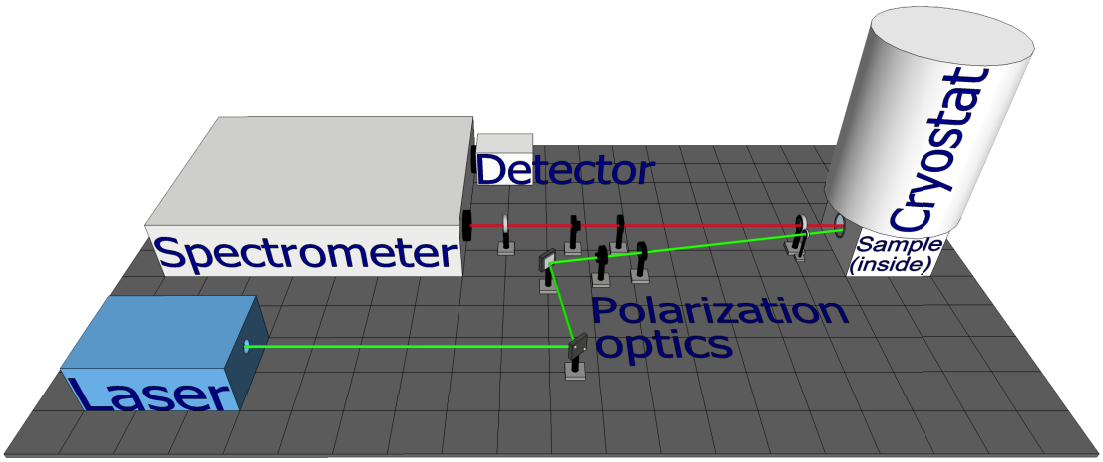

Figure 3-2: Basic optical setup consisting of a laser, polarization optics, a cryostat, a spectrometer and a detector. The sample is kept inside the cryostat and is excited by the laser light (green beam), its emission (red beam) propagates towards the spectrometer. The polarization optics (round, black) consist of a Glan-Taylor prism and a retardation plate in the excitation path and in reversed order in the detection path. Lenses are indicated by white outer rings; mirrors are angular shaped.

excited states, as well as the transfer of excitation between different states. Furthermore, it is worthwhile to mention that the luminescence peaks in PL and PLE spectra differ slightly, as the PL (emission) spectrum is shifted towards lower energies (Stokes shift) compared to the PLE (absorption) spectrum. The size of the Stokes shift depends on the widths of the peaks and is due to thermalization and relaxation of the charge carriers by phonon emission (see chapter 6 in [19]).

PL and PLE spectroscopy setups both require a laser for excitation, a monochromator for spectrally analyzing the luminescence and a detector. A basic PL(E) setup is depicted in figure 3-2. For a PL setup, a monochromatic laser with a fixed energy larger (non-resonant) or about equal (quasi-resonant) to the bandgap energy is sufficient. Contrarily, a PLE setup requires either a tunable laser or a white light lamp dispersed via a monochromator. The luminescence from the sample, which is kept in a cryostat, is analyzed by a monochromator or spectrometer. The obtainable energy resolution depends on its focal length and the used grating, among others. To detect the dispersed luminescence, either a photomultiplier tube (PMT) or a semiconductor-based detector, e.g. a charge-coupled device (CCD) camera, may be used. The choice of the detector depends on the emitted photon energy, available measurement time and required resolution. Although PMTs are very sensitive and offer a high spectral resolution in combination with a monochromator, their drawback is a long measurement time due to a necessary scanning through a spectral range. Contrastingly, CCD cameras cover a large spectral range in a usually fast single acquisition due to their multichannel detection technique. However, their time-saving usage may be accompanied by a loss of spectral resolution.
Furthermore, both spectroscopy techniques offer polarization resolved measurements, which is important to identify dependencies on the angular momentum. For this purpose, the combination of Glan-Taylor prism and polarizer like a linear- or a quarter-wave retardation plate defines the light polarization of the exciting laser light and analyzes the polarization of the sample's emission. The polarization of the emitted light is typically

aligned about a crystallographic axis of the sample, since it depends on the orientation of a dipole oscillator. Changes in the sample structure result in a change of the allowed transitions according to the selection rules. For example, due to confinement in QDs the lh and hh degeneracy is lifted, which defines an angular momentum quantization axis along the growth axis denoted typically by z (see chapter 3.1.6 in [24]). Hence, the excitation energy may be tuned to excite either hh or lh via the appropriate laser light polarization. Additionally, polarization anisotropy may arise from dielectric mismatch, bond asymmetries, alloy composition, modulation, strain or spin-related phenomena [259].

In some materials, **upconversion luminescence** spectroscopy or upconversion PL occurs for an emission energy higher than the excitation energy due to, e.g., two-photon processes, Auger processes, or thermally assisted surface state processes [259]. For the two-photon process, a real (not virtual) intermediate state is required, leading to a two-step two-photon absorption. Compared to conventional PL, upconversion PL avoids disturbing background luminescence and damage to the sample, but the upconversion process efficiency is much lower than the PL recombination efficiency, thus the signal intensity is relatively low.
Another two-step process with real intermediate state is the so-called **resonant photoluminescence**. Hereby, photons with a specific energy are absorbed and rapidly re-emitted with the same energy. Solely the wavevector of the outgoing light is changed (see chapter 6.1 in [43]). Its spectral properties are determined by the interaction of the optical absorption and the radiative recombination. Therefore, the energy of the incident light must correspond to a specific exciton state in the material (resonant excitation). This secondary radiation hence depends on the incident energy, due to this it may also be seen as light scattering. Thus, this phenomenon is generalized under resonant secondary emission, since it may either be interpreted as resonant PL or as resonant Rayleigh scattering [43], as described in the next section However, in contrast to inelastic light scattering, this secondary emission is scattered elastically, resonantly and coherently.

3.2 Inelastic laser-light scattering

Light scattering describes a process, in which the atoms in a material absorb light and re-emit it in different directions and with different intensities. The most general description of scattered light is obtained from the Mie solution to Maxwell's equations with boundary conditions, which characterizes the diffraction of an electromagnetic plane monochromatic wave by a homogeneous sphere of any diameter and composition [260]. The solution for particles with spherical symmetry may be applied to a variety of problems: from the colors of metallic suspensions, the study of atmospheric dust to the theory of rainbows and the solar corona (see chapter 14.5 in [261] and [262]). Mie scattering may be approximated via Rayleigh scattering, which describes the elastic scattering of light by spheres that are much smaller than the wavelength of light [261]. For example, the blue color of the sky is explained by Rayleigh scattering due to entropy fluctuations of the particles in the air (see chapter 7.2 in [23]). The elastic scattering results from the electric polarizability of the subwavelength particles, which carry out forced oscillations. Although the classical treatment of light scattering has some drawbacks, e.g., it cannot be used to describe spontaneous scattering processes like a quantum-mechanical description, the model of Rayleigh is accurate within the frame of this thesis considering the

ratio of excitation wavelength to structure size. The laser light obtains wavelengths from $400 - 900\,\text{nm}$; in contrast, the size of the quantum dots is up to 50 nm in diameter with a usual height of $< 5\,\text{nm}$, while the 2D materials have a height of 0.7 nm and a diameter of $< 50\,\mu\text{m}$. Hence, both structures are much smaller than the used light wavelengths, so that the light may be treated as a classical field.
The directly related inelastic scattering of light was first theoretically proposed by Brillouin [263] and Mandelstam and Landsberg [264], and later experimentally verified by Raman and Krishnan [265] in experiments studying molecular vibrations. Inelastic scattered light emerges when the particle's emission resulting from its induced polarization is modulated by density fluctuations of the material. Hence, besides a **change in the direction and intensity**, the incident light may also change its energy (or frequency) due to scattering interactions within a material, e.g., by phonons. The incoming particles **gain or lose energy** due to the scattering process and the final energy is blue- or red-shifted. The scattering process, described in detail in section 3.2.1, leads to a change of the internal state of the involved particles. The process follows selection rules based on conservation laws, see section 3.2.2. Thus, information about the intra- and intersubband levels of the material are gained. The name of the scattering process is defined by the scattering partner: Elastic scattering by imperfections and inhomogeneities in solids is called Rayleigh scattering, while inelastic scattering by phonons is either called **Raman scattering** for optical phonons or (**Mandelstam-**)**Brillouin scattering** for acoustic phonons. Moreover, light may scatter by (free) charge carriers, resulting from charge- or spin-density fluctuations. This includes not only charge carriers like electrons and holes, but also bound-excitation complexes like excitons and trions, and quasi-particles like magnons and plasmons (see sections 2.2 and 2.4.1). Note that the involvement of another scattering partner lowers the scattering efficiency: elastic scattering has a scattering efficiency $\eta_s \approx 10^{-1} - 10^{-2}$ (about 0.1 % to 0.01 % of the incident light), on the contrary inelastic Raman scattering has a scattering efficiency of only about $\eta_s < 10^{-9} - 10^{-12}$. Hence, a suitable scattering setup requires a highly sensitive final detection system, as described in section 3.2.3.

3.2.1 The scattering process

A typical **scattering process** consists of three steps: an incident photon excites an electron-hole pair (photoexcitation), the electron of this complex scatters by, e.g., an acoustic phonon (scattering event), and the electron-hole pair recombines under emission of a scattered photon (recombination). For a resonant scattering process, the incident photon's energy is equal to an electron-hole transition of the nanostructure. The physical basis of a scattering process is explained using the above-mentioned classical approach, starting with a localized electric dipole $P(t)$ (a full semi-classical approach may be found in chapter 6.2.2 in [23], a quantum-mechanical approach in [266, 267]). The scattered eigenfrequencies of the oscillator are calculated in an external electromagnetic field $E(t)$, e.g., an oscillating light field. In the **electric dipole approximation**, only the electric field is involved in the interaction, since the magnetic field interacts only weakly with the spin and the orbital effects are negligible in first order approximation. However, magnetic dipole or electric quadrupole transitions may become relevant when electric dipole transitions are forbidden by selection rules (see chapter 5.3 in [24] or chapter 4.2 in [5]). The electric dipole oscillator fulfills the equation of motion for an externally

perturbed harmonic oscillator with eigenfrequency ω_0:

$$\frac{d^2}{dt^2}P(t) + \omega_0^2 P(t) = \gamma(t)E(t), \tag{3.1}$$

with a periodic varying field $E(t) = E_i \cos(\omega_i t)$ coupled to the electric dipole. The coupling $\gamma(t)$ consists of a constant γ_0 and a time dependent part $\gamma_t \cos(\omega_q t)$ with modulation frequency $\omega_q \ll \omega_0$. The oscillating electric light field acts on the charges within a particle, which becomes a small radiative dipole with the solution:

$$P(t) = \frac{\gamma_0 E_i}{\omega_0^2 - \omega_i^2} \cos(\omega_i t) + \frac{\gamma_t E_i}{\omega_0^2 - (\omega_i \pm \omega_q)^2} \cos\left[(\omega_i \pm \omega_q)\, t\right]. \tag{3.2}$$

The radiation from the dipole is the observable scattered light, as the external light perturbation forces the dipole to oscillate at the frequency ω_i of the incident photon and at the combined frequencies $\omega_i \pm \omega_q$. The modulation energy $E = \hbar\omega_q$ corresponds to the energy spacing between two eigenstates of the system or, in terms of the modulation frequency ω_q, to any phonon mode. The oscillations with initial frequency correspond to Rayleigh scattering, which describes elastic scattering without the involvement of phonons. It retains a fixed phase relation with the driving light field, as noted under resonant PL (or resonant secondary emission) in the previous section. The oscillations with frequency change describe inelastic light scattering, or Raman scattering, which, in contrast, is accompanied by the annihilation and creation of phonons. It is characterized by a two-photon process where the photon absorption and emission occur via a virtual intermediate state. Virtual states are intermediate scattering states, which are not eigenfunctions of any system operator. These virtual states obtain a very short lifetime according to the uncertainty principle. Furthermore, inelastic light scattering is divided into Stokes and anti-Stokes process. The Stokes (anti-Stokes) process denotes the emission (absorption) of energy, corresponding to the generation (annihilation) of an elementary excitation, hence the scattered light has a lower (higher) energy than the incident light.

Like the aforedescribed photoluminescence, the inelastic scattering process consists of three steps: photoexcitation, scattering event and recombination process. Thereby, the two relevant interactions are the electron-radiation interaction and the electron-(acoustic) phonon interaction. In general, all interaction processes conserve energy, momentum and angular momentum, following the dipole selection rules listed in the next section. During the photoexcitation and recombination process, the electron interacts with the photon via **electron-radiation interaction**. The interaction creates an electron-hole pair (or exciton) and couples it with the photon to form a mixed mechanical-electromagnetic wave (see chapter 6.3 in [23]). Contrastingly to PL, the final electron-hole pair recombination or interband transition occurs quasi-resonantly to the incident photon. Hence, inelastic scattering allows for studying interband electronic transitions, excitons and electron-phonon interactions (see chapter 7.2 in [23]). During the scattering event, the electron interacts via **electron-phonon interaction**. The photo-excited electron scatters by a phonon deformation potential, which describes the energy change by distortions of the crystal lattice (see chapter 3.3 in [23]). Depending on the involved phonon type and the interaction range, the electron-phonon interaction may be distinguished into, e.g., piezoelectric electron-acoustic phonon interaction, deformation potential interaction or electron-longitudinal optical phonon (Fröhlich) interaction (see details on phonons in sec-

tion 2.4). The typical phonons (TA, LA, TO, and LO) involved in the scattering process obtain small wavevectors ($\vec{k}$ near Γ, long wavelength region) and their interaction may be further distinguished according to their strain effects, e.g. volume dilation or shear stress [23].
In the studied structures, scattering occurs mostly via short-range interaction with an acoustic phonon deformation potential by the dominantly contributing longitudinal acoustic phonons. Therein, the electron scatters from the state n to n' (intraband transition). This leads to an energy change within the same subband (indirect intrasubband transition) or to a different subband which may be accompanied by a reversal of the electron's spin orientation (direct intersubband transition). The energy change with spin reversal is denoted as inelastic **spin-flip scattering** (SFS). Hereby, the incident photon's energy is in resonance with a degenerate electron-hole transition, which is split due to, e.g., an external magnetic field. During the SFS process, the phonon mixes the spin-split levels via spin-orbit interaction [127]. Note that not only the electron's spin may flip, but the spin of the hole, of both charge carriers or of an interaction partner, or other angular momentum-flips may take place [268]. Apart from scattering by phonons via electron-phonon interaction [269], SFS may be mediated by carrier-carrier interaction [270], isotropic exchange interaction [271], electron-nuclear hyperfine interaction [272], and others [98, 273], depending on the specific conditions of the studied structure. Furthermore, the phonons regarded so far are zone-center phonons. (Near) Zone-edge phonons may scatter electrons from a band minimum at the zone center to a band minimum at the zone edge. Additionally, in materials where the electrons are located in degenerate conduction band minima which are not at zone center, electrons may be scattered from one degenerate valley to another via **intervalley scattering** (IVS) (see chapter 3.3.6 in [23]). This type of scattering plays an important role in optical absorption at indirect energy gaps, where short-range (large wavevector) phonons may scatter electrons between equivalent conduction band valleys, independent on wavevector.

3.2.2 Selection rules

Inelastic scattered light contains information about the phonons and crystallinity of the material and allows for determining the energy, lifetime and symmetry properties of the scattering partner, their coupling to electronic states and the effect of perturbations. However, the information gained about the scattering interaction are solely obtained indirectly based on the properties of the incident and scattered photons. The properties that may be determined in the measurement are the energy shift, polarization configuration, linewidth and lineshape and the scattering intensity, which depend on the involved charge carrier or carrier complex and the internal parameters determined by the sample structure. Thus, understanding a scattering process and its underlying interaction and the determination of the scattering partner require the help of the following **selection rules** based on **conservation laws**.

The first hint on the underlying scattering mechanism is given by the **energy shift** ΔE of the scattered photon compared to the incident photon. The incident light must be in resonance with the interband electron-hole transition (resonant excitation), hence from the conservation of **energy** as required by the homogeneity of time follows:

$$\hbar\omega_s = \hbar\omega_i \pm \hbar\omega_q, \tag{3.3}$$

with the reduced Planck constant $\hbar$, frequency ω_s of the scattered photon, frequency ω_i of the incident photon and frequency ω_q of the generated or annihilated elementary excitation. Thus, the conservation of energy during the scattering process is ensured via the participation of, e.g., phonons with frequency ω_q. Specifically, the energy difference of a SFS process from s to $-s$, corresponding to a Zeeman level transition in an external magnetic field B, is

$$\Delta E = \hbar\omega_q = g\mu_\mathrm{B}B, \tag{3.4}$$

with the Bohr constant μ_B. Hence, the energy shift ΔE of a spin-flip line allows for determining the level splitting as it is directly proportional to the absolute value of the gyromagnetic or Landé factor g of the charge carrier or carrier complex. However, the spin splitting is comparatively small and usually below the detection limit. The application of an external magnetic field enhances the Zeeman level splitting; thus, allowing for measuring the energy shift. Moreover, the spin-flip probability rises as the magnetic field lifts the restrictions imposed by the selection rules [52] and the spin-flip intensity may increase with rising magnetic field strength due to an increased confinement of the charge carriers [274].

The identification of the scattering partner and its interaction with the electronic states requires further information about the properties of the measured scattered light emission. Despite the energy shift, further hints on the underlying scattering mechanism are given by the **polarization configuration**, which depends on **momentum, parity and angular momentum** conservation.
Specifically for bulk crystals, helpful insights may be gained by **momentum** conservation, as required by the homogeneity of space:

$$\vec{k}_s = \vec{k}_i \pm \vec{q}, \tag{3.5}$$

with the **wavevector** $\vec{k}_s$ of the scattered photon, wavevector $\vec{k}_i$ of the incident photon and wavevector $\vec{q}$ of the generated or annihilated elementary excitation. The magnitude of the scattered photon's wavevector is determined by the scattering geometry, it is minimal for forward (transmission) scattering and maximal for backward (reflection) scattering, where the incident and scattered light propagate in opposite directions. However, it must be kept in mind that a lack of translational symmetry lifts the restriction for the wavevector. This means that in quantum wells the wavevector's z-component along the growth axis is excluded from momentum conservation, while for QDs there are no limitations for the wavevector at all. Still, the propagation direction of the scattering partner's wavevector may depend on the direction of the incident wavevector in case the scattering process occurs in non-restricted directions or the scattering partner stems from non-confined regions within the sample [269].
The conservation of **parity** leads to further restrictions, limiting the probability of the scattering process. Since this selection rule results from inversion symmetry, it only applies for centrosymmetric structures. The allowed transitions can be derived by the symmetry of the transition matrix element $M_\mathrm{fi} = \langle \Psi_f | \, \hat{p} \, | \Psi_i \rangle$, with the wavefunctions Ψ_i and Ψ_f of the involved states. The wavefunctions $|\Psi\rangle$ of the electron states in a spherically symmetric structure are classified according to the total angular momentum and the parity operator $\hat{P}$ (see chapter 3.3.1 in [24]). The electron momentum operator $\hat{p}$ of the electron-photon interaction Hamiltonian in the transition matrix element requires a change of parity. As the operator has odd parity under inversion, the transition matrix

element obtains non-zero matrix elements only for wavefunctions with different parity [23]. The allowed optical transitions may be derived by determining the irreducible representation of the operator and the irreducible representations of the crystal's point group using group theory [275]. For example, at the zone center in the bulk tetrahedral group-IV, III-V, and II-VI semiconductors, the conduction bands have antisymmetric, or s- (antibonding), character with odd parity under inversion, while the valence bands have symmetric, or p- (bonding), character with even parity. Thus, electric dipole transitions at the absorption edge are allowed by the parity selection rule. Contrastingly, in the bulk cubic semiconductor copper oxide with spherical symmetry, the lowest conduction band and the highest valence band both have even parity. Hence, the transition matrix element is zero and the electric-dipole transition at the absorption edge is not allowed (see chapter 2.3.4 in [23]). However, parity conservation may be neglected in the studied low-dimensional structures due their inversion asymmetry [125], leading to crystal fields which break the parity selection rule [276]. Specifically in III-V semiconductors, the antisymmetric pseudopotential breaks the inversion symmetry (see chapter 2.6.1 in [23]), while single monolayers with diatomic basis lack an inversion center [277]. A detailed introduction into the parity selection rule and its dependence on the net dipole moment for inter- and intraband transitions in quantum dots can be found in chapter 2.5 in [21]). Besides the at least partially lifted conservation of momentum and parity, the isotropy of space or rotation invariance leads to the conservation of the **angular momentum** in the observed centrosymmetric structures and defines the observable polarization configurations. As mentioned above, the electron states $|\Psi_i\rangle$ and $|\Psi_f\rangle$ may be described by their total angular momentum and the parity operator (see chapter 3.3 in [24]). Aside from a change of parity, the momentum operator in the transition matrix element requires that the states must satisfy certain symmetry criteria, following group theoretical considerations (see chapter 5.2.1 in [24] and chapter 26.5 in [5]). Therefore, the quantum number of the states have to be regarded, as any arbitrary quantum state with full spherical symmetry $|\Psi\rangle = |n, l, m_l, s\rangle$ may be described by its **quantum numbers**, see section 2.3. These consist of the principal quantum number n and the quantum numbers of the orbital angular momentum l, its projection m_l onto the z-axis and the spin s.
During the photon absorption process, the angular momentum of the photon is transferred to the electron-hole pair, and vice versa for the photon emission process. In ideal quantum wells, these interband transitions are allowed with the same principal quantum number $\Delta n = 0$ (see chapter 6 in [19]). Contrastingly, all transitions are principally allowed in low-dimensional structures with finite confinement potentials. Yet, the transitions with $\Delta n \neq 0$ obtain only small or vanishing oscillator strength and may be neglected (see chapter 6 in [19]). As the oscillator strength is directly proportional to the number of photo-excited charge carriers, mainly emission of the transitions with corresponding energy levels is observable [26]. Furthermore, the incident circular-polarized photon has a total angular momentum of $l = \pm 1$, depending on the light helicity. Hence, for photoexcitations with circularly polarized photons, the orbital angular momentum l and its projection m_l onto the z-axis follow:

$$\Delta l = \pm 1 \text{ and } \Delta m_l = 0, \pm 1. \tag{3.6}$$

For linearly polarized light, as a superposition of left- and right-circularly polarized light, the projection of its angular momentum is zero. Moreover, the electromagnetic light field coupled to the electron does not affect the spin s in the first approximation of the

electron momentum operator in the transition matrix element. Thus, $\Delta s = 0$ for the photoexcitation and recombination processes (see chapter 9.1 in [5]). Obviously, for spin-flip transitions $\Delta s \neq 0$ is required.
In atomic physics, the electron spin couples to the orbital angular momentum via **spin-orbit interaction**, see equation (2.18), resulting in the total angular momentum $j = l \pm s$ (see chapter 2.6.2 in [23]). Hence, technically, SFS should rather be denoted as (total) angular momentum-flip scattering. The orbital angular momentum eigenstates switch to the basis of total angular momentum states $|j, j_z\rangle$, which, additionally to $\Delta l = \pm 1$, obey the following electric dipole selection rules:

$$\Delta j = 0, \pm 1 \text{ and } \Delta j_z = 0, \pm 1. \tag{3.7}$$

The transitions with $\Delta j_z = \pm 1$ are circularly or $\sigma^{\pm}$ polarized, since they involve a net transfer of angular momentum. The classification of the photon angular momentum for circular-polarized light follows analogously: left-handed or σ^- circularly polarized light transfers $j = l = -1$ and right-handed σ^+ circularly polarized light transfers $j = l = +1$. The $\Delta j_z = 0$ transitions are denoted as linearly or π polarized, which corresponds to linearly polarized light: an equal superposition of both light states with opposite helicities which carries zero average angular momentum, $\bar{j} = 0$. The overall process of photoexcitation, scattering and recombination is additive and, thus, always follows $\Delta j = 0, \pm 2$ in the backscattering process (see chapter 6.6 in [43]. This, however, does not give hints about the specific scattering mechanism and should not be confused with the selection rules for the individual photoexcitation, scattering and recombination processes.
Concerning the conservation of the total angular momentum it has to be considered that not all scattering partners transfer angular momentum. Specifically, phonons as quasi-particles without spin do not obtain angular momentum typically. Nevertheless, it has been shown that phonons can change the momentum of electrons, in particular in the presence of spin-phonon interaction. By assuming spherical phonons resulting from the superposition of two orthogonally polarized phonons, roughly 2 % of all phonons transfer an orbital angular momentum of $\Delta l = \pm 1$ [278, 279, 280]. Thus, for angular momentum conservation the total angular momentum j_m of the local system covering **all involved particles** has to be regarded:

$$j_s = j_i \pm j_m, \tag{3.8}$$

with the angular momentum j_s of the scattered and j_i of the incident photon.
The conservation of the angular momentum defines a more valid selection rule for the scattering process than the preservation of the wavevector. However, there are cases in which the conservation of the total angular momentum may be lifted. Examples include anisotropic exchange interaction as a spin-nonconserving interaction [98, 268] or mixed states due to symmetry reductions in nanostructures through external stress or fields (see chapter 26.5 in [5]), leading to weakened angular momentum selection rules. Additionally, the group-theoretical approach cannot specify the magnitude of the allowed transitions, nor the ordering of the bands, and the symmetries of the eigenstates are defined only for $k = 0$, a direct bandgap at the Γ-point, which is not suitable for all semiconductors.

Specifically for SFS, the conservation of the angular momentum enables a reliable identification of the involved charge carriers or carrier complexes as observable by the polarization characteristics of the spin-flip line [98]. An **example of a SFS process** is depicted in figure 3-3 and explained in the following. The scattering mechanism is evaluated by

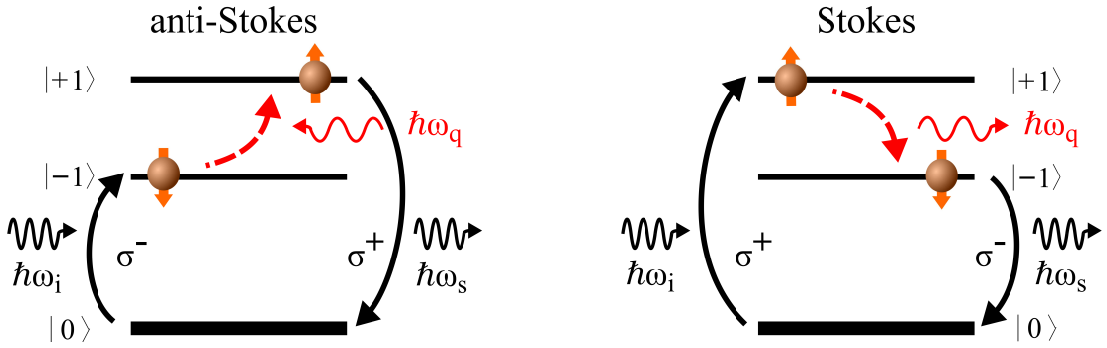

Figure 3-3: Spin-flip scattering mechanism for an exciton in the anti-Stokes (left) and the Stokes process (right).

analyzing the above-mentioned selection rules for electric dipole transitions. In **Faraday geometry**, with parallel alignment of magnetic field direction and sample growth axis ($\vec{B} \parallel \vec{z}$), the exciton states of bulk III-V semiconductors split, as explained in section 2.2. The exciton states $|j_z\rangle = |j_{\mathrm{e},z}; j_{\mathrm{hh},z}\rangle$ with contribution from the hh states divide into optically bright and dark states in the dipole approximation. The bright exciton states with $|j_z\rangle = |\mp 1/2; \pm 3/2\rangle = |\pm 1\rangle$ (antiparallel electron and hole spins, spin singlet state) are excited with circularly polarized light ($\Delta j = \Delta l = \pm 1$) and recombine to the ground state. Contrastingly, transitions from exciton states with $|j_z\rangle = |\mp 1/2; \mp 3/2\rangle = |\mp 2\rangle$ (parallel electron and hole spins, spin triplet state) are principally **forbidden**, they are called optically dark since they require $\Delta j = \pm 2$. Still, an excitation or recombination of dark excitons is possible through higher order processes via interactions with phonons or defects (see chapter 2.5.2 in [24]), but they are much less probable and hence less efficient. Thus, in Faraday geometry single spin flips of electrons ($\Delta j_{\mathrm{e},z} = \pm 1$) or hh ($\Delta j_{\mathrm{hh},z} = \pm 3$ or $\Delta j_{\mathrm{lh},z} = \pm 1$) in excitons are not observable, as they lead from bright to dark exciton states [98].

An **allowed** scattering process is the following: circular-polarized light with $\Delta j = -1$ excites the bright exciton state $|j_z\rangle = |-1\rangle = |+1/2; -3/2\rangle$. This exciton scatters via an acoustic phonon, leading to spin flips of both the electron ($\Delta j_{\mathrm{e},z} = -1$) and the hole ($\Delta j_{\mathrm{h},z} = +3$) to the $|j_z\rangle = |+1\rangle = |-1/2; +3/2\rangle$ bright exciton state (via $\Delta j_{\mathrm{X},z} = \Delta j_{\mathrm{e},z} + \Delta j_{\mathrm{hh},z} = +2$). The angular momentum of $\Delta j = +2$ may either be transferred via the scattering partner, e.g. polarized (circular) phonons, or the phonon mixes the spin-split states through spin interactions. The exciton recombines via the emission of $\Delta j = +1$ circular-polarized light to the ground state and the scattered light is observable in this crossed polarization configuration. Thus, the allowed spin flips in this geometry relate to contributions from bright excitons with electron and hh spin flips. However, note that the spin flip in this example may also result from trions where the unpaired charge carrier flips its spin, as allowed by Pauli's exclusion principle. Both processes obtain the same energy shift and need further elaboration to be distinguished. The above-mentioned example works solely in backscattering Faraday geometry, where the magnetic field direction and sample's growth axis are oriented parallel ($\vec{B} \parallel \vec{z}$). Here, the exciton states consist of electron and (heavy) hole spin basis eigenstates. In **Voigt geometry**, the magnetic field is oriented perpendicular to the sample's growth axis ($\vec{B} \perp \vec{z}$) and to the light wavevector. This mixes the electron spin basis eigenstates and leads further to mixed bright and dark exciton states described by a transverse electron g factor [159]. Moreover, this **state mixing** lifts the angular momentum selection rules.

Thus, for non-Faraday geometry single spin flips in bright excitons mixed with the dark exciton states become allowed (see chapter 4.4.1 in [26]). The contribution of the spin basis eigenstates to the specific spin state is controlled by the tilting angle θ between the magnetic field direction and the sample's growth axis z for oblique orientations of the magnetic field ($0 < \theta < 90°$) [98, 281], see also section 2.2. Additionally, the former degenerate lh and hh are slightly mixed due to uniaxial in-plane strain in QDs leading to symmetry reductions. This further weakens the selection rules, as the exciton spin-flip line becomes visible in other polarization configurations, but with lower intensity depending on the amount of mixing [98]. Furthermore, note that in Faraday geometry the spin flip of the exciton consisting of electron and lh is principally allowed; however, due to its energy separation of about 10 meV it is usually not observable. Generally, light scattering involving the spin flip of a charge carrier becomes allowed for any perturbation lowering the symmetry of the electron-hole pair complex.

Further information about the interaction mechanism leading to the scattering process are gained via the **linewidth** and the **lineshape** of the scattered light. The linewidth w of the scattered light depends on the **lifetime** $\tau_\mathrm{L} = \hbar/w$ of the excited state resulting from the electron-hole pair recombination process. Hence, from the measured linewidths conclusions about the lifetime dependences of the involved states may be drawn. Hereby, the linewidth has three contributions: ideal δ-function form, homogeneous and inhomogeneous broadening. The ideal form results as a consequence of wavevector conservation. Since the wavevector of the recombination process is equal to the photon wavevector with $k \approx 0$, the resulting emission spectrum should be in the form of a δ-function [282]. However, the observable emission spectrum has a Lorentzian lineshape as a consequence of the uncertainty principle considering the finite lifetime of the excited state (see chapter 7.1.4 and chapter 9.4.1 in [23]). This lifetime broadening gives the lower limit for the linewidth (natural linewidth). Besides this homogeneous **line broadening**, the linewidth of the emitted light varies slightly with the local environments, especially in solids, leading to inhomogeneous spectral broadening. Specifically for ensemble measurements like in the studied QD structures, most lines obtain a Gaussian lineshape. It results from the overlap of many sharp (Lorentzian) peaks due to the distribution of many electron-hole pairs with slightly different transition energies. This inhomogeneous broadening may lead to an increasing broadening of the emission line with magnetic field. The linewidth may also be affected by the trion spin relaxation rate and by nuclear spin fluctuations [272], by width and alloy fluctuations that influence the lh admixture to the hh states [32, 98] or by other mechanisms that affect the lifetime of the intermediate scattering state. In addition, owing to experimental limitations the emission line may be broadened by the width of the laser line or by additional instrumental broadening, e.g. by the resolution of the spectrometer. This results in an experimental or measurable lower limit of the linewidth. Under the assumption of independent, but combined broadening effects, the observed line profile is a convolution of both profiles (Lorentzian and Gaussian), leading to a Voigt line profile. Further deviations from the lineshape may be attributed to underlying interaction mechanisms as explained in chapter 4.

Furthermore, the **intensity distribution** of the emitted light may give additional hints about the scattering mechanism. The light intensity I_S of a scattering process may be

calculated via the induced oscillation of the electric dipole from equation (3.2). It follows:

$$I_{\mathrm{S}} \propto \left(\frac{\partial^2 \alpha_{\mathrm{p}}}{\partial t^2} \right)^2_{q_0} \cdot (\omega_{\mathrm{L}} \pm \omega_q)^4 \cdot E_0^2 \tag{3.9}$$

for Stokes (-) and for anti-Stokes (+) Raman scattering. Hence, the intensity of the Raman scattering process may be enhanced by increasing the laser power via the electric field amplitude E_0 or by increasing the laser frequency ω_{L}. Note that the equilibrium polarizability $\alpha_{\mathrm{p},0}$ of the material influences solely the Rayleigh scattering intensity, while the polarizability gradient $\frac{\partial^2 \alpha_{\mathrm{p}}}{\partial t^2}$ and the phonon frequency ω_q provide nanoscopic information about the system under study (see chapter 3.2.3 in [283]). The time- and space-averaged intensity of the scattered light is proportional to the overall power emitted by the induced dipole moment and relates directly to the absolute value of the emitted electric field: $\langle I_{\mathrm{S}} \rangle \propto \langle | \frac{d^2}{dt^2} P(t) | \rangle \propto \langle |E|^2 \rangle$.
The intensity I_{SF} of a spin-flip signal, including photon absorption, an acoustic phonon-induced spin flip, and secondary photon emission, is determined by:

$$I_{\mathrm{SF}} \propto I_{\mathrm{i}} W_{\mathrm{abs}} \tau_{\bar{j}} W_{\mathrm{SF}} \tau_j W_{\mathrm{em}}, \tag{3.10}$$

with the intensity of the incident light $I_{\mathrm{i}} \propto E_0^2$ [16]. It is usually kept constant during the measurements and can be excluded as influencing factor. Likewise, the probability rates W_{abs} for photon absorption and W_{em} for photon emission depend on the resonance energy of the excited charge carrier or carrier complex, which does not change significantly within a low temperature range. The determining factor is the spin-flip **transition probability** rate W_{SF}, which is determined by the Pauli exclusion principle and the electric-dipole selection rules and may be calculated via the scattering efficiency η_s or transition probability $|M_{\mathrm{fi}}|^2$ using Fermi's golden rule (see chapter 6 in [19]). Thus, it is very sensitive to the experimental geometry and, for zincblende-type semiconductors, is proportional to the square of the magnetic field strength [284]. Moreover, the SFS intensity is directly affected by the lifetime $\tau_{\mathrm{L},j}$ ($\tau_{\mathrm{L}\bar{j}}$) of the excited charge carrier or carrier complex with the angular momentum j ($\bar{j} = -j$). Specifically, it is directly proportional to the third power of the exciton lifetime: $I_{\mathrm{SF}} \propto \tau^3_{\mathrm{L,X}}$ [285]. Hence, a longer lifetime of the charge carrier or carrier complex is not only related to a smaller linewidth, but also to a higher spin-flip intensity. Note that absorption and PLE intensities should be independent of the lifetime. Furthermore, although typical spin-flip scattered light intensities are quite small, the spin-flip intensity ratios are of main importance for determining the involved charge carriers in the spin-flip interaction process.

Summing up, in the electric dipole approximation the fulfillment of the selection rules resulting from conservation laws allows for light scattering. Each scattering process shows a specific energy shift, polarization configuration, linewidth, lineshape and intensity distribution depending on the involved charge carrier or carrier complex and the internal sample structure. The probability for scattering processes rises for weakened or lifted selection rules. However, by this means the conclusions that can be drawn about the scattering mechanism from the appearance of the scattered light are less clear. Further hints about the scattering interaction may be gained by measuring the above-mentioned properties in dependence on external parameters like magnetic field strength and orientation, power density, temperature, excitation energy, experimental geometry, and others. The variation of the intensity distributions of the scattered light in the various polariza-

tion and experimental geometry configurations delivers valuable insights in the scattering mechanism.

3.2.3 Detection of scattered light

The measurement of scattering events should principally be possible in every semiconductor that fulfills the aforedescribed selection rules. Similar to the requirements for PL spectroscopy, the basic devices for the detection of scattered light, or for a **scattering setup**, are a (tunable) laser, a spectrometer and a detector. Hereby, the laser should satisfy at least three specifications: firstly, it must be spectrally narrow to achieve a high spectral resolution. As the spectral width of the laser defines the minimum width of the spin-flip line, its linewidth should be small for minimizing broadening effects and enabling measurements close to the laser line. Secondly, the laser should be tunable for varying the resonant excitation energy. The scattered emission lines become more easily detectable by choosing a suitable excitation energy position where the ratio between scattered light intensity and background intensity is enhanced, e.g., at an edge of the PL band or in the anti-Stokes regime, which is mostly absent from a PL background. Thirdly, the laser should have an adjustable sufficiently large excitation power density to increase the scattered light intensity when necessary. This not only enhances the scattered light intensity but facilitates the measurement in case of different dependences of the above-mentioned intensities on the optical power density. Furthermore, polarization optics are useful for investigating on the underlying angular momentum selection rules to identify the scattering mechanism. Additionally, the spectral overlap between the laser stray light and the scattered light is reduced in cross-linear polarization configuration, which is helpful to overcome the obstacle of scattering lines indistinguishable from the background.
To detect scattering lines with small energy shift close to the laser line, a spectrometer with high spectral resolution and strong stray light suppression is mandatory. Its spectral resolution is mostly defined by the spectrometer settings like the focal length, the number of grooves of the grating per mm, the widths of the entrance and exit slits and the alignment and quality of the optics. Still, it may be decreased by aberrations and diffractive effects or by opened slits of the spectrometer to enhance the light throughput. Besides the reflected laser light from the sample surface and elastically scattered light, background stray light may also stem from imperfections in the optics and from scattering off walls and dust inside the spectrometer (see chapter 7.2.3 in [23]). A comparison of the stray light suppression for the different spectrometers, related to the minimally observable energy shift [32], is shown in the next section 3.3. Additionally, a sensitive detector with high quantum efficiency and large signal-to-noise ratio is necessary. A high quantum efficiency converts a large amount of incoming photons into electrical signal. Hereby, the amount of incoming photons is already reduced due to experimental limitations, as the light cannot be collected in all directions, but only within a cone with a solid angle along the optical axis. Thus, a suitable lens configuration close to the sample is necessary to reach a significantly large number of collected photons, resulting in a high light gathering power. Moreover, the gathered light intensity may be limited by an inappropriate lens configuration at the spectrometer entrance, e.g., the light intensity decreases when the focused beam diameter exceeds the entrance slit width. Hence, the slit width of the spectrometer should be chosen in such a way that the light throughput

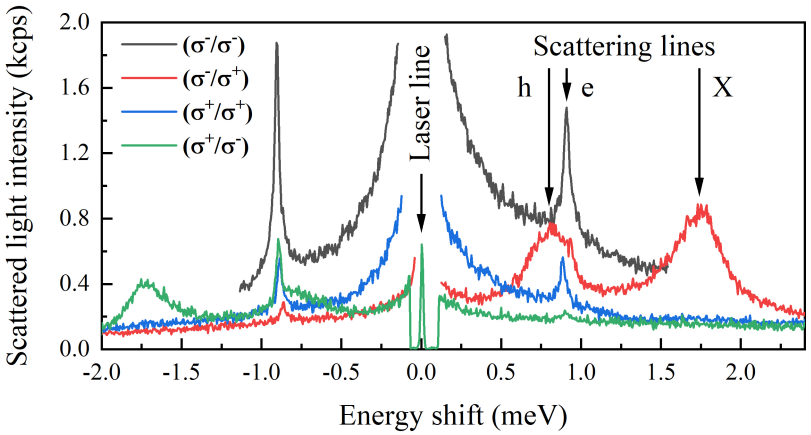

Figure 3-4: Spin-flip scattering spectra fulfilling all experimental requirements show the spin-flip signals of electron, hole and exciton with characteristic energy shifts and polarization configurations in a quantum well. The signal of the laser line is cut off using neutral-density filters.

is maximized while the line profile stays the same. Furthermore, the signal-to-noise ratio depends on the specific detector and may be improved by using cooled detectors. To achieve reasonable spectra, the noise should mainly be determined by the shot noise of the signal, with negligible readout and thermal noise.

Aside from cooling the detector, the spectroscopic experiments themselves are performed at low temperatures. This reduces the linewidth of the scattering lines and allows for a more facile interpretation of the scattering process (see chapter 25.1.1 in [5]). Such low temperatures over the whole sample area are realized within the variable temperature insert of a cryostat based on liquid helium. Additionally, an external magnetic field may be necessary to enlarge the energy shift of spin-split states, so that the level splitting between the scattering states becomes detectable. For this purpose, a cryostat with superconducting coils allows for applying high magnetic fields. In combination with a rotatable sample holder this allows for measuring at arbitrary angles between the magnetic field direction, the optical axis and the sample growth axis.

An obstacle that complicates the definite identification of the scattering lines is an oscillatory PL background, especially in case of similar oscillation periods and scattering linewidths [251]. The oscillatory behavior may result from the layered structure of the sample or from coherent LO phonon emission [286]. Apart from that, the oscillations may also stem from the used devices, e.g., from an oscillatory fluorescence background of the laser emission itself or from a condensate film on the cryostat or camera window. Interferences of the emitted light in the vacuum window of the CCD camera may be avoided using a camera window with an anti-reflection coating, which approximately halves the oscillation amplitude [251]. Oscillations stemming from an etaloning of the charge-coupled device camera can be avoided by using a front-illuminated CCD camera [32, 287], whose quantum efficiency is however lower than that of a back-illuminated CCD.

Although the measurement of scattered light should principally be possible in every semiconductor that fulfills the aforedescribed selection rules, the detection of spin-flip scattered light may be hindered. Specifically, spin-flip scattered light should be observable for a laser excitation energy resonant to the electron-hole pair, a sufficiently large level splitting, e.g., by lifting the energy degeneracy under application of a magnetic field,

and an optically active final scattering state, e.g., by a symmetry reduction of the system [251]. However, its observation may be hindered by a low scattering efficiency η_s of the scattering process resulting in a low scattered light intensity, by a small energy shift of the scattering line so that it appears close to the laser line, and by strong resonant secondary emission which obscures the scattering line. Further obstacles of measuring scattered light are explained in detail here [32, 251]. When all experimental requirements are fulfilled, the scattering lines are observed on top of a background contributed by resonant excited PL and stray light, as shown in figure 3-4.

To conclude, inelastic light scattering is a versatile and well-established technique that offers many opportunities to investigate phonons and their interactions inside a material. In this regard, SFS allows for determining the spin level structure and spin interactions. Besides SFS, other scattering processes from, e.g., inter- or intravalley levels, where the angular momentum is changed, are detectable as well. Hence, this method is useful for investigating any small energy level splitting. Sophisticated measurement techniques and devices are required to overcome the described obstacles for detecting and recognizing the scattering mechanism. The devices used in this thesis are explained in detail in the following section 3.3.

3.3 Optical setups

A basic optical setup to measure light emission properties is shown in figure 3-2. Foremost, it consists of a laser with a specific excitation energy whose light is focused with well-defined polarization onto a sample kept in a cryostat. The depicted bath cryostat allows for measuring at cryogenic temperatures and for applying an external magnetic field. The light emitted from the sample is collimated and is analyzed in dependence on the polarization with polarization optics, a spectrometer and a detector. An overview of the main devices used is given in figure 3-5. The measurement of the various dependencies as mentioned in the previous section requires additional devices which are listed in table 3-1. It is divided into excitation path, sample area and detection path, analog to the division in the following characterization of the utilized setups. After the description of the laser systems, the standard setup ("macro-setup") is explained in section 3.3.1, which is used to measure the QD samples. This setup configuration of a helium bath cryostat combined with long-focus (LFOC) lenses is already described similarly here [32] and here [288]. The standard setup may be modified by nanopositioners and a short focus (SFOC) lens inside the sample chamber of the cryostat to allow for measuring on 2D materials, which requires a high spatial resolution ("micro-setup SFOC"). Besides that, the excitation and detection paths have to be slightly changed as well. For measuring 2D materials without magnetic field, the bath cryostat may be exchanged by a flow cryostat with integrated piezo stages allowing one to obtain a high spatial resolution by using a microscope objective (MO) ("micro-setup MO"), see section 3.3.1. Finally, the utilized spectrometers (section 3.3.3) and detectors (section 3.3.4) are described.

An essential part of all setups is the **laser** system to optically excite the sample in the cryostat. Depending on the bandgap energy of the sample and the properties of the emitted light, lasers with different excitation energies are used. Two high-energetic diode lasers (Coherent Cube and Coherent Sapphire) with respective fixed wavelengths of 405 nm (3.061 eV) and 488 nm (2.540 eV) are solely used for PL spectroscopy of the

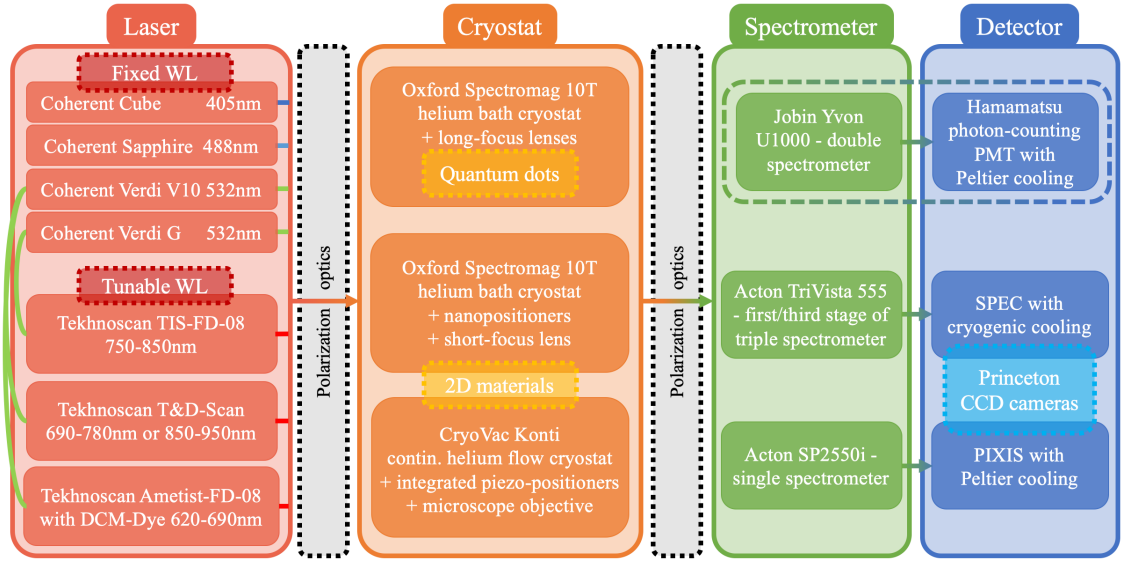

Figure 3-5: Overview of the devices used in the setups.

QD samples. Additionally, the second harmonic (532 nm, 2.33 eV) of the diode-pumped Nd:YVO_4 lasers (Coherent Verdi G and Coherent Verdi V10) may be used for PL spectroscopy as well, although the main function of these high-power lasers (up to 10 W) is to pump wavelength-tunable dye and Ti:Sapphire lasers. These tunable lasers are used for (quasi-)resonant excitation of the samples, e.g., for PLE spectroscopy and inelastic light scattering. The Ti:Sapphire lasers (Tekhnoscan TIS-FD-08 and Tekhnoscan T&D-Scan) have a modifiable wavelength range from 690 to 1050 nm (1.18 to 1.80 eV), which is achieved through a change of the mirror set. For measurements on the QD samples with PL energies from 825 to 910 nm (1.36 to 1.50 eV) two lasers are used: the TIS-FD-08 pumped by Verdi G in the configuration from 750 to 850 nm (1.46 to 1.65 eV) and the T&D-Scan pumped by Verdi V10 in the configuration from 850 to 950 nm (1.31 to 1.46 eV). For measurements on the 2D materials with PL energies from about 600 to 775 nm (1.60 to 2.06 eV), the mirrors of the T&D-Scan are changed to the wavelength range from 690 to 780 nm (1.59 to 1.80 eV). Additionally, the tunable dye laser (Tekhnoscan Ametist-FD-08) with DCM dye solved in ethylene glycol or DMSO (Dimethyl Sulfoxide) is used with a wavelength range from 615 to 705 nm (1.76 to 2.02 eV). The actual wavelength of the tunable lasers is measured by a wavelength meter (Coherent Wavemaster) with a resolution of (0.001 ± 0.005) nm. For this purpose, a glass plate in the beam path separates a small part of the laser light into a fiber coupled to the wavelength meter while allowing for performing measurements simultaneously.
As mentioned in the previous section, the scattering linewidths are limited by the width of the laser line; hence, a small laser linewidth is especially important for a high spectral resolution. For this purpose, continuous-wave (cw) lasers with a narrow emission linewidth are used. The linewidths of the Ti:Sapphire lasers are about 0.03 cm^{-1} (2.3 pm or 4 µeV) at the central wavelength (870 nm). Hence, they are below the best spectral resolution (5 pm) of the spectrometers and, compared to a typical electron SFS linewidth of 0.08 meV [32], the scattering lines are not limited by the laser linewidth [251]. Contrastingly, the linewidth of the dye laser is much larger with 3 cm^{-1} (about 135 pm or 0.4 meV) at a central wavelength of 660 nm, making it unsuitable for resonant scattering measurements, but adequate for quasi-resonant PLE spectroscopy. For measuring

Table 3-1: Parameters under study using the devices listed with their characteristics. The ranges for the spectrometers are their mechanical ranges, their smaller spectral ranges are defined by the used grating within these ranges (see text).

Parameter	Device	Characteristics
Excitation path		
Excitation wavelength	Tunable lasers	$\Delta\lambda = 560 - 1050\,\mathrm{nm}$
	Non-tunable lasers	$\lambda = 405, 488, 532\,\mathrm{nm}$
Excitation power	Neutral filter, noise eater	$P \leq 150\,\mathrm{mW}$
Polarization	Prism + wave plates	$\lambda/2$ (π) or $\lambda/4$ ($\sigma^{\pm}$)
Sample area		
Temperature	Cryostat with cryogenics	$1.5\,\mathrm{K} \leq T \leq 300\,\mathrm{K}$
Magnetic field	Superconducting magn. coils	$B \leq \pm 10\,\mathrm{T}$
Field geometry	Rotatable sample holder	Faraday & Voigt, $\theta \leq 90°$
Spatial resolution	Nanopositioners	min. step size: 10 nm
	Integrated piezo stages	min. step size: 15 nm
Detection path		
Polarization	Wave plates + prism	$\lambda/2$ (π) or $\lambda/4$ ($\sigma^{\pm}$)
Detection wavelength	Double spectrometer	$\Delta\lambda = 327.5 - 910\,\mathrm{nm}$
	Triple spectrometer	$\Delta\lambda = 185 - 2200\,\mathrm{nm}$
	Single spectrometer	$\Delta\lambda = 185 - 1400\,\mathrm{nm}$
Light intensity	Photodetector:	Quantum efficiency:
	PMT	10 % (at 850 nm)
	CCD camera	32 % (at 850 nm)

PLE, additional longpass and shortpass filters are used to suppress scattered laser light and possibly disturbing secondary emission, as listed in the respective chapter 5. The usage of color filters is generally useful to obtain sober and smooth spectra. Specifically, the strong background emission of the Sapphire diode laser is greatly reduced using an adequate bandpass filter.

3.3.1 Macro-setup

In the excitation path for the standard **macro-setup**, as illustrated in figure 3-6, the laser beam passes through two iris diaphragms, followed by a noise eater and polarization optics before being focused onto the sample in the cryostat. The iris diaphragms (ID) serve as a reference for the laser spot position and allow for a quick change between the laser systems. Besides, they may be used to select the central part of the beam cross section in case of a slightly divergent laser beam. The following noise eater (Thorlabs NEL03/M) stabilizes the laser power. Inside, the light is attenuated by a variable retarder, consisting of a liquid crystal retarder and output polarizer. A small part of the incoming light is separated through a beamsplitter onto a photodiode connected to a servo-controller unit, creating a feedback loop. By applying an appropriate adjustment voltage, the liquid crystal retarder is manipulated to lower or raise the through-passing laser power. Consequently, the noise eater (NE) requires linearly vertically or horizontally polarized incoming light depending on the orientation of the noise eater. In case the laser polarization does not match the required polarization of the noise eater, it is

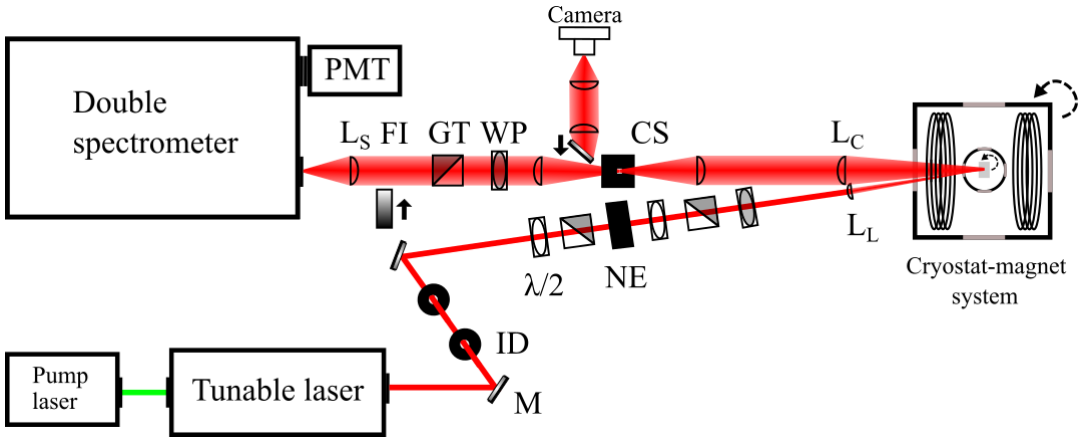

Figure 3-6: Scheme of the macro-setup used to study the QD samples. The abbreviations are explained in the main text.

adjusted by a prior-set half-wave plate ($\lambda/2$), which delays one linear polarization against the other by half a wavelength. Additionally, a Glan-Taylor prism (GT) whose fast axis is adapted to that of the noise eater is installed in between the half-wave plate and the noise eater, as a sober polarization of the incoming light improves the noise attenuation, as does a well-centered perpendicular beam path. Finally, the desired laser power is set by adjusting the resistance of the noise eater's potentiometer.
Further fine adjustments of the laser power are realized by the consecutive half-wave plate combined with a Glan-Taylor prism. This prism ensures a definite linear polarization of the laser light, which is cross-linear polarized to the prism in the detection path. Since the polarization of the prism in the detection path matches the optimal polarization direction of the grating in the spectrometer, the cross-linear polarization plane of the incident laser light minimizes laser stray light and possible damage to the detector by intense laser light. The ensuing quarter-wave plate ($\lambda/4$) converts the light polarization from linear into circular by delaying one polarization against the other by a quarter of a wavelength. The achromatic retardation or wave plate (WP) at this position depends on the magnetic field geometry and sample geometry. A quarter-wave plate is suitable for measurements in Faraday geometry, while a half-wave plate is typically chosen in Voigt geometry. The laser power is measured by a power meter (Thorlabs PM100D), which is inserted manually into the beam path in front of the cryostat before and after the measurement. For intensity-sensitive measurements, a small part of the laser beam may be split by a glass plate onto the power meter for constant power monitoring. This glass plate should be placed after the noise-eater and before the last wave plate for a sober polarization and correct power values. Hereby, a correctly set wavelength at the power meter is crucial for an accurate power calculation as its photodiode's responsivity depends on the wavelength. Note that a laser power loss at the cryostat windows is always neglected hereby. Finally, the laser light is focused onto the sample in the cryostat by the lens L_L.

The sample part depends on the used cryostat and the desired spatial resolution. Both the macro-setup and the micro-setup SFOC use the bath cryostat explained first, while the flow cryostat used in the other micro-setup is explained afterwards. A scheme of the inner part of the helium bath cryostat with the corresponding long-focus lens arrangement is shown in figure 3-7. The samples are mounted on a sample holder inside the sample

chamber (or variable temperature insert, VTI) of the cryostat. By closely enveloping them in black paper or cardboard they are mounted in a strain-free way. This paper is glued onto a brass holder (with conventional glue) and fixed with screws, if necessary. The brass sample holder is screwed on the sample rod in the VTI of the cryostat. Hence, the samples can be rotated by rotating the whole sample rod. Another possible non-magnetic material for the holder is 3D-printed plastic, which allows for easier modifications of the holder, as illustrated in figure 3-10. By mounting the samples on both sides of the holder, up to ten samples may be mounted simultaneously for small sample sizes, e.g., each with a height of 5 mm. In case a stable detection position on the sample surface is important, additional masks made from Torlon with a hole diameter of $100 - 500\,\mu\text{m}$ may be added. The usage of masks allows for estimating the laser spot size $\Phi_{\text{m,L}}$ on the sample surface to about 300 µm in diameter. With a measured standard laser power $P = 30\,\text{mW}$ for measurements on the QDs, an average power density $p_d = P/A$ of roughly $0.4\,\text{W/mm}^2$ is applied. It may be varied from 0.001 up to $2\,\text{W/mm}^2$. Nevertheless, although they were used in the beginning, masks were not necessary for the study of the QD samples, as the signal was independent of the position. Note that the way of mounting the samples depends on the studied nanostructures and the used cryostat.

The **bath cryostat** (Oxford Instruments Spectromag 10 T) allows for cooling down to a temperature of 1.5 K using pumped liquid helium. For low temperature measurements above 4.2 K, the samples are first cooled down by immersion into liquid helium, since lowering the sample's internal temperature only by the flow of gaseous helium is rather slow. Afterwards, the samples are heated up to the desired temperature via an ohmic resistor located near the capillary tube connecting the VTI with the helium reservoir at the bottom part of the VTI. At the desired temperature, they are brought into a stable thermal equilibrium between electrical heating and cooling by gaseous helium from the exhaust of the liquid helium reservoir. For high temperatures up to 300 K the samples are heated up directly using electrical heating and a low helium gas flow. Temperatures below 4.2 K, which is the boiling point of liquid helium, are reached by transforming the normal-fluid helium into its superfluid phase using additional pumping.

At the sample's position in the middle of the VTI, a magnetic field of up to 10 T may be applied homogeneously with a superconductive split-coil magnet cooled by liquid helium. Optical access to the sample is gained via quartz windows, one on each side of the cryostat and on the VTI, respectively, allowing for measuring the sample in Faraday ($\vec{B} \parallel \vec{z}$, $\theta = 0°$), Voigt ($\vec{B} \perp \vec{z}$, $\theta = 90°$) and tilted ($0° < \theta < 90°$) geometry. The orientation of the sample is set through manual rotation of the sample rod with an accuracy of about $\pm 2°$, allowing for measuring dependences on the tilting angle of the magnetic field. Note that any movement of the samples may require a realignment of the laser spot and the light collection position on the sample by adjusting the lenses in front of the cryostat (L_L and L_C).

Additionally, the sample can be excited either in backward (reflection) or in forward (transmission) **scattering geometry**, as depicted in figure 3-7. Forward and backward scattering differ in the direction of the wavevector $\vec{k}$ of the exciting laser light, while the k-vector direction of the scattered emission light is the same. Thus, in forward scattering geometry the k-vector is minimal since the light paths have the same direction. Moreover, note that the cryostat windows show the Faraday effect in an external magnetic field (see chapter 3 in [289]), just as lenses close to or inside the cryostat. The Faraday effect describes the rotation of the light polarization plane inside a medium by a parallel applied magnetic field. Hence, in forward scattering geometry the polarization plane with

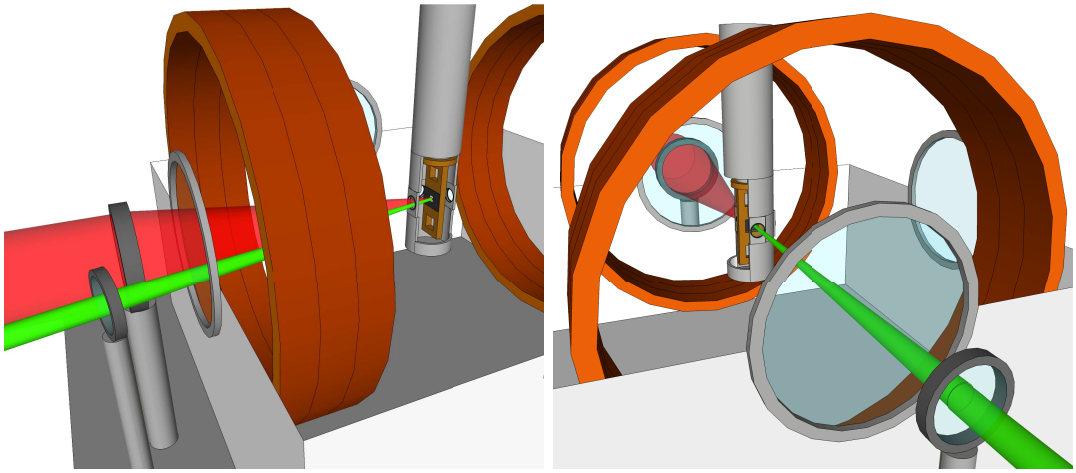

Figure 3-7: Scheme of the inner part of a bath cryostat in Faraday geometry ($\vec{B} \parallel \vec{z}$, $\theta = 0°$), with partly cut-out sample chamber for clarity. The sample is enveloped in black paper glued onto the sample holder (brass) in the sample chamber in between the magnetic coils (copper). The sample may be excited either in backward scattering geometry with slightly tilted incidence (left), with the excitation laser (green beam) and the emitted light (red beam) passing the same window, or in forward scattering geometry (right). The emitted light is collected in the direction of the spectrometer for both. The amount of collected light is limited by the diameter and focal length of the collimating lens.

excitation under an angle of about 15° is rotated by roughly 2° per Tesla [32, 290]. For backward scattering geometry, the light passes the magnetic field in opposite directions and the change of the polarization plane is revoked. Note that the samples need to have a polished backside for transmission measurements.
Furthermore, SFS experiments are typically performed in backscattering geometry with opposite light propagation directions of the incident (z) and the scattered (z') light. Hence, the light polarization configuration is denoted as $z(\sigma^{\pm}, \sigma^{\pm})z'$ or in short $(\sigma^{\pm}, \sigma^{\pm})$ [98, 291]. The circular polarization of the incident light is denoted by the first $\sigma^{\pm}$, while the second $\sigma^{\pm}$ denotes the circular polarization of the scattered light. Their sign depends on the photon angular momentum projection on the light propagation direction. Contrastingly, in Voigt geometry the angular momentum selection rules are lifted. Hence, the light polarization required for the analysis of the scattering signal changes from circularly polarized in Faraday geometry to vertically or horizontally linear-polarized in Voigt geometry, as mentioned earlier.

The detection path starts with the collimation of the light emitted from the sample inside the cryostat. The properties of the lens L_C are chosen in order to reach the highest light gathering power of the optical system within the experimental limitations. Note that all lenses in the detection path are achromatic and coated in the near-infrared range, which ensures a low reflectance from 650 nm to 1050 nm. The light gathering power is related to the numerical aperture $N_A = \nu \sin(\vartheta)$ with the half-angle ϑ of the light-cone, which depends on the diameter D and the focus f of the lens (chapter 10.3 in [287]). The refractive index ν is determined by the medium between the sample and the lens, ranging from $\nu = 1$ for vacuum up to $\nu = 1.027$ for superfluid helium at 2.2 K [32, 292]. However, for the long-focus lenses the part in the helium-filled VTI contributes only about 5 % of the total distance; hence, the differences in the refractive indices are negligible for the calculation of the numerical aperture and $\nu \approxeq 1$. Contrarily, a smaller light cone

resulting from a larger focal length or a smaller lens diameter reduces the signal intensity to a much greater extent. Therefrom, the lens L_C is chosen such that it is placed as close towards the samples as possible; however, for the macro-setup the distance is limited by the outer dimensions of the cryostat. The chosen lens with focus $f = 250\,\text{mm}$ and diameter $D = 50\,\text{mm}$ has a resulting numerical aperture $N_A = 0.10$, as shown in table 3-2. When choosing a lens with $f = 300\,\text{mm}$, the resulting numerical aperture is $N_A = 0.08$ and the light intensity is reduced by 20 %. However, compared to the micro-setup both overall intensities are comparatively low. The minimal spot diameter of the laser beam on the sample surface is calculated from the focal length and the diameter of the lens (or of the laser beam) via $\Phi_\text{m} = 4\lambda f/\pi D$. For a wavelength $\lambda = 800\,\text{nm}$, the diameter of the laser spot is roughly $\Phi_\text{m,L} = 25\,\mu\text{m}$, while the diameter of the observed sample position is only $\Phi_\text{m,S} = 5\,\mu\text{m}$ small. In this configuration, the observed spot is always smaller than the area of the laser spot due to the smaller diameter of the incident laser beam of about $D \approx 10\,\text{mm}$ compared to the diameter of the scattered light beam, which depends on the diameter of the lens L_C. Note that under real experimental conditions, all spots are roughly an order of magnitude larger.

After this first collimating lens, the parallelized light is focused by a second lens onto a cross slit (CS). Behind the cross slit, the light either continues through another collimating lens in the direction of the detector or towards a camera by tilting a flip-mirror in or out of the optical beam path. The flip-mirror allows for reflecting the light beam via two lenses onto a camera. In this way, an intermediate image of the sample with the laser spot position is obtained. The image magnification on the camera may be altered using lenses with different focal lengths. Furthermore, it is helpful to use a color filter in front of the camera, since in this way only the lower-energetic luminescence of the sample is spotted on the camera chip. Thus, the laser spot may be easily adjusted towards a sample position with high luminosity by moving the final focusing lens L_L of the excitation path. The observed position on the sample is changed by moving the lens L_C in the focus plane of the sample. Moreover, the cross slit may be decreased to select a homogeneously illuminated sample region, so that only the emitted light from the chosen position is able to pass through to the detector. An additional white light source for diffuse illumination of the sample is helpful to observe the sample by the camera.

The light, after being focused onto the cross-slit, defocuses and is parallelized by another collimating lens before it passes the ensuing analyzing polarization optics. The $\lambda/4$ (or $\lambda/2$) wave plate is used to study the polarization of the emitted photons. The consecutive Glan-Taylor prism generates linearly polarized light whose orientation matches the light orientation with the highest efficiency of the diffraction grating. Before the light is finally focused onto the entrance slit of the spectrometer, an insertion for neutral density filters (FI) is placed in the detection path. This insertion is required for scattering experiments with signals in close vicinity to the laser line, because it protects the photomultiplier tube (PMT) detector from the intensive laser light during the measurement of the laser line. The numerical aperture of the final focusing lens L_S should match the spectrometer's nominal focal ratio or N_F-number, which quantifies the spectrometer's light gathering power. To achieve maximum light throughput (optical matching), the numerical aperture of the lens should match $N_F = f/D$, depending on the focal length f and the diameter D of the lens. For the double spectrometer with $N_F = 8$, or aperture $F/8$, the maximal throughput is achieved with an $f = 400\,\text{mm}$-lens for a fixed beam diameter $D = 50\,\text{mm}$, as shown in table 3-2. However, the beam diameter is reduced to $D = 30\,\text{mm}$ owing to the smaller diameter of the largest available polar-

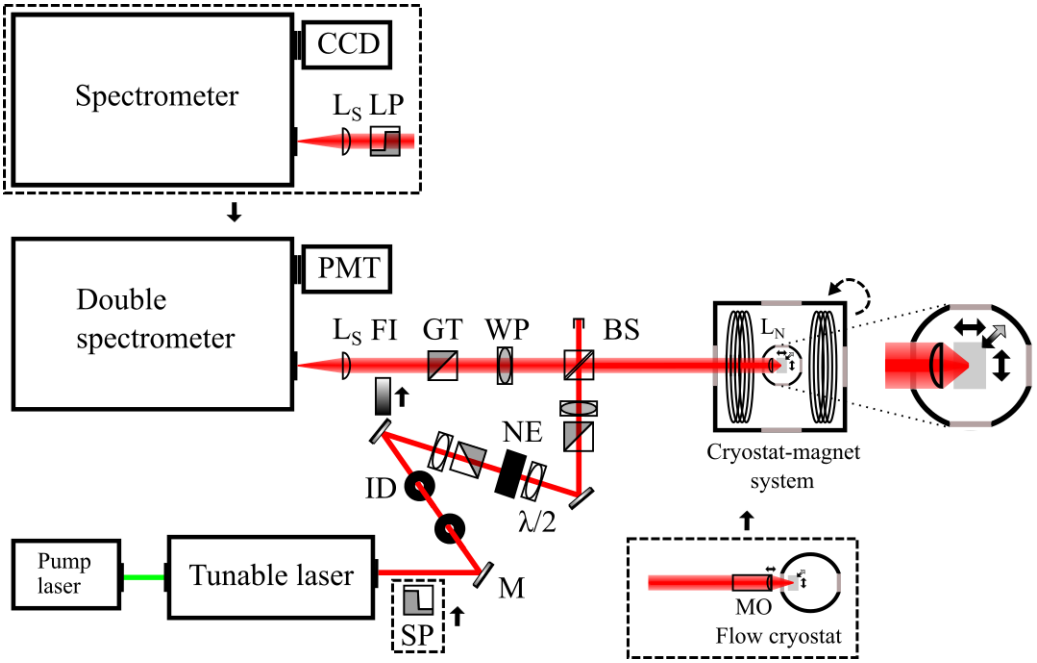

Figure 3-8: Scheme of the micro-setups. The inset on the right side shows the magnified VTI with the small-focus lens, the sample and the directions of movement that are allowed by the nanopositioners. The inset on the bottom shows the arrangement containing the flow cryostat with its integrated piezo stages and the microscope objective, with the allowed directions of movement. The inset on the top shows a single spectrometer attached with CCD detector. The usage of this system typically requires the installation of additional filters, here a shortpass filter in the excitation path behind the laser and a longpass filter in the detection path. The abbreviations are explained in the main text.

ization optics, resulting in a desired lens L_S with $f \approx 250\,\text{mm}$. In this configuration a lens with $f = 250\,\text{mm}$ is an optimal choice, as it reduces the light intensity only slightly, but matches the focal length of the other lenses in the detection path, allowing for a 1:1 mapping of the real-sized sample image at the spectrometer entrance slit. Note that the huge intensity loss (only about 36 % of light can pass) resulting from the smaller diameter of the polarization optics could be avoided by decreasing the beam diameter behind the cross-slit with a lens with $f = 150\,\text{mm}$ or smaller.

3.3.2 Micro-setups

The characterization of the **micro-setup** with high spatial resolution starts with changes in the light path, ensued by the description of the nanopositioners and the flow cryostat configuration. These setups are used to study the samples which require a higher spatial resolution. For example, the study of 2D materials with largest flake sizes of up to 30 µm in diameter require a high spatial resolution to safely identify the signal of a monolayer from neighboring bilayer, multilayer or bulk signals in the detected emission. In addition, for the macro-setup with a laser spot size $\Phi_{m,L}$ of about 300 µm in diameter on the sample surface, the laser spot is too large to excite only a single monolayer. As already shown, the spot sizes $\Phi_{m,L}$ and $\Phi_{m,S}$ depend on the focus f and the diameter D of the lenses L_L and L_C and, assuming the experimentally identified laser spot size as correct size dimension, need to be reduced by an order of magnitude at least. Hence, lenses with a small focus,

$f < 25\,\mathrm{mm}$, are required to improve the spatial resolution. For magnetic field-dependent measurements with the bath cryostat, this consequently demands this lens L_N to be placed inside the VTI of the cryostat. Besides, due to experimental limitations, only one lens can be used for simultaneously exciting the sample with the laser and collecting the sample emission in backscattering geometry. The usage of a single lens requires a change in the light path to align the laser beam with a beamsplitter along the optical axis. Additionally, the desired high spatial resolution requires to use a set of three nanopositioners inside the VTI to enable accurate movements of the sample, since the lens shall keep a fixed position on the optical axis. In case a magnetic field is not required, a **flow cryostat** with integrated piezo stages in combination with a microscope objective is used. Both configurations are depicted in figure 3-8.

The excitation light path for both micro-setup configurations resembles the macro-setup excitation path with the laser beam passing through two iris diaphragms (ID), noise eater (NE) arrangement and polarization optics (GT and WP) before being focused onto the sample in the cryostat. However, after passing the two iris diaphragms, the laser light is not directly guided towards the sample in the cryostat. Rather, it is reflected by another mirror (M) towards a beamsplitter cube (BS). The beamsplitter acts like a partially transparent mirror that allows for coupling the laser beam into the optical axis between cryostat and spectrometer while transmitting the sample emission (nearly) unchanged. The laser beam is reflected at the beamsplitter in direction of the sample in the cryostat, where it travels the same path as the outgoing sample emission. Hence, avoiding an interference with the sample emission beam, the polarization optics are placed before the beamsplitter. The light path is oriented perpendicular to the lens and the sample surface to maximize the amount of collected light, in contrast to a tilted laser incident angle for the macro-setup. Thus, note that a careful alignment of the shared beam path is needed, as the spatial position on the sample surface is sensible to movements of the laser beam.
Inside the VTI of the cryostat, the laser is focused by the lens L_N onto the sample. With a focal length $f = 3.1\,\mathrm{mm}$ and a diameter $D = 6.33\,\mathrm{mm}$, a minimal spot size $\Phi \geq 0.5\,\mu\mathrm{m}$ is achieved. Due to spherical aberrations, the real spot size may be an order of magnitude larger. This lens obtains a fixed position on the optical axis and is attached on the sample holder. Hence, this arrangement does not allow for tilting the samples, since otherwise the lens shifts out of the optical axis on the one hand. On the other hand, the shape and intensity of the sample emission might not be homogeneously distributed over the monolayer flake, thus any imprecise movement of lens and sample should be avoided. This inhomogeneous distribution also calls for a properly aligned laser beam. To align the laser beam on the optical axis, the beamsplitter cube is mounted on a precisely adjustable three-axis stage with micrometer-resolution. The alignment is checked by defocusing the sample and surveying the reflected image in the detection path. In case of a radially symmetric homogeneous illumination during movements of the sample, the incident beam is properly aligned along the optical axis and the sample is positioned perpendicular to the optical axis. Additionally, the reflected image shows the magnified sample surface. Accordingly, the position on the sample is chosen by moving the desired flake position in the middle of the reflected image with the nanopositioners, making the usage of cross-slit and camera obsolete. The nanopositioners allow for an independent movement of the sample in the focus plane of the lens L_N. The sample position should be checked specifically after detuning the dye laser over a large wavelength range, as

this might move the incident beam, and after ramping high magnetic fields, since this might move the sample holder in the VTI or the partly magnetic beamsplitter cube holder. To avoid movements of the holder, an appropriate distance between cryostat and beamsplitter cube has been chosen.

The emitted light of the sample is collected by the same lens and collimated towards the beamsplitter. It transmits through the beamsplitter and passes the polarization optics (WP and GT). After passing a neutral density filter, the light is focused onto the entrance slit of the spectrometer by the lens L_S. The numerical aperture of this final focusing lens should match the spectrometer's nominal focal ratio or N_F-number, which quantifies the spectrometer's light gathering power. To achieve maximum light throughput (optical matching), the numerical aperture of the lens should match $N_F = f/D$, depending on the focal length f and the diameter D of the lens. For the double spectrometer with $N_F = 8$, the maximal throughput is achieved with an $f = 50\,\text{mm}$-lens for a fixed beam diameter $D = 6.33\,\text{mm}$, as shown in table 3-2. For the other spectrometers with $N_F \approxeq 6$, the maximal throughput is achieved with an $f = 40\,\text{mm}$-lens for a fixed beam diameter $D = 6.33\,\text{mm}$.
The detection path mainly differs therein that the collected light must transmit the beamsplitter cube, which leads to an intensity reduction. The beamsplitter's ratio of reflected to transmitted light (R:T) is chosen such that a constant and sufficiently high laser power density on the sample surface during scanning of the whole laser frequency range is reached while maximizing the transmitted sample emission. Compared to the macro-setup, the reachable laser power density $p_d = P/A$ is much higher in this configuration due to the smaller spot diameter on the sample. Hence, solely laser powers in the µW-range are needed to reach equivalently high-power densities and the at first used 50 : 50 beamsplitter was neglected in favor of a 30 : 70 cube, increasing the amount of detected light by 40 %. Moreover, the reflection of the incident laser at the beamsplitter induces an additional phase shift of $\pi/2$ and tilts the polarization plane of the incident light by 90°. Further it should be noted that, although the beamsplitter is labeled as non-polarizing, the polarization plane may be slightly altered. The differences on the order of $1-3\,\%$ in the observed wavelength range result from reflection and transmission differences of the polarization plane for perpendicular (s-) and parallel (p-) polarized light. This imprecision of the polarization degree also accounts for the reflections at mirrors. Hence, in case the spectrometer is not aligned along the optical axis and can only be reached with additional mirrors, all polarization optics shall be placed before the first mirror to minimize this effect on the measured polarization properties.
The optimal tilting of the polarization plane is affected by the alignment of the gratings in the spectrometer and their blaze angles, for which the highest efficiency in the specific wavelength range is reached. Hence, an additional wave plate allows for tilting the polarization plane after the GT to align it respectively to the specific spectrometer settings. In this thesis, different kinds of spectrometers are used depending on the type of measurement, as pictured in figure 3-8. For SFS experiments, the double spectrometer with horizontal aligned gratings is used with attached photomultiplier tube (PMT), for which the usage of neutral-density filters is important. For PL(E) measurements, a single spectrometer with vertical aligned gratings in combination with a charge-coupled device (CCD) is used to cover a broad spectral range. Here, two different kinds of filters are used to suppress laser artifacts in the examined wide wavelength range. Shortpass filter (SP) are utilized in the excitation path to suppress lower energetic luminescence,

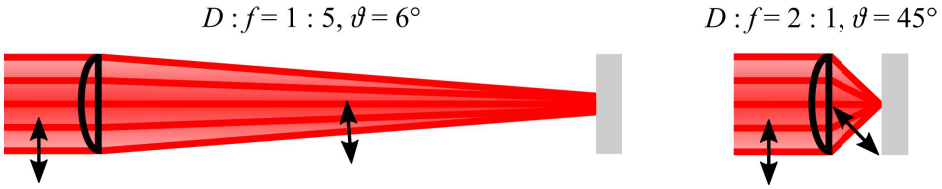

Figure 3-9: Scheme of different detection lens systems. The polarization plane, denoted by the black arrows, is oriented perpendicular to the beam normal. For the macro-setup (left), with diameter D to focus f ratio of $1:5$, the polarization vector is just slightly tilted by the half-angle of the light-cone, $\vartheta = 6°$. Only LO phonons are excited. For the micro-setup (right), with $D:f=2:1$, the polarization vector is tilted by $\vartheta = 45°$. Thus, it obtains a large component parallel to the surface normal and all phonon modes are excited. After Fig. 21.3 in [283].

specifically of the dye laser, and longpass filters (LP) in the detection path minimize laser light reflections inside the spectrometer. The choice of these filters depends on the examined wavelength range, and it may be necessary to change them in between measurements to achieve the highest light intensity.
The final point that needs consideration in the context of using a small-focus lens is the increase of the **light gathering power**. It is linked to the numerical aperture $N_A = \nu \sin(\vartheta)$ with the half-angle ϑ of the light cone, which depends on the diameter D and the focus f of the lens L_N (see chapter 4.8.2 in [261]). The refractive index ν is determined by the medium between the sample and the lens, here ranging from $\nu = 1.00004$ for gaseous helium at 0 °C to $\nu = 1.027$ for superfluid helium at 2.2 K [292]. For the small-focus lens arrangement, the numerical aperture is stated as $N_A = 0.68$ by the manufacturer (Thorlabs). Measurements in liquid helium slightly improve the light intensity $I_L \propto N_A$ by $\sim 2.5\,\%$. The related properties are listed in table 3-2, assuming identical refractive indices $\nu \approxeq 1$ for the shown numerical apertures. Compared to the macro-setup with $N_A = 0.10$ ($N_A = 0.08$), the gathered light intensity improves by 680 % (850 %). Thus, the usage of a small-focus lens or a comparable high numerical aperture device allows for much more precise measurements and a more efficient detection of scattering events. However, a large numerical aperture may result in measuring additional phonon modes, as illustrated in figure 3-9. In an ideal backscattering experiment, the electric field of the laser light is oriented perpendicular to the surface normal and only information from longitudinal phonons are obtained (see chapter 21.1.4 in [283]). For the macro-setup with large focus to diameter lenses, the polarization vector is minimally tilted by the half-angle of the light-cone, $\vartheta = 6°$. Contrastingly, for lenses with large numerical apertures, the polarization vector of the incident laser is not strictly perpendicular anymore and also has an out-of-plane component. For the micro-setup with $D \approx 2f$, the polarization vector is tilted by $\vartheta \approx 45°$ and the out-of-plane component is about the size of the in-plane polarization vector component. Hence, all phonon modes (LO, TO and LA, TA) are excited and parts of the out-of-plane polarized emission are collected.

The required high spatial resolution for the micro-setup is achieved by using **nanopositioners** attached to the sample rod in the VTI of the bath cryostat, as depicted in figure 3-10. As already mentioned, they move the desired sample position in the focus point of the lens L_N by moving the custom-designed and 3D-printed sample holder. The sample holder made of PLA (polylactic acid) plastic filament consists of a plane with fitting holes, for screwing it onto the bottom positioner, and a perpendicular plane with a rectangular cut-out for transmission measurements, where the sample is glued. The size

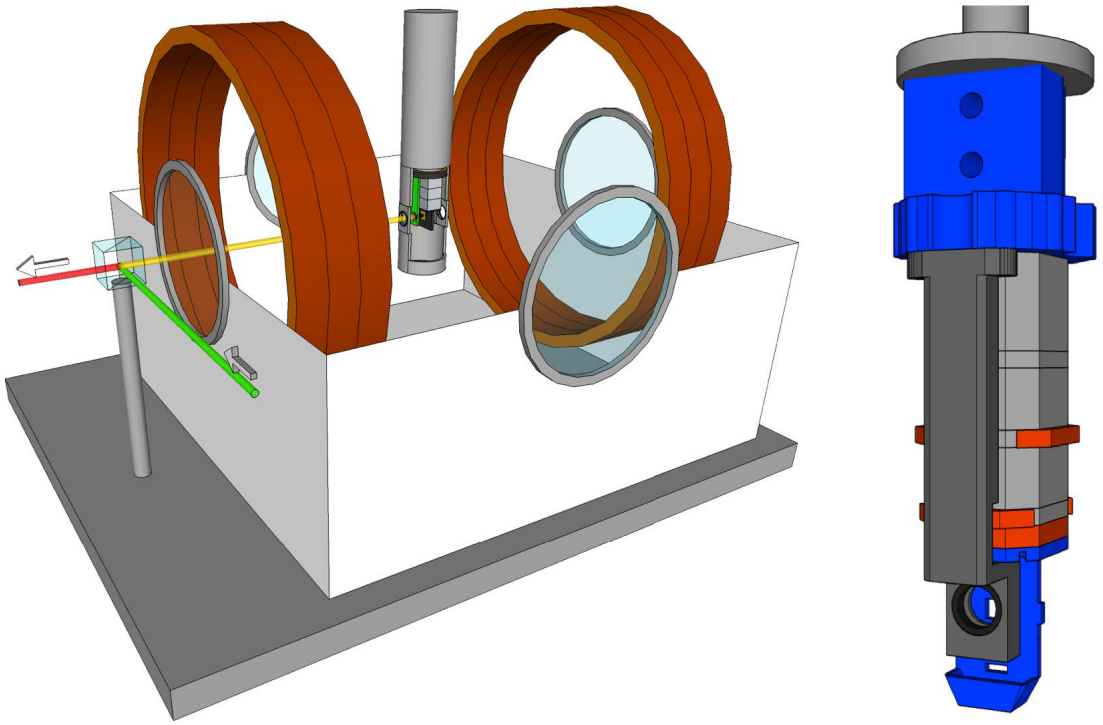

Figure 3-10: Scheme of the micro-setup SFOC in the cryostat (left) and a close-up of the sample holder with attached nanopositioners (right). Each nanopositioner (light gray) has a specific travel range (red), in which the sample may be moved relative to the lens in the lens holder (left: green, right: dark gray). The sample holder (bottom right) and other blue-colored pieces are custom-designed and 3D-printed with PLA.

of this cut-out fits the travel ranges of the nanopositioners; hence, the area on the sample that matches the area of the cut-out is observed by moving the sample holder relative to the lens. For reflection measurements, the sample is glued with silver conductive varnish onto a metal plate, which is glued with conventional glue onto the sample holder. As the sample covers the cut-out, the reachable area is denoted by protruding edges on the sides and by another, smaller cut-out near the bottom. Below this area, a collecting tray for the samples is attached, which allows to pick up the samples in case the glue gets brittle when exposed to low temperatures. In case the delicate samples detach from the sample holder and fall to the bottom of the VTI, the samples probably would be destroyed, while the collecting tray does not damage the samples as proven by experience.
The nanopositioners allow for a movement of the sample in all three directions and, in case of a parallel alignment between sample surface and lens, they allow for moving the sample in the focus plane of the lens. Moreover, by defocusing the sample off the focus point, the alignment of the incident beam and the sample may be checked. The nanopositioners are based on piezo elements made of PZT (lead-zirconate-titanate) ceramics and are used as a set of three. This set consists of independently moving linear positioners (Attocube attoMOTION), two for in-plane movement (y- and z-axis) with a travel range of 3 mm and one for out-of-plane movement (x-axis) with a travel range of 2.5 mm. Compared to other nanopositioners they offer a large travel range achieved with their slip-stick inertial drive, in which the integrated piezo element moves forward and backward for moving one step in one direction. The high spatial resolution results from their small step size down to 10 nm, which depends on precisely adjusted friction.

In the used non-magnetic titanium variant, they are suitable for high-magnetic field measurements up to 31 T and for low temperatures down to 10 mK. For operating the nanopositioners, some rules should be obeyed besides the general advice that delicate devices should be handled carefully. As piezo-based positioners, they are very sensitive towards the accumulation of internal electric charges, e.g., due to compression from shocks or temperature changes. Hence, during temperature changes they should always be connected to the controller in ground mode or switched off. Shocks can be avoided by dampening the working area with some foam or pad. Careful handling also applies for wet conditions, excessive vibrations and big loads. The maximum loads of the positioners are 50 g for vertical movements and 25 g for horizontal movements. This should be kept in mind specifically when a screw is inserted to mount them, as one should always hold exactly the piece in hand in which the screw is inserted. Furthermore, connecting the piezo elements with the correct polarity is essential. In case they are wired the wrong way, the polarity inversion leads to non-homogeneous movement or none at all and may lead to lasting damage like depolarization or complete failure. Additionally, a polarity inversion leads to a wrongly measured actuator capacitance of the piezo elements, which is crucial for applying the correct power limit. In this way, the capacitance indicates an electrically functional system and unusual values give hints about broken or disconnected piezo elements and cables. Thus, before operating the nanopositioners in a new setting, always check the actual capacitance and, if in doubt, use a smaller operating voltage (maximum 9 V in coarse positioning mode). The nanopositioners are operated with the modular piezo motion controller (attocube ANC300). The controller mainly serves for driving the open-loop nanopositioners with the correct power limit composed of step frequency and voltage calculated by the measured capacitance of the piezo elements. Under ambient conditions with a capacitance around 1.1 µF, they work fine with a step frequency of 1 kHz and a voltage of 30 V. At low temperature their capacitance sinks to roughly 0.2 µF. Hence, they may be driven with a higher voltage, e.g. 45 V, specifically for smooth movements of the out-of-plane positioner. In this way, the capacitance may serve as an indicator for the temperature of the piezo elements and, in turn, in the VTI. For determining a correct power limit, the capacitance should be measured after each temperature change.

In case no magnetic field is required, the high spatial resolution is achieved by using a helium flow cryostat with integrated piezo stages in combination with a **microscope objective**. The microscope objective is placed outside of the flow cryostat, with the sample placed inside and close to the window as illustrated in figure 3-8. Using microscope objectives allows for achieving a similar small spot size comparable with the focal length of the small-focused lens due to the small working distance of the objectives. Most objectives are based on refractive optics and contain several lenses combined to a relay lens system. Hence, magnification and numerical aperture are sufficient for quantifying the essential objective's properties and often the focal length is not specified. Here, a microscope objective (Olympus LMPLFLN VIS 2) with 50× magnification and numerical aperture $N_A = 0.50$ is used, which focuses the light onto a ≥ 1 µm-sized spot [15, 254]. Reasonable estimations lead to a realistic spot size of $\Phi \approx 4$ µm on the sample [177]. Note that the optical performance of multi-element lens systems like microscope objectives is often significantly better than the performance of single lenses, e.g. due to spherical aberrations. Hence, the spot sizes in both micro-setup configurations are probably of this size.

The emitted light is collected through the same objective. With a long working distance of 10.6 mm and including the objective's edge dimensions, a focal length $f = 15.8\,\mathrm{mm}$ is estimated, as stated in table 3-2. Compared to the macro-setup with $N_A = 0.10$ ($N_A = 0.08$), the gathered light intensity $I_\mathrm{L} \propto N_A$ increases by 500 % (625 %). However, in comparison to the micro-setup SFOC with $N_A = 0.68$, the gathered light intensity decreases by 27 %. Note that the media contained in the working distance of the microscope objective are air, 1 mm quartz glass and vacuum. As the sample is kept in vacuum, the numerical aperture $N_A = \nu \sin(\vartheta)$ cannot be improved by using a medium with high refractive index like liquid helium within the working distance. For the micro-setup MO using the mentioned microscope objective, maximum light throughput (optical matching) is achieved when the numerical aperture of the lens $\mathrm{L_S}$ with focal length f and diameter D matches the nominal focal ratio or $N_F = f/D$-number of the spectrometer. The objective typically has a standardized mounting thread end piece that allows for screwing it onto the nosepiece of a microscope. In this way, the largest possible beam diameter of the exiting beam is defined by the thread diameter $D = 18.2\,\mathrm{mm}$. Hence, for the double spectrometer with $N_F = 8$, the maximal throughput is established with an $f \approx 150\,\mathrm{mm}$-lens. For the other spectrometers with $N_F \cong 6$, the maximal throughput is realized with an $f \approx 100\,\mathrm{mm}$-lens.
The sample is optically accessible via two quartz windows, either one at top or one on the bottom of the cryostat. In the used configuration, the sample is top-mounted into the cryostat onto a cold plate (or cold finger). Thus, only measurements in backward (reflection) geometry via the top window are possible. The height-movable mounting plate allows for adjusting the distance between the sample surface and the microscope objective. Furthermore, the objective itself may be moved along the z-axis with a micrometer stage. The laser light position on the sample is chosen by independently moving the sample in the focus plane of the objective with the x-y piezo stages. The integrated piezoelectrical positioning system for the sample adjustment is driven by an inertial step motor with low drift and vibrations (controller: Mechonics CU30CL), allowing for resolutions down to 50 nm. The stages based on piezo elements are inside the microscope-type cryostat with an in-plane travel range of 5 mm and a minimal step size of 15 nm. The cryostat (CryoVac Konti) is a gas flow type cryostat in horizontal orientation which offers a temperature range from 3.5 to 325 K (up to 500 K), depending on the particular construction. It is operated at low temperatures with helium supply from an external reservoir (helium vessel) and a heat exchanger, which cools the cold plate on which the sample is attached. The temperature is set by regulating the helium flow through a needle valve of the transfer tube. The heat exchanger is mounted at the bottom of the experimental chamber and distributes the cooling fluid homogeneously to the cold plate. Hence, the sample is not immersed in liquid helium, but is kept in vacuum ($p_v \leq 10^{-5}\,\mathrm{mbar}$) mounted at the external side of the heat exchanger. The cooling occurs via direct heat conduction, which allows for keeping delicate samples cryogen-free. However, the cooling procedure is often not as efficient since the thermal contact between the sample and the heat exchanger is not perfect; thus, a sizeable temperature gradient between both exists. Apart from this, it is advised to use heat-conductive paste for a good heat transfer between the sample and the cold plate. However, this direct contact, here mediated by silver conductive paint, does not allow for a strain-free sample mounting.

Table 3-2: Overview of several optical parameters, for the different setups and for different apertures ($F/8$ for the double spectrometer and aperture $\approx F/6$ for the triple and single spectrometer). SFOC denotes the setup with short-focus lens, while MO denotes the setup using a microscope objective.

							$F/8$	$F/6$
Setup	N_A	ϑ	$f_{\mathrm{L_{C/N}}}$	$D_{\mathrm{L_{C/N}}}$	$\Phi_{\mathrm{m,L}}$	$\Phi_{\mathrm{m,S}}$	$f_{\mathrm{L_S}}$	$f_{\mathrm{L_S}}$
		(°)	(mm)	(mm)	(µm)	(µm)	(mm)	(mm)
Macro	0.10	6	250	50	25	5	400	300
				30			240	180
	0.08	5	300	50	30	6	400	300
				30			240	180
Micro-SFOC	0.68	43	3.1	6.33	0.5		50	40
Micro-MO	0.50	30	15.8	18.2	1		150	100

3.3.3 Spectrometers

The type of measurement determines which **spectrometer** is adequate, e.g., regarding the spectral resolution and wavelength coverage. These properties mainly depend on the focal lengths of the spectrometer stages, the number of gratings and their groove density, the finite widths of the entrance and exit slits and the alignment and quality of the optics. Generally, the usage of a multi-spectrometer with high-groove density gratings enhances the spectral resolution and reduces the wavelength coverage, since the light is diffracted more than once. For SFS measurements with their typical small energy shifts and low intensities, a spectrometer is required that offers a high spectral resolution and a high stray light rejection, like, e.g., the double spectrometer. In combination with a cooled photomultiplier tube it offers a high sensitivity and a low noise level. Hereby, strong neutral-density filters must be used to decrease the laser intensity and avoid damage of the detector when scanning over the laser line. Contrastingly, a wide wavelength coverage is of higher importance than a high resolution for PL and PLE with their rather broad spectra. Although a broad spectrum can be scanned with multiple small steps, this may lead to spectral artifacts due to software and experimental limitations and should be avoided. Moreover, laser stray light artifacts inside the spectrometer are suppressed using shortpass and longpass filters. Hence, the usage of a single spectrometer with lower resolution is preferential over a multiple additive spectrometer for PL and PLE measurements. The possibility to scan a wide range, up to 56 nm in one step for a low-groove density grating in a single spectrometer stage, also affects the used detector. For example, a PMT only offers a very time-consuming scanning in order to cover a wide spectral range. Thus, a multichannel detector like a CCD camera is advantageous since it works much faster.

Besides the spectral resolution and wavelength coverage, another important property of a spectrometer is its useful **working range**, defined by the mechanical and spectral wavelength range. The mechanical range of a spectrometer is limited by the mechanical rotation capability of the grating drive system. Furthermore, the largest achievable wavelength depends also on the grating's groove density, e.g., it decreases down to 833 nm for a groove density of 1800 g/mm in the triple spectrometer [293]. The spectral range of a spectrometer depends on the range of its optical elements: the diffraction gratings and mirrors. The spectral range of the mirrors is defined by their reflection coating,

comparable to the coating of the lenses in the optical path. Although their efficiency is typically higher than the efficiency of the grating, a substantial amount of light intensity is lost at the mirrors. For example, the optical throughput decreases by about 40 % in the double spectrometer solely due to the reflection at the nine mirrors with an estimated averaged reflectance of 95 %. Note that a standard reflectance of 85 % at 800 nm leads to an intensity loss of roughly 80 %. The spectral range of the used reflection gratings is rather broad, while their first-order diffraction efficiency over the visible wavelength range strongly depends on the polarization of the incident light. Specifically, the diffraction efficiency varies significantly with polarization and wavelength for ruled gratings with their sawtooth-shaped step structure. However, this also applies for holographic gratings with their sinusoidal-formed grooves, since it results as a solution of the Helmholtz equation with different boundary conditions for p- and s-polarized waves [294]. Depending on whether the incident light is polarized parallel (p-polarized, transverse electric) or perpendicular (s-polarized, transverse magnetic) relative to the grating grooves, the efficiency strongly varies. For the non-blazed and horizontally aligned gratings in the double spectrometer, an averaged efficiency of 80 % is reached for perpendicular polarized light in the wavelength range from $500-850$ nm (and possibly higher). For lower wavelengths, the efficiency is higher for parallel polarized light, with an averaged efficiency of 60 %. Often, an overall higher efficiency is achieved by blazing the gratings. The blaze wavelength indicates the optimal wavelength for which the maximal power is concentrated in the desired diffraction order and for which the highest efficiency is reached. For the ruled gratings with blaze wavelengths in the visible range (here 500 nm) in the single and triple spectrometers, the highest efficiency is also achieved with perpendicular polarized light in the studied near-infrared spectral region. However, note that the gratings in these spectrometers are oriented vertical. Hence, an additional half-wavelength retarder in front of the spectrometer entrance is useful to maximize the optical throughput by matching the polarization plane of the incident light regarding the orientation of the grating with the highest efficiency.

The **stray light suppression** is described by the stray light rejection ratio of a spectrometer, which depends on the grating, specifically on its blaze wavelength and groove type. To improve stray light suppression, the optical throughput must be maximized and stray reflections minimized. The optical throughput may be maximized by choosing a grating with suitable blaze wavelength. This improves the diffraction efficiency, while minimizing random stray light reflections, as less light is diffracted into other diffraction orders. In addition, such randomly scattered light may stem from surface imperfections on any optical surface, e.g. from low-quality optics. Directional or focused stray light may result from errors in ruled gratings, as these are focused in the dispersion plane. Non-periodic errors in the ruling of the grating grooves may lead to stray light that worsens the signal-to-noise ratio. Periodic errors, such as ghosting, may result, e.g., in an oscillatory background. These errors may be avoided using holographic gratings, which produce less stray light due to their sinusoidal groove shape.

In this thesis, three different spectrometers and detectors are used, in which the **double spectrometer** shall be explained in the following in detail. Basically, the light path is the same for all spectrometers, as all are built in the Czerny-Turner design consisting of two concave mirrors and one plane diffraction grating. Minor differences result from the orientation of the gratings and the amount of coupled stages. An example is depicted in figure 3-11, showing a scheme of the double spectrometer (Jobin-Yvon U1000). The main components of this spectrometer are two identical monochromators in additive asymmet-

ric Czerny-Turner configuration, adding up to a focal length of $2 \times 1\,\mathrm{m}$ and F/8 aperture. It is equipped with two non-blazed holographic gratings with 1800 grooves/mm mounted on a single shaft parallel to the grating grooves. The spectrometer is able to cover a mechanical wavelength range between $327.5 - 910\,\mathrm{nm}$, as denoted in table 3-1, and a spectral range of $440 - 750\,\mathrm{nm}$ [295]. The grating itself is suitable for a range of $450 - 850\,\mathrm{nm}$ (and higher), depending on the chosen light polarization. The double spectrometer is an excellent choice for measuring small energy shifts in close vicinity down to $1\,\mathrm{cm}^{-1}$ to the laser line [295] due to its high spectral resolution $\Gamma_{\mathrm{sr}} \geq 0.16\,\mathrm{cm}^{-1}$ (5 pm or 20 µeV), minimal step size of 0.5 pm ($0.02\,\mathrm{cm}^{-1}$) and strong stray light suppression. The strong stray light suppression offered by the double spectrometer results from the intermediate slits in combination with the additional light path in between the monochromators, leading to a stray-light rejection ratio r_s of 10^{-14}. Considering the efficiencies of the gratings and mirrors mentioned above, the overall transmission drops to 40 % at best.
The light path of the double spectrometer starts at the entry slit on the top left front side on which the beam containing the light emitted from the sample is focused by the lens $\mathrm{L_N}$. The light passes the entry slit and defocuses onto the first concave mirror on the backside. For a correct adjustment with maximal signal intensity and minimal linewidth, it is of highest importance that the illuminated light area matches the whole size of the first mirror. This is realized by choosing an appropriate lens $\mathrm{L_N}$ corresponding to the N_F-number of the spectrometer, see table 3-2. The concave mirror collimates the beam onto the horizontally aligned grating, which is attached on the front side below the entrance slit. From here, the light is spectrally diffracted onto a second concave mirror below the first one, which collects the remaining light and focuses it onto a second slit. Note that all concave mirrors have the same focal length corresponding to the distance between the mirrors fixated on the backside and the slits on the front side. The once diffracted light then exits the main body of the spectrometer on the bottom left front side and enters an outer compartment, in which two plain mirrors reflect the light into the middle chamber of the spectrometer. Herein, a third collimating mirror collects the defocused light and refocuses it back into the second part of the outer compartment. Note that this intermediate mirror is shifted forward due to the additional beam path in the outer compartment. After being reflected by the second set of two plain mirrors in the outer compartment, the light passes the third slit and enters the second monochromator. In this way, the exit slit of the first monochromator is imaged onto the entry slit of the second monochromator on the bottom right front side. Both intermediate slits should be kept at a width of $\leq 100\,\mu\mathrm{m}$ for a strong stray light suppression. In the second monochromator, the light path is reproduced upside-down (asymmetric Czerny-Turner design) until, finally, the twice diffracted light passes the exit slit and enters the detector on the top right front side, here a PMT is installed. In front of the exit slit, a swing-away mirror may deflect the light onto a multichannel detector like a CCD camera. Both entry and exit slit widths are kept at the same value in between 80 to 140 µm, depending on the desired spectral resolution and required optical throughput. In case the slits are open more widely, the spectral resolution decreases while the light throughput increases, which allows one to reduce the measurement time for the sake of spectral resolution. Hence, opening the slits to maximize the light intensity should only be done to such an extent that the scattering line profile does not change.
In this context it should be noted that specifically the stepping motor of the spectrometer, but also other movable parts, are sensitive to vibrations, which are able to change the optical alignment of the spectrometer. Thus, they highly benefit from a stable and

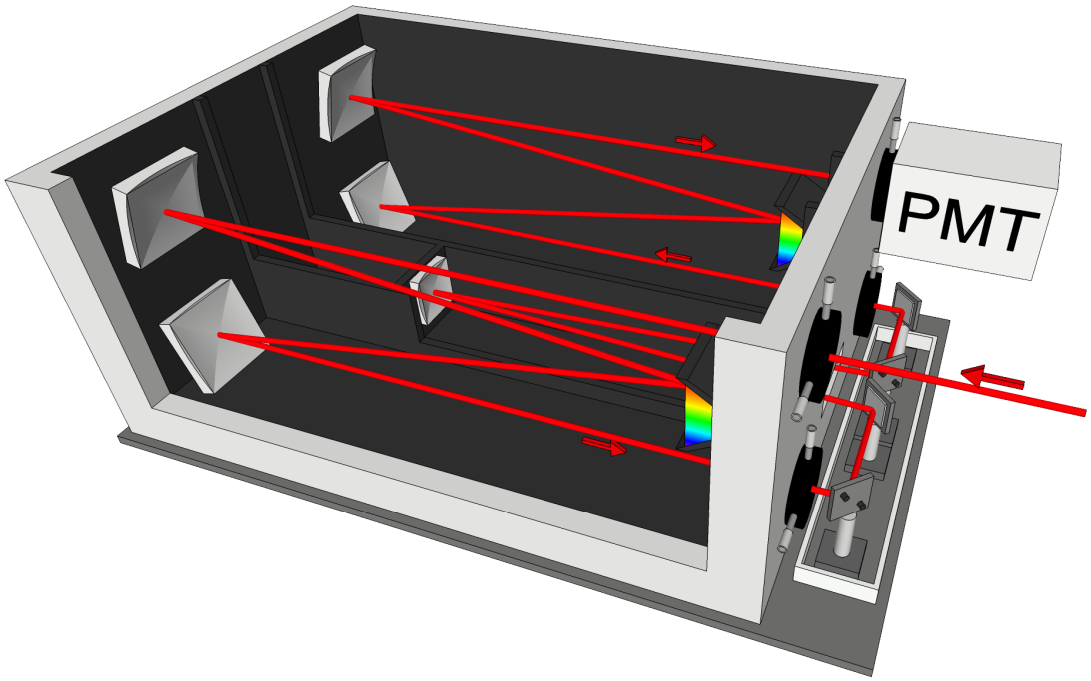

Figure 3-11: Scheme of the light path in the U1000 double monochromator with attached photomultiplier tube. After Fig. 4 in [295].

rigid table and an additional damping, here realized via clamping the spectrometer body to the neighboring optical tables. Otherwise, these parts might move over time, resulting in a slow but steady intensity decrease.

Similar to the double spectrometer, the **triple spectrometer** (Acton TriVista 555) consists of three coupled stages with a focal length adding up to $3 \times 0.5\,\mathrm{m}$. These stages are oriented symmetrically (Czerny-Turner design) in the horizontal plane with aspheric mirrors and may be used either in additive or subtractive mode. In additive mode, the triple spectrometer offers a comparable high spectral resolution Γ_{sr} down to $0.44\,\mathrm{cm}^{-1}$ (13 pm or 50 µeV) with a minimal step size of 2.5 pm ($0.1\,\mathrm{cm}^{-1}$). In subtractive mode, it obtains an excellent stray-light rejection ratio r_s of 10^{-12}. However, in this thesis the spectrometer is not used for SFS measurements but for PL(E) spectroscopy, which requires a broad wavelength coverage instead of a high spectral resolution. Since each stage may work as a separate individual spectrometer, only a single stage of this spectrometer is used, and its spectral resolution is entirely defined by this stage. Every stage may be operated with either front or side entrance or exit allowing for more usage options, while the side paths each require an additional mirror. The first stage is usually addressed directly from the side entry, slightly decreasing the optical throughput, while the third stage is addressed with fibers from the front side. In both stages, the detector is attached at the front exit. The mechanical range of the spectrometer reaches from 185 nm to 2.2 µm, however it is further limited by the choice of the grating. For the typically used grating with 900 g/mm, the mechanical scan range decreases to 1667 nm. The spectral range of the spectrometer with F/5.9 aperture depends on the efficiency of the mirrors and the gratings. Here, the light passes maximal four mirrors and, hence, the overall optical throughput decreases less than for the double spectrometer. With an averaged efficiency of 70 % per grating and 92 % per mirror, a light intensity loss of

40 % (50 %) for two (four) mirrors in a single stage must be considered. Note that the transmission drops to 15 % when using all three stages (consisting of three gratings and ten to twelve mirrors). Thus, in case the third stage of the spectrometer shall be used, a higher transmission is reached by using an optical fiber which gathers the light in front of the first stage and deflects it towards the front entry slit of the third stage. The spectral range of the vertically aligned ruled gratings ranges from 330 to 900 nm (330 to 850 nm) for the grating with 900 g/mm (1800 g/mm) and 500 nm blaze wavelength, leading to a wavelength coverage of approximately 52 nm (17 nm) at 800 nm. Three gratings are mounted on a motorized interchangeable turret that allows for a fast and easy exchange between different gratings.

A **single spectrometer** (Acton Spectra Pro 2550i) was used, which has similar properties like a single stage of the triple spectrometer. It is built likewise in horizontal Czerny-Turner design with aspheric mirrors, a focal length of 0.5 m and an F/6.5 aperture. The spectral range of the grating with 1800 g/mm varies from 450 to 1100 nm (350 to 600 nm) for s-(p-)polarized light. For the grating with 600 g/mm, the spectral range covers 350 to 850 nm (350 to 650 nm) for s-(p-)polarized light, leading to a wavelength coverage of up to 56 nm (24 nm for 1800 g/mm) at 436 nm. Note that the efficiency for the 600 g/mm grating accounts only about 50 % at 800 nm, compared to 85 % at the blaze wavelength of 500 nm. This leads to an overall transmission of 35 % in combination with two mirrors. Both vertically aligned ruled gratings are mounted on a motorized interchangeable triple grating turret. With a minimal step size of roughly 2.5 pm (0.1 cm^{-1}) and under perfect alignment conditions, a spectral resolution of roughly 100 µeV is achieved. Furthermore, note that for both spectrometers an entry slit width of 100 µm is advisable, which does not alter the line profile significantly and leads to an appropriate light throughput.

3.3.4 Detectors

Finally, the diffracted light enters the **detector** at the output of the spectrometer and is converted into an electronic signal either by a photomultiplier tube (PMT) or by a charge-coupled device (CCD) camera. A CCD camera is a multi-channel detector composed of an array of photodiodes that allows the immediate detection of complete spectra, decreasing the measuring time. Contrastingly, the photon-counting PMT is a single-channel detector with low noise levels and ideally suited for measuring small signals in close vicinity to the laser line.
The accumulation of the signal from the double spectrometer is performed by the attached **photomultiplier tube (PMT)** (Hamamatsu Photonics R943-02), which is a sensitive detector with fast response and high signal-to-noise ratio. This device converts the incoming photons into electrons via a GaAs-based photocathode activated with caesium with a photo-sensitive area of about 14 mm in diameter. The electrons are amplified by an electron multiplication system with a gain of 5×10^5 and are transformed into an electric signal, which may reach up to 10^4 A/W. This electron current output of the PMT is connected to a preamplifier (Advanced Research Instruments Corporation, F-100T), which forms pulses with a fixed duration and amplitude for each detected photon. Moreover, it functions as a discriminator and rejects low amplitude pulses that might be due to thermal electrons. Thus, it ensures an optimal signal-to-noise ratio and a low average background noise, which is decreased by cooling to about five counts per second. For this purpose, a temperature of −20 °C is recommended, which is reached by cooling

with a Peltier element. The modified electric pulses are counted by the control unit of the double spectrometer.
The sensitivity of the PMT covers roughly a wavelength range of 160 to 930 nm with a peak wavelength range of the photocathode from 300 to 850 nm and the highest quantum efficiency of approximately 23 % at 300 nm. For higher wavelengths the quantum efficiency gradually decreases down to 10 % at 850 nm and then declines, with roughly 1 % efficiency at 900 nm. This rapid energy-dependent efficiency decrease above 860 nm is further enhanced by the gratings with 1800 grooves/mm mounted in the double spectrometer, which cover a spectral range from 450 to 850 nm. The recorded spectra thus need to be corrected and the data must be weighted with the efficiency dependence of

$$\Phi(E) = 1.028 + \frac{9.183 \times 10^{-4} - 1.028}{1 + \exp[(E - E_0)/0.0106\,\mathrm{eV}]} \tag{3.11}$$

with $E_0 = 1.4171\,\mathrm{eV}$. Additionally, during operation it must be taken into account that strong light may damage the highly sensitive detector, e.g. during identification of emission lines. As mentioned above, the insertion of neutral filters during scanning over the laser line is absolutely necessary to reduce the danger of an overwhelming light incidence. Besides, a major drawback of the PMT is the time-consuming scanning to record a wide spectral range. The scattering intensity is measured at a certain spectral wavelength, which has to be repeated several times to receive a full spectrum. Hence, for wide-range measurements, multichannel detectors are preferable.

Charge-coupled device (CCD) detectors are used whenever the measurement of a broad spectral range is required, e.g., for basic characterizations of the PL. They are capable of taking quasi-instant PL spectra without scanning. While their spectral coverage of a full-chip read-out depends on the used grating, it is comparatively large due to their multi-channel signal acquisition. However, CCD cameras are usually inferior in sensitivity and resolution; hence, they are less suitable for measuring inelastic light scattering while being superior for PL(E) spectroscopy. The image sensor of such a CCD camera is composed of a silicon-photodiodes array, each connected to a capacitor. The conversion from light into electronic signals in the photodiode functions with the help of an internal electric field, which separates the electron-hole pairs created by the detected photons. The collected electrons are stored in the capacitor, while the last capacitor in the array dumps its charge into a charge amplifier, which converts the charge into voltage. By repeating the process, the whole array is transformed into a sequence of voltages. These are detected as an electronic signal (see chapter 4.4.8 in [283]).
In this thesis, two different kinds of Si-based CCD cameras are used. The liquid-nitrogen cooled, front-illuminated CCD camera (Princeton Instruments SPEC-10:2KF/LN), connected to the triple spectrometer, is composed of silicon-photodiodes cooled down to −120 °C. Its readout noise and thermal noise are negligible in comparison to the shot noise of the signal, leading to a high signal-to-noise ratio when combined with a 100 kHz readout-amplifier. Its ultraviolet-enhanced sensitivity ranges from 180 to 1080 nm, with the highest quantum efficiency of 47 % at 700 nm and a spectral resolution of roughly 0.2 nm for the 900 g/mm grating. However, the quantum yield at 800 nm reduces to 40 % and to 24 % at 900 nm. The Peltier-cooled CCD camera (Princeton Instruments PIXIS: 256E), connected to the single spectrometer, works very similar. Its sensitivity ranges from 200 to 1080 nm with the highest quantum efficiency of 58 % at 760 nm, which reduces down to 35 % at 900 nm. It mainly differs regarding its Peltier-element cooling, which

works with thermoelectric cooled air down to $-70\,^{\circ}\mathrm{C}$. As cooling leads to a reduced camera-generated dark current, less cooling leads to a slightly higher thermal noise level in this camera, which is still within the low-noise range. Both front-illuminated cameras show no-etaloning behavior, reducing the possibility for artificial oscillations. However, slight oscillatory PL behavior may result from interferences of the emitted light in the vacuum window of the CCD cameras, besides their anti-reflection coatings.

To conclude, the choice of a specific setup depends on the characteristics of the studied sample and the examined light properties. All setup configurations allow to vary the temperature, set the polarization of the incident laser beam, vary its power density and analyze the polarization of the light emitted from the sample. They mainly differ in their light gathering power, which is much higher for the micro-setups. Still, the macro-setup is sufficient for the QD samples, as they yield a high light intensity distributed homogeneously over the sample. Moreover, it allows for applying an external magnetic field and is comparatively robust towards external influences. Specifically, the possibility of tilting the sample's growth axis with respect to the magnetic field axis is a crucial parameter in the (spin-flip) scattering measurements. Additionally, these measurements require a tunable frequency-stable laser with narrow laser linewidth. For light-scattering measurements on the 2D materials, a high spatial resolution is required which is gained by using the micro-setup with small-focus lens and nanopositioners in the bath cryostat. This configuration offers a spatial resolution in the high nanometer-range in combination with an external magnetic field. However, it does not allow to tilt the sample respectively to the magnetic field axis. Besides, the nanopositioners fixated on the sample rod are rather delicate to handle. Contrastingly, the micro-setup with microscope objective and flow cryostat is chosen for measurements on these materials that do not require an external magnetic field. The integrated piezo stages allow for the same high spatial resolution but are more robust. Still, the horizontal orientation of the flow cryostat, requiring additional mirrors and optical posts, might be considered as suboptimal. Finally, the observation of weak spin-flip lines requires a high efficiency of the detection system consisting of the spectrometer and the photon detector. Herein, the efficiency of the spectrometer mainly depends on the diffraction efficiency of the gratings, but also on the absorption of the mirror surfaces. The former influence the spectral resolution and the stray light rejection ratio. In addition, a high quantum efficiency and a large signal-to-noise ratio of the detector are essential, which may be enhanced via cooling. Thus, all setups offer specific advantageous properties depending on the studied light emission and sample properties. The sample properties are listed in the following section.

3.4 Details on the samples

The examined semiconductor samples have different characteristics resulting from their underlying crystal structure, as explained in section 2.1. The growth procedure and the sample fabrication technique shall be explained in this section.

3.4.1 InGaAs quantum dots

The **quantum dot** (QD) samples examined in the first part of this thesis contain self-assembled InGaAs dots on a GaAs substrate. The small dimensions of the dots in the

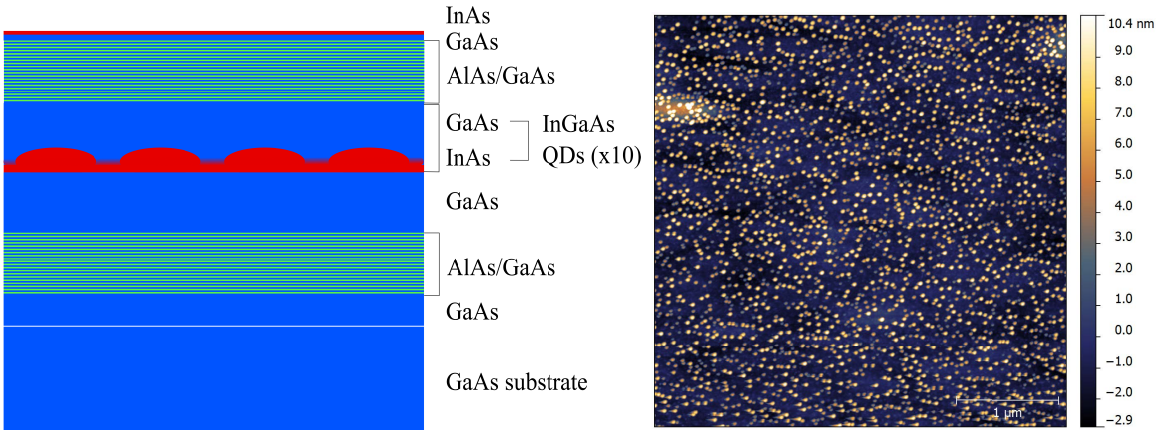

Figure 3-12: Schematic cross section (left) of the InGaAs QD samples (GaAs = blue, AlAs = green, InAs = red). Atomic force microscopy (AFM) image (right) of a QD ensemble. Top view on a $3 \times 3\,\mu m^2$ area of InGaAs QDs. The image was taken by the atomic force microscope (Bruker) before capping the QD layer. The average height of the shown QDs is slightly above 10 nm. The average diameter of the QDs is about (40 ± 4) nm.

nanometer-range confine the wavefunctions of the particles, resulting in a quantization of the energy levels as described in section 2.1. Contrastingly to ordinary atoms, the characteristics of such optically active QDs are tunable, including their size, shape, and material (see chapter 1.3 in [24]). The samples studied in this thesis were grown by molecular beam epitaxy on (100)-oriented GaAs substrate with a dot density of around 1.4×10^{10} dots/cm^2. These dots are nominally undoped, meaning that no resident charge carriers are present in the dots. They are formed by the Stranski-Krastanov growth method, which is characterized by island formation on a thin wetting layer. When InAs is grown onto GaAs, the mismatch of 7 % [296] between their lattice constants leads to the formation of InAs islands on an InGaAs wetting layer, with a layer thickness of about 1.7 monolayers, as a result of increasing strain. The dots form without external control due to local interactions, leading to randomly distributed dots (self-assembly). The single QD layers are separated by about 100 nm-thick layers of GaAs. These ten layers of QDs were grown in between aluminum arsenide (AlAs) interlayers. The encapsulation of the dots in between the AlAs/GaAs buffer layers reduces the strain between the dots and the substrate. Finally, an InAs capping layer is grown on top for protection. The sample structure, resulting from the specific growth procedure as mentioned in the growth sheet, is depicted in figure 3-12 (left).

After the growth process the optical properties of the dots are fine-tuned by annealing, which describes a heating of the samples. This heating leads to an enhanced interdiffusion of atoms in the QDs and the surrounding matrix and changes the dots' composition and size. Specifically, three main effects on the quantum confinement shall be noted. Firstly, a decrease in the dots' height leads to a blue-shift of the bandgap. The size of the shift depends on the heating duration and temperature: longer time and higher temperature lead to larger emission energy shifts. However, this process is only applicable to a certain extent, since a too high annealing temperature degrades the sample quality. Secondly, the quantum confinement is altered by an increase of the dots' diameter, which leads to a decrease of the energy spacing between the shells. Thirdly, the dots become more homogeneous in size, which leads to a narrowing of the inhomogeneous linewidth of the sample's PL. Overall, the different QD profiles change the energetic position, level-

Table 3-3: Overview of the QD samples, their annealing temperatures and the energy E_{PL} of their PL maximum at 6 K.

Sample 14824-	T_{RTA} (°C)	E_{PL} (eV)	Sample 14824-	T_{RTA} (°C)	E_{PL} (eV)
IIe	850	1.383	IIh	915	1.424
IIb	870	1.393	IIa	900	1.433
Ic	855	1.408	IIg	930	1.437
IIc	885	1.416	#1 Ib	910	1.443
IIf	905	1.420	#2 IIi	950	1.451
#3 IId	895	1.421	IIj	970	1.460

spacing and linewidth of the photoluminescence. An ensemble of the lens-shaped QDs with size variations is depicted in figure 3-12 (right), with a height of about 10 nm and lateral size of about 40 nm (dimension ratio of $1:4-5$).
The samples under study were processed by rapid thermal annealing (RTA). In this process, the samples are heated up to a comparatively high temperature of $850-970\,^{\circ}\mathrm{C}$ for a short period of time, between $30-240$ s. The PL of the dots is tuned to match the spectral range of the spectrometer, namely below 900 nm for the double spectrometer. This tuning of the bandgap was confirmed using PL spectroscopy to measure the emission spectra of the dots at 77 K by A. Ludwig, Ruhr-University Bochum, where the samples were grown and annealed. At 6 K the main emission peak of the samples ranges from 1.383 eV (896 nm) to 1.460 eV (849 nm), see table 3-3. Therein, the examined samples are listed with annealing temperature and the energetic position of the s-shell or PL maximum after which they are sorted. The energy splitting between the shells is about $10-25$ meV, in dependence of the specific annealing temperature and resulting QD size. Note that two samples from the first growth series, denoted as I, have slightly deviating properties compared to the samples of the second growth series, denoted as II.

3.4.2 TMDC monolayers

In the second part of this thesis, investigations on semiconducting monolayers as part of the **transition metal dichalcogenides** (TMDCs) were performed. The structures WSe_2, $MoSe_2$, their alloy $Mo_{1-x}W_xSe_2$ with different compositions x, and MoS_2 are studied. They possess a hexagonal crystal structure with strong intralayer covalent bonds and weakly van der Waals-bound interlayer planes. This allows for exfoliating monolayers from bulk crystals, as explained in the following. As monolayers, their height is only one unit cell, here around 7 Å, thus they are also known as two-dimensional (2D) layers or 2D materials. Although their lateral size in on the order of several micrometer, their still small sample size demands the usage of a confocal (collinear) setup as described in the previous section. For these structures, the fabrication process is of high importance to achieve bright and narrow luminescence peaks.
The first knowingly produced 2D material graphene was discovered by exfoliating graphite with adhesive tape [6, 297, 298]. Up to now, this procedure hasn't changed much, although it was partly optimized for TMDCs. Other procedures like molecular beam epitaxy [299] and chemical vapor deposition [300], and can also be used to grow monolayers, however, mechanically exfoliated monolayers are still superior regarding their optical properties, e.g. the linewidth of the exciton. Additionally, mechanical exfoliation is cheap and rather facile, although time-consuming. All investigated monolayers in this

thesis were fabricated by mechanical exfoliation (J. Jadczak, Wrocław University of Science and Technology).
The starting point for the exfoliation procedure is a conventional bulk TMDC crystal with a few mm lateral extension purchased from 2D semiconductors grown by chemical vapor transport technique [15, 254]. A thin piece of it is placed on adhesive tape so that the layers are aligned parallel to the tape surface. This crystal is thinned by repeatedly tearing off tape strips until only thin multilayers as well as monolayers remain. These residual crystal flakes are pressed onto a visco-elastic polydimethylsiloxane (PDMS) film. If the tape is removed quickly enough, the flakes stick easily to the film. Hereafter, the crucial point of monolayer identification follows. The thickness of the flakes is examined with an optical microscope in reflection mode. The optical contrast of the flakes depends on their number of layers, with only a small difference between mono- and bilayers. An experienced observer may thus safely distinguish monolayers optically from other layers on the PDMS. Otherwise, the monolayer character of the flakes may be confirmed using Raman scattering, PL spectroscopy, or atomic force microscopy imaging (after the transfer). Note that only a small fraction of the flakes on the PDMS are monolayers, if there are any at all. If no monolayers or only small or crippled ones are found, the above listed procedure must be repeated. In case an appropriately sized monolayer is found (at least $10\,\mu m \times 10\,\mu m$, preferentially larger), the PDMS film is placed upside down on a glass slide and is brought in close proximity to the target position on the chosen substrate. Here, the substrate of choice is a roughly $10\,mm \times 10\,mm$ sized silicon plate coated with approximately 300 nm silicon dioxide (SiO_2/Si) [254]. The desired substrate position must be microscopically clean and smooth to avoid stress on the flake. Hence, it is advisable to clean the substrate directly before the transfer process to avoid contamination such as dust grains. The glass slide with the monolayer is mounted on a three-dimensional micrometer stage, while the slide with the substrate is placed on some kind of rotational stage. This allows for aligning the flake respective to the substrate with micrometer precision. The transparency of the involved materials allows for observing the stacking process under the microscope and gives control over the transfer process. Finally, the PDMS film with the monolayer is gently pressed down on the substrate. Hereby, a slow speed to bring the materials in and out of contact is crucial for reducing the amount of stress on the flake. When slowly removing the PDMS film, the flake should stick to the substrate. In this way, this method, known as all-dry stamping method [301], allows for deterministically transferring monolayers to a variety of substrates with precise position. Moreover, it allows for stacking multiple layers on top of another, leading to so-called van der Waals-heterostructures. A typical microscope image of such a heterostructure can be seen in figure 3-13. The fully stacked sample is glued with silver conductive varnish onto a copper plate, which must be removed for measurements in the cold finger flow cryostat to ensure a proper thermal contact, while it may stay attached in the bath cryostat.
After the transfer procedure of each flake, the sample may be annealed for 20 minutes at 180 °C on a hot plate in air. After the whole heterostructure assembly, the sample may be annealed for another two hours at 200 °C in air, see e.g. [15, 254]. This improves the contact between the layers and reduces strain-induced bubbles and wrinkles. However, note that this procedure sometimes may damage the flakes or stack them differently, e.g., folding monolayers to bilayers. For single monolayer flakes, the annealing should be performed in vacuum, as otherwise oxygen might be injected which leads to a faster deterioration. Besides for annealing, monolayer flakes should generally be stored under vacuum in an exsiccator, as they tend to degrade and age under ambient conditions:

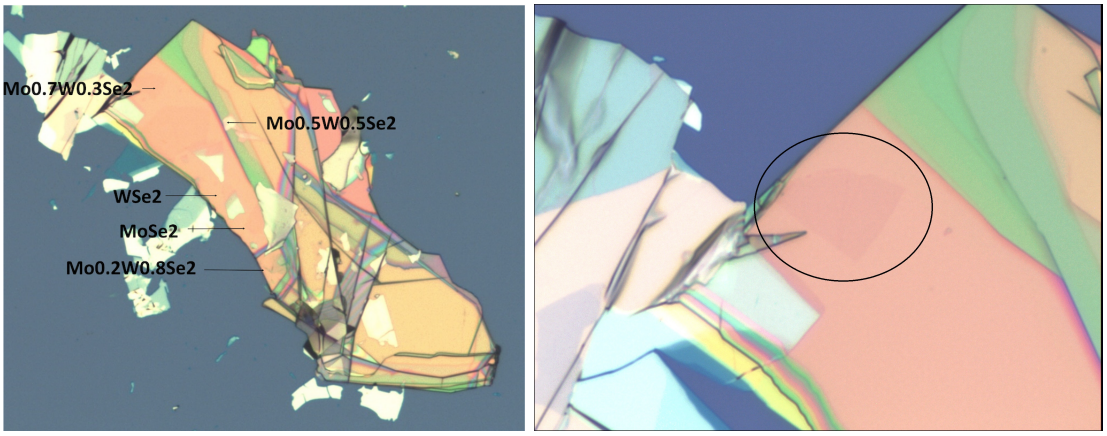

Figure 3-13: Microscopic images of a TMDC sample with different enlargements. The monolayer flake $Mo_{0.7}W_{0.3}Se_2$ (inside the circle on the right) has a size of about 10 µm × 10 µm.

over days or weeks depending on the specific material. Under the influence of oxygen and moisture, charge traps and molecular adsorbates accumulate, which lead to line broadening, additional defect lines and an overall PL decrease [68].
The degradation process is slowed down significantly by encapsulating the monolayer with few-layer hexagonal boron nitride (hBN) flakes, which is a layered insulator with large bandgap in the UV range. This encapsulation suppresses environmental effects and stops the gradual oxidation and passivation of the monolayer flake. The monolayers can either be encapsulated only at one side or at both sides. This encapsulation with hBN has further effects on the optical properties, see also section 2.1.4, as it changes the dielectric screening of the monolayer [66]. For example, hBN-encapsulation decreases the bandgap and the exciton binding energy depending on the observed material, while increasing the exciton size [67], and the monolayer gets more robust towards high power densities [61]. In addition, as these layers have an atomically flat surface with low defects, the linewidth narrows approaching 2 meV at low temperatures [72, 73]. Hereby, a high quality of the hBN is crucial, as it directly influences the minimal achievable linewidth, and thus, allows for observing subtle optical and spin-valley properties of the monolayer materials. However, note that the thin layered structure of the samples may result in an oscillatory PL behavior from interference effects due to internal PL reflections [251].
Although all the observed samples are nominally undoped, their specific trion-to-exciton ratio varies, indicating variations in their doping levels, which may have several reasons. On the one hand, exfoliated TMDCs generally have a higher trion-to-exciton ratio, indicating that the fabrication method introduces more doping in the layers than other methods, e.g. via trapped and attached molecules [70]. On the other hand, the exciton-trion ratio varies for encapsulated and non-encapsulated samples, as an encapsulation strengthens the exciton PL and weakens the trion PL, indicating a lower electron doping [74]. Hence, it is of general importance to consider the effect of the dielectric environment on the monolayer emission properties.

4 Optically probing dark excitons via Fano resonances

Semiconductor quantum dots (QDs) open up new opportunities in diverse fields due to their reduced size, leading to restricted electron motion, a discrete electronic structure and size-dependent energy levels [4, 302, 303, 304]. Their tunable physical properties offer applications in different kinds of nanomaterials, e.g., from photovoltaics to lasers, displays and many more. These optical devices that exploit their light absorption and emission properties. Besides, the assembly of QDs into semiconducting solids allows for, e.g., more efficient optoelectronic photodetectors and transistors. Moreover, QDs may be used in quantum computers and quantum communication. In quantum computing, the intrinsic angular momentum or spin of an electron is exploited. Investigating this spin property allows for using semiconducting QDs to store data and perform logic operations; and even coined the term "spintronics" for solid-state quantum information [305, 306]. Specifically, bound electron-hole pairs (excitons) obtain two distinct spin states, which may be used as quantum bits in semiconductor QDs. They realize a coherent two-level system for quantum information processing. Quantum bits in semiconductor QDs show further advantages compared to other solid-state systems such as miniaturization, scalability and integration. Yet, their short radiative lifetime limits the processing of quantum information tasks considerably.

Although much research has been done already, mostly on electron spins in QD ensembles [307, 308], research in this active field still offers new insights useful for quantum information technology. The main point of consideration is to obtain a robust electron spin coherence. Therefore, instead of using the optically active (bright) exciton states, the optically inactive (dark) exciton states obtain lower interaction channels due to their optical inaccessibility. Their significantly longer lifetime opens up for potential applications as extremely long-lived matter quantum bit [309]. It may be addressed optically either via biexcitonic spin-triplet states [310] or (strong) in-plane magnetic-field induced **bright-dark exciton level mixing** in quantum dots [162, 311, 312, 313, 314]. Knowledge about the level hierarchy of bright and dark excitons and their mutual interplay is important for determining their radiative features for diverse applications in optoelectronics, magneto-optics and spintronics. Still, the longer coherence time of the dark exciton may be limited by spin interactions, e.g., electron-nuclear interaction or other spin-nonconserving coupling mechanisms. Specifically, electron-phonon interactions cause a rapid loss of coherence by thermal phonons. However, such interactions may also be exploited to discover unknown interference effects. In this thesis, a novel **Fano-type quantum interference** between the exciton states and a continuum composed of two orthogonally linear-polarized acoustic phonons is identified to deliver optical access to the dark exciton. The interference known as Fano effect [315] was first discovered by G. Breit and E. Wigner [316] and theoretically explained in Rydberg series of autoionized states by U. Fano [317]. Up to now, the Fano effect has been observed in similar systems in which a transition in an electronic continuum interferes with a discrete

phonon transition [318] or in which a discrete phonon transition interferes with a phonon continuum in ordinary Raman spectra [319]. The effect, easily recognizable due to its asymmetric lineshape [315, 317, 320, 321], is exploited in spin filters [322] and transistors [323] using its rapid energy-dependent change of the intensity.

In this thesis, a state-selective excitation and detection of the dark exciton in a QD ensemble coupling to a phonon continuum is shown, which is robust up to a temperature of 60 K. This coupling may be tuned non-linearly and dramatically by an external magnetic field and the optical pumping intensity, which change the visibility of the Fano quantum interference. Hence, the **coupling between the excitonic spin transition and the acoustic phonon continuum** may be probed sensitively by external parameters, which provides a unique method to detect weak couplings of a two-level quantum system. Moreover, the shape of the Fano resonance becomes inverted for specific light-polarization settings and detection energies. This indicates the contribution of either absorbing or emitting phonons. This helicity-dependent switch from a bipolar to a Voigt-like resonance shape allows for distinguishing between the real exciton eigenstates and virtual states, which are not subjected to electron-hole exchange interaction. The virtual states obtain a short lifetime, which strongly reduces the probability of a quantum interference with the phonon continuum. Additionally, the Fano quantum interference reveals a negative exciton interaction for the QD p-shell, where the bright exciton is lowest in energy in the exciton level hierarchy. This surprising finding highlights the importance of gaining access to optically hidden states exposed to external confinement in semiconductor nanostructures. The unusual exciton level hierarchy results in an asymmetry in the magnetic-field dependent shift of the Fano resonance energy. It is explained by the presence of a low-energetic bright exciton, whose orbital wavefunction is compressed by an out-of-plane magnetic field.

The gathered insights of this resonant optical phenomenon associated with Fano-type quantum interferences opens up the way for applications in photonics and nanotechnology [315, 320, 324]. The understanding of this interaction is crucial for a successful design of photonic devices, which are exploited in optical switching and sensing. The observations of this thesis allow for studying optically inactive carrier complexes in semiconductor structures by the spin-phonon Fano effect. Moreover, the results are applicable to other semiconductor systems hosting excitonic excitations. Hence, the discovery of this effect may have far-reaching technological consequences in addition to its scientific significance and novelty.

4.1 Materials and methods

All of the uncharged InGaAs/GaAs QD ensembles presented in section 3.4.1 show Fano-type quantum interference. An overview about their properties (annealing temperature and corresponding energetic position of the photoluminescence maximum) is given in table 3-3. An atomic force microscopy image of such a QD ensemble may be found in figure 3-12 (b). The studied dependencies in the **uncharged InGaAs/GaAs QD ensembles** were strongest in samples 14824-IIb and 14824-Ib with an annealing temperature of 870 °C and 910 °C, respectively. The results presented in this thesis are therefore based on these two samples. Further details on the studied samples may be found in the stated section.

A sample containing a singly charged QD ensemble was studied for comparison in figure 4-19, see also [52]. It was grown by molecular beam epitaxy and annealed at 945 °C. The charging was realized by modulation doping the QD layers with silicon donors, which are located 20 nm below each layer. In total, this sample consists of 20 layers with lens-shaped QDs.

The samples were attached strain-free to a rotation holder in a bath cryostat with a superconducting split-coil magnet, where they were exposed to external magnetic fields up to 10 T and low temperatures down to 1.8 K. They were probed by photoluminescence (PL) spectroscopy (details in section 3.1) and resonant spin-flip scattering (SFS) technique (section 3.2). The resonant optical excitation and detection were performed using the macro-setup (section 3.3.1). The QDs were excited by the light of cw wavelength-tunable dye and Ti:Sapphire lasers with a linewidth < 1 GHz (section 3.3). The laser emission (light energy) was monitored spectrally by an interferometric wavelength meter. Their power (light intensity) was additionally stabilized by a liquid-crystal amplitude modulator providing a laser-light amplitude stabilization of 0.05 %. The QD emission was analyzed by a double monochromator in additive mode (total focal length of 2 m), see section 3.3.3. The widths of the four monochromator slits (entrance/intermediate/intermediate/exit) were typically set to 80/100/100/80 µm yielding a spectral resolution of 2.5 µeV. The spectrometer was equipped with a Peltier-cooled photon-counting detector (photomultiplier tube), see section 3.3.4. The exposure time was typically one second per spectral point. As the efficiency of the GaAs-based detector is energy dependent, particularly for values reaching 1.38 µeV (900 nm), the intensities of the spectra from 1.38 to 1.48 µeV were weighted by the function (3.11). The polarization of the incident and detected light was defined each by a combination of a Glan-Taylor prism and an achromatic quarter-wave retardation plate. The circular polarization of light is denoted by $\sigma^{\pm}$, where the signs $\pm$ are determined by the sign of the photon angular momentum projection on the optical z-axis (light k-vector is parallel to z). The light propagation direction opposite to z is denoted by z'.
Unless specified otherwise, the measurements were performed at a temperature of 6 K in backward scattering geometry. The energy of the incident laser light was tuned to the center of the p-shell QD PL, with a typical power of 30 mW (measured in front of the focusing quartz lens L_L).

Typically, light emission is spectrally characterized by a certain continuous probability distribution. The peaks may appear as normal distribution, Cauchy distribution, or Voigt profile, which is a convolution of both distributions. Thereby, the PL of a single QD is typically a Cauchy distribution and may be modeled by a Lorentzian function. The emission of an ensemble of QDs is typically described by a normal distribution, which may be modeled by a Gaussian. It reflects the influence of homogeneous and inhomogeneous spectral broadening, see section 3.2.2 in the paragraph on linewidth and lineshape. The asymmetric lineshape of the Fano-like quantum interference is a result of the interference between two scattering amplitudes: a continuum of states (background) and an excitation of a discrete state (resonance). This probability distribution is typically modeled via a Breit-Wigner function of the form [325]:

$$f(q,\epsilon) = \frac{2A}{q^2\Gamma_L\pi}\left[\frac{(q+\epsilon)^2}{1+\epsilon^2} - 1\right], \tag{4.1}$$

with the asymmetry factor q, the reduced energy $\epsilon = 2(E - E_{\mathrm{Fano}})/\Gamma_{\mathrm{L}}$ and amplitude A. Therein, the energy E_{Fano} denotes the spectral position of the Fano resonance. It is situated in the center of the resonance, near the inflection point between the extrema, see figure 4-1 for $q \approx 1$. As it depends on the asymmetry of the resonance, it may be shifted fully towards the maximum for $|q| \gg 1$ and towards the minimum for $q \approx 0$, compare figure 4-4.
The Breit-Wigner function from equation (4.1) does not yet include the broadening effect of the QD ensemble, as the Breit-Wigner distribution has a Lorentzian shape [326]. The resonant optical excitation of a QD ensemble with an infinitesimal narrow laser linewidth addresses a larger subensemble of all dots. The spread of this excited QD subensemble is normally distributed [150, 160]. This distribution of (exciton) energies is best described by a Gaussian, as the Gaussian full width at half maximum corresponds to the experimental energy spread [325]. The broadening due to the energy spread is typically described by Voigt line profiles, which may quantify the influences of both Lorentzian and Gaussian contributions in an emission line. The interference with such an inhomogeneously broadened subensemble leads to a Fano resonance profile which deviates significantly from the Breit-Wigner function. Hence, the modeling of Fano resonances is performed via the **Fano profile convolved with a Gaussian function** according to Refs. [325] and [327]. The convolution leads to the expression:

$$f^*(q, E) = \frac{2A\sqrt{\ln 2}}{\Gamma_{\mathrm{G}}\sqrt{\pi}}\{(1 - q^{-2})\Re[w(\kappa)] - \frac{2}{q}\Im[w(\kappa)]\}. \tag{4.2}$$

Here, A denotes the amplitude of the Fano profile function from equation (4.1) and Γ_{G} (Γ_{L}) the full width at half maximum of the Gaussian (Lorentzian) function. The Faddeeva function $w(\kappa) = \exp(-\kappa^2)\,\mathrm{erfc}(-i\kappa)$ is a scaled complex error function with the parameter $\kappa = x + iy$. It consists of $x = 2\sqrt{\ln 2}(E_{\mathrm{Fano}} - E)/\Gamma_{\mathrm{G}}$ and $y = \Gamma_{\mathrm{L}}\sqrt{\ln 2}/\Gamma_{\mathrm{G}}$. The asymmetry of the profile results from the imaginary part $-2/q\Im[w(\kappa)]$. For large asymmetry factors $q \gg 1$, the Fano profile becomes Voigt-shaped. In addition to the convolved Fano profile, the backgrounds of the spectra are fitted by a polynomial function of third order. The values of the background intensity I_{back} are taken from the additive non-energy dependent term of the fit function.

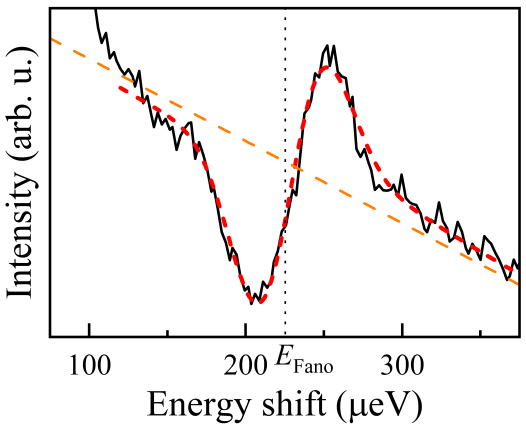

Figure 4-1: Modeling of a Fano resonance spectrum (black) via the Gaussian convolved Fano profile (short-dashed red), shown with polynomial background function (dashed orange). Denoted is the energy shift of the resonance E_{Fano} (dotted line), whose position on the spectrum depends on the asymmetry.

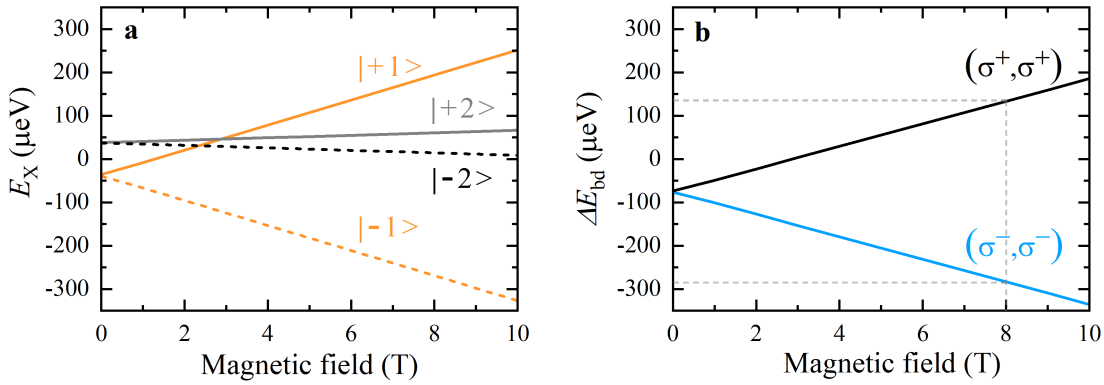

Figure 4-2: Magnetic field dependence of (a) the exciton fine structure and (b) the respective bright-dark-exciton energy difference ΔE_{bd} in Faraday geometry ($\vec{B} \parallel \vec{z}$). The energy difference between the transition $|+1\rangle \rightarrow |+2\rangle$ is displayed in black, the transition $|-1\rangle \rightarrow |-2\rangle$ in blue. The dashed line indicates the energy shifts at $B = 8\,\mathrm{T}$.

4.2 Theoretical expectations

An empty (uncharged) QD is excited resonantly with circularly polarized laser light by a single photon. Thereby, an electron is lifted from the VB to the CB, and a hole is left behind in the VB. The photon transfers its energy and angular momentum to this electron-hole pair. The electron and the hole are attracted into a bound state due to Coulomb interaction, so that a neutral exciton (X) is formed. As explained in section 3.2.2 and depicted in figure 3-3, the respective electric-dipole transition is given by the transition from the exciton ground state $|0\rangle$ to the excited exciton states $|\pm 1\rangle$ using $\sigma^{\pm}$ circular-polarized light. The exciton states in III-V semiconductor QDs are formed by an electron and a heavy hole with opposite spin orientations in the configuration $|+1\rangle = |-1/2; +3/2\rangle$ or $|-1\rangle = |+1/2; -3/2\rangle$. They are known as bright exciton states, as they may be excited from the ground state via an electric-dipole allowed transition (radiatively or optically active). Besides, two further exciton states with parallel spin orientations are possible: $|+2\rangle = |+1/2; +3/2\rangle$ or $|-2\rangle = |-1/2; -3/2\rangle$. However, these exciton states cannot be excited from the QD ground state, they are denoted as dark (optically inactive). Such a transition would imply a transfer of an angular momentum of $\Delta j = \pm 2$, which is not realized by a photon with an angular momentum of only $j = \pm 1$. Hence, when the electron (or the hole, respectively) in the bright exciton flips its spin, the recombination of this exciton is electric-dipole forbidden. Moreover, the exciton's electron spin-flip scattering cannot be accessed directly, and neither its spin splitting; the electron spin is also optically inaccessible [328].

The bright and dark exciton states form the **exciton fine structure**. The splitting between the exciton doublets, the fine structure splitting, is caused by the electron-hole exchange interaction, which couples the spins of electron and hole, and is affected by the Zeeman interaction with an (internal or external) magnetic field [96]. The exchange interaction, which defines the hierarchy of the exciton energy levels, may be divided into a short-range and a long-range part [92, 329]. The short-range, isotropic part is responsible for the splitting into bright and dark states, while the long-range part splits the bright states in asymmetric QDs and also contributes, to a small extend, to the **bright-dark splitting**. Typically, the dark exciton is lower in energy than the bright

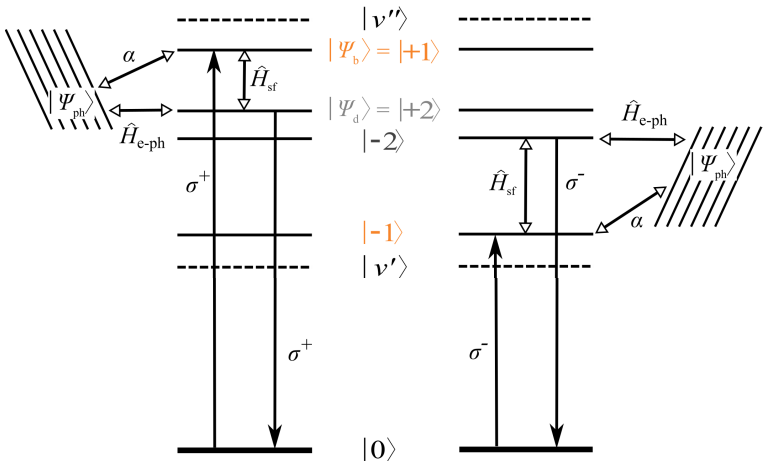

Figure 4-3: Scheme of the spin-phonon Fano resonance with scattering mechanism for σ^+-(left) and σ^--(right) polarized excitation for $B > 2.9\,\mathrm{T}$. The virtual intermediate states are denoted with $|v\rangle$.

exciton. This impedes separate electron or hole spin flips, which would cause a transition to a higher-energetic state. A less probable spin-flip probability and solely non-radiative decay channels lead to a significantly longer lifetime of the dark exciton [330]. The Zeeman interaction denotes the splitting of states into several components under a static magnetic field due to their different associated magnetic dipole moments. The energies of the bright (b) and dark (d) exciton states in dependence of a magnetic field are calculated by adding the electron-hole exchange Hamiltonian (equation (2.16)) to the electron and hole Zeeman Hamiltonians (equation (2.19)). Using the simplifications from [96, 331], the energies of the exciton states are:

$$E_{\mathrm{X},\pm1} = \frac{1}{2}\left(+\delta_0 \pm \sqrt{\delta_\mathrm{b}^2 + E_{\mathrm{Z},1}^2}\right), \quad E_{\mathrm{X},\pm2} = \frac{1}{2}\left(-\delta_0 \pm \sqrt{\delta_\mathrm{d}^2 + E_{\mathrm{Z},2}^2}\right). \tag{4.3}$$

The resulting magnetic field dependence of the fine-structure splitting is presented in figure 4-2 (a). Note that the bandgap and binding energies are neglected, since they are similar for both exciton states. The splitting δ_0 between the bright and dark X is negative and set to $-75\,\mu\mathrm{eV}$ based on the experimental data. Moreover, the bright (dark) X doublets are split at zero magnetic field due to anisotropic electron-hole exchange, which is estimated to $\delta_\mathrm{b} = 4\,\mu\mathrm{eV}$ ($\delta_\mathrm{d} = 1\,\mu\mathrm{eV}$) [160, 332, 333]. The Zeeman (Z) energy

$$E_{\mathrm{Z},i} = \mu_\mathrm{B}\left(g_{\mathrm{hh},z} - (-1)^i g_{\mathrm{e},z}\right) B \tag{4.4}$$

induces a splitting between the two bright and the two dark exciton states [331, 334], compare equation (2.22) for the splitting of the electron spin eigenstates. Therein, the external magnetic field $\vec{B}$ is applied along the QD growth axis $\vec{z}$. The Zeeman energy consists of the Bohr magneton μ_B, the absolute value $i = 1, 2$ of the excitonic total angular momentum, the strength B of the magnetic field along $\vec{z}$ and the longitudinal g-factors g_z of the electron (e) and heavy hole (hh) with $g_{\mathrm{e},z} = -0.55$ and $g_{\mathrm{hh},z} = -0.45$ [52, 160]. The **energies evolve asymmetrically with magnetic field** relative to $E_\mathrm{X} = 0$ due to their nonzero exchange constants. This results in an asymmetric energy difference evolution for the electron spin-flip transition from $|+1\rangle$ to $|+2\rangle$ via σ^+-polarized light (or from $|-1\rangle$ to $|-2\rangle$ via σ^--polarized light). As seen in figure 4-2 (b), the respective energy differences ΔE amount to about $\Delta E_{\mathrm{bd}+} = E_{\mathrm{X},+1} - E_{\mathrm{X},+2} = +135\,\mu\mathrm{eV}$ and $\Delta E_{\mathrm{bd}-} = E_{\mathrm{X},-1} - E_{\mathrm{X},-2} = -285\,\mu\mathrm{eV}$ at $B = 8\,\mathrm{T}$.

As explained in section 3.2.2, the recombination of the dark exciton becomes allowed for

any perturbation lowering the symmetry of the states; specifically, for any mechanism that mixes the optically bright with the dark states. Possible admixture mechanisms are a reduced symmetry of the exciton via, e.g. an oblique magnetic field which mixes the electron spin states [162, 311, 312, 313, 314, 335, 336], or an application of stress which mixes the hh and lh states with nonzero orbital angular momentum [337, 338]. However, the results of this thesis reveal a mechanism which maintains the symmetry of the exciton while providing optical access to properties of the dark exciton: a novel Fano-type quantum interference. Moreover, this quantum inference allows for distinguishing between virtual and real exciton states present in the QD ensemble. The virtual intermediate scattering states $|v\rangle$ obtain a very short lifetime, which strongly reduces the probability of a quantum interference with the phonon continuum. The proposed mechanism bases on the **resonant interference between the electron spin transition**, from the bright $|\Psi_\mathrm{b}\rangle$ to the dark $|\Psi_\mathrm{d}\rangle$ exciton state, **and a pair of polarized acoustic phonon modes**. A scheme displaying this interaction for both circularly polarized excitations is shown in figure 4-3. Therein, the wavefunction of the two-phonon continuum is denoted as Ψ_ph with the eigenvalue E_ph. The states interact via the electron spin-flip Hamiltonian $\hat{H}_\mathrm{sf}$, the electron-phonon interaction Hamiltonian $H_\text{e-ph}$ and the polarizability tensor operator α. The physical origin of this interference is a cancellation of the scattering amplitude and the formation of a coupled mode. The resulting amplitude of the scattering process from $|\Psi_\mathrm{b}\rangle$ to $|\Psi_\mathrm{d}\rangle$, denoting the coupled discrete-plus-continuum state, may be calculated via the transition matrix element [319, 339]:

$$\langle\Psi_\mathrm{d}|\,\hat{T}_\mathrm{Fano}\,|\Psi_\mathrm{b}\rangle = \frac{\Big[W\,\langle\Psi_\mathrm{d,0}|\,\hat{H}_\mathrm{sf}\,|\Psi_\mathrm{b}\rangle + (E - E_\mathrm{res} - F)\,\langle\Psi_\mathrm{ph}|\,\alpha\,|\Psi_\mathrm{b}\rangle\Big]}{[(E - E_\mathrm{res} - F)^2 + (\pi|W|^2)^2\,]^{1/2}}. \tag{4.5}$$

Hereby, $W = \langle\Psi_\mathrm{d,0}|\,H_\text{e-ph}\,|\Psi_\mathrm{ph}\rangle$ indicates the transition rate between the unperturbed dark exciton state (the discrete state) and the two-phonon continuum via electron-phonon interaction. The operator $\hat{T}_\mathrm{Fano}$ represents the transition operator between the initial state $|\Psi_\mathrm{b}\rangle$ and the final state $|\Psi_\mathrm{d}\rangle$ [317, 319]. Moreover, the unperturbed dark exciton state $|\Psi_\mathrm{d,0}\rangle$ is perturbed by the coupling to the pair of acoustic phonons which causes a lineshift of the resonance position E_res by the value F. It denotes the resonance level shift resulting from the interaction with the continuum [340]. Depending on the magnitude of the interactions, the level shift F may be negligibly small [341, 342]. When passing through resonance at $E = E_\mathrm{res} + F$, there is a sharp variation of the transition matrix element, and with it of the scattering amplitude. In the studied Fano-type interference, the resonance occurs at $E = \Delta E_\mathrm{bd}$ which matches the continuum energy of the phonons E_ph. To understand the effect of this variation on the scattering lineshape, two new functions for the reduced energy variable ϵ and the asymmetry factor q are defined:

$$\epsilon = \frac{E - E_\mathrm{res} - F}{\pi|W|^2} \quad \text{and} \quad q = \frac{\langle\Psi_\mathrm{d,0}|\,\hat{H}_\mathrm{sf}\,|\Psi_\mathrm{b}\rangle}{\pi W\,\langle\Psi_\mathrm{ph}|\,\alpha\,|\Psi_\mathrm{b}\rangle} = \cot\zeta. \tag{4.6}$$

The asymmetry factor q relates to the phase shift ζ of the continuum. Thereby, the ratio of the transition probability to the final dark exciton state and that to the continuum follows a family of curves of the form $f(q,\epsilon) = (q+\epsilon)^2/(1+\epsilon^2)$ [317] by comparison of their scattering cross sections, see figure 4-4 and equation (4.1).
As indicated in section 4.1, the Fano resonance profile $f(q,\epsilon)$ strongly varies with the asymmetry factor q (see figure 4-4). For values $|q|$ around 1 ($\zeta = \pi/4$ or $3\pi/4$), the

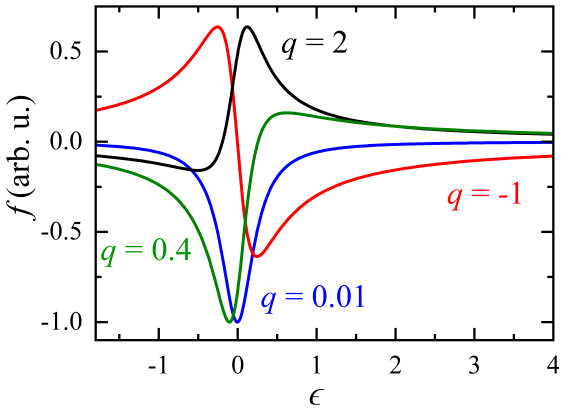

Figure 4-4: Fano profiles $f(q, \epsilon)$ calculated for different asymmetry factors q. The profiles for $q < 1$ are normalized to -1.

typical asymmetric resonance is visible, indicating a coupling between discrete state and continuum. Hereby, the interaction of the discrete state with the continuum distorts the lineshape and causes the transition probability to pass through zero relative to the superimposed continuum [319, 339]. Note that the profile is reversed when the sign of q is changed. For $|q| \gg 1$ ($\zeta \to 0$ or 1), no coupling to the continuum is present. Thus, the profile becomes a symmetric Lorentzian function and the width $\Gamma = 2\pi|W^2|$ of the resonance reflects the natural linewidth of the perturbed discrete state. As W is determined by the transition rate between the uncoupled dark state and the phonon continuum, the resonance profile has zero width ($\Gamma \to 0$) when the dark exciton state does not couple to the continuum and has infinite lifetime. Thus, for $q \approx 0$ ($\zeta = \pi/2$) no coupling to the discrete state is present, leading to a symmetric quasi-Lorentzian antiresonance (AR) in the continuum spectrum [315].

The continuum that couples to the discrete dark exciton state consists of a pair of acoustic phonons. These phonons have to fulfill **three requirements** regarding their polarization, total energy and spatial distribution of their wavefunction probability to account for the background process of the resonant Fano interference. First, regarding the **polarization**, the whole scattering process follows the selection rules from angular momentum conservation. Hence, when the electron flips its spin from bright to dark exciton state, an angular momentum of $\Delta j = \pm 1$ has to be transferred. The corresponding angular momentum may be transferred either by a circularly polarized phonon or by **two transverse acoustic phonons** which are orthogonally linear-polarized with a phase shift relative to their polarization directions [343]. Circularly polarized or circularly rotating chiral phonons, as e.g. in TMDCs [217, 344], describe nondegenerate modes, in which the motion of the ions along the mode eigenvectors is intrinsically circular. In contrast, the magnetic moment of a general elliptically polarized phonon mode is a superposition of two orthogonal linearly polarized phonon modes that shows a circular motion. The participation of a circular-polarized phonon in the Fano resonance is neglected in the following, as in GaAs-based structures the phonons are spin-zero quasi-particles (magnetic moment $\vec{\mu} \approx 0$) [345]. In the case of two transverse phonons, they contribute each by $\frac{1}{\sqrt{2}}(|H\rangle \pm i\,|V\rangle)$ to the superposition state $|\Psi_{\mathrm{ph}}\rangle$ with total angular momentum of ± 1. Their single wavevectors are no longer restricted to the zone center, so that their spectra may be a broad continuum determined by their joint density of states.
Second, the **total energy of both phonons must match the transition energy**, which ranges from tens of µeV ($B = 0\,\mathrm{T}$) to about 300 µeV ($B = 10\,\mathrm{T}$). The two acoustic phonons are coupled by an anharmonic potential, which is based either on the

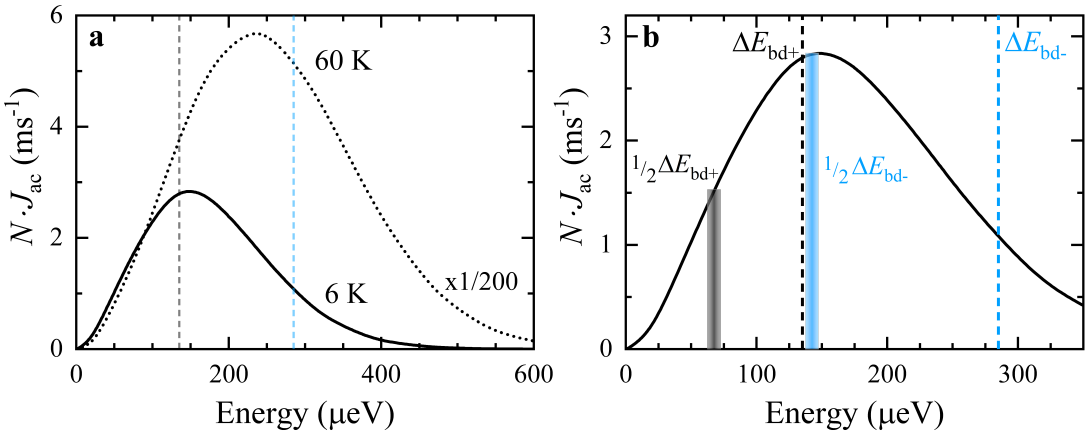

Figure 4-5: (a) Weighted spectral density of the transverse acoustic phonons confined in InGaAs QDs shown with bright-dark-exciton energy difference $\Delta E_{\mathrm{bd}\pm}$ between the transitions $|+1\rangle \rightarrow |+2\rangle$ (dashed black) and $|-1\rangle \rightarrow |-2\rangle$ (dashed blue) at $B = 8\,\mathrm{T}$ for $T = 6\,\mathrm{K}$ (solid) and $T = 60\,\mathrm{K}$ (dotted). (b) Low-temperature distribution with additional broadened lines indicating the phonon energies E_{ac} with highest probability at about half the respective energy differences.

deformation or piezoelectric potential [79]. Typically, the deformation potential coupling is dominant in such QDs due to the large electron-hole overlap, which strongly reduces all polar interaction mechanisms [202, 229]. Yet, the deformation potential coupling couples only to LA phonons, while the piezoelectric potential couples to both LA and TA phonons [346] and is dominant for small energy splittings ($< 0.5\,\mathrm{meV}$) [347]. The restriction to transverse acoustic phonons is supported by the fact that these phonons contribute dominantly to the spectral density in the region of very low energies [348]; besides that, longitudinal phonons do not fulfill the requirement regarding the angular momentum transfer as explained in the first point. The two acoustic phonons create the background continuum [319, 349, 350]. Therein, the same final continuum level, matching the energy range of the bright-to-dark exciton transition, may result from different combinations of phonon modes. Due to the anharmonic interaction, the phonons in the continuum become mixed with a higher probability when their energies are similar [351]. Specifically, when **each phonon energy is equal to half of the transition energy**: $E_{\mathrm{ac}} = {}^1/_2\Delta E_{\mathrm{bd}\pm}$. The spectral density J_{ac} of the acoustic phonons may be estimated by the expression [233]:

$$J_{\mathrm{ac}}(E) = AE^3 \exp(-E^2/E_c^2), \quad \text{with} \quad A = E_{\mathrm{piezo}}^2/(4\pi^2\rho\,\hbar^4 v_{\mathrm{T}}^5). \tag{4.7}$$

Herein, E_{piezo} denotes the piezoelectric coupling energy, $\rho = 5350\,\mathrm{kg\,m^{-3}}$ the mass density of InGaAs [352], and $v_{\mathrm{T}} = 3290\,\mathrm{m\,s^{-1}}$ the sound velocity of the transverse acoustic phonons [353, 354]. The low-energy (cut-off) bound $E_c = \sqrt{2}\hbar v_{\mathrm{TA}}/a_{\mathrm{loc}}$ of the acoustic phonon-mode spectrum depends on the carrier localization length a_{loc} of the nanostructure [355, 356]. For spherical QDs with $a_{\mathrm{loc}} = D$, the cut-off energy is estimated to $E_c \approx 150\,\mu\mathrm{eV}$ for a size of $D = 20\,\mathrm{nm}$. It indicates the maximum of the spectral density function, where the phonons bear the major impact on the carrier dynamics [233]. The temperature dependence of the spectral density distribution J_{ac} is taken into account by the thermal occupation number $N(E,T) = 1/\{\exp[-E/(k_{\mathrm{B}}T)] - 1\}$ [357]. In figure 4-5, two weighted spectral density distributions $N(E,T)J_{\mathrm{ac}}$ are shown exemplary for a low and high temperature. The distribution for high temperature is significantly larger and

its maximum is shifted to higher energies. Each distribution covers a certain range, which fits with the energy difference between the dark and bright excitons. Hence, the acoustic phonon pairs fulfill the criterion $2E_{\mathrm{ac}} = \Delta E_{\mathrm{bd}\pm}$. This allows for establishing the continuum process in the Fano-like quantum interference. However, although the spectral density J_{ac} rises and broadens for higher temperatures, the shift of the distribution towards higher energies lowers the probability of matching phonon pairs. Only a smaller number of phonons obtains the fitting energy to participate in the Fano resonance at higher temperatures.

The third point regards the **spatial distribution of the wavefunction probability** of the phonons. The phonon wavefunction directly affects the interaction matrix element and, thereby, the scattering rate [358]. The interaction between phonons and electron is strongest when their wavefunction probability distributions overlap spatially. Hence, it is important to determine the electron and phonons' wavefunctions in dependence of the QD characteristics. In the studied InGaAs/GaAs QDs, the acoustic phonons behave mostly bulk-like, as the acoustic mismatch between the QD and the barrier/wetting layer materials is small [201]. The specific acoustic impedances are determined by the mass density ρ times the sound velocity v_{g} of the materials [359]. Both the mass densities ($\rho_{\mathrm{InGaAs}} = 5350\,\mathrm{kg/m^3}$ and $\rho_{\mathrm{GaAs}} = 5310\,\mathrm{kg/m^3}$) [233, 352, 360] as well as the longitudinal ($v_{\mathrm{L,InGaAs}} = 4670\,\mathrm{m/s}$ and $v_{\mathrm{L,GaAs}} = 4770\,\mathrm{m/s}$) and transversal ($v_{\mathrm{T,InGaAs}} = 3290\,\mathrm{m/s}$ and $v_{\mathrm{T,GaAs}} = 3368\,\mathrm{m/s}$) sound velocities are comparable to each other [353, 354, 361]. Thereby, the QD composition is assumed to consist of $\mathrm{In_{0.10}Ga_{0.90}As}$. Hence, the acoustic phonons, or rather the acoustic displacement field, are seen as delocalized as the resulting acoustic impedances of the QD and the surrounding material are similar. Accordingly, acoustic waves are extended over distances which exceed the QD size and the average space between the QDs.

Hitherto, the phonons in semiconductor QDs have been treated as phonons in infinite bulk. However, the carrier-phonon interaction may be different for bulk phonons than for phonon modes in confined structures. For example, confined phonon modes may be reflected at the surfaces of the nanostructure, which leads to a partial mode conversion between longitudinal and transverse phonons, so that the phonon modes cannot strictly be classified [362]. Besides, surface phonons are concentrated close to the surfaces, leading to mixed modes that behave surface mode-like in their longitudinal component and bulk mode-like in their transverse component [362]. Hence, the spatial characteristics of phonons in semiconductor QDs may be studied further by modeling the QDs as nanospheres embedded in an elastic medium. The approach follows Lamb's elastic theory of a homogeneous free sphere [363]. In this way, the bulk phonon properties may be modified to reflect the confinement of the nanostructure, including strain [364]. However, note that the electron-acoustic phonon coupling function resembles the phonons in an infinite bulk (under finite strain) superimposed by a complex fine structure rather than resembling fully confined phonons [362, 364]. Lamb's model describes the frequency shift and damping of acoustic vibrations as well as the (de)localization of the associated displacement field [266]. The acoustic-phonon displacement field $\boldsymbol{u}_{l,n}$ results from Navier's equation

$$\rho \frac{\partial^2 \boldsymbol{u}_{l,n}}{\partial t^2} = (\lambda_{\mathrm{L}} + \mu_{\mathrm{L}}) \nabla (\nabla \boldsymbol{u}_{l,n}) + \mu_{\mathrm{L}} \nabla^2 \boldsymbol{u}_{l,n}, \tag{4.8}$$

which is the vector equation of equilibrium in linear elasticity with no body forces [266, 365]. Therein, the vibrational modes are described by the radial quantum number n and orbital quantum number l. The Lamé coefficients λ_{L} and μ_{L} also define the longitudinal

and transversal sound velocities: $v_{\mathrm{L}} = \sqrt{(2\mu_{\mathrm{L}} + \lambda_{\mathrm{L}})/\rho}$ and $v_{\mathrm{T}} = \sqrt{\mu_{\mathrm{L}}/\rho}$ [366]. The Navier equation is solved by introducing a scalar potential and a vector potential involving spherical harmonics $Y_{l,m}(\theta, \phi)$, with the azimuthal quantization number $m_l \leq l$, and first-order spherical Bessel functions $j_l(k_n r)$ [266, 367, 368]. This leads to the phonon wavefunction being defined by $\Psi_{l,m}(k_n r) = j_l(k_n r) Y_{l,m}(\theta, \phi)$, with the position vector r. The quantized phonon wavevector k_n may be expressed by ω/v_{L} or ω/v_{T}. Since the phonon eigenenergies are degenerate in m_l [369], only the quantum numbers n and l have to be considered [370], and m_l is set to zero. The lowest-energy, fundamental mode of an acoustic phonon with transverse character is characterized by the radial quantum number $n = 1$ and by the orbital quantum number $l = 0$ [266, 370], which gives the acoustic phonon wavefunction:

$$\Psi_{00}(k_1 r) = j_0(k_1 r) Y_{00}(\theta, \phi) = \sqrt{\frac{1}{4\pi}} \frac{\sin(k_1 r)}{k_1 r}. \tag{4.9}$$

The wavefunction of the first-excited phonon mode with $n = 1$ and $l = 1$ is given by:

$$\Psi_{10}(k_1 r) = j_1(k_1 r) Y_{10}(\theta, \phi) = \sqrt{\frac{3}{4\pi}} \left[\frac{\sin(k_1 r)}{(k_1 r)^2} - \frac{\cos(k_1 r)}{k_1 r} \right] \cos\theta. \tag{4.10}$$

The electron's wavefunction probability distributions may be determined similarly, see [32, 46]. While the electron and phonon wavefunctions differ in their normalization factors particularly, their resulting shapes, depending on the spatial and angular coordinates, are very similar. Specifically, the phonon wavefunctions in equations (4.9) and (4.10) are similar to the wavefunctions of s- and p-shell electrons confined in QDs, respectively, [371, 372, 373].

The probability distributions $|\Psi_{l,m}|^2$ of the acoustic phonon and electron wavefunctions are shown in figure 4-6 for the modes with (a) $l = 0$ and (b) $l = 1$. These modes are described by spherical Bessel functions, compare section 2.1.2 on QDs with spherical confinement. The fundamental mode Ψ_{00} in (a) is described by a radial-symmetric Bessel distribution (zeroth spherical Bessel function), which is nonzero at the center. Its shape corresponds to the lowest-energetic transversal acoustic phonon mode with $l = 0$ and to the electronic s-shell. The first-excited mode in (b) yields a dipolar-like distribution (first spherical Bessel function) with the wavefunction probability tending to zero at the center of the x-y-plane. This applies to the wavefunction probabilities of all higher modes. The $l = 1$ mode and higher modes possess maxima away from the center, whereas the fundamental mode possesses a maximum in the QD center. Correspondingly, the shape of the mode Ψ_{10} correlates to the transversal acoustic phonon mode with $l = 1$ as well as to the electronic p-shell. In real QDs, the widths and heights of the probability densities of the acoustic phonons and electrons may change due to different elongations in the in-plane directions and distribution alignments along the z-direction. These depend on the composition profile as well as the dot size and shape and may lead to differently strong localized phonons and electrons within the QDs. A cross section of the radial distribution of the respective relevant squared phonon and electron wavefunction distributions is shown in figure 4-6 (c), visualizing their overlap. Therein, neither longitudinal phonon modes nor the transverse acoustic phonon mode with $l = 0$ are displayed, since they do not fulfill the requirement regarding the polarization (no angular momentum transfer of $\Delta j = \pm 1$ possible) [374]. As outlined, the transfer of angular momentum is only possible by transversal phonons which are orthogonally linear-polarized with a phase

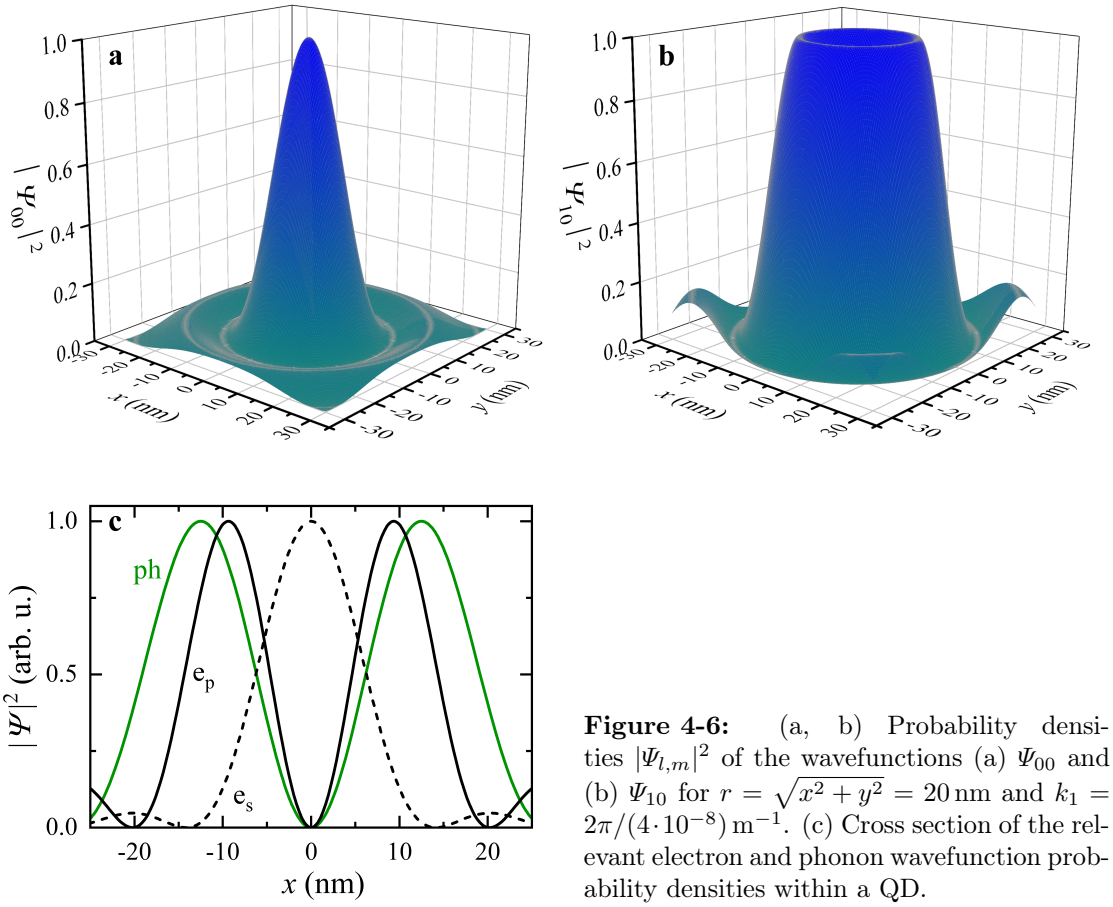

Figure 4-6: (a, b) Probability densities $|\Psi_{l,m}|^2$ of the wavefunctions (a) Ψ_{00} and (b) Ψ_{10} for $r = \sqrt{x^2 + y^2} = 20\,\mathrm{nm}$ and $k_1 = 2\pi/(4 \cdot 10^{-8})\,\mathrm{m}^{-1}$. (c) Cross section of the relevant electron and phonon wavefunction probability densities within a QD.

shift relative to their polarization directions, e.g., transverse acoustic phonons with $l = 1$ or higher. The **phonons with l = 1** obtain a **dipolar-shaped** probability distribution ($|\Psi_{10}|^2$) like the **p-shell electron** ($|\Psi_{\mathrm{e,p}}|^2$), leading to a **high wavefunction probability distributions overlap** in comparison to the s-shell electron ($|\Psi_{\mathrm{e,s}}|^2$). As the transverse acoustic phonons and the electron interact with each other more strongly when their wavefunction probability distributions overlap [358, 375, 376], the Fano-like quantum interference is expected to appear, in particular, for resonantly addressing excitons with p-orbital electrons. Moreover, note that, although excitons also consist of (heavy) holes with $l = 1$, these holes do not contribute to the scattering process, as can be ruled out from the measured polarization configuration, see e.g., figure 4-13 in comparison to figure 3-4.

To sum up, the acoustic phonons which form the continuum that couples to the discrete dark exciton state has to fulfill three requirements: first, the continuum is formed by a phase-shifted phonon pair so that they may transfer an angular momentum of ± 1. Second, their total energy must match the transition energy, which is more likely for phonons with half energy each due to their anharmonic potential coupling and at low temperatures due to the overall small energy of the electron spin transition. Third, the coupling between bright and dark exciton states, mediated by acoustic phonons, is highest for matching overlaps of the wavefunction probabilities. As the spatial distribution of the transversal phonons' wavefunction probability is approximately similar to the dipolar-like distributions of the p-shell electrons, the coupling is most probable for the wavefunction distributions of the p-shell or higher shells.

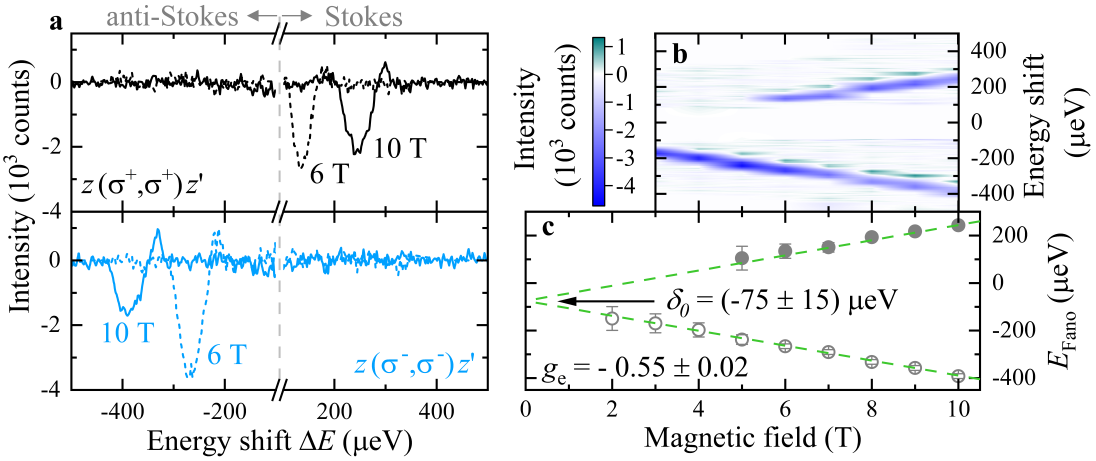

Figure 4-7: Magnetic field dependences of the Fano AR in Faraday geometry for resonant p-shell excitation. (a) Background subtracted spectra for two different magnetic fields. (b) Spectral magnetic field dependence. (c) Fitted magnetic field dependence. The closed (open) circles denote the spectral positions of E_{Fano} on the Stokes (anti-Stokes) side.

4.3 Probing dark excitons and negative exchange energy in polarized QD emission spectra

The presented requirements in the previous section lead to the conclusion that quantum dots (QDs), as semiconductor nanostructures with strong spatial confinement and atom-like level structure, are ideal candidates to observe Fano-like quantum interferences. In fact, the interaction of such a discrete level with a broad continuum via Fano resonance has been observed before [315, 320, 377], whereas these systems shows substantial differences regarding the participating (quasi-)particles (e.g. pure phonon interaction, electronic background). Here, such a Fano resonance is studied in an undoped and rapidly thermally annealed ensemble of InGaAs/GaAs QDs. As explained in section 3.4.1, rapid annealing of the QDs allows for tuning the QD emission energy and reduces the defect density. The exciton emission of the studied QD ensemble at $T = 6\,\mathrm{K}$ is shown in figure 4-8. Besides the energetically lowest s-shell, higher shells also contribute to the emission due to shell filling with photocarriers generated in the wetting layer. By tuning the excitation energy E_{exc} through the ensemble, excitons in different shells of the emission are probed as well as QDs of different sizes in the specific shells. The different shells (s-, p-, d- and f-shell) within the photoluminescence (PL) band are indicated by Gaussian fits (dashed lines). Besides, note that the bandwidth of the laser is very narrow, approximately $4\,\mu\mathrm{eV}$, and, hence, only a small fraction of QDs is excited.
In figure 4-7 (a), exemplary spectra with subtracted background of a resonant excitation of the p-shell at $E_{\mathrm{exc}} = 1.4571\,\mathrm{eV}$ is shown, with a spectral range of $\pm 500\,\mu\mathrm{eV}$. The spectral positions in such inelastically scattered light spectra are specified with respect to the excitation energy E_{exc} so that the energy shift $\Delta E = E_{\mathrm{exc}} - E_{\mathrm{signal}}$ is used for data presentation. By this definition, higher energetic scattered light has a negative sign, correspondingly to anti-Stokes processes in Raman scattering where energy is absorbed. In contrast, Stokes processes correlate to positive energy shifts, where energy is emitted. With an external magnetic field applied along the QD growth axis $\vec{z}$ (Faraday geometry), no exciton emission is observed: neither emission of the bright exciton resonance

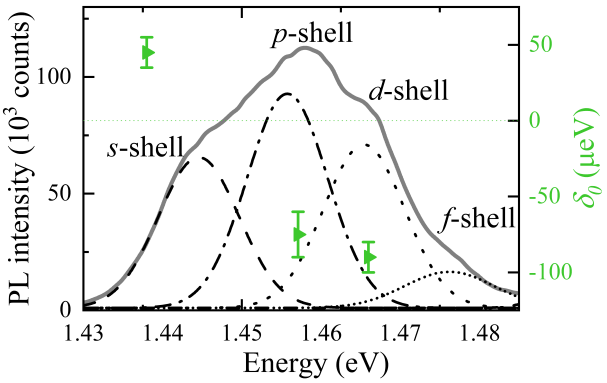

Figure 4-8: Photoluminescence of the undoped InGaAs QD ensemble excited at 1.533 eV at 6 K and dependence of δ_0 on the excitation energy. The zero-field offset δ_0 is obtained for exciting excitons at different QD shells. The data were measured in a tilted geometry with $\theta = 30°$ to allow for evaluating δ_0 at the s-shell. The dotted green horizontal line serves as a guide to the eye.

nor a spin-flip line based on virtual intermediate scattering states. The exciton emission resulting from single charge-carrier spin flips in this longitudinal magnetic field and polarization configuration is forbidden by the selection rules in the electric-dipole approximation, as explained in section 3.2.2. However, clear **Fano antiresonances** (ARs) with asymmetry factors of $q \leq 0.1$ are present. These ARs are observable at both sides of the laser line: on the low-energetic side with $E_{\text{Fano,+}}$ for $\Delta E > 0$ (Stokes) and on the high-energetic side with $E_{\text{Fano,-}}$ for $\Delta E < 0$ (anti-Stokes). The ARs are observable **only in a specific polarization configuration**: when the circular polarization of the incident laser light is equal to that of the emission, see also figure 4-13 (a). For $z(\sigma^+,\sigma^+)z'$ polarization configuration, the Fano AR is at the Stokes side. This hints at the excitation of the bright $|+1\rangle$ p-shell exciton, while the **AR denotes the dark $|+2\rangle$ exciton state**, representing the Fano-like quantum interference. The scheme belonging to the interference is depicted in figure 4-3 (left), with the Stokes process (left) and the anti-Stokes process (right). The Fano AR is at the anti-Stokes side for $z(\sigma^-,\sigma^-)z'$, where it displays the dark $|-2\rangle$ exciton state. Thereby, the bright $|-1\rangle$ p-shell exciton is excited. This behavior indicates two important aspects: first, the dark exciton state $|+2\rangle$ ($|-2\rangle$) participate in the optical process with σ^+ (σ^-) co-circularly polarized configuration. Second, the **bright $|-1\rangle$ exciton is the energetically lowest state in the p-shell**. These aspects, the access to the dark exciton as well as the exciton level hierarchy, manifest in distinct polarization selection rules.

When changing the external magnetic field strength, the spectral positions of the Fano ARs shift, as depicted exemplarily for $B = 6\,\text{T}$ and $B = 10\,\text{T}$ in figure 4-7 (a). A detailed **magnetic field dependence** is shown in figure 4-7 (b) and the spectral positions $E_{\text{Fano}}(B)$ as a function of the magnetic field B are presented in (c). Therein, $E_{\text{Fano,+}}$ at the Stokes side equals the bright-dark-exciton energy difference $\Delta E_{\text{bd+}} = E_{\text{X},+1} - E_{\text{X},+2}$, while $\Delta E_{\text{bd-}} = E_{\text{X},-1} - E_{\text{X},-2}$ equals $E_{\text{Fano,-}}$ at the anti-Stokes side, in agreement with figure 4-2 (b). Note that the widths of the Fano ARs slightly broadens with magnetic field, which is due to the increasing dispersion of the electron and hole g-factors for higher magnetic fields. The spectral position of the Fano ARs both shift with a linear slope of about $|E_{\text{Z},i}/B| = (32 \pm 1)\,\mu\text{eV/T}$. The slope indicates the energy difference between bright and dark exciton by the electron Zeeman splitting and corresponds to an absolute in-plane g-factor of 0.55 ± 0.02. The value is characteristic for the **electron spin splitting** in InGaAs/GaAs QDs [52, 160]. However, the absolute spectral positions of the Stokes and anti-Stokes Fano ARs do not match: they deviate significantly in energy from each other by, e.g., $|E_{\text{Fano,+}}| = 250\,\mu\text{eV}$ to $|E_{\text{Fano,-}}| = 390\,\mu\text{eV}$ at $B = 10\,\text{T}$. Using a linear estimation (dashed line in figure 4-7 (c)), the deviation at $B = 0\,\text{T}$ equals

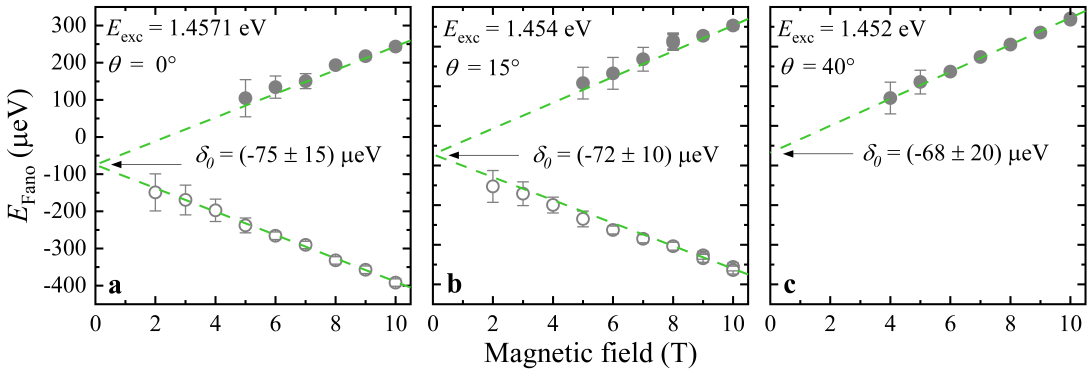

Figure 4-9: Magnetic field dependence of the spectral positions of the Fano ARs excited at (a) 1.45 eV and 0°. The energies of the bipolar Fano resonances as function of B are shown measured at (b) 15° and (c) 40°. The temperature was set to 6 K, while the laser power was 30 mW. The closed (open) circles denote the spectral positions of E_{Fano} on the Stokes (anti-Stokes) side.

(-75 ± 15) µeV. This **zero-field offset** corresponds to the axially symmetric part δ_0 of the exchange interaction between bright and dark excitons (see equation (4.3)). The negative sign of the offset determines an exciton fine structure with the optically bright $|-1\rangle$ exciton as energetically lowest state, fairly different from typical exciton fine structures [96].

The **sign and value** of δ_0 significantly **depend on the excitation energy**, as presented in figure 4-8. While the exciton exchange energy $\delta_0 = (-85 \pm 15)$ µeV at the energetically higher d-shell is similar to the value at the p-shell, it becomes positive for excitation at the lowest QD shell, the s-shell: $\delta_0 = (+45 \pm 10)$ µeV at $E_{\mathrm{exc}} = 1.438$ eV. It indicates that the **level hierarchy** of the bright and dark excitons **is reversed**. The dark exciton is energetically lowest only at the s-shell, while for higher shells the bright exciton is the energetically lowest state. Furthermore, figure 4-8 includes the photoluminescence of the InGaAs QD ensemble detected at 6 K under wetting-layer excitation. The different QD shells are indicated by Gaussian fit function curves; the energy splitting between the QD shells is about 15 meV. The zero-field offsets δ_0 are obtained for resonantly exciting the excitons at the different shells of the QDs by tuning the laser energy. Contrastingly, the sign and value of δ_0 vary only negligibly with the magnetic field alignment. When addressing the p-shell excitons, the exciton exchange energy $\delta_0 = -70$ µeV (extrapolated linearly from $E_{\mathrm{Fano}}(B)$) remains practically constant for tilting the magnetic direction with respect to the QD growth axis. This dependence is shown in figure 4-9 for $\theta = 0°, 15°$ and 40° for an excitation energy $E_{\mathrm{exc}} \approx 1.45$ eV. Instead, the tilting angle of the magnetic field affects the Fano resonance in different ways, see section 4.4. Therein, the positive exciton exchange energy at the s-shell results in a different level hierarchy and leads to Voigt-like emission lines in the scattering spectra for tilted magnetic field geometries, similar to the peaks in figure 4-19 (c). The Fano resonance remains non-observable at the s-shell due to the different level hierarchy.

The Fano-type quantum interference leading to the Fano AR varies significantly for the different shells of the exciton emission energies, as revealed in the **excitation energy dependence** in figure 4-10 (b). At pure s-shell excitation energies (below $E_{\mathrm{exc}} < 1.440$ eV) the spectra show a smooth background without Fano AR. The Fano AR appears for resonantly probing the p-shell states of the QDs, where it is significantly pronounced. For higher energetic excitation energies (p-shell to f-shell), the depth of the Fano AR

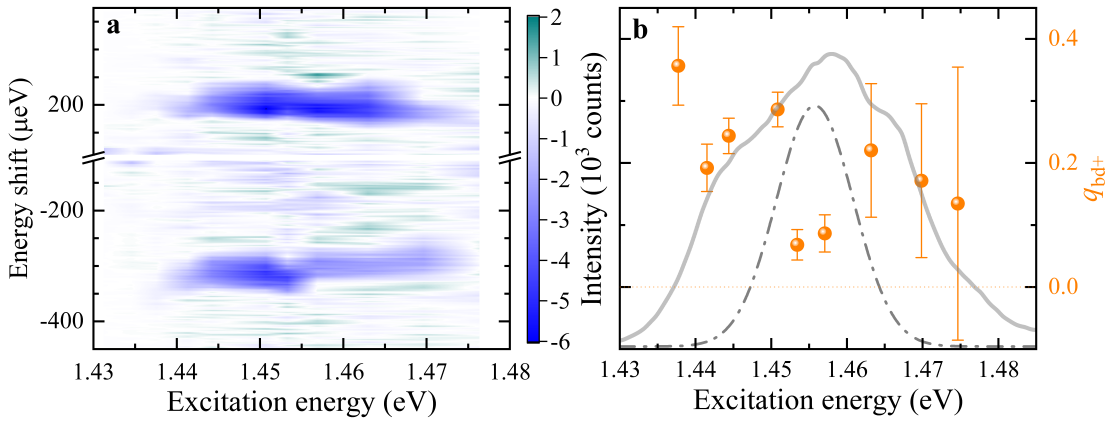

Figure 4-10: (a) Excitation energy dependence of the Fano AR spectra in Faraday geometry at $B = 8\,\mathrm{T}$ across the QD shells. The spectra at positive [negative] energy shifts were measured in (σ^+, σ^+) $[(\sigma^-, \sigma^-)]$ polarization configuration. (b) Asymmetry factor for the Fano process involving the $|{+1}\rangle$ and $|{+2}\rangle$ excitons (at positive energy shifts), including the PL with accentuated p-shell of the undoped InGaAs/GaAs QD ensemble. The dotted orange horizontal line serves as a guide to the eye.

continuously decreases for increasing excitation energy. Besides the mentioned change in δ_0, the magnetic-field induced Zeeman splitting of the electron also slightly changes: the spectral position of the **Fano AR slightly shifts towards lower energies** for increasing E_{exc} from 1.440 to 1.480 eV. The shift fulfills the well-known Roth-Lax-Zwerdling equation, which describes a reduction of the electron spin splitting with energy [27, 139]. At $B = 8\,\mathrm{T}$, this reduction is about 30 µeV or about 10 % [52, 378]. Moreover, note that in a tilted magnetic field geometry the Fano resonance is also pronounced mostly at the p-shell to f-shell.

As explained in section 4.1, the Fano resonance shape may be modeled by a convolution of a Gaussian function and the Breit-Wigner-Fano function in order to provide a more quantitative analysis of the Fano resonance shape [325, 327]. This convolution accounts for the inhomogeneous broadening of the optical QD transitions, leading to Voigt-like instead of Lorentzian signal shapes [379, 380]. From this function, the asymmetry factor q (see equation (4.6)) is evaluated and presented in figure 4-10 (b). The Fano AR at the Stokes side in longitudinal geometry (tilting angle $\theta = 0°$) is characterized by $q_{\mathrm{bd+}}$ factors ranging about 0.07 ± 0.03 at the center of the p-shell emission. For other excitation energies, $q_{\mathrm{bd+}}$ slightly increases, as observable in the spectra by a less distinct shape of the Fano AR. The **clear shape of the Fano ARs at p-shell** exciton resonances indicates that the Fano process mainly takes place for the p-shell electron. The reason for this is the **large overlap of the dumbbell-shaped wavefunction probability distribution** at the p-shell with that of the transverse acoustic phonons. Contrastingly, the wavefunction probability distribution of the s-shell exciton states barely overlaps with that of the transverse phonons, leading to a much weaker interaction.

4.4 Tuning the Fano resonance: Impact of tilting angle

The Fano resonance is not only visible as anti-resonance in longitudinal field (Faraday geometry), but is visible in its typical **asymmetric shape for tilted magnetic field**

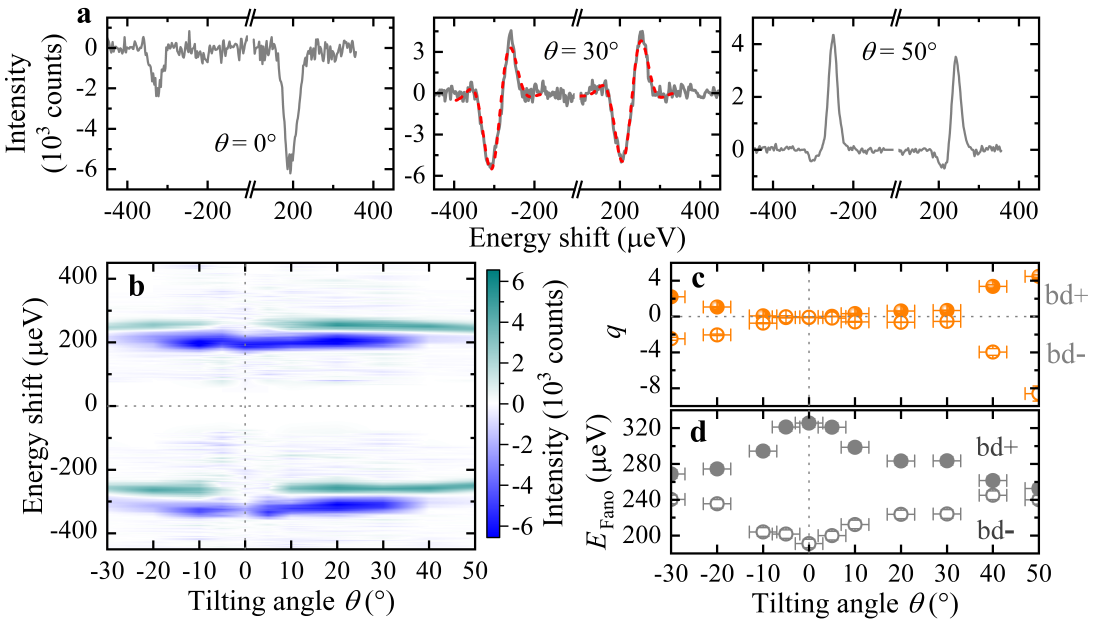

Figure 4-11: (a) Scattering spectra with subtracted background for different tilting angles θ with Fano interference shapes depending on the asymmetry factor q, at $B = 8\,\mathrm{T}$ for Stokes in (σ^+, σ^+) and anti-Stokes in (σ^-, σ^-) for resonant p-shell excitation. The red-dashed line indicates the convolved fit function curve. (b) Dependences of the Fano resonance on the tilting angle, of (c) the asymmetry factor and (d) the energy shift. The closed (open) circles denote the asymmetry factors on Stokes (anti-Stokes) side, corresponding to the spectral positions of E_{Fano} on the Stokes (anti-Stokes) side. The dotted lines serve as a guide to the eye.

geometries. Tilting the magnetic field direction by the angle θ with respect to the QD growth axis yields bipolar-shaped spectra, see top middle graph in figure 4-11. The spectra change their shape and obtain different asymmetry factors q for different tilting angles θ, as shown for single spectra in figure 4-11 (a). The intensities of the Fano resonances involving the $|+1\rangle \rightarrow |+2\rangle$ and $|-1\rangle \rightarrow |-2\rangle$ transitions are mapped angle-resolved in figure 4-11 (b) with θ varied from $-30°$ to $+50°$. The mapping demonstrates that only at $\theta = 0° \pm 5°$, the Fano AR is present, with asymmetry factor $q \rightarrow 0$ (left graph in figure 4-11 (a)). Outside that range from about $-30°$ up to about $+35°$, a pronounced bipolar Fano shape is visible. The asymmetric **bipolar shape** with $|q| \rightarrow 1$ occurs **for intermediate tilting angles** (see middle graph in figure 4-11 (a): $\theta = 30°$). At further increasing angles θ, the respective asymmetry factors deviate significantly from zero ($|q| > 1$), as shown in the right graph of figure 4-11 (a) for $\theta = 50°$. For tilting angle $|\theta| \rightarrow 90°$, or **Voigt geometry**, the interference is barely visible, but rather a **Voigt-like shaped peak**. Moreover, the spectral position E_{Fano} shifts with increasing θ to higher (lower) energies for the Fano resonance at the $|+2\rangle$ ($|-2\rangle$) dark exciton state, as depicted in figure 4-11 (d). For $|\theta| \rightarrow 90°$ (perpendicular magnetic field), the energy difference between bright and dark excitons is enhanced (lowered) for the Stokes (anti-Stokes) process. In such strongly tilted geometries, the **Fano resonance energies** of Stokes and anti-Stokes **converge to each other** $|E_{\mathrm{Fano},+}| \approx |E_{\mathrm{Fano},-}|$. This approaching agrees well with the angular dependence of the bright and dark exciton energy differences: a calculation leads to $\Delta E_{\mathrm{bd}+} \approx \Delta E_{\mathrm{bd}-} \approx 245\,\mu\mathrm{eV}$ for $\theta = 90°$ at $B = 8\,\mathrm{T}$, see figure 4-12 (b).

The energies of the bright ($E_{\mathrm{X},\pm1}$) and dark ($E_{\mathrm{X},\pm2}$) excitons in QDs with a symmetry

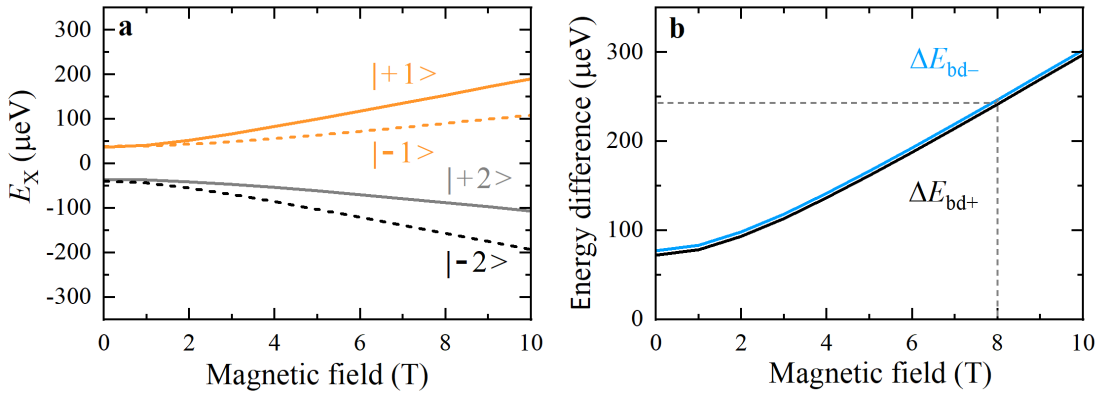

Figure 4-12: Magnetic field dependence of (a) the exciton fine structure and (b) the respective bright-dark-exciton energy difference ΔE_{bd} in Voigt geometry. The energy difference between the transition $|+1\rangle \rightarrow |+2\rangle$ is displayed in black, the transition $|-1\rangle \rightarrow |-2\rangle$ in blue. The dashed line indicates the energy shift at $B = 8\,\mathrm{T}$.

lower than D_{2d} may be calculated via [96]:

$$\begin{aligned} E_{\mathrm{X},\pm1} &= +\frac{1}{4}\left[\mp(\delta_\mathrm{b}+\delta_\mathrm{d}) + \sqrt{(2\delta_0 \mp \delta_\mathrm{b} \pm \delta_\mathrm{d})^2 + 4(g_{\mathrm{e},x} \pm g_{\mathrm{hh},x})^2\mu_\mathrm{B}^2 B^2}\right] \text{ and} \\ E_{\mathrm{X},\pm2} &= -\frac{1}{4}\left[\mp(\delta_\mathrm{b}+\delta_\mathrm{d}) + \sqrt{(2\delta_0 \pm \delta_\mathrm{b} \mp \delta_\mathrm{d})^2 + 4(g_{\mathrm{e},x} \mp g_{\mathrm{hh},x})^2\mu_\mathrm{B}^2 B^2}\right]. \end{aligned} \tag{4.11}$$

Therein, the exchange-based splitting between the bright and dark excitons amounts to $\delta_0 = -75\,\mu\mathrm{eV}$, the zero-field splitting of the bright exciton states is $\delta_\mathrm{b} = 4\,\mu\mathrm{eV}$ and $\delta_\mathrm{d} = 1\,\mu\mathrm{eV}$ of the dark exciton states. The QD in-plane g-factor of the electron (e) is $g_{\mathrm{e},x} = -0.50$ and the g-factor of the hh is $g_{\mathrm{hh},x} = -0.15$ [147, 150, 160]. Note that a diamagnetic shift is discarded since it would provide only weak corrections. The **in-plane magnetic field** disturbs the rotational symmetry of the excitons in the QDs. It leads to a **mixing of the bright and dark exciton states**. In Faraday geometry, the exciton states cross each other with increasing magnetic field strength, see figure 4-2 (a). In Voigt geometry, the spin splitting demonstrates a kind of **anticrossing** of the exciton states, as depicted in figure 4-12 (a). Thereby, the energies of the bright (dark) exciton states are increased (reduced) by rising magnetic field. In addition, the bright excitons lie energetically above the dark excitons due to the sign change of the squared term with δ_0. In figure 4-12 (b), the differences $\Delta E_{\mathrm{bd}-} = E_{\mathrm{X},-1} - E_{\mathrm{X},-2}$ and $\Delta E_{\mathrm{bd}+} = E_{\mathrm{X},+1} - E_{\mathrm{X},+2}$ are shown. These energy differences coincide with each other in Voigt geometry, contrasting their diverging behavior in Faraday geometry (see figure 4-2 (b)). Similar energy differences ($\Delta E_{\mathrm{bd}+} \approx \Delta E_{\mathrm{bd}-}$) in Voigt geometry, which were probed by the Stokes and anti-Stokes spectra, are also observed in experiment, cf. Ref. [52].

The Fano resonance changes its shape from the anti-resonance to the bipolar asymmetric shape due to the mixing of the electron spin basis eigenstates $|+1/2\rangle$ and $|-1/2\rangle$ of both the bright as well as the dark exciton states. In an **oblique magnetic field geometry** with $\vec{B} = B(\sin\theta, 0, \cos\theta)$, the component $1/2\mu_\mathrm{B}(g_{\mathrm{e},\perp}\sin\theta\ \sigma_x B_x)$ of the Zeeman Hamiltonian, with the Pauli matrix σ_x as deduced from equation (2.19), couples the $|+1/2\rangle$ and $|-1/2\rangle$ states [16, 381]. Hence, the spin states in tilted magnetic field direction are superpositions of the form $|\Psi\rangle = \cos(\theta/2)\,|\pm1/2\rangle \pm \sin(\theta/2)\,|\mp1/2\rangle$. The magnetic-field induced mixing strengthens the discrete transition between the bright and dark exciton states

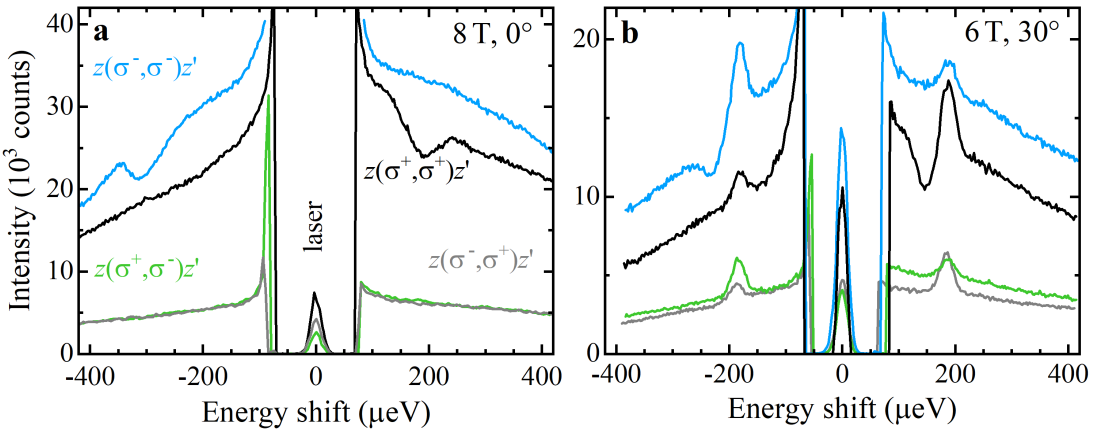

Figure 4-13: Scattering spectra in all four circular-polarized configurations for resonant p-shell excitation in (a) Faraday-geometry and (b) tilted geometry.

and weakens the coupling to the acoustic phonon continuum. This leads to a **change of the coupling strength** between the discrete state and the continuum with the tilting angle. It is noticeably by a **change in the asymmetry factor** varying from $q = 0$ at $\theta = 0°$ to $|q| \gg 0$ at $|\theta| > 0°$. Moreover, the mixing leads to a **brightening of the dark exciton**.

So far, the coupling strength of the Fano process may be tailored via the exciton exchange energy for different shell excitations and via the mixing of the spin basis eigenstates in tilted magnetic field directions. In tilted geometries, in addition to the shape change of the Fano profile, **Voigt-like peaks** appear in the opposite co-circular and in both cross-circular polarization configurations, as shown in figure 4-13 for all polarization configurations. The peaks in cross-circular polarization configuration may result from a coupling of the hole states by anisotropic electron-hole exchange interaction and hh-lh state mixing [52]. The **co-circular peaks** appear at the energy side opposite to that of the Fano resonance in $z(\sigma^+,\sigma^+)z'$ $[z(\sigma^-,\sigma^-)z']$ at the anti-Stokes (Stokes) side. Here, the electron of the photoexcited $|+1\rangle$ $(|-1\rangle)$ exciton may scatter into the energetically higher (lower) lying $|v''\rangle$ $(|v'\rangle)$ virtual state, as shown in figure 4-3. Hence, the spectra in tilted geometry show two possible scattering mechanisms of the electron of the bright exciton state in the co-circular polarization configurations. Firstly, the electron scatters via a two-phonon process in the Fano-like quantum interference in $z(\sigma^+,\sigma^+)z'$ on Stokes side and in $z(\sigma^-,\sigma^-)z'$ on anti-Stokes side. Secondly, the electron flips its spin via **scattering into virtual states** in the opposite co-circular polarized configurations due to mixed electron spin states. Virtual intermediate states that do not coincide with QD eigenstates are a common assumption in scattering processes, e.g., in (spin-flip) Raman scattering [98, 382], see also chapter 4.1 in [43]. Such virtual states obtain very **short lifetimes** $\tau_{\mathrm{L},v}$, which limit their interaction possibilities. When virtual states with short lifetimes were to interact via Fano resonance, the resulting resonance spectra should be strongly broadened, as $\Gamma = 2\pi\hbar^2/\tau_{\mathrm{L},v}^2$. A strong broadening implies that the coupling between such virtual states and a continuum is much less efficient. Hence, the probability of a quantum interference between the phonon continuum and virtual states is strongly reduced. Instead of a Fano resonance shape, the involvement of the virtual states $|v''\rangle$ or $|v'\rangle$ gives rise to Voigt-like emission lines as displayed in the scattering spectra of

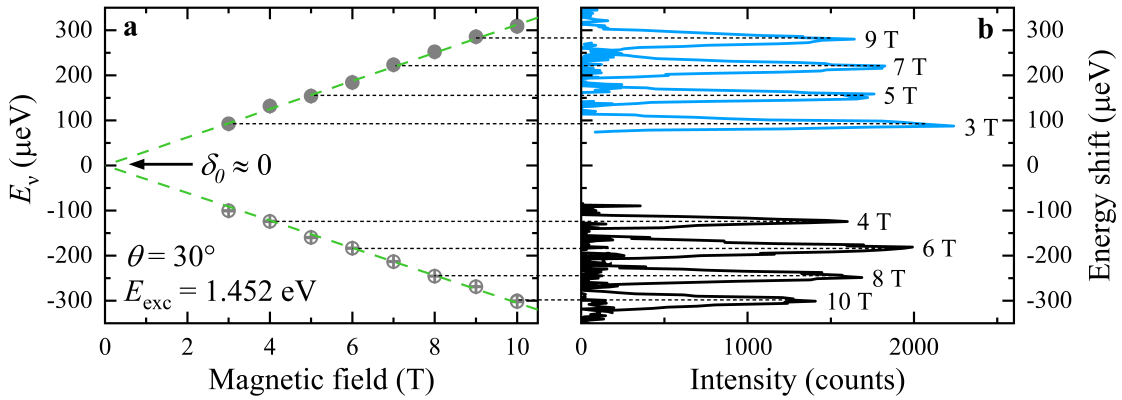

Figure 4-14: (a) Magnetic field evolution of the Voigt-like peak positions in (σ^+, σ^-) and (σ^-, σ^+) polarization. The linear extrapolation of E_v reveals a negligible exciton exchange energy. (b) Spectra of the Voigt-like peaks for different magnetic fields, related to the energies shown in (a). The closed circles denote the spectral positions of the $|+1\rangle \rightarrow |v''\rangle$ transitions, the open circles of the $|-1\rangle \rightarrow |v'\rangle$ transitions. The dotted lines serve as a guide to the eye.

figure 4-13 (b).
In figure 4-14 (a), the magnetic field dependence of these peaks is shown for exciting the central part of the p-shell PL in an oblique magnetic field geometry. The magnetic field dependence shows the evolution of the peak positions and their linear extrapolation to 0 T (green dashed lines). The single Voigt-like peaks are presented for different magnetic fields in figure 4-14 (b). Their **Stokes and anti-Stokes energy shifts agree** with each other, with negligible excitonic exchange energies ($\delta_0 \approx 0$), as virtual states are not subjected to electron-hole exchange interaction. The short lifetime of the virtual exciton accounts for only weakly correlated electron and hole spins, in addition to the fast hole spin-relaxation time in tilted magnetic field geometries. The spin orientations are unstable and, in turn, exchange interactions do not play a role [383]. Thus, the energies E_v of these virtual states differ from E_X by the electron spin splitting, or electron Zeeman splitting $|g_{e,z}B|$. Note that, for the same co-polarized geometries, the scattering into the virtual state may be superimposed on the Fano-like quantum interference: as the scattering into the virtual state shows the same energy shift as the scattering into the discrete state, the intensity of the virtual scattering process may be superposed on the intensity of the Fano resonance. This may lead to an intensity enhancement of the discrete state contributing to the Fano resonance in tilted geometries, which may explain that the asymmetry factor is close to $q \approx 1$ already for a tilting angle of $\theta = 30°$. Naively, one would expect an equal interaction strength between the discrete state and the continuum for a tilting angle of about 45°.

A note on resonant s-shell excitation regarding the impact of the tilting angle: the exciton exchange energy for this shell is positive and hinders the occurrence of Fano ARs in Faraday geometry, as explained in section 4.3. In tilted magnetic-field geometries, Voigt-like peaks appear in all polarization configurations. The interaction mechanism for both co-polarized polarization configurations is the same, via virtual intermediate states, as explained above for the opposite co-polarized scattering spectra of the higher shells. The resulting spectra resemble the usual spin-flip scattering spectra of similar n-doped InGaAs/GaAs QD ensembles, compare Refs. [248, 272].

4.5 Tuning the Fano resonance: Influence of temperature

Further insights into the scattering mechanism of the Fano resonance may be gained by dependences on laser excitation power P_{exc} and lattice temperature T of the bipolar Fano resonance. A change in (lattice) temperature induces a local heating of the phonon system, thereby increasing the density of populated acoustic phonon modes [248], while a higher laser excitation power increases the local temperature and, additionally, the density of photoexcited charge carriers [273]. This leads to an overall signal increase, up to the point when the exciton delocalizes and its lifetime reduces [98]. For studying the influence of temperature, a tilting angle of $\theta = 30°$ is chosen, as this allows for tuning the asymmetry factor in both directions. At this angle, the coupling strength is equally balanced between discrete state and continuum ($q \approx 1$) at standard conditions of $T = 6\,\mathrm{K}$ and $P_{\mathrm{exc}} = 30\,\mathrm{mW}$.

The spectral **laser power dependence** is shown in figure 4-15 (a). The asymmetry factor q_{bd} and the background intensity I_{back} obtained from fitting the Fano resonance shape are shown separately in figure 4-15 (b). From $P_{\mathrm{exc}} = 0.1\,\mathrm{mW}$ to about $50\,\mathrm{mW}$ the asymmetry factor $q_{\mathrm{bd}+}$ (as circles in the image) in (σ^+, σ^+) polarization ($|{+1}\rangle \rightarrow |{+2}\rangle$ transition) decreases steadily with power by factor 5 from about 5 to 1. This corresponds to an increase of the inverse asymmetry factor from about $1/q_{\mathrm{bd}+} \approx 0.2$ to 1, and to a tuning a the Fano lineshape from a Voigt profile at low P_{exc} to a bipolar shape. In addition, the background intensity I_{back} (as squares in the image) of the scattering spectra increases linearly by factor 500. The laser light drives both processes: the discrete bright-dark exciton transition indirectly by generating bright excitons in the p-shell, and the spectrally broad background emission scattered inelastically by acoustic phonons. This emission resembles the acoustic phonon sideband of the bright excitonic zero-phonon transition [194, 384]. The intensity enhancement of the background indicates that the **bright-dark exciton transition couples more strongly to the acoustic phonon continuum**. Higher powers modestly heat the phonon system and increase the spectral density of the phonons J_{ac} [385]. Hence, it is more likely to find two acoustic phonons whose total energy $2E_{\mathrm{ac}}$ matches $\Delta E_{\mathrm{bd}\pm}$. This leads to the acoustic phonon continuum coupling more strongly to the exciton transition, until both transitions are coupled equally strong ($q_{\mathrm{bd}+} \approx 1$).

For **high excitation powers** $P_{\mathrm{exc}} > 50\,\mathrm{mW}$, the asymmetry factor q increases, while the background intensity goes into saturation. This corresponds to a tuning a the Fano lineshape back to a Voigt profile and denotes a **decoupling from the continuum**. The **high laser power strongly heats the phonon system** and thereby shifts the maximum of the phonon spectral density J_{ac} to higher energies, see figure 4-5. Consequently, the probability of finding two acoustic phonons whose total energy corresponds to $\Delta E_{\mathrm{bd}\pm}$ decreases. Hence, only a smaller number of acoustic phonon pairs with suitable energy contributes to the Fano process and q starts to rise again. Furthermore, the observed decoupling may also be related to a weaker coupling strength. The piezoelectric coupling of the phonons, which is a polar interaction, may be screened out by free charge carriers [227, 386]. Such free charge carriers may be generated in an electron-hole plasma by an increase of the excitation power. In this way, the coupling strength of the Fano resonance may be reduced by a screening of the piezoelectric mediated exciton-acoustic phonon interaction [350]. Moreover, a decoupling from the continuum due to strong local heating may result from a stronger coupling to single phonons. For example, quadratic

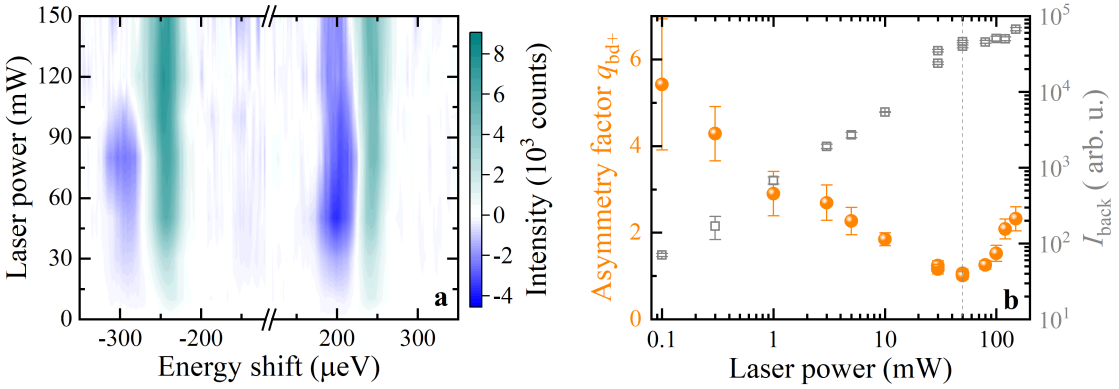

Figure 4-15: Dependence on the excitation power P_{exc} for a tilting angle $\theta = 30°$ at $B = 8\,T$ for resonant p-shell excitation. (a) Spectral dependence, (b) Inverse of the asymmetry factor $1/q$ at Stokes side (orange circles) in (σ^+, σ^+) polarization and background intensity I_{back} (gray squares) for comparison. The dotted line indicates the minimum of the asymmetry factor and the beginning saturation of the background intensity, as a guide to the eye.

coupling to single acoustic phonons is an important thermal dephasing mechanism for p-shell excitons at elevated temperatures [387]. In addition, a decoupling from the continuum may also result from a shortening of the dark exciton lifetime with increasing temperature, leading to a broadening of the Fano resonance. The exciton line broadening results from an increased exciton-phonon interaction, which is larger for the dark exciton than for the bright exciton [388]. Further temperature-related effects are mentioned in the following paragraph on temperature dependence. Thus, locally heating the phonon system using high powers is a second way of manipulating the coupling strength of the Fano resonance, besides the magnetic-field induced electron spin mixing discussed in the previous subsection.
In this context, note that multi-exciton interaction on the rate of the bright-dark exciton transition is neglected. These electron spin transitions allow for the optical generation of further p-shell exciton in the same QD when the resonantly excited p-shell exciton relaxes to the lower lying s-shell. This, however, would require a fast inter-shell relaxation and an unusually long s-shell exciton lifetime. Hence, only an insignificant impact of a mutual exciton interaction is expected and the electron spin-flip rate, as defined by the Pauli exclusion principle, is independently of the excitation power for resonant exciton excitation in each QD.

Further insights on the Fano resonance may be gained by directly changing the lattice temperature, as shown in figure 4-16. In figure 4-16 (a), the bipolar Fano resonance is observed at temperatures rising from $T = 6\,K$ to about $T = 40\,K$, for both the $|+1\rangle \rightarrow |+2\rangle$ and the $|-1\rangle \rightarrow |-2\rangle$ transitions. The **temperature evolution** reveals intensity and shape variations as well as the appearance of a Brillouin scattering line. The asymmetry factor q_{bd+} lies below 1 until 20 K ($1/q_{bd+} > 1$, as circles in the image), see figure 4-16 (b). For higher temperatures, the asymmetry factor increases to large positive values ($1/q_{bd+} \rightarrow 0$). This denotes a **decoupling from the continuum**. Likewise, the background intensity I_{back} (as squares in the image) exhibits a similar temperature dependence: it remains at a high level up to 20 K and decreases for rising temperatures. The asymmetry factor and the background intensity behave similarly with the lattice temperature, stressing the **relevance of the acoustic phonons participating in the**

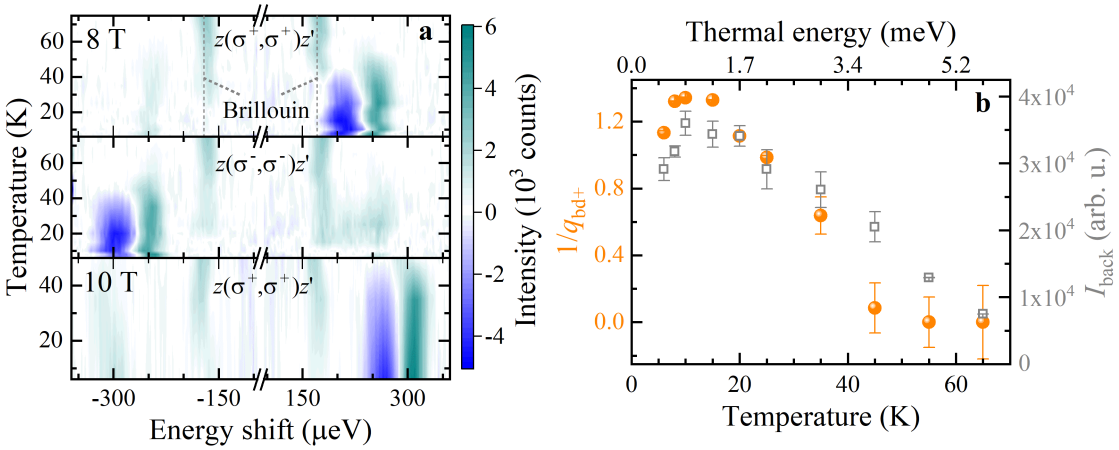

Figure 4-16: Modifying the bipolar shaped Fano resonance of the p-shell exciton by temperature at $\theta = 30°$ for resonant p-shell excitation. (a) Temperature evolution of the Fano resonance, revealing intensity and shape variations as well as the appearance of a Brillouin scattering line. The dotted lines serve as a guide to the eye. (b) Dependence of the inverse asymmetry factor (orange circles) and background intensity (gray squares) on the temperature.

Fano process. Note that the exciton **PL remains about stable** over the whole temperature range, see figure 4-17 (a), up to about 90 K. The bandgap reduces slightly with increasing temperature leading to a small redshift of the emission by about 2.8 meV from 5 K to 50 K. This thermally induced shift agrees well with previous measurements on singly charged InGaAs QDs [248]. Hence, the influence of this shift on the excitation and detection conditions of the Fano resonance including particularly p-shell excitons is negligible.

The dependence of the inverse asymmetry factor $1/q_{\mathrm{bd+}}$ on the inverse temperature is demonstrated in figure 4-17 (b). Its behavior is modeled by an Arrhenius-like exponential expression: $1/q_{\mathrm{bd+}}(T^{-1}) = A_0 - A_1 \exp(-E_{\mathrm{deac}}/k_{\mathrm{B}}T)$ [389, 390]. The parameters $A_0 = 1.3$ and $A_1 = 3.0$ from the fit curve (black line) lead to a deactivation energy $E_{\mathrm{deac}} = (5.3 \pm 0.3)\,\mathrm{meV}$. This corresponds to a temperature of $T = 60\,\mathrm{K}$. Typically, the deactivation of the scattering process is thermally induced by exciton dephasing [248, 391, 392]. Here, the **thermal deactivation** is rather **induced by the mismatch between the energies** of the transition ΔE_{bd} and $2E_{\mathrm{ac}}$, specifically by the decrease in probability of finding two phonons with this total energy. The highest probability of finding acoustic phonon pairs, whose joint energy $2E_{\mathrm{ac}}$ is equal to ΔE_{bd}, is in the range from 6 to 20 K, as indicated by the peaking in $1/q_{\mathrm{bd+}}$ and I_{back}. For higher temperatures $T > 20\,\mathrm{K}$, $1/q_{\mathrm{bd+}}$ strongly reduces as the phonon spectral density J_{ac} shifts and, relatively, less acoustic phonon pairs with suitable energies are present, see figure 4-5. Additionally, the increase of the asymmetry factor with temperature may result from a lifetime shortening of the dark exciton state due to thermal mixing between bright and dark states [393, 394]. The thermalization between bright and dark states may be mediated by one acoustic phonon whose energy matches the bright-dark splitting. The population of these acoustic phonon modes, and, thus, the exciton-phonon interaction, increases with temperature [395]. This leads to a reduction of the coupling strength by exciton line broadening. Similarly, one-phonon processes lead to a higher thermal dephasing and may reduce the coupling strength of the Fano-type quantum interference [387]. Note that a similar nonmonotonous function of temperature of the carrier-phonon

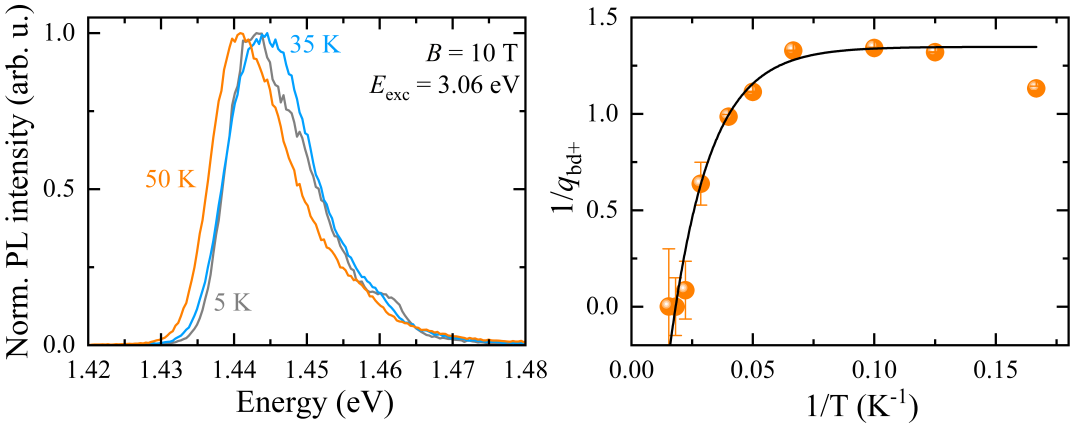

Figure 4-17: (a) Temperature dependence of the QD PL: normalized PL spectra measured at a nonresonant laser power of 35 mW and different temperatures. (b) Dependence of $1/q_{\mathrm{bd}+}$ on the inverse temperature for p-shell excitation at $\theta = 30°$. The data points are fitted by an Arrhenius-like equation.

coupling in QDs has been reported in [396], where the coupling depends sensitively on the peak structure of the form factor.
The deactivation energy $E_{\mathrm{deac}} \approx 5\,\mathrm{meV}$ further corresponds to about 20 times the bright-dark exciton splitting at 8 T. Hence, the spin-phonon Fano process is **robust against elevated cryogenic temperatures** close to the liquid nitrogen temperature. This is probably due to the coherent nature of both the resonantly excited exciton states as well as the Fano quantum interference. Noticeably, the low-temperature point at $1/T = 0.166\,\mathrm{K}^{-1}$ deviates from the fitting curve. The decrease of the coupling strength at such low temperatures may result from the freezing out of thermal phonons, which decreases the density of populated acoustic phonon modes [248]. Additionally, the discrepancy may be explained by the presence of several different deactivation energies depending on the size and composition of the QDs and, in turn, on the resonant excitation energy.

A further interesting point is a peak appearing at about 170 µeV in co-circular polarization configurations at $T > 20\,\mathrm{K}$, see figure 4-16 (a). Its peak intensity increases with rising temperature. The peak appears for resonantly probing the InGaAs QD ensemble at the s-shell and p-shell. The spectral position of this line shifts as a function of the excitation energy, but does not shift with external magnetic field and is even present at zero field, see figure 4-18. Yet, an application of the magnetic field enhances the intensity of the scattering line, while the peak intensities in Stokes and anti-Stokes polarizations are rather similar. This indicates that this **additional peak results from Brillouin scattering**, specifically, from the fundamental ($n = 1$) longitudinal acoustic phonons confined in the InGaAs QDs. The energy of this spheroidal ($l = 0$) mode is given by $E_{nl} = E_{10} = 2E_{\mathrm{exc}}\frac{\nu}{c}v_{\mathrm{L}}\sin\left(\frac{\varphi}{2}\right)$ [397], with the speed of light in vacuum $c = 2.998 \times 10^8\,\mathrm{m/s}$. In InGaAs, the refractive index is $\nu = 3.6$ [398] and the longitudinal sound velocity is given by $v_{\mathrm{L}} = 4670\,\mathrm{m/s}$ [361, 399]. As indicated in the inset in figure 4-18, the angle $\varphi \measuredangle(\vec{k}_{\mathrm{exc}}, \vec{k}_{\mathrm{det}}) = 180° - \theta$ is calculated via the angle $\theta \measuredangle(\vec{B}, \vec{z})$ and antiparallel wavevectors in backscattering geometry. As the optical axes of the incident and detected light are rotated approximately 10° from each other, the scattering angle $\varphi = 170°$. Hence, $E_{10} = (163 \pm 9)\,\mu\mathrm{eV}$ follows for an excitation energy of

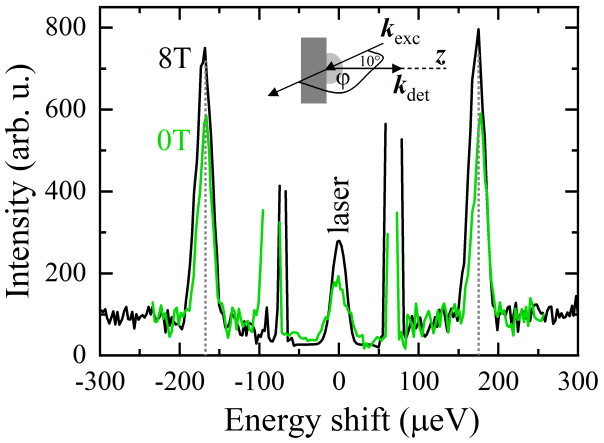

Figure 4-18: Brillouin scattering peaks at zero and 8 T external magnetic field strength ($\vec{B} \parallel \vec{z}$) at $T = 30$ K. Inset: Scheme of sample with a lens-shaped QD and the directions of the incident and detected light paths. The dotted lines serve as a guide to the eye.

$E_{\mathrm{exc}} = 1.455$ eV. This energy of the acoustic phonon modes agrees well with the spectral positions of the lines detected in the experiments. Furthermore, the preservation of the helicity underlines that purely radial acoustic modes ($l = 0$) are probed, whose spherical symmetry does not disturb the polarization properties [400, 401, 402]. The intensity enhancement with magnetic field might be contributed by the additional magnetic confinement of the acoustic phonon mode. The additional confinement induces a slight spatial anisotropy of the acoustic mode and, in turn, may lead to a relaxation of the helicity preservation.
Finally, it is remarkable that **both the Brillouin scattering line and the Fano resonance are simultaneously detected and may overlap with each other** in specific cases. This behavior reflects the **different types of acoustic phonons** involved in the scattering processes: the Brillouin light scattering is mediated by longitudinal acoustic phonons with $l = 0$. Contrastingly, the electron spin transition of the Fano resonance is coupled to lowest-energy transverse acoustic phonons with $l = 1$. These phonons result from the resonant optical creation of the phonon sideband of the zero-phonon exciton transition and behave similarly to the background intensity of the scattered light.

4.6 Discussion

The **Fano-type quantum interference reveals the dark exciton optically**, although forbidden by the electric-dipole selection rules. The necessary oscillator strength is transferred from the optically bright to the dark exciton via the interference between the discrete electron spin transition (magnetic-dipole transition) and a pair of orthogonally polarized acoustic phonons. The interference is sensitive to the energy and spin differences between the bright and dark exciton states and to the similarity of the electron and phonon wavefunction distributions. Hence, also the observation of the dark exciton and, in turn, the spin-phonon Fano resonance mechanism are sensitive to these dependences. The energetic dependence discloses in a broadening of the Fano AR for increasing magnetic field strength, see figure 4-7 (a). This is due to a dispersing Zeeman splitting of the exciton states as well as a shortening of the exciton spin lifetime. Moreover, the Fano resonance is most distinctive for resonantly exciting the p-shell excitons, it depends non-linearly on the exciting laser power and is thermally robust up to several tens of K. In addition, its shape, specified by the asymmetry factor $q = \cot\zeta$ with corresponding

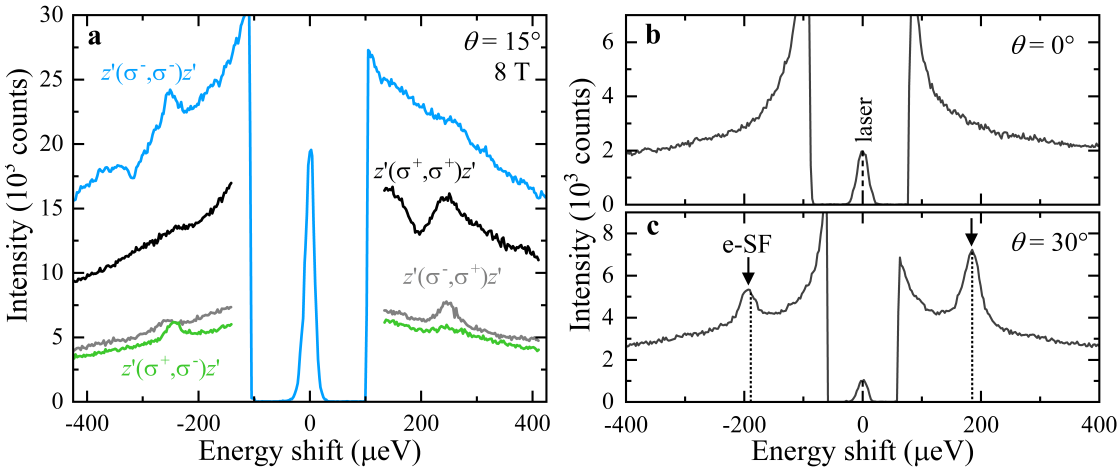

Figure 4-19: (a) Resonant excitation of the p-shell of the undoped InGaAs QDs in transmission geometry and at $T = 6\,\mathrm{K}$, $E_{\mathrm{exc}} = 1.465\,\mathrm{eV}$, $P_{\mathrm{exc}} = 30\,\mathrm{mW}$. Fano resonances are detected in the co-circularly polarized configurations. (b, c) Emission spectra close to the laser line for resonantly exciting negative trions at the p-shell of singly charged InGaAs QDs and at $B = 6\,\mathrm{T}$, $T = 6\,\mathrm{K}$, $E_{\mathrm{exc}} = 1.448\,\mathrm{eV}$, $P_{\mathrm{exc}} = 30\,\mathrm{mW}$ with: (b) In Faraday geometry only background emission is observed. (c) In tilted geometry ($\theta = 30°$) a sharp Gaussian emission line appears at the Stokes and anti-Stokes side. The energy shift of the dotted lines corresponds to $(187 \pm 2)\,\mu\mathrm{eV}$.

phase shift ζ, is tuned by the orientation of the external magnetic field in dependence of the magnetic-field induced mixing of the electron spin states.

The **shapes** of the bipolar Fano resonances involving the $|+2\rangle$ ($q_{\mathrm{bd}+} > 0$) and $|-2\rangle$ dark exciton ($q_{\mathrm{bd}+} < 0$) are **inverted** to each other. Thereby, the interference with $q_{\mathrm{bd}+} > 0$ ($q_{\mathrm{bd}+} < 0$) is realized by the **emission (absorption) of two orthogonally linear-polarized acoustic phonons** with $|\Psi_{\mathrm{ph}}\rangle = |+1\rangle$ ($|\Psi_{\mathrm{ph}}\rangle = |-1\rangle$) and transfers an angular momentum of $+1$ (-1). The two acoustic phonons differ by a phase shift of π from each other, which results in an inversion of the Fano resonance shapes. Accordingly, the Fano process with $q_{\mathrm{bd}+} > 0$ is characterized by the phase ζ shifting from $\pi/2$ to 0, while ζ changes from $-\pi/2$ to 0 for the $q_{\mathrm{bd}+} < 0$ process. These phase shifts are **independent of the scattering geometry**: they remain valid for changing from the reflection to the transmission geometry. The different scattering geometries vary in the orientation of the wavevectors. In transmission (forward scattering) geometry, the excitation is performed on-axis, so that the wavevector in excitation and detection have the same direction: $k_{\mathrm{exc}} \parallel k_{\mathrm{det}}$. Thereby, the bipolar shape of the Fano resonances and the sign of the asymmetry factors do not change significantly, see figure 4-19 (a). Additionally, the Fano shape also remains the same for switching the polarity of the external magnetic field. Note that due to a slightly oblique magnetic field orientation of $\theta = 15°$, the polarization vector of the laser light obtains a component parallel to the sample surface normal [283]. This leads to the excitation of the $|+1\rangle$ ($|-1\rangle$) exciton state via σ^- (σ^+) polarized light. Yet, this parallel component has only a weak intensity, so that only a Voigt-shaped line is detected in cross-circular polarization configurations. These observations substantiate previous findings: that the acoustic phonons mainly propagate within the QD plane perpendicular to the light propagation and the magnetic field direction (in Faraday geometry) [403, 404].

Another interesting finding in this context is that **neither a Fano AR** in Faraday geometry **nor a bipolar shaped Fano resonance** in tilted geometries are observed **for**

resonantly exciting singly charged InGaAs QDs. These QDs are charged on average by a single electron. The corresponding spectra show only Gaussian shaped lines in tilted geometry, whose spectral position follows the electron Zeeman splitting, see figure 4-19 (b). Both QD ensembles obtain comparable PL energies. While excitons are excited in the uncharged QDs, negatively charged excitons (negative trions) are probed in the singly charged dots due to the resident electrons. Thus, dark excitons cannot be probed. In these dots, isotropic and anisotropic exchange interactions between the carriers of the trion dominate against couplings with acoustic phonons [52, 248, 272]. Specifically, the scattering line in the spectrum at the Stokes or anti-Stokes side indicates the flip of an electron spin caused by the exchange interaction between the electrons of the trion. This spin flip is accompanied by an energy change equal to the electron Zeeman splitting [52, 272]. The results of the singly charged QDs underline that in neutral QDs the dark excitons and acoustic phonons govern the Fano resonance. Moreover, no absorption line of the dark exciton is visible in the background intensity. Hence, a pure trion or exciton absorption does not account for detecting the Fano AR, as this line should appear for both the neutral as well as the singly charged QDs. Furthermore, polaronic effects shifting the exciton energies may be excluded. These become significant only in QDs with diameters of a few nanometers and the shifts would be proportional to the phononic confinement length L^{-2} [367, 405, 406].

The negative exciton exchange energy, evidenced by the magnetic field dependence of the Fano ARs, reveals an **exciton level hierarchy in which the bright exciton is lowest in energy for higher QD shell states**. This level hierarchy makes the $|-1\rangle$ exciton state energetically favorable. Typically, the reason for such a change lies in a **lowered symmetry**. Here, the out-of-plane magnetic field and, in turn, its force along the QD plane with weak spatial confinement compresses the non-zero orbital wavefunctions of the excitons [92, 407] and enhances the asymmetry in the electron-hole interaction radius. In Voigt geometry ($\vec{B} \perp \vec{z}$), the magnetic force is parallel to the strongly confining QD axis. Thus, the dark exciton states lie below the bright states.

Another explanation is that the different interactions contributing to the full Hamiltonian of the QDs interacting with light leads to this unexpected level hierarchy. The latest theoretical considerations are based on a configuration interaction approach using an **envelope function model** [36], compare section 2.1.2. Therein, different interactions like Zeeman interaction, valence band mixing, direct Coulomb and short-range exchange interaction are taken into account. According to the approach, the bright excitonic transitions in the p-shell lie energetically below the dark transitions. Starting point of this approach are the higher energetic p-shell excitons. The p-shell excitons are fourfold degenerate, including spin, and are typically split by 10 meV for cylindrical dots [157]. The states may be further differentiated according to their envelope functions which point in x- and y-direction, leading to p-shell states labeled p_x and p_y, respectively. These states obtain an orthogonal linear polarization [408]. Due to the lateral asymmetry of the QDs, the two p-shell electron states p_x and p_y are not degenerate [409]. The envelope functions of the p_x and p_y states are energetically split, originating from the interplay between Coulomb interaction and valence band mixing. The splitting is caused by the difference between the confinement lengths in x and y directions, which causes a larger separation of the single-particle energies [36]. The resulting fine structure splitting of the electron p-levels is typically about $0.01 - 1$ meV in InGaAs QDs [157], with the p_x-state being lower in energy [410]. Furthermore, in the studied QDs, the transitions $\mathrm{p}_x \rightarrow \mathrm{p}_x$ and $\mathrm{p}_y \rightarrow \mathrm{p}_y$ are bright exciton states. Here, the first (second) state refers to the

heavy-hole (electron) in the VB (CB) so that the transition $p_x \rightarrow p_x$ describes the p-shell exciton, whose hh and electron both possess envelope functions in the x-direction. Note that the two hh states are not pure but include a small admixture of lh states. Besides these bright transitions, the transitions $p_x \rightarrow p_y$ and $p_y \rightarrow p_x$ with envelope functions in the x- and y-directions are optically dark owing to their **different envelope function overlap**. Although all p $\rightarrow$ p transitions are spin-allowed, their envelope functions overlap differently: the overlap is complete for both x- (or both y-)orbitals and the states are optically active, while the orbitals are perpendicular to each other (as $\vec{x} \perp \vec{y}$) for the mixed transitions. Thus, the mixed states are not optically active. As a consequence of the valence band mixing via the off-diagonal elements of a four-band Luttinger model [36], the symmetry rules for couplings are reduced. Hence, the **dark $\mathbf{p_x \rightarrow p_y}$ and $\mathbf{p_y \rightarrow p_x}$ transitions couple to the bright p $\rightarrow$ p states**. Moreover, symmetry reduction due to direct Coulomb interaction allows further formerly dark states to couple to the bright s $\rightarrow$ s and p $\rightarrow$ p transitions, e.g., $p_z \rightarrow p_x$ / p_y and d_{xy} / d_{xz} / $d_{yz} \rightarrow$ s. The coupling of the different transitions leads to a **transfer of oscillator strength**, so that the dark states become slightly bright and the bright states lose intensity [411]. Moreover, the **spin configurations and** the resulting **selection rules are less well defined**. This may lead to strong deviations of the usual energetic level structure [36]. The extent of state mixture depends on the number of neighboring states as well as the energetic distance between the neighboring dark and bright transitions [36]. Furthermore, the different ordering of the polarization axes from the different wavefunction symmetries leads to different orientation of the electron-hole exchange interaction [412]. Hence, the resulting exciton exchange energy δ_0 for the different shells has different values, indicating a strong anisotropic part of the electron-hole exchange due to a significantly different overlap between the p- and d-shell wavefunctions of the electron and the hole compared to the respective s-shell wavefunctions.
In the studied QDs, the transition $p_x \rightarrow p_x$ lies below the formerly dark $p_x \rightarrow p_y$ and $p_y \rightarrow p_x$ transitions and the dark and bright states become mixed, since they are energetically close. Note that in such QDs the p $\rightarrow$ p transitions are typically only 50 % pure states or lower [36, 157]. Similar exciton fine structures with multiple closely lying electron and hole levels comprising p-shell excitons and, e.g., affecting the dephasing, have been obtained in InAs QDs [387] and CdTe QDs [412], and theoretically computed for CdSe QDs [36]. A similar state mixing is induced by including the Bir-Pikus Hamiltonian, which characterizes the influence of phonons on the valence band mixing [348]. In this way, the state mixing allows for the coupling of acoustic phonons with a strongly bright and an almost dark exciton state from the p- or higher lying shells. This interaction is only significant for excitons occupying at least the p-shell, assuming that the phonon and, in particular, electron wavefunctions overlap with each other. Due to level mixing, the exciton level hierarchy in the studied QDs comprises the bright exciton as lowest state for the excited shells (p-shell and higher), while in the s-shell the dark exciton is the lowest state.

To conclude, this chapter shows a novel type of quantum interference between the discrete bright-dark exciton transition and the continuum formed by a pair of orthogonally linear-polarized acoustic phonons in QD ensembles. These determine the spin-phonon Fano process. Therein, the Fano ARs show dark excitons in forbidden symmetries defined by the orientation of the external magnetic field and the QD growth axis. The change of the Fano resonance shape with polarization allows for distinguishing between real and virtual

exciton states. Hence, the spin-phonon Fano effect is a highly attractive mechanism for studying dark excitons and/or other carrier complexes confined in semiconductor structures. Moreover, it provides an optical method to elucidate real and virtual intra- and interband transitions which may even be forbidden by symmetry. These results on the exciton level hierarchy highlight that excited QD shells may be highly useful for light demanding applications in the optoelectronics. Additionally, the tunability of the exciton exchange energy allows for a much easier dynamic decoupling on exchange-coupled spins in terms of, e.g., standard noise error corrections during gate operations.

5 Exciton-phonon coupling in transition metal dichalcogenide heterostructures

Atomically thin two-dimensional (2D) crystals obtain unique physical properties related to their low dimensionality. Compared to the well-studied graphene monolayer with zero-energy bandgap [6, 298, 413, 414], monolayers of group-VI **transition metal dichalcogenides** (TMDCs) show a direct bandgap in the visible energy range and a very efficient light-matter coupling, thus making them suitable as new platforms for optoelectronic applications [8, 57, 415]. Their energy gap is located at the two inequivalent K points of the hexagonal Brillouin zone [7]. This arrangement results from a lack of inversion symmetry in combination with strong spin-orbit (SO) coupling and allows for exciting carriers with distinct spin and valley indices using circularly polarized light. This leads to a unique feature of these materials: spin-valley locking, which describes the coupling between the spin degree of freedom and the valley degree [55, 184, 416, 417]. The valley-contrasting spin-splitting is larger for the valence bands (VBs) than for the conduction bands (CBs) and gives rise to the formation of so-called A- and B-excitons [55, 418]. Therein, the CB spin-splitting is smaller and results in a splitting between the dark and bright exciton subbands. These bright (dark) excitons are composed of an electron from the CB and a hole from the valence band at the same valley with the same (opposite) spin. These excitons possess binding energies of a few hundreds of meV [419], which are orders of magnitude larger than those in quasi-2D quantum wells [420, 421].
The weak van der Waals (vdW) interaction between the single monolayers (MLs) allows for stacking different materials together, e.g., TMDCs combined with each other, with graphene or with encapsulating hexagonal boron nitride (hBN). The stacking of such vdW heterostructures alters the dielectric screening of the excitons in the MLs and allows for modifying the optical and spin properties of the materials. Moreover, the ***interlayer*** **electron-phonon coupling** between adjacent layers strongly impacts the physical properties of the heterostructures and may improve or limit their potential device performance [220, 221, 422]. Specifically, the encapsulation of TMDC MLs within high-purity hBN flakes significantly improves the ML quality and narrows the emission lines [72, 73]. It protects the ML from possible charge transfers (physi- and chemisorption during the experiment) and local electric field fluctuations stemming from the substrate [73]. In addition to that, several coexisting neutral and charged excitons and biexcitons are observed in PL spectroscopy [173, 423, 424]. The charged excitons also have large binding energies of tens of meV, resulting in their stability even at room temperature [425, 426, 427]. Furthermore, gray excitons and momentum-indirect dark excitons activated by scattering with defects or phonons may be observed [428, 429, 430, 431].

The discovery of TMDCs as direct band-gap semiconductors in their monolayer form, with up to 20 % absorption per single layer at the exciton resonance, initiated intense research activities as well as progress in techniques for producing, characterizing, and

manipulating these atomically thin layers [8]. Their unique physical properties promise a high usability for future applications in novel electronic devices as well as in spintronics and valleytronics. However, their full potential has been limited by challenges in observing and understanding **subtle optical and spin-valley properties**. The findings obtained in this thesis shed light on some of the excitonic properties and material parameters of 2D TMDCs and their heterostructures. In particular, vdW heterostructures composed of different kinds of TMDC MLs and hBN layers are examined. These heterostructures offer a unique platform for studying exciton properties and electron-phonon interactions that were previously challenging to observe in structures exfoliated directly on standard SiO_2/Si substrates. The first part focuses on interaction processes in WSe_2 MLs, while the second part deals with the fine structure of excitonic complexes in MoS_2 and exciton-energy splittings in the alloy $Mo_{0.7}W_{0.3}Se_2$.

In the first part, the interlayer electron-phonon interaction in hBN/WSe_2/hBN heterostructures leads to the observation of a strong increase in the emission intensity. This **intensity gain** is **attributed to a double resonance**, where the laser excitation and a combined Raman mode resonate with the ground and the excited states of the A exciton in the WSe_2 ML. Moreover, the helicity preservation of the exciting light in the emission of all observed excitonic complexes is studied. This enhancement of the circular polarization degree is highest, of more than 60 %, for the neutral biexciton and the negatively charged exciton in its triplet state. Furthermore, signatures of polaritons are observed in the photoluminescence excitation (PLE) spectra of a heterostructure consisting of a WSe_2 ML placed on hBN. Such **exciton-phonon polaritons**, or phonoritons, are created through the optical excitation of an excitonic state and a phononic mode. Here, an anticrossing is observed at the exciton and trion PL lines in the WSe_2 ML when crossed by the ZO (hBN) and the combined ZO (hBN) + A'$_1$ (WSe_2) phonon modes. The phonon-polariton anticrossing is most pronounced at the exciton resonance for the out-of-plane ZO (hBN) phonon mode. At the exciton resonance energy, the Raman line is strongly enhanced in its intensity, both line energies are shifted and the linewidths are narrowed. In this way, an anticrossing-like behavior of the Raman line of the phonon mode and the exciton or trion PL line is observed. The optical properties of WSe_2 encapsulated in hBN are examined further; specifically, ways of **brightening dark excitons and trions** using upconversion photoluminescence (PL) are studied. The dark intervalley exciton upconverts light into a bright intravalley exciton via electron-electron scattering. Thereby, resonances below the neutral exciton are revealed in the upconverted PL. The required energy gains are explained by cooling of resident electrons or by exciton scattering with Λ- or K-valley phonons. An elevated temperature and a moderate concentration of resident electrons are necessary for observing the upconversion resonances. This interaction process stresses the importance of dark excitons in shaping the optical behavior of TMDCs.

In the second part, the **fine structure of excitonic complexes** in vdW heterostructures based on single-layer MoS_2 is studied. The heterostructures consist of either uncapped MoS_2 stacked onto hBN layers of different thicknesses and of hBN-encapsulated MoS_2 MLs, leading to different doping levels. Therein, the fine structure of the excitonic complexes as well as the effective excitonic g-factor are found to significantly vary in the different structures in dependence on the electron concentration. This highlights the **influence of encapsulation and doping** on the excitonic behavior of MoS_2 within different vdW heterostructures. Furthermore, exciton-energy splittings in the alloy $Mo_{0.7}W_{0.3}Se_2$ are studied. The polarization-resolved magneto-PL reveals **large effec-**

tive *g*-factors, $|g| = 6 - 7$, of the different excitonic complexes, which are substantially larger than typical effective excitonic g-factors in binary TMDC MLs. Moreover, a rising circular polarization degree is found, whereas the optical orientation does not change with magnetic field. Finally, polarization-resolved scattering spectra expose different dependences for the exciton, trion, and intervalley exciton. These findings, presented in the outlook, disclose the valley g-factor via resonant intervalley cross-scattering.

The novel findings presented in this section provide valuable insights and open up new possibilities for utilizing TMDCs in different vdW heterostructures for various applications in photonics and nanotechnology. The enhanced understanding of interlayer electron-phonon coupling, the mechanisms of upconversion from dark to bright excitons, and the fine structure of excitonic complexes offer ways for designing and optimizing electronic and optoelectronic devices based on these materials. Moreover, the control and manipulation of excitonic properties, such as the excitonic g-factor, provide opportunities for further advancements in spintronics and quantum information processing. Thus, these findings pave the way for future research and technological innovations in this highly active research field.

5.1 Exciton-phonon coupling in WSe_2 heterostructures

The studied **WSe_2 ML** were mechanically exfoliated from bulk crystals grown by the chemical vapor transport technique, see section 3.4.2. The MLs and the hBN flakes with different thicknesses are then stacked on Si substrates using the deterministic all-dry stamping method. Typical flake sizes exceeded 10 µm × 10 µm, see figure 5-1. The samples were annealed directly after the transfer of each subsequent layer, for 20 min at a temperature of 180 °C on a hot plate in air. Additionally, after the transfer of the last top **hBN layer**, the heterostructure was annealed for 2 h at 200 °C in air. The **annealing** improved the contact between the transferred layers, and strain-induced bubbles and wrinkles were reduced, as can be seen by comparing the atomic force microscopy images in figures 5-1 (a) before and (b) after the annealing. A line profile of the ML along the red line is presented in [254], showing a height of roughly 1 nm of the ML after the annealing.
The samples were mounted at the cold plate of a flow cryostat, movable via nanopositioners, where they were exposed to low temperatures down to 3.5 K. They were probed by different kinds of PL and PLE spectroscopy (details in section 3.1). The resonant optical excitation and detection were performed using the micro-setup MO (section 3.3.2). The samples were excited non-resonantly by the light of the second harmonic (532 nm, 2.33 eV) of a continuous-wave single-mode Nd:YVO_4 laser. For (quasi-)resonant excitation, the light of a cw dye laser equipped with DCM and wavelength-tunable in the range from 610 nm to 685 nm (from 2.03 eV to 1.81 eV, respectively) and a Ti:Sapphire laser with a wavelength range from 690 to 850 nm (1.80 to 1.45 eV, respectively) were used (see section 3.3). The laser emission (laser photon energy) was monitored spectrally by an interferometric wavelength meter, while the laser power (light intensity) was additionally stabilized by a liquid-crystal amplitude modulator providing a laser-light amplitude stabilization of 0.05 %. The laser light was focused on the sample under normal incidence using a high-resolution, long-working distance 50× microscope objective (WD = 10.6 mm, N_A = 0.50), leading to an excitation spot diameter of about 4 µm.

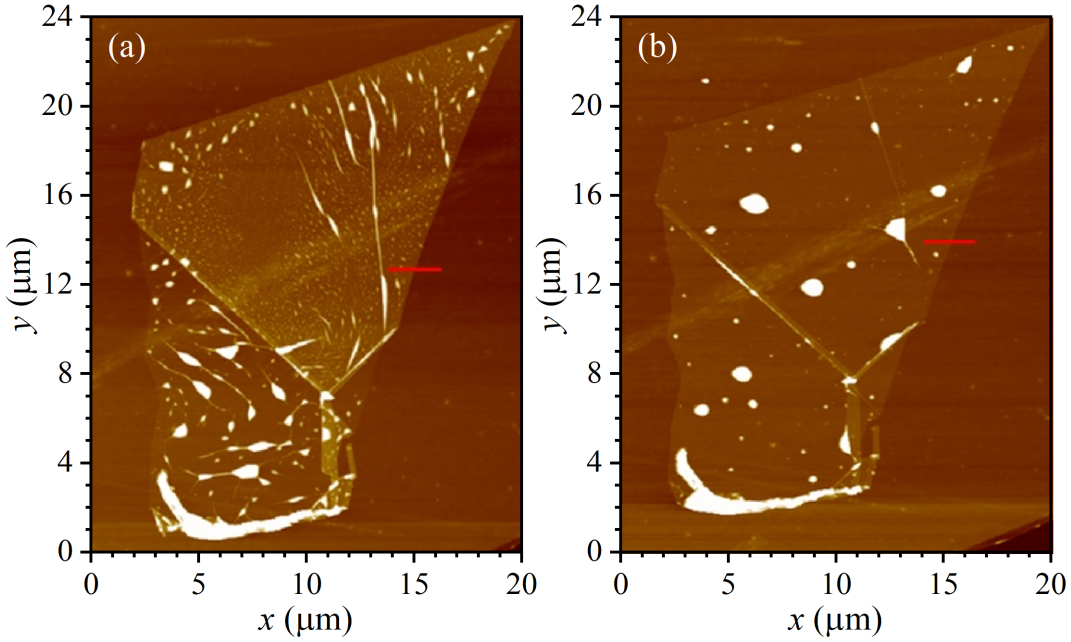

Figure 5-1: AFM images of the WSe_2 flake on the top of the annealed hBN layer: (a) before and (b) after the annealing. The size is approximately 17 µm × 10 µm.

The ML emission was collected by the same microscope objective and was analyzed by a single monochromator (focal length of 0.5 m), see section 3.3.3, with a spectral resolution of about 100 µeV. The spectrometer was equipped with a 600 g/mm, 900 g/mm and 1800 g/mm grating. Its choice was dependent on the desired resolution, see section 3.3.3. The spectrometer was further equipped with a cooled Si CCD camera, see section 3.3.4. Unless specified otherwise, the measurements were performed at a temperature of 7 K in backward scattering geometry with a laser power typically set to < 1 mW. The polarization of the incident and detected light was set each by a combination of a Glan-Taylor prism and an achromatic half-wave (or quarter-wave) retardation plate. Scattered laser light was reduced by using appropriate long- and short-pass edge filters.

5.1.1 Enhancement of excitonic emission via resonant phonon modes

The optical spectra of TMDC MLs are dominated by excitonic transitions [421], similar to 2D semiconductor heterostructures where the two-dimensional confinement and the reduced dielectric screening affects the excitonic properties [432, 433]. In such heterostructures, the recombination of neutral (X) and charged (X^+ and/or X^-) excitons are visible as well-resolved lines in the PL spectra. Their binding energies are enhanced by the reduction in dimensionality, which makes these quasi-particles much more robust. They are also visible in the PL spectrum of TMDC MLs, compare figure 5-2. Additionally, the spectrum shows several emission lines that are typical for WSe_2 MLs encapsulated in high-quality hBN flakes [173, 423, 424]. This rich emission is attributed to a **variety of excitonic complexes**. The peak with the highest energy at $E = 1.725$ eV is assigned to the neutral A exciton (X_A) in the ground state (1s). The exciton states are split mainly due to the SO interaction with the transition-metal d-orbitals, leading to a giant spin splitting of the bands. As explained in section 2.1.4, the optically ac-

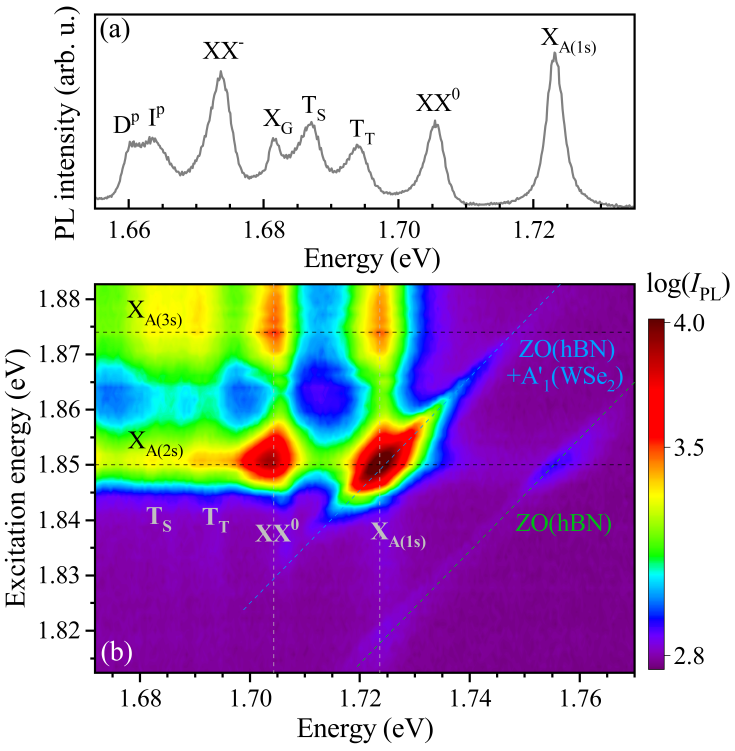

Figure 5-2: Unpolarized PL(E) spectra of an hBN/WSe_2/hBN heterostructure recorded at $T = 7\,\mathrm{K}$. (a) PL spectrum excited non-resonantly with laser energy $E_{exc} = 2.33\,\mathrm{eV}$. (b) PLE spectra recorded at excitation energies ranging from $E_{exc} = 1.81$ to $1.88\,\mathrm{eV}$.

tive A exciton is formed by the electron in the top spin-split conduction subband and the hole in the upper spin-split valence subband. The B-exciton is associated with the lower spin-split valence subband. Due to the spin structure of the bands, it is optically inactive [126]. It is one of several dark excitons in ML WSe_2 and may be detected at about $E = 2.2\,\mathrm{eV}$ using absorption, reflectivity contrast or upconversion PL [434, 435]. The peak at $E = 1.710\,\mathrm{eV}$ is assigned to the neutral biexciton (XX^0), whereas the peak at $E = 1.673\,\mathrm{eV}$ is appointed to the negatively charged biexciton (XX^-). In MLs that are not encapsulated, the biexciton emission is typically hidden due to inhomogeneous broadening and due to the presence of defect bands. The neutral four-particle state XX^0 may be determined by power-dependent PL, showing a superlinear behavior [424]. The negatively charged five-particle state XX^- indicates that the two-dimensional electron gas concentration in the ML is low, but still significant to allows for XX^- formation. It is related to unintentional residual doping [70]. This state may either be understood as a bound state of a bright exciton with a dark trion, or a bright trion with a dark exciton [424]. The two peaks located at $E = 1.695\,\mathrm{eV}$ and $E = 1.685\,\mathrm{eV}$ result from negatively charged excitons: the intravalley spin-triplet and intervalley spin-singlet trions (T_T and T_S, respectively). Thereby, the singlet (intravalley) trions are observable even at ambient conditions whereas the triplet (intervalley) trions are only efficient at low temperatures [436]. Note that the intervalley triplet state is preferred (energetically lower) due to the dark exciton ground state in ML WSe_2. This trion fine structure, namely the splitting between optically bright singlet and triplet trions, arises due to predominantly electron-hole exchange interaction [437]. As explained in section 2.2.3, a singlet (triplet) state is characterized by an antiparallel (parallel) alignment of their spins. Typically, the two electrons involved in the trion complex appear in the singlet (bound) state. However, the two electrons of a trion may also originate from the same CB valley forming a triplet (unbound) state. Specifically in TMDCs, the exchange interaction between the two elec-

trons is significantly weakened [436]. Here, the triplet trions may involve two electrons with the same spin but each from a different valley. In this way, the electrons still obtain a different quantum state: with the valley pseudospin as distinguishing quantum number. The energy separation between the different states is about 10 meV. It corresponds to the exchange interaction of the excess electron with the electron-hole pair in the opposite valley, whereby all particles have the same spin orientation [437, 438]. The peak at $E = 1.681\,\mathrm{eV}$ is attributed to the spin-forbidden dark exciton, or gray exciton (X_G). The emission of this exciton propagates along the ML plane, as its spin-flip dipole matrix element is directed perpendicular to the ML plane (out-of-plane dipole moment), see section 2.3.4. In contrast, the bright exciton complexes propagate perpendicular to the ML plane due to their in-plane optical dipole momenta. Yet, the high-numerical aperture of the microscope objective collects the in-plane and the out-of-plane emission of all excitons [173, 439], compare figure 3-9. This gives rise to the observation of X_G. Finally, the peaks at $E = 1.665\,\mathrm{eV}$ and $E = 1.661\,\mathrm{eV}$ are assigned to a pair of zone-corner chiral-phonon replicas of the dark exciton states (I_{ph}) [428, 440].

Further insights into the exciton properties are obtained by studying the emission intensity in dependence on the excitation energy. Therefore, the laser energy is tuned from $E_{exc} = 1.88\,\mathrm{eV}$ (above the energy of the A exciton in the 3s state) down to $E_{exc} = 1.81\,\mathrm{eV}$. The figure 5-2 displays the measured PLE spectra as a 2D color plot. The horizontal and vertical axes correspond to the emission and excitation energy, respectively, and the emission intensity is displayed in a logarithmic color scale. Here, two additional peaks that shift linearly with the laser excitation energy appear at the high energy side of the emission spectrum. These peaks are attributed to Raman scattering phonon modes [220, 221]. The Raman scattering process appears at the interface between the different vdW materials. Although Raman scattering is typically weak compared to infrared absorption, it may be enhanced by matching the energy of either the incident or inelastically scattered photon with an electronic (or excitonic) transition [441, 442]. The mode at about 100 meV ($820\,\mathrm{cm}^{-1}$) is assigned to the B_{1g} ZO mode in hBN, which is a silent mode in isolated hBN. It has even parity under inversion and is associated with an out-of-plane electric dipole [221]. In vdW heterostructures, the mode gains intensity by more than two orders of magnitude due to the resonant coupling to electronic transitions in the WSe_2 ML. The mode at about 130 meV ($1070\,\mathrm{cm}^{-1}$) is attributed to a superposition of the A_{2u} ZO mode from the hBN layer and the A'$_1$ mode from the WSe_2 ML. The A_{2u} mode in hBN has odd parity under inversion and is infrared active but Raman silent. This mode corresponds to the relative displacement between the B and N atoms, creating an out-of-plane dipole. The dipole interacts with the charge distribution in the planes of WSe_2, which resembles two layers of dipoles in opposite orientations. These dipoles are changed by the out-of-plane A'$_1$ (ZA) phonon mode. In this way, the phonon modes are coupled via dipole-dipole interaction, which then interact with the exciton in WSe_2. When the combined mode ZO (hBN) + A'$_1$ (WSe_2) matches energetically with the radiative recombination of the A exciton, its emission and that of the neutral biexciton become strongly increased.

This **emission enhancement** was already observed in a previous study of a similar heterostructure at a temperature of $T = 77\,\mathrm{K}$ [220, 221]. In this study, the enhancement is attributed to a double resonance, in which the outgoing photon energy corresponds to the energy of the 1s A exciton in WSe_2, whereas the ingoing laser excitation energy is in resonance with a hybrid state existing only in hBN/WSe_2/hBN. Contrastingly, in this

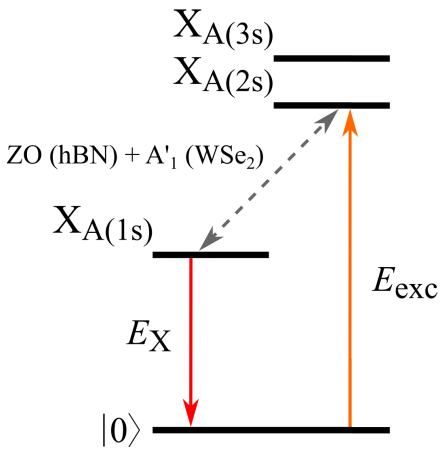

Figure 5-3: Schematic representation of the double resonance process. The ingoing (outgoing) photon is in resonance with the 2s (1s) A exciton. The energy of the combined phonon mode ZO (hBN) + A'$_1$ (WSe_2) is equal to the energy separation between the exciton states.

heterostructure it is evident from the PLE spectra (and confirmed via additional reflectivity contrast measurements in [254]) that the outgoing (ingoing) photon is in resonance with the 1s (2s) A exciton. When the energy separation between the 2s and 1s exciton states equals the energy of the phonon mode, the double resonance condition is fulfilled and the excitonic emission is enhanced. This **double resonance process** is schematically displayed in figure 5-3. The process involves two states of the same exciton (1s and 2s), which provides a reasonable explanation for the significantly enhanced emission intensity. Additionally, the fulfillment of the double resonance condition leading to a strong increase in the emission intensity of the neutral biexciton XX^0 is observed for the first time. This is due to the neutral biexciton being a combination of the bright, spin-allowed exciton at the K_+ valley and the dark, spin-forbidden exciton at the K_- valley [424, 443]. A further interesting point is that all detected PL lines are enhanced when the laser excitation energy is equal to the energy of the 3s A exciton state at $E = 1.875\,\mathrm{eV}$. This intensity enhancement is however not as strong as in the double resonance process. It is due to the fact that this process is governed by a single resonance when only the ingoing photon resonantly excites the 2s A exciton.

The electron-phonon coupling in the hBN/WSe_2/hBN heterostructure is further evaluated by studying the dependence of the circular polarization degree (CPD) of the PL lines on the helicity of the laser light as a function of the excitation energy. The CPDs of the excitonic complexes in different TMDC MLs have already been discussed, e.g., in Refs. [436, 437, 444]. Therein, the most efficient mechanism responsible for quenching the circular polarization of the excitonic emission is the scattering of the neutral A exciton between the different K valleys. Other relaxation processes are assumed to be less efficient. For example, the scattering of singlet and triplet trions between the K valleys requires spin flips of the electrons and holes, which is likely a slower process and, hence, less efficient.
Here, the impact of the **interlayer electron-phonon coupling** on the **preservation of the exciting light helicity** in the light emission is examined. For this purpose, several helicity-resolved emission spectra are detected at different excitation energies with two circular polarization configurations, as shown in figure 5-4. The polarization configurations of the exciting and emitted light are either co-polarized (σ^+, σ^+) (red line) or cross-polarized (σ^+, σ^-) (blue line). The excitation energies range from $E_{\mathrm{exc}} = 1.8774\,\mathrm{eV}$ to $E_{\mathrm{exc}} = 1.8117\,\mathrm{eV}$, corresponding to the energy range applied in the unpolarized PLE experiments. The respective evolution of the CPD of each individual

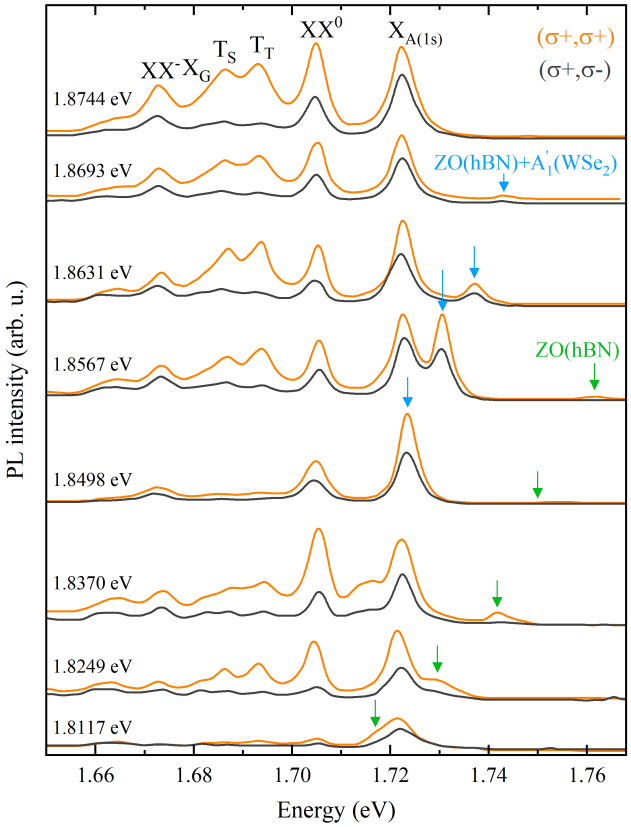

Figure 5-4: Polarization-resolved PL spectra for a series of excitation energies recorded in two circular polarization configurations of excited and emitted light: co-polarized (σ^+/σ^+ - orange line) and cross-polarized (σ^+/σ^- - black line) configuration. Excitation energies are marked at the left corner of each spectrum. The origins of PL lines are given in the upper panel. The Raman phonon modes ZO (hBN) + A'$_1$ (WSe_2) and ZO (hBN) are indicated by blue and green arrows, respectively.

PL line is presented in figure 5-5. The CPD for σ^+-polarized excitation is calculated by $P^+_{\mathrm{circ}} = (I_{\mathrm{co}} - I_{\mathrm{cross}})/(I_{\mathrm{co}} + I_{\mathrm{cross}})$. Herein, I_{co} and I_{cross} denote the PL intensity in the co-polarized [here (σ^+, σ^+)] and cross-polarized [here (σ^+, σ^-)] configuration, respectively. These intensities are obtained by fitting a Gaussian curve to each PL line. Although each PL line exhibits its own behavior, some common features are figured out in the evolution of the different CPDs. Firstly, the CPDs of all PL lines have a local maximum when the excitation energy corresponds to the energy of the excited A exciton in the 3s state at $E_{\mathrm{exc}} = 1.8774\,\mathrm{eV}$. Secondly, the CPDs of all lines decrease at first when lowering the laser excitation energy. Thirdly, when the excitation energy crosses the energy corresponding to the double resonance observed in the unpolarized PLE spectra, the CPDs gradually increase. In general, a CPD increase for the excitonic lines at the double resonance condition is related to a lower probability of scattering processes of the charge carriers and of spin flips via exchange interaction. Yet, the excitation energy at which the CPDs begin to increase is slightly different for the different PL lines.

The evolution of the helicity-resolved spectra leading to the CPD as a function of the excitation energy is analyzed separately for each PL line, starting with the neutral exciton and the neutral biexciton, as displayed in figure 5-5 (a). The line of the neutral A exciton in the 1s state obtains a CPD of about 20 % for $E_{\mathrm{exc}} = 1.8774\,\mathrm{eV}$, in resonance with the 3s state. It gets slightly smaller with decreasing excitation energy, until a minimum value of about 15 % at $E_{\mathrm{exc}} = 1.8631\,\mathrm{eV}$. At this energy, the excitation energy and the (combined) phonon modes are out of resonance with any optical transition of the WSe_2 ML. A further decrease of the excitation energy increases the CPD of the neutral exciton until it saturates at almost 30 %. At this energy, the complex Raman mode ZO (hBN)

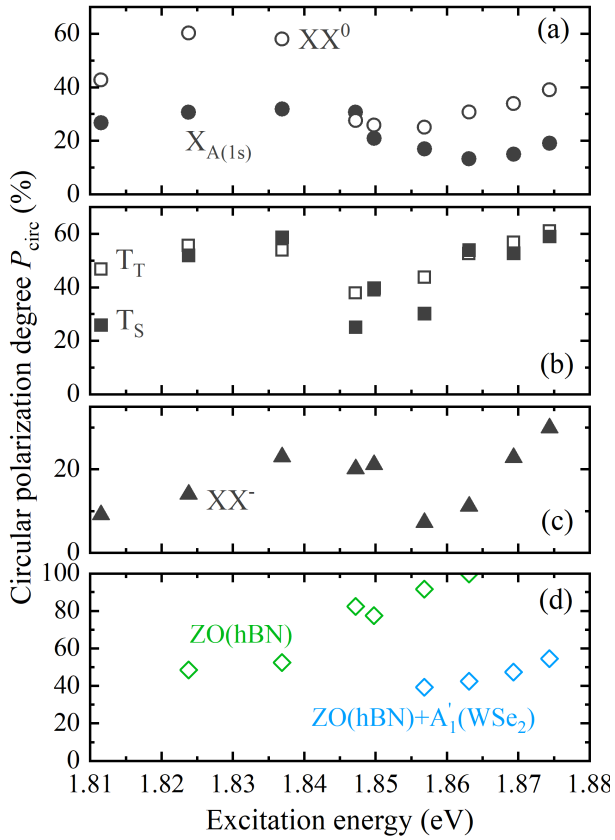

Figure 5-5: Degree of circular polarization plotted as a function of excitation energy for: (a) neutral 1s A exciton (X_A) and biexciton (XX^0), (b) negative trion in the singlet (T_S) and triplet (T_T) state, (c) negatively charged biexciton (XX^-), (d) Raman modes ZO (hBN) and ZO (hBN) + A'$_1$ (WSe_2).

+ A'$_1$ (WSe_2) crosses the neutral biexciton.
The line of the neutral biexciton exhibits a CPD of about 40 % for an excitation energy resonant with the 3s state of the neutral exciton, $E_{exc} = 1.8774\,eV$. Likewise, it slightly decreases with decreasing excitation energy and reaches a minimum value of about 25 % at $E_{exc} = 1.8567\,eV$. Note that the combined Raman mode at this excitation energy is the most intense line in the co-polarized spectra; it has a higher intensity than the emission lines of all excitonic complexes. Although this mode is close to the exciton resonance with $\Delta E \approx 4\,meV$, which roughly corresponds to the excitonic linewidths, both lines are still well resolved in the emission spectrum, as displayed in figure 5-4. For lower energies, between $E_{exc} = 1.8370\,eV$ to $1.8249\,eV$, the CPD of the biexciton increases until it reaches a broad maximum at 60 %. At these energies, the combined phonon mode is located at the low-energy wing of the neutral A exciton emission. Below these energies, the combined phonon mode merges with the neutral biexciton and they cannot be distinguished in the spectra anymore.
The difference between the CPDs of the neutral exciton and biexciton originates from their intra- and intervalley character, respectively. The bright exciton is formed by carriers residing at the same valley, while the biexciton is established by excitons located at the K_+ and K_- valley; thus, it has an intervalley character. Typically, intervalley quasi-particles have a slower valley depolarization than bright excitons, like indirect excitons. The bright exciton experiences strong long-range electron-hole exchange interaction, which yields an efficient depolarization [445]. Hence, the CPD decreases more strongly for the neutral exciton than for the biexciton and other intervalley states.

The CPD evolution of the trion lines follows a similar behavior like the other excitonic

emission lines, as shown in figure 5-5 (b). The trion lines also show an initial CPD decrease and subsequent increase in their CPDs as the excitation energy decreases. In addition to that, the CPDs of both trion types are about the same order. The dynamical polarization of resident electrons and holes, induced by the circular excitation [446], is stronger for the triplet states than for the neutral exciton states, since trions in such TMDCs live longer than the bright excitons. Accordingly, the CPDs of the trions are particularly higher than that of the neutral exciton. However, the triplet states exhibit a notable variation of their relative CPD at particular excitation energies. For the laser excitation energies at $E_{\mathrm{exc}} = 1.8567\,\mathrm{eV}$ and $1.8475\,\mathrm{eV}$, the CPD of the triplet trion is about 1.5 times larger than the CPD of the singlet trion. At the excitation energy $E_{\mathrm{exc}} = 1.8117\,\mathrm{eV}$, the triplet trion CPD is even about two times larger than the singlet trion CPD. The differences in the CPDs have been observed in WS_2 MLs before [436, 437, 444]. Therein, the differences have been attributed to their different dephasing rates: the electron-hole pair forming the triplet trion at one valley is scattered to the opposite valley due to electron-hole exchange interaction, where it forms the singlet trion. This scattering process is the fastest and hence the most efficient scattering mechanism responsible for quenching the polarization degree, as the singlet state is energetically favorable [444]. Since WS_2 obtains the same ordering of the spin-split CB and VB leading to a dark exciton ground state, this model may also be applied to WSe_2 MLs. For this scattering process, phonons with appropriate energies and momenta are required, which may originate from the WSe_2 ML, the hBN layers or even the Si substrate. Moreover, the process is more efficient when the ingoing and outgoing photons are in resonance with the singlet and triplet trions, at a double resonance. This double resonance is accessed at particular excitation energies, visible in the variation of the triplet-singlet CPD ratio.

Finally, the CPD of the negatively charged biexciton is presented in figure 5-5 (c). It behaves similar to the other excitonic complexes, with a (global) maximum of 30 % at $E_{\mathrm{exc}} = 1.8774\,\mathrm{eV}$, in resonance with the 3s state of the A exciton. Thereafter, a strong decrease is followed down to 5 % at $E_{\mathrm{exc}} = 1.8567\,\mathrm{eV}$ with decreasing excitation energy. Both CPD minima of the neutral and of the negatively charged biexciton are at the same excitation energy. The excitation energy of the CPD minimum for the neutral A exciton is slightly higher ($\Delta E = +6\,\mathrm{meV}$) and slightly lower for the trion complexes ($\Delta E = -9\,\mathrm{meV}$). The CPD minimum is followed by a rapid CPD increase up to 20 % from $E_{\mathrm{exc}} = 1.8498\,\mathrm{eV}$ to $1.8370\,\mathrm{eV}$. Further decreasing the excitation energy reduces the CPD down to 10 % at $E_{\mathrm{exc}} = 1.8117\,\mathrm{eV}$. The overall lower CPD hints at a higher depolarization rate of the charged biexciton compared to the other intervalley states, such as the triplet states or the neutral biexciton. Note that the neutral biexciton consists of a spin-zero bright exciton in one valley and a spin-one dark exciton in the other. The negatively charged biexciton, or quinton, is considered either as an electron-bound biexciton complex [423] or as an intervalley complex involving a bright singlet trion and a dark exciton residing in two different valleys [443]. It is assumed that the dissociation of the biexcitonic complexes occurs via the recombination of a bright exciton, since a dark exciton would emit linearly polarized light [423, 424]. However, the overall low CPD of the charged biexciton compared to the neutral biexciton may instead result from a significant contribution of the dark exciton recombination, decreasing the CPD. Additionally, the higher amount of recombination mechanisms may also contribute to the overall lower CPD.

Besides the CPDs of the PL lines, the CPD evolution of the Raman modes is presented in

figure 5-5 (d). The data for the single ZO (hBN) mode and for the combined ZO (hBN) + A'$_1$ (WSe_2) mode are plotted at the excitation energies at which they are separable from the PL lines. Their CPDs evolve differently with respect to the PL lines. The ZO (hBN) mode is almost completely polarized at high excitation energies and gradually loses its high CPD with decreasing excitation energies down to 50 %. The combined ZO (hBN) + A'$_1$ (WSe_2) mode has a comparatively low initial CPD of only about 50 %; it gradually decreases down to 40 %. The combinatorial interlayer phonon mode originates from the interactions between the adjacent WSe_2 and hBN layers [220]. The ZO phonon mode in hBN is not Raman active and thus not observable in the Raman spectra of pure hBN, due to the opposite out-of-plane motions of the B and N atoms. It manifests itself as an optically silent out-of-plane polarized B_{1g} (ZO) mode in few-layer hBN [447]. Since the interaction between the WSe_2 ML and the hBN layers lowers the symmetry of the heterostructure, the WSe_2/hBN interface has a reduced symmetry of C_3. This results in a change of the phonon mode: the original B_{1g} (ZO) mode becomes an A mode in the combined system, which is an allowed mode at the WSe_2/hBN interface [220]. Hence, this mode is Raman active with an in-plane electric field when the incident and outgoing light polarization are parallel, leading to well-defined polarization selection rules. Similarly, the A'$_1$ (WSe_2) phonon mode oscillates the Se atoms in an out-of-plane movement and is helicity-conserving [213, 220]. As both phonon modes vibrate out-of-plane, they are able to couple effectively. The product of both modes is still an A representation, so that the combinatorial mode has the same polarization dependence [220]. In contrast, the in-plane $E_{2g}(WSe_2)$ mode, which has about the same frequency, combined with the ZO (hBN) mode breaks the polarization selection rules.
The high CPD (circular co-polarization) of the phonon modes is a common feature for non-resonantly excited Raman scattering lines which preserve the circular polarization of the incident laser light. Yet, the combined mode has a significantly lower CPD than the pure mode at the same excitation energies, although both the pure and the combined phonon modes are helicity-preserving [213, 220]. The reason for this may lie in the electron-phonon (or exciton-phonon) interaction, since the CPD of both phonon modes is lowered when approaching the excitonic resonances. The phonon modes interact via deformation potential coupling, wherein the volume-changing lattice vibration modifies the crystal potential [234]. In this way, the out-of-plane electric field induced by the hBN phonon mode interacts with the in-plane dipole moment of the exciton in the WSe_2 ML. The induced field may lead to a rotation / distortion of the exciton and its dipole moment, and vice versa of the induced electric field of the phonons itself. Thus, the induced field may reduce the CPD of the phonon modes when the phonons approach and couple to the exciton states. Additionally, the CPD of the excitonic emissions may be weakened by the distortion of the exciton dipole moment. Moreover, the induced electric field may break the crystal symmetry, mixing the exciton spin eigenstates and reducing the valley polarization of the excitonic emissions [209].

The study of the interlayer electron-phonon coupling in a vdW heterostructure consisting of a WSe_2 ML encapsulated in high-quality hBN reveals a remarkable impact of the coupling on the excitonic transitions. First of all, the intensity of the WSe_2 ML emission is strongly increased due to a double resonance. This resonance appears when the 2s A exciton in WSe_2 is resonantly excited and the energy of the combined phonon mode ZO (hBN) + A'$_1$ (WSe_2) is equal to the energy separation between the 2s and 1s exciton states. The outgoing emission is hence in resonance with the 1s A exciton in WSe_2.

Moreover, the emission of the neutral biexciton XX^0 at the double resonance condition is strongly intensified. In addition to that, the interlayer electron-phonon coupling preserves partially the exciting light helicity in the emission of the neutral and charged excitons and biexcitons. The highest CPD of up to 60 % is observed for the emission of the neutral biexciton and the triplet trion. In contrast, the maximum CPD of the neutral A exciton is about two times smaller, whereas the CPD of the singlet trion depends highly on the excitation energy. Thereby, the electron-phonon interaction demonstrates a pronounced interlayer effect on the CPD of the excitonic emissions in WSe_2. These results, which have been published in [254], highlight a further detail in the electron-phonon coupling in TMDCs and present a way of enhancing the CPD of excitonic emissions. The latter point could be of interest for spintronic scenarios where information is optically imprinted into quantum materials and is read out with a high fidelity.

5.1.2 Anticrossing of photoluminescence and Raman scattering lines

Excitons in TMDC MLs obtain large binding energies and giant oscillator strengths, which makes them an attractive platform to study polaritonic physics. Polaritons are the result of an electromagnetic wave interacting with a polar excitation in matter, e.g., an electronic (exciton) or vibrational (phonon) resonance. They occur when the wavelength and energy of the (quasi-)particles are similar. Typically, polaritons are observed in optical microcavities where a solid material is embedded in a resonator [448, 449, 450]. Such a resonator may be an external structure consisting of, e.g., planar microcavities, plasmonic nanostructures or dielectric resonators [451, 452], and has a large quality factor and a small mode volume [451, 453]. The embedded material may be a bulk crystal or a quantum well showing a **strong light-matter coupling at an electronic (or vibrational) transition** with a high transition dipole moment [454, 455, 456]. Thus, polaritons have been observed in vdW materials [457, 458], including TMDC MLs [459, 460].

When the interaction rate between the cavity photons and the elementary excitations in the resonator is faster than the dissipation from the light and matter entities, a strong coupling regime is reached [460]. Therein, the strong coupling leads to the **formation of new eigenstates**, which are half-light, half-matter bosonic quasi-particles termed (exciton or phonon) polaritons. Polaritons draw fast dynamics and ease of transport from light, while they inherit the ability to collide with each other from matter [461]. The basic spectral features of polaritons are explained via the two-coupled-oscillator model. In this model, the strong coupling between a cavity photon and an elementary excitation results in two new eigenstates, labeled as upper and lower polariton. These are both linear superpositions of the cavity photon and the elementary excitation. The upper (lower) polariton mode is characterized by the photonic and exciton/phonon fields oscillating in-phase (with phase-opposition). Their **energetic separation** at the anticrossing is proportional to the coupling strength. This separation is the result of a level repulsion between the two coupled oscillators: when the coupling strength between the oscillators increases, the lower frequency decreases and the higher increases, leading to a larger splitting.

Strong light-matter interaction occurs when the electromagnetic field is confined and resonates in a cavity [452]. The usage of a cavity leads to an increased robustness of the polaritons and allows for studying the effects of external fields controlled by the cavity

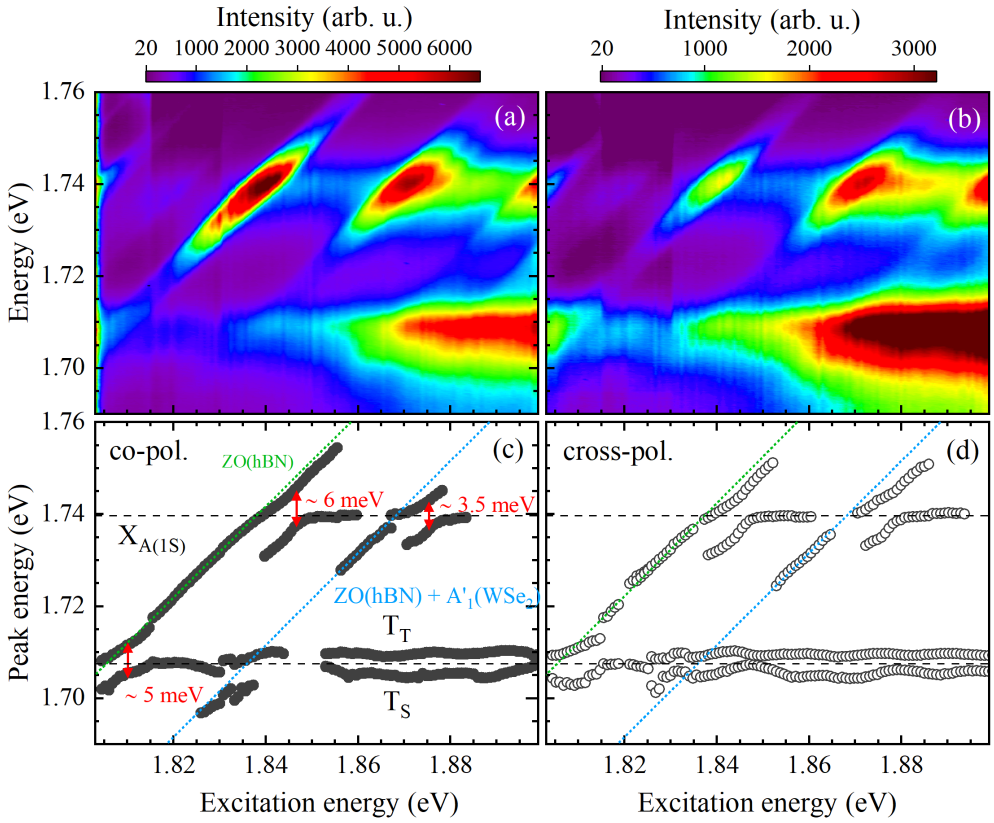

Figure 5-6: Anticrossing of PL and Raman scattering lines for circularly (a, c) co-polarized and (b, d) cross-polarized configuration: (a, b) Image plots and (c, d) fit results of the peak energy with possible anticrossing behavior; $T = 6\,\mathrm{K}$ and $P = 0.5\,\mathrm{mW}$.

geometry [459, 461]. A similar way is to use open cavities such as using simple flat metal films or nanorods [462, 463]. They are more accessible, but also require an external object to provide the optical mode confinement. Yet, the optical confinement may also be attained without a separate cavity, when the material containing the elementary excitation itself plays the role of a confining resonator [451]. These arrangements are termed self-hybridized, self-coupled or **cavity-free polaritons**, and have been realized in various material systems. For example, flakes of layered TMDCs and hBN with a thickness down to 40 nm have been identified as low-quality resonators that can reach the strong-coupling regime [464, 465, 466, 467]. Although the substrate plays an increasing role for decreasing layer thickness, TMDC flakes exhibit resonances themselves due to their high background refractive index in the visible range.

Here, we study a vdW heterostructure consisting of a WSe_2 ML placed on hBN. The thickness of the hBN layer is about 26 nm. In the PLE spectra displayed in figure 5-6, signatures of polaritons are observed at the exciton and trion resonance energies. They are created through the optical excitation of an exciton or trion in the WSe_2 ML and the ZO phonon in the hBN layers, leading to the creation of a **phonoriton** [468, 469, 470]. It is an elementary excitation that emerges from the hybridization between exciton, phonon, and photon, wherein the coherent superposition nature of phonoriton states is evidenced by the hybridization of exciton-polariton branches with phonon replicas. Although the excitation typically occurs at very different energy scales, they may be tuned

into resonance. The phonoriton anticrossing is most pronounced at the exciton and trion resonances for the out-of-plane ZO(hBN) phonon and the combined ZO(hBN) + A'$_1$ (WSe_2) mode. Driving a phonon mode into resonance with an exciton transition leads to an enhancement of the Raman scattering signal from that particular phonon mode. This resonance behavior has been observed for WSe_2 and $MoSe_2$ MLs encapsulated in hBN [220, 221, 422], see also section 5.1.1. At the exciton resonance energy, the Raman line is strongly enhanced in its intensity and the line energies are shifted in a significant way. Such an anticrossing-like behavior of the phonon mode and the exciton or trion PL line indicates the formation of a polariton or phonoriton, respectively.
The PLE spectra in figure 5-6 (a) are shown for the co-polarized (σ^+, σ^+) polarization configuration. Therein, the line of the neutral A exciton (X_A) in the 1s ground state is located at 1.740 eV. The negatively charged excitons are at 1.704 eV (singlet trion) and at 1.710 eV (triplet trion). The excitonic complexes are slightly shifted in comparison to figure 5-2 due to the different dielectric environments of the ML samples. As explained in section 5.1.1, the circular polarization degrees of the phonon modes are very high, so that they are mainly observable in co-polarization. Still, they gradually lose their polarization when approaching the excitonic states, compare figure 5-5 (d). This supports the observation of phonoritons also in the cross-polarized (σ^+, σ^-) PLE spectra, compare figure 5-6 (b). However, the resonant intensity enhancement is much less pronounced in cross-polarization, by a factor of four for the ZO (hBN) mode at the exciton PL line. The intensity enhancements at the other level-crossings are much weaker in both polarization configurations. In figures 5-6 (c) and (d), the peak energies fitted as a function of the excitation energy are shown for both polarization configurations. For increasing excitation energy, the peak energies of excitonic lines demonstrate a lineshift from low to high energies, while the Raman (phonon) lines are shifted from high to low energies, leading to an **anticrossing-like behavior**. The energy splittings at these level-crossings amount to about $3.5 - 6$ meV.
Additionally, the exciton and Raman lines are narrowed when they are tuned into resonance with each other, as depicted in figures 5-7 (a) and (b) for the neutral exciton and the ZO (hBN) phonon mode. The width of the exciton PL line is reduced from about 6 to 5 meV (20 % reduction), corresponding to the **linewidth reduction** of free polaritons [471]. In addition, the phonon Raman line is narrowed by more than 1 meV. Typically, the exciton PL is homogeneously broadened due to their radiative decay and their interaction with phonons [76]. Their inhomogeneous broadening is caused instead by the dielectric disorder of the substrate material, which induces local fluctuations of the exciton binding energies and of the free carrier bandgap [472]. The different contributions may be estimated by a fitting of the lines using a Voigt function. However, this is omitted owing to the quite pronounced background intensity. The results for the curve fittings may become indistinct, since the background intensity may interfere with the low-intensity wings of the Lorentzian distribution. As reported in Refs. [471, 473], the inhomogeneous broadening is reduced for excitons strongly coupled to cavity phonons caused by motional narrowing. Here, the reduction in the emission linewidths is also assumed to be a consequence of motion narrowing, when the polariton size is larger than the spatial size of the disorder-induced potential fluctuations. In this way, the linewidth broadening effect of the disordered dielectric potential is significantly reduced for the hybridized polariton mode. A detailed study of the linewidths shall be performed in future, also in consideration of the possible creation of phonoritons.
The energy splitting at about $E_{\mathrm{exc}} = 1.84$ eV, at the level-crossing where the exciton and

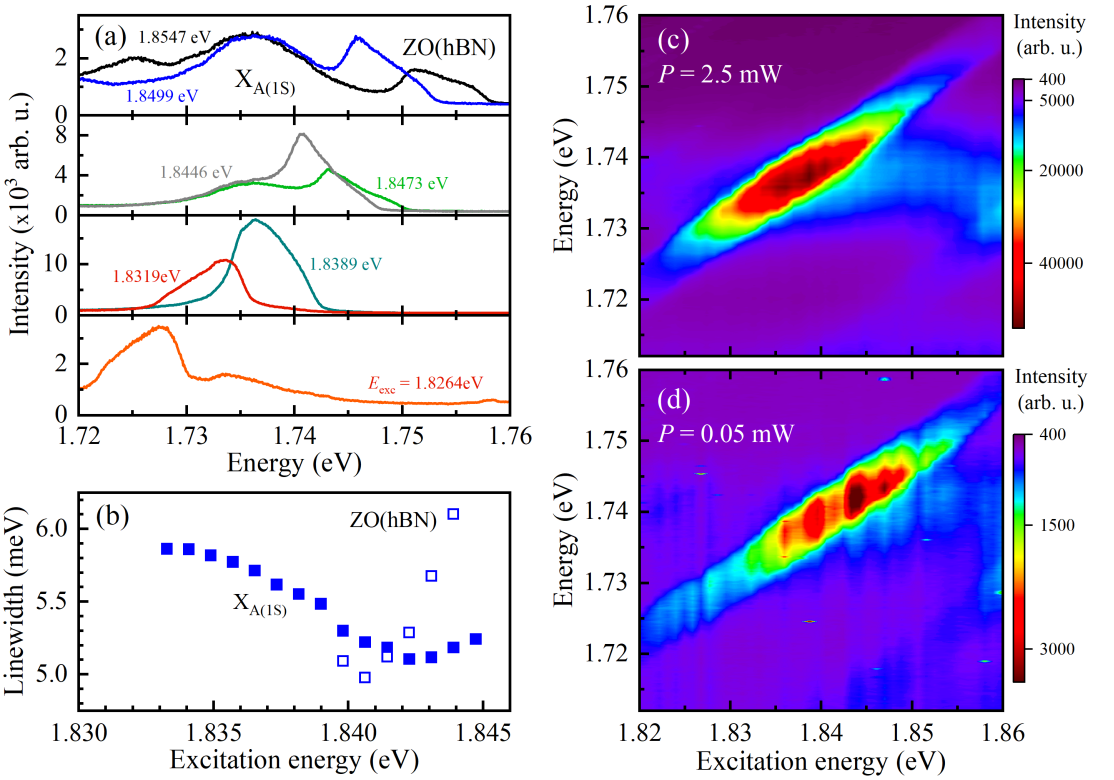

Figure 5-7: (a) Emission spectra of the WSe_2 ML for different excitation energies. (b) Linewidth reduction near the possible anticrossing for the exciton PL line and the ZO (hBN) Raman line. (c, d) Image plots of the exciton PL and Raman scattering line for (c) $P = 2.5\,\mathrm{mW}$ and (d) $P = 0.05\,\mathrm{mW}$.

ZO mode are in resonance, is further investigated using two different excitation powers. The resulting PLE spectra are displayed in figure 5-7 (c) and (d). For high laser power ($P = 2.5\,\mathrm{mW}$) the shape of the anticrossing differs from that measured at low laser power ($P = 0.05\,\mathrm{mW}$). Particularly at high excitation power, the intensity profile exhibits the asymmetric shape similar to that illustrated in figure 5-6 (a). This indicates a **higher light-matter coupling strength** for the high excitation power. The power dependence of the phonoriton characteristics is thus worth to be investigated further. Note that the exciton PL is shifted by $2-3\,\mathrm{meV}$ to lower energies values, for $P = 2.5\,\mathrm{mW}$. This likely due to a laser-induced thermal shift of the bandgap energy, but it could also be caused by the strong repulsion of the phonoriton levels.

The coupling strength of the observed phonoriton states may be determined by using a **semi-classical coupled harmonic oscillator model** [474]. It predicts upper and lower phonon-exciton/trion branches in agreement with the quantum-mechanical Jaynes-Cummings picture. The model describes the system of a two-level atom interacting with a quantized mode of a bosonic field, e.g. with a quantized electromagnetic field. The Hamiltonian in the semi-classical coupled oscillator model, consisting of the free field Hamiltonian, the atomic excitation Hamiltonian, and the Jaynes-Cummings interaction Hamiltonian [475], leads to the eigenenergies: $E_\pm = 1/2(E_\mathrm{phn} + E_\mathrm{X}) \pm \sqrt{g_\mathrm{c}^2 + \delta_\mathrm{t}^2/4}$ [476]. Here, g_c is the coupling rate, E_phn and E_X are the phonon and exciton resonance energies, and $\delta_\mathrm{t} = E_\mathrm{phn} - E_\mathrm{X}$ is the detuning. Strong coupling is achieved when the polariton linewidth is smaller than the corresponding Rabi-splitting energy $\hbar\Omega$

[474]. These may be determined from the curve fittings. With an exciton linewidth of $\gamma_X = 5.0 - 6.0\,\text{meV}$ and a phonon linewidth of about $\gamma_{phn} = 4.7 - 6.5\,\text{meV}$, the polariton linewidth $\gamma_{pol} = (\gamma_X + \gamma_{phn})/2$ amounts to about $(5.6 \pm 1.0)\,\text{meV}$. The splitting between the upper and lower polariton branches lies within a similar range of maximum $\hbar\Omega = 2g_c \leq 6\,\text{meV}$. Accordingly, the criterion for strong coupling is not definitely fulfilled. This corresponds to **leaky polariton modes** in the probed WSe_2/hBN non-cavity heterostructure. Instead, it is rather surprising to observe any polariton modes in this thin cavity-free heterostructure at all, which may be due to the high background refractive index of the TMDCs used [464, 477]. It allows for achieving a significant coupling between the phonon and the light/exciton without a cavity structure by enabling the self-hybridization of the combined mode.

The study of a vdW heterostructure consisting of a WSe_2 ML placed on top of a few hBN layers reveals a remarkable anticrossing in the PLE spectra as well as a significant intensity enhancement and linewidth reduction in both polarization configurations when the phonon mode ZO (hBN) and the combined phonon mode ZO (hBN) + A'$_1$ (WSe_2) cross the exciton and trion PL lines. These features are assigned to a phonoriton mode, which is a hybridization between exciton, phonon and photon. The two-coupled oscillators, exciton polariton and trion polariton (in TMDCs) as well as phonon polariton (in hBN) have been observed in vdW heterostructures [457, 458]. A hybridization of these polaritons into a phonoriton, a three-coupled oscillator, seems likely due to the strong exciton-phonon interaction and the very efficient light-matter coupling in these materials. This coherent superposition may also emerge with the trion states instead of the exciton state, when a significant part of the oscillator strength is transferred from the exciton resonance to the trion resonance [478]. The oscillator strength, which is reflected in the Rabi splitting and not the PL intensity, is controlled by the position of the Fermi level, hence by the uncontrolled doping of the sample [479]. Accordingly, the oscillator strength is larger for the exciton than for the trion, as reflected by their splitting energies of about 6 meV (X + ZO) and 5 meV (T + ZO). The interaction of exciton, photon, and two phonon modes, as in the combined phonon mode ZO (hBN) + A'$_1$ (WSe_2), leads to a biphonoriton eigenstate, showing a less pronounced resonant character of the dispersion [468]. This is reflected by a splitting energy of about 3.5 meV at the neutral exciton resonance. Additionally, the anticrossing at the X + ZO (hBN) resonance is studied for two different laser powers, revealing changes in the light-matter coupling and thus confirming the hybridization of the three modes. These results stress the importance of the electron-(exciton-)phonon interaction for the excitonic emissions in WSe_2. The occurrence of a three-oscillator combined mode opens up new possibilities to realize integrated devices with wide applications [457]. Further investigations are necessary, exploiting the tunable and distinct properties of polaritons, e.g., using an hBN-encapsulated WSe_2 ML for dielectric engineering of the heterostructure, enhancing the strong light-matter coupling by placing the heterostructure in an open-cavity system, and studying the laser power dependence for modifying the cavity-matter coupling strength.

5.1.3 Upconversion of exciton emission

TMDC MLs are well suited to study both intra- and intervalley excitons and trions as well as electronic and phononic interactions. As explained in section 5.1.1, the two-dimensional confinement of charge carriers and their reduced dielectric screening provoke

a variety of excitonic complexes in the emission spectra. In these structures, the valley contrasting spin splitting resulting from the strong SO coupling gives rise to spin and valley degrees of freedom [55]. The ordering of the spin-split CB and VB leads to a **dark exciton ground state** in tungsten-based materials, see figure 5-9 and additionally figure 2-9 (c). Thus, a large number of excitonic features may be positioned energetically below the bright exciton state, compare figure 5-8. The excitonic transitions in WSe_2 have been identified as bright singlet and triplet trion states [436, 437] and neutral and charged bright biexcitons [443, 480]. Additionally, spin-forbidden dark excitons [173, 439], dark (gray) trions [429, 430], and momentum-indirect dark excitons activated by scattering with defects or phonons [428, 431] may appear depending on the electron concentration [15]. The different excitons may be addressed either via conventional PL spectroscopy or using upconversion (UPC) photoluminescence [249, 435, 438, 481]. UPC PL differs from conventional PL in the way that the emission is detected at energies above the excitation energy, involving an energy gain, as explained in section 3.1. The required energy is taken from quasi-particles of the material. In this way, UPC PL provides information on both the energy spectra and on scattering processes, e.g., related to exciton-exciton, exciton-electron, or exciton-phonon interaction [249, 435, 481].

Here, UPC PL is used to study the interactions in hBN-encapsulated WSe_2 ML heterostructures with different thicknesses of the bottom hBN layer. The hBN-encapsulation narrows the emission lines and reduces local electric field fluctuations stemming from the substrate [73]. The bottom layer acts as a buffer layer between ML and substrate, likely due to charged defects or inhomogeneities in the charge distribution at the SiO_2 surface [15]. In this way, the **hBN bottom layer affects the electron concentration** in the ML [70, 168, 249]. The variable thickness of the bottom hBN from 10 to 250 nm thus leads to different two-dimensional electron gas concentrations. Specifically, three different samples with thicknesses of about $d = 240\,\mathrm{nm}$ (f_1), 30 nm (f_2) and 14 nm (f_3) have been investigated in detail, compare [15]. Note that the top hBN layer has a thickness of about 10 nm in all heterostructures. Moreover, the hBN-encapsulation reduces the photodoping effect caused by laser excitation. The samples are excited at excitation energies below the bright intravalley exciton energy in the nominal transparency window of the WSe_2 ML. The sample emission is detected at the energy of the bright exciton with an energy gain up to 50 meV. The emission intensities are investigated as a function of the excitation energy, revealing resonances in the UPC PLE spectra.
In figure 5-8 (a), the PL spectrum of the heterostructure with a bottom hBN layer thickness of 30 nm is presented for $T = 80\,\mathrm{K}$ and for $E_{\mathrm{exc}} = 2.33\,\mathrm{eV}$. Therein, the signatures of the singlet trion (T_S) and triplet trion (T_T) as well as of the neutral biexciton (XX^0) and the negatively charged biexciton (XX^-) are designated as a function of the energy difference of these emission lines relative to the neutral exciton (X). The neutral biexciton is observed about $-20\,\mathrm{meV}$ below the exciton, which is the energetically highest peak. The peaks at $-30\,\mathrm{meV}$ and $-37\,\mathrm{meV}$ are attributed to the spin-triplet and spin-singlet trion, respectively, forming the **trion fine structure**. The peak at about $-52\,\mathrm{meV}$ is assigned to the charged biexciton [443, 480]. The green curves indicate the fitting curves using five Lorentzian functions. Note that the PL of a similar $hBN/WSe_2/hBN/SiO_2/Si$ structure with the same excitonic complexes is shown in figure 5-2 at $T = 7\,\mathrm{K}$. The peaks of the excitonic complexes in the different samples differ in their intensities. This may be used to qualitatively estimate the electron doping of the samples, specifically, using the intensities of the neutral exciton and the triplet trion. Their peak intensities are about

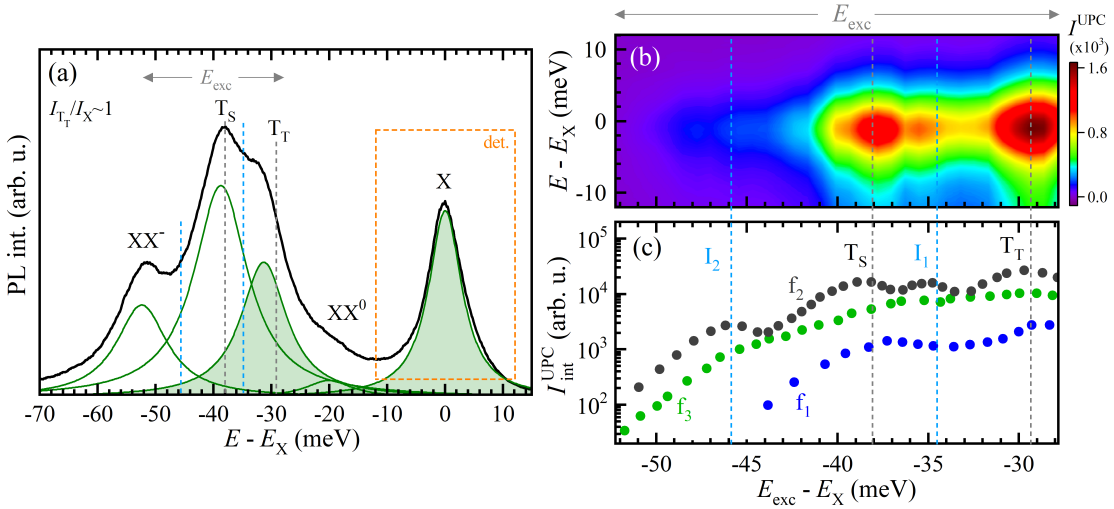

Figure 5-8: (a) PL spectrum of the hBN/WSe_2/hBN structure (sample f_2) at $T = 80$ K excited at $E_{exc} = 2.33$ eV, shown as a function of the energy difference with regard to the neutral exciton. The green lines result from a decomposition using five Lorentzian functions fitted to the PL. (b) Color map of the UPC PLE spectra and (c) integrated UPC PL of the neutral exciton for excitation energies ranging from 52 to 28 meV below the X resonance, between the XX^- and T_T peak, marked by gray arrows in (a). I^{UPC}_{int} is shown for all three samples f_1, f_2, f_3 with increasing electron density.

similar in this sample f_2. Thus, the ratio of the intensities I_{T_T}/I_X amounts to 0.98 at this temperature. The electron concentration is thus estimated to about $(1-2) \times 10^{11}$ cm^{-2} [15]. In this sample, the ratio decreases with higher temperature, when the trion peak increases, whereas it is different in the sample with the lower electron doping [15]. Moreover, the ratio increases with decreasing hBN layer thickness, indicating an increase of the trion peak intensity due to higher electron doping. A higher electron doping is further related to a slightly increasing exciton-trion energy splitting and a red-shift of the trion with respect to the neutral exciton [15].

The corresponding UPC PLE of the excitonic emission in the sample f_2 is displayed in figure 5-8 (b). As explained above, the UPC emission is detected at the energy of the bright exciton, indicated by the orange dashed box in the PL spectrum. Hence, the UPC PLE spectrum shows the neutral exciton PL line as a function of the excitation energy E_{exc} detuned from E_X using a color map. For this spectrum, the excitation energy is tuned between the XX^- peak and the high-energy flank of the T_T peak (marked by gray arrows in the PL spectrum). The energy difference $|E_{exc} - E_X|$ is denoted by the UPC energy gain ΔE. The integrated UPC PL intensity I^{UPC}_{int} over the exciton PL energy range of sample f_2 (black curve) yields the dependence shown in figure 5-8 (c). It reveals three **resonances** at the energy gains $\Delta E = 29.5$ meV, 34.5 meV, 38.0 meV and a weaker resonance at about 46 meV. The resonances at 29.5 and 38.0 meV correspond to the spectral positions of the **spin-triplet and spin-singlet trions** shown in figure 5-8 (a), marked in light blue. The resonances at 34.5 and 46 meV do not match any obvious PL transitions. Instead, the peaks named I_1 and I_2 may correspond to transitions observed in low-temperature PL spectra in gated hBN/WSe_2/hBN heterostructures [482]. Therein, the transitions are observed near the neutrality point for a slightly negative gate voltage, for low electron concentration. The peaks are assigned to **dark momentum-forbidden excitons**. They are assumed to be phonon replicas for neutral dark excitons produced

by the valley phonon-assisted momentum relaxation mechanism. However, their exact origin is still under debate [428, 431, 482] and possible explanations are discussed in the following.
Furthermore, figure 5-8 (c) demonstrates the integrated exciton PL upconverted at different resonance energies for the three samples with different electron concentration. The electron concentrations of the samples are roughly classified using the I_{T_T}/I_X ratio, which increases with decreasing bottom hBN layer thickness, from f_1 to f_3. The ratio of the sample f_1 with hBN thickness $d = 240\,\text{nm}$ amounts to about 0.25, where the exciton peak is significantly higher than the trion peak. This indicates a low electron concentration. The sample f_3 with thickness $d = 14\,\text{nm}$ has instead a higher trion peak, with a ratio of about 1.35. Due to the lower hBN layer thickness, the WSe_2 ML is less protected from the substrate and obtains a higher electron concentration. At $T = 80\,\text{K}$ the UPC intensity enhancements at the singlet and triplet trion states are visible for low (f_1), intermediate (f_2) and high (f_3) resident electron concentration. Nevertheless, the enhancement is significantly weaker at high electron concentration (f_3, green curve). Note that at low electron concentration (f_1, blue curve) the integrated UPC PL intensity is significantly weaker overall. As mentioned above, the peaks I_1 and I_2 are only observed in the structure with **medium electron concentration** (f_2).

The **upconversion of the spin-triplet trion to the neutral exciton** is attributed to **double-resonant Raman scattering** mediated by the A'$_1$ optical phonon. Thereby, the energy gain of the upconverted spontaneous anti-Stokes emission is about $28-30\,\text{meV}$. This energy gain closely matches the energy of optical phonons in WSe_2 [483]. In the UPC process, the absorption of an optical phonon promotes a trion into a state composed of an unbound electron and a neutral exciton [438, 483]. As shown in Ref. [483], both the energetically degenerate A'$_1$ and E' phonon modes contribute to the UPC process; both the homopolar A'$_1$ out-of-plane phonon and the in-plane E' LO phonon obtain an energy of 31 meV. This leads to an efficient population transfer between exciton and triplet trion mediated by the phonons. The efficiency of this process strongly depends on the temperature, electron density and dielectric environment of the heterostructures [483]. The **upconversion of the spin-singlet trion to the neutral exciton** has a slightly higher energy gain of about 38 meV. Hence, a population transfer between exciton and singlet trion may be explained by the **absorption of two optical phonons**. This multiphonon model is consistent with the increasing probability for multiphonon absorption at elevated temperatures [249].
The **upconversion of the I_1 and I_2 peaks**, assigned to dark excitons that upconvert light into bright intravalley excitons, may be explained either due to **exciton-phonon or exciton-electron coupling**. The gained energy that is required for the UPC process may be collected either from ML excitations, such as phonons or resident electrons, or from the incident laser excitation via (multi-)photon absorption. Since only low excitation densities are used for the excitation of the sample, the latter is neglected in the following. Instead, the exciton-phonon and exciton-electron coupling mechanisms are expounded, whereby both mechanisms fulfill energy, spin, and momentum conservation. These mechanisms are displayed in figures 5-9 (a) and (b). Note that intervalley transitions of the hole are disregarded, so that only the electron is the relevant interaction partner. At elevated temperatures, the process may be caused by non-linear optical processes [435, 481]. Thereby, the energy may be taken from the crystalline lattice (via phonon absorption [249]) or from resident electrons (via electron-electron scattering).

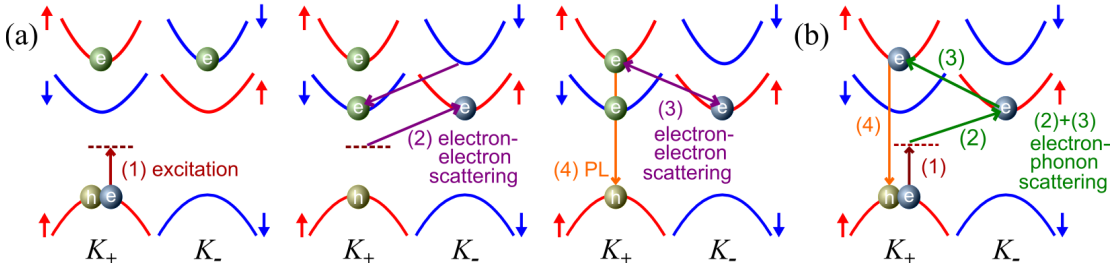

Figure 5-9: Schematic presentation of the exciton PL upconverted by an intervalley exciton acting as intermediate real state assisted by (a) resident electrons and (b) chiral optical phonons.

The electron-electron interaction allows for treating the process as an **anti-Stokes scattering of light**, with small wavevectors of the incident and emitted photons compared to the electrons. Since the resulting intensity of the UPC process is enhanced for real intermediate states, the intervalley exciton is assumed to be generated in the intermediate state. As the resonances in the UPC PLE spectra vary with electron density, the electron-assisted mechanism is more likely and explained first.
For this process, the **resident electron gas** that is formed in doped structures **delivers the required energy gain**. The electron-assisted mechanism via exciton-electron coupling consists of four steps, see figure 5-9 (a). Firstly, an incident photon with energy $\hbar\omega_{\mathrm{exc}}$ and negligible wavevector is absorbed and a virtual (direct-momentum) exciton state is formed (excitation). Secondly, the **electron-electron scattering** between the photoelectron (blue colored) and a resident electron (green colored) induces a change of their valleys under spin conservation. Through this process, the photoelectron gets in a real intermediate state, , which is the intervalley (dark) exciton due to the Coulomb binding between the photogenerated electron and hole. Thirdly, a second spin-conserving electron-electron scattering leads again to a valley switching. The final state is a bright direct exciton whose energy exceeds that of the incident photon. The fourth step is the electron-hole recombination (PL): a photon is emitted with the energy $\hbar\omega_{\mathrm{f}} = \hbar\omega_{\mathrm{exc}} - \Delta E_1 - \Delta E_2$, with the energy change ΔE_i of a given electron ($i = 1, 2$). This process is possible when electrons at the bottom of the excited conduction subbands scatter toward the bottom of the ground spin subbands (neglecting electron-hole interaction). The UPC process hence corresponds to a cooling of the resident electron gas. It may take place for an energy $E_{\mathrm{X}} - 2\Delta_{\mathrm{c}}$ with an exponential flank at the low-energy side, reflecting the thermal distribution of resident electrons, and a step-like feature at $\hbar\omega_{\mathrm{exc}} \geq E_{\mathrm{X}} - 2\Delta_{\mathrm{c}}$. The CB spin splitting Δ_{c} is evaluated to 17.3 meV and the energy differences between the intra- and intervalley exciton to 28.8 meV.
As mentioned above, the scattering process may also be induced via electron-phonon interaction, where the energy needed for the UPC process is taken from the crystalline lattice. The phonon-assisted mechanism also consists of four steps, see figure 5-9 (b). Again, the wavevectors of the photons are small compared to the wavevectors of the phonons, and the intervalley exciton is in the intermediate state. This process is analogous to the recombination of momentum-dark intervalley excitons via individual phonons. Likewise, the coupling between the dark intervalley and the bright intravalley exciton states may be mediated by single phonons and their combinations. The required spin-conserving transitions may be obtained under the assumption of **two chiral intervalley phonons** that are involved in the scattering. Note that defects may also act as scattering partners. Firstly, the incident photon with energy $\hbar\omega_{\mathrm{exc}}$ and negligible wavevector creates

a virtual exciton state. Secondly, an intervalley chiral phonon ($K_+ \rightarrow K_-$) with energy $\hbar\Omega_K$ is absorbed and transfers the electron in the exciton to the real intermediate state at the opposite valley (**electron-phonon scattering**). Like in the alternative electron-electron process, the change of the valleys conserves the spin. Thirdly, a second electron-phonon coupling process scatters the electron. This second intervalley chiral phonon ($K_- \rightarrow K_+$) transfers the electron to the real final state back at the initial valley. The fourth step is again the electron-hole recombination, where a photon is emitted with the energy $\hbar\omega_\mathrm{f} = \hbar\omega_\mathrm{exc} + 2\hbar\Omega_K$. The peak in the UPC spectra is thus observable at $\hbar\omega_\mathrm{exc} = E_\mathrm{X} - 2\hbar\Omega_K$, with $E_\mathrm{X} = \hbar\omega_\mathrm{f}$.
The two phonon-assisted mechanism demands phonons with energies $\hbar\Omega_K$ of about 17.3 meV (140 cm^{-1}) and 23 meV (180 cm^{-1}) to explain the required energy gain of the I_1 and I_2 peaks, respectively. Using helicity-resolved Raman scattering [15], a suitable candidate for the phonon mode contributing to the I_2 feature is revealed: the K-valley phonon mode K_3 [branch LO(E') [217]] with an energy of about 26 meV. This chiral phonon mode provides a dominant mechanism for an intervalley transition in the conduction band [482]. The absorption of two K_3 phonons may thus explain the UPC process of the I_2 resonance. The UPC process of the I_1 resonance may instead be explained by scattering via the Λ- or K-point LA phonons [484]. These obtain energies of about 14 meV and 18 meV, respectively. In this context, note that the exciton states at the Λ-valley may serve as intermediate states in the exciton formation and relaxation [485, 486]. Hence, exciton-phonon scattering may likely occur between the K- and Λ-valleys, which fits to the aforementioned model of the phonon-assisted UPC mechanism. The explanation of the UPC processes is concluded with final remarks on other scattering mechanisms. The trion UPC process may also be mediated via phonon scattering [483] or via electron-electron scattering. In the latter, the trion interacts with a free resident electron in the excited subband and merges to the exciton plus two free electrons ($\mathrm{T} + e' = \mathrm{X} + 2e$) [487]. The energies at the resonance in this process are $E_\mathrm{T} = \hbar\omega_\mathrm{exc}$ and $E_\mathrm{X} = \hbar\omega_\mathrm{f}$. Furthermore, the UPC process of the exciton may take place via other mechanisms, including defect-assisted processes. In these, the momentum is dissipated by a defect while the energy is contributed either by a phonon or an electron [15].

The study of WSe_2 MLs via UPC spectroscopy reveals remarkable insights into exciton-electron and exciton-phonon interactions. Therefore, the emission intensity of the exciton is studied as a function of the excitation energy and shows resonances due to the trions and biexcitons, but also two additional lines below the bright exciton. The lines are most pronounced at about $T = 80\,\mathrm{K}$ in heterostructures with moderate electron concentration, which is varied via the bottom hBN layer thickness. Their temperature and electron-doping dependences indicate that both electron-electron and electron-phonon interactions are relevant mechanisms in the UPC process. Moreover, the energy gain ΔE of the lines indicates the contribution of indirect (intervalley) excitons. The most likely UPC mechanism is mediated by the dark intervalley exciton in the presence of resident electrons. Thereby, the required energy and momentum of the scattering process are provided by the photogenerated and resident electrons. They scatter between the upper and lower spin subbands at the K-valleys. This leads to a cooling of the resident electron gas. Another proposed UPC mechanism involves the dark intervalley exciton via exciton-phonon interaction with chiral intervalley phonons. Therein, the phonons provide the energy and momentum necessary for the scattering process. Both fourth-order processes show pronounced signatures in the UPC PLE spectra, although they are not

observable in the PL spectra. These results, which have been published in [15], highlight a further detail in the exciton-electron and exciton-phonon coupling in TMDCs via brightening dark excitons. They help to clarify uncertainties in the interpretation of intervalley exciton spectra. Moreover, the brightening of spin or momentum dark excitons allows detailed insights into the light-matter interaction physics of excitons in TMDC MLs.

5.2 Magnetic field dependence of exciton-energy splittings in MoS_2 and $Mo_{0.7}W_{0.3}Se_2$ monolayers

The studied high-quality vdW **heterostructures** are assembled from hBN-encapsulated TMDC MLs, which enable observations of subtle optical and spin-valley properties. The assemblage of the structures using hBN allows for the detection of these features, which was beyond reach for structures exfoliated directly on standard SiO_2/Si substrates. The heterostructures studied in section 5.2.1 are based on **uncapped single layer MoS_2 stacked onto hBN layers of different thicknesses and hBN-encapsulated monolayers**. The heterostructure studied in section 5.2.2 is based on the **compound monolayer $Mo_{0.7}W_{0.3}Se_2$**, consisting of 70 % molybdenum and 30 % tungsten. It is displayed in figure 3-13. All Mo-based MLs were mechanically exfoliated from bulk crystals grown by the chemical vapor transport technique, see section 3.4.2. The MLs and the hBN flakes with different thicknesses are stacked to heterostructures, with typical flake sizes exceeding 10 µm × 10 µm. Thereby, the MLs are either stacked on top of a hBN flake or encapsulated in hBN using the deterministic all-dry stamping method. After the transfer of each layer, the heterostructures were annealed for 20 min at a temperature of 180 °C on a hot plate in air. The annealing improved the contact between the transferred layers, and strain-induced bubbles and wrinkles were reduced. The different hBN thicknesses lead to **different doping levels** of the MLs, so that the fine structure of excitonic complexes in molybdenum compounds is revealed, i.e., showing neutral and charged excitons as well as singlet and triplet trion states.
The samples were studied using a bath cryostat, which allows for measuring at cryogenic temperatures down to 1.5 K and for applying an external magnetic field of up to 10 T. They were mounted on a sample holder inside the VTI and were movable via nanopositioners, which allows one to address the different adjacent heterostructures. The samples were probed by PL and SFS spectroscopy (details in sections 3.1 and 3.2). The resonant optical excitation and detection were performed using the micro-setup SFOC (section 3.3.2). Non-resonant excitation of the samples was performed by the light of the second harmonic (532 nm, 2.33 eV) of a continuous-wave single-mode Nd:YVO_4 laser. The samples were excited (quasi-)resonantly using the light of a cw wavelength-tunable Ti:Sapphire laser with a wavelength range from 690 to 850 nm (1.80 to 1.45 eV, respectively) and with a linewidth < 1 GHz (see section 3.3). The laser-light power was additionally stabilized by a liquid-crystal amplitude modulator providing a laser-light amplitude stabilization of 0.05 %. The laser emission (light energy) was monitored spectrally by an interferometric wavelength meter. The laser light was focused on the sample under normal incidence using a high-resolution lens with a small focus ($f = 3.1$ mm) inside the VTI, leading to an excitation spot diameter of about 4 µm. The ML emission was collected by the same lens and was analyzed for PL experiments by a single monochroma-

tor (focal length of 0.5 m, with a spectral resolution of about 100 µeV). The spectrometer was equipped with a 600 g/mm, 900 g/mm and 1800 g/mm grating. Its choice was dependent on the desired resolution, see section 3.3.3. The spectrometer was further equipped with a cooled Si CCD camera. For SFS experiments, the emission was analyzed by a double monochromator (total focal length of 2 m). This spectrometer was equipped with a Peltier-cooled photon-counting detector (photomultiplier tube), see section 3.3.4. The widths of the four monochromator slits (entrance/intermediate/intermediate/exit) were typically set to 140/100/100/140 µm yielding a spectral resolution of 2.5 µeV. Furthermore, the exposure time was typically one second per spectral point. Unless specified otherwise, the measurements were performed at a temperature of 6 K in backward scattering geometry with a laser power typically set to < 1 mW. The polarization of the incident and detected light was set each by a combination of a Glan-Taylor prism and an achromatic quarter-wave (or half-wave) retardation plate. The circular polarization of light is denoted by $\sigma^{\pm}$, where the signs $\pm$ are determined by the sign of the photon angular momentum projection on the optical z-axis (light k-vector is parallel to z). The light propagation direction opposite to z is denoted by z'. Scattered laser light was reduced by using appropriate long- and short-pass edge filters.

5.2.1 Exciton-energy splittings in MoS_2

Similar to 2D semiconductor heterostructures, the optical spectra of TMDC MLs are dominated by excitonic transitions [421]. Herein, the two-dimensional confinement and the reduced dielectric screening enhance the excitonic properties, e.g., the binding energies and the robustness of the different excitonic complexes [432, 433]. This allows for observing the recombination of neutral (X) and charged (X^+ and/or X^-) excitons, visible as well-resolved lines in the PL spectra of MoS_2, compare figure 5-10 (b). Although **commonly seen as a bright TMDC material** with optically accessible excitons as the ground state, the excitonic configuration of this material was long under debate and required further investigation.
In comparison to other TMDCs, MoS_2 has been widely used as a dry lubricant and as a catalyst, before TMDC MLs became interesting due to their direct bandgap. MoS_2 differs from the other TMDCs by its **small spin-splitting of the CB** of about +3 meV [488], compare section 2.3.4 and figure 2-9. Although the single-particle arrangement of spin-polarized CBs in MoS_2 is bright, its excitonic ground state configuration (bright or dark) was unclear [168]. Recent theoretical results reveal a dark excitonic ground state in MoS_2 due to electron-hole exchange interaction and different effective masses of spin-split conduction bands [418]. The study of these subtle optical and spin-valley properties that were previously hidden in broad PL peaks [425] was facilitated by encapsulating the MLs with hBN, which improved their optical quality. It allows for narrowing the exciton linewidth down to 2 meV at low temperatures [73]. In this way, it could be shown that, similar to tungsten-based TMDCs, MoS_2 obtains a trion fine structure [436, 489, 490]. This supports that MoS_2 has a **dark excitonic ground state**, despite having a **bright single-particle CB arrangement**. Interestingly, substantially different effective exciton g-factors were determined in hBN-encapsulated MoS_2 heterostructures; $g_X = -1.7$ in magneto-PL experiments [73] and nearly two times higher $g_X = -3.0$ in magneto-transmission measurements [491]. Moreover, a large electron mass leads to a heavier than predicted reduced mass of the exciton [166, 488, 492]. The interplay of the band

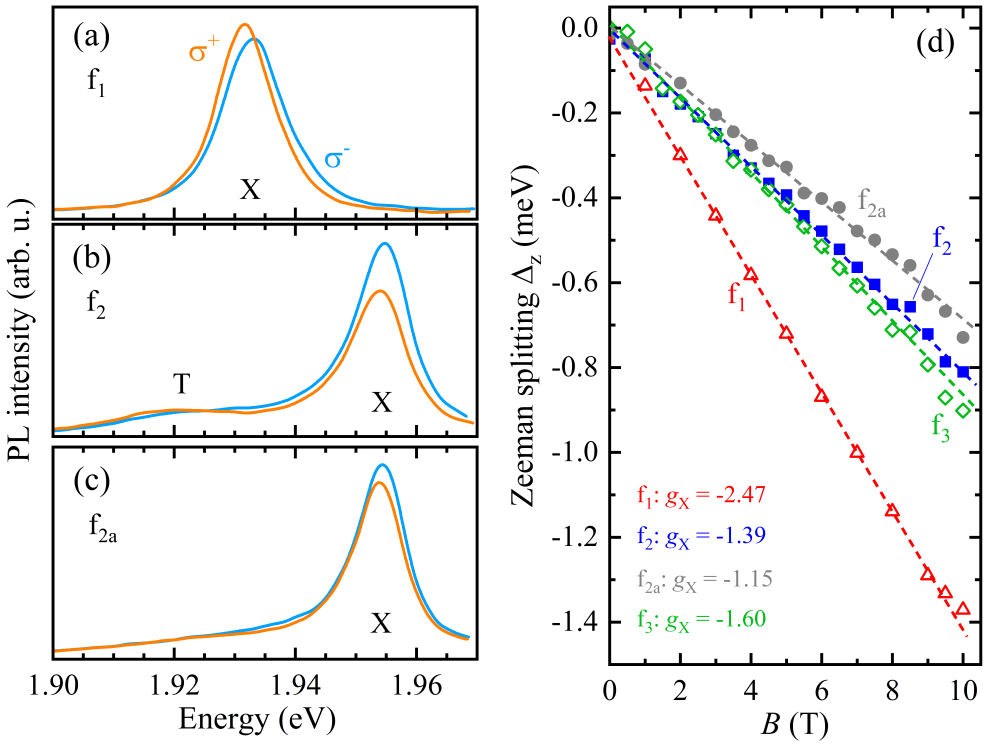

Figure 5-10: Circularly polarized PL spectra at $B = 10\,\mathrm{T}$ for different MoS_2 MLs: (a) hBN-encapsulated (f_1), (b) MoS_2 on 120 nm hBN (f_2), and (c) MoS_2 on 100 nm hBN (f_{2a}). (d) Exciton Zeeman splitting for the different samples, including MoS_2 on 250 nm hBN (f_3).

structure [488], electron-electron interactions [493, 494], enhanced spin-splitting [495] and other contributions [496] make MoS_2 one of the most challenging materials to understand and worthwhile to investigate further.

In this part, the optical properties of uncapped (MoS_2/hBN) and hBN-encapsulated (hBN/MoS_2/hBN) MLs of MoS_2 are studied. Thereby, the investigated uncapped MLs are stacked onto hBN layers of different thicknesses. The optical properties are examined using magneto-PL spectroscopy. In the optical spectra of the different MLs, neutral and charged excitons are observable. Thereby, the trion lines appear depending on the doping levels, or **electron concentrations**, of the MLs, which can be **varied via the hBN thickness**. The doping level is estimated to be very low (or nearly neutral) in the hBN-encapsulated structure f_1. The PL is dominated by the neutral exciton linewidth with a FWHM of about 4 meV [168], compare figure 5-10 (a). This structure has thicknesses of the bottom and top hBN layer of about 120 nm and 10 nm, respectively. The uncapped MLs f_2 and f_{2a} obtain relatively higher doping levels, visible by a broad trion line showing up in the PL spectra, see figures 5-10 (b) and (c), compared to (a). They obtain thicknesses of the bottom hBN layer of about 120 nm (f_2) and 100 nm (f_{2a}). The higher electron concentration is further supported by a transfer of the oscillator strength of the neutral exciton to the negatively charged exciton [168, 497]. The f_2 structure has a slightly higher electron concentration than f_{2a}, since the higher hBN thickness leads to a higher electron doping, as reflected by the higher trion peak in the PL. This is assumed to stem from a naturally n-doping of MoS_2, whereas positively charged defects embedded in SiO_2 reduce the electron charge in MoS_2 heterostructures. Likewise, a fourth MoS_2 ML on 250 nm hBN (f_3) obtains a high doping level, visible by the emerging trion fine

structure in the PL spectrum [168]. Note that the uncapped heterostructures are further subjected to photo-doping effects caused by the laser excitation, in contrast to the hBN-encapsulated sample.
By applying a magnetic field, the magneto-optical response is observed in the PL spectra, allowing for the calculation of the exciton g-factor. Figures 5-10 (a)-(c) show the low-temperature ($T = 5\,\mathrm{K}$), polarization-resolved PL spectra at $B = 10\,\mathrm{T}$ recorded for the heterostructures with low and medium electron doping. The samples are excited using linearly polarized laser excitation with an excitation energy of $E_{\mathrm{exc}} = 2.33\,\mathrm{eV}$. The Zeeman splitting $\Delta E_{\mathrm{Z}} = E_{\sigma^+} - E_{\sigma^-} = g_{\mathrm{X}}\mu_{\mathrm{B}}|\vec{B}|$ is calculated via the shift between the σ^+ and σ^- polarized components of the PL, compare equation (2.20). The splitting depends linearly on the magnetic field, as shown in figure 5-10 (d). The resulting exciton g-factors are $g_{\mathrm{X}} = -2.47 \pm 0.01$ for the encapsulated sample f_1, and $g_{\mathrm{X}} = -1.15 \pm 0.01$ for sample f_{2a}, $g_{\mathrm{X}} = -1.39 \pm 0.01$ for sample f_2, and $g_{\mathrm{X}} = -1.60 \pm 0.01$ for sample f_3. For the hBN-encapsulated ML sample, the exciton g-factor is distinct and the lowest. For the MoS_2/hBN structures without a cap layer, the **exciton g-factor decreases with rising thickness of the hBN layer** (with rising electron concentration). Note that the trion features in the higher doped samples are not sufficiently resolved in the spectra to estimate their effective g-factors.
The effective exciton g-factor in the f_{2a} structure (MoS_2 on 100 nm hBN) is studied further, as its emission spectrum is dominated by a relatively narrow X line. The temperature dependence of this sample is displayed in figure 5-11. Figure 5-11 (a) compares typical PL spectra of the structure at a magnetic field of $B = 10\,\mathrm{T}$, measured at different temperatures ($T = 5\,\mathrm{K}$, 20 K, 40 K, and 60 K). Thereby, the sample shows a broadening of the X emission line and a shift to lower energies with temperature. The Zeeman splitting of the exciton at the four different temperatures is shown in figure 5-11 (b). The resulting effective exciton **g-factor decreases** from -1.15 to -1.74 **for increasing temperature** from 5 K to 60 K, see figure 5-11 (c). This corresponds to a decrease of the exciton g-factor by about 34 %. The decrease is related to the temperature broadening of the X emission. Additionally, it may also result from different thermal distributions of the electrons in the spin-split subbands. This assumption is based on the observation that there is no temperature effect on the exciton g-factor for the hBN-encapsulated ML sample f_1 [168].
The observed exciton g-factor of the encapsulated MoS_2 ML, $g_{\mathrm{X}} = -2.47$, lies in between the values of the g-factors determined for similar samples with very narrow exciton linewidths ($2 - 4\,\mathrm{meV}$), with $g_{\mathrm{X}} = -1.7$ [73] and $g_{\mathrm{X}} = -3.0$ [491]. However, the Zeeman splitting and hence the g-factors seem to depend on the doping level and overall optical quality of the sample. Likewise, the optical quality may be estimated by the linewidth of the PL. In comparison to other TMDC MLs, the small exciton Zeeman splitting in MoS_2 may arise from the interaction with energetically close spin- and valley-forbidden dark excitons [176, 491]. These semi-dark and dark excitons have been identified at 14 meV below the bright states in the PL spectra of hBN-encapsulated MoS_2 [104]. The energy difference of the exciton splitting depends on the CB SO splitting, the exciton binding energies and the electron-hole exchange interaction. The effective g-factor, which reflects the bright-dark exciton interaction, may further be tuned by the electron concentration and the dielectric environment. In this way, it may be possible to change the magnitude of the bright-dark splitting for different MoS_2/hBN heterostructures. Yet, this point needs further theoretical input.

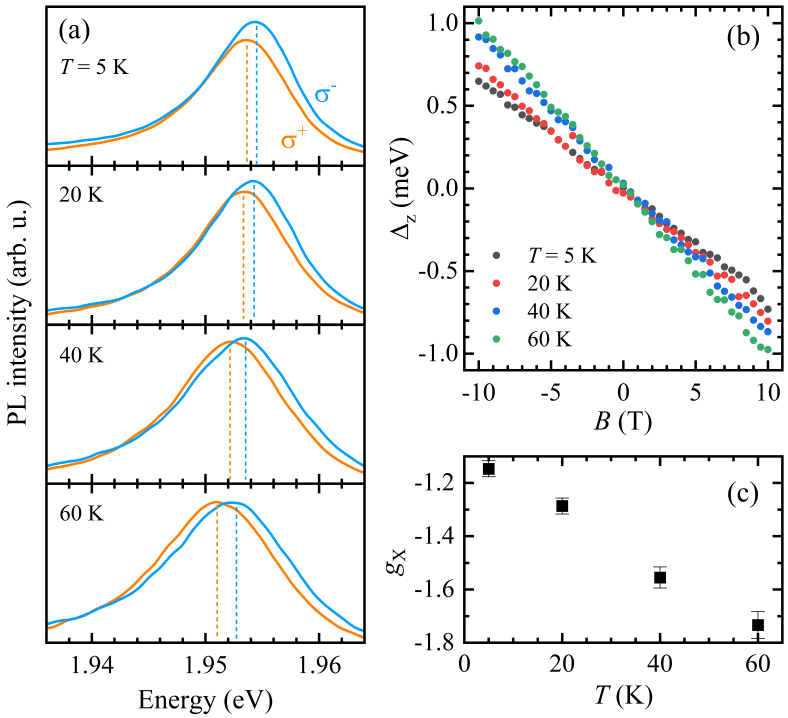

Figure 5-11: (a) Polarization-resolved PL spectra of the uncapped structure f_{2a} recorded at $T = 5\,\mathrm{K}$, 20 K, 40 K, and 60 K. (b) Exciton Zeeman splitting for the different temperatures. (c) Temperature evolution of the effective exciton g-factor.

The study of MoS_2 ML samples via polarization-resolved magneto-PL spectroscopy reveals distinct doping levels estimated qualitatively based on the shape of the PL. The different levels lead to different effective exciton g-factors of the ML samples. The g-factor reaches the lowest value of -2.47 in the hBN-encapsulated structure with a nearly neutral doping regime. In the uncapped MoS_2 structures with a relatively large number of resident electrons, the excitonic g-factor varies from -1.15 to -1.60 depending on the thickness of the bottom hBN layer, which changes the electron concentration. Moreover, the g-factor decreases with rising temperature in the uncapped samples. Besides broadening effects, the decrease may result from different thermally dependent electron distributions in the spin-split subbands. These results, which have been published in [168], highlight the coupling of electron spins in TMDCs to magnetic fields and shed light on the interpretation of the excitonic properties in MoS_2. Since the effective g-factor determines the behavior of electron spins, its knowledge allows one to understand the interaction between the particle spin and its solid-state environments. Thus, the measurement and control of a confined electron spin are important for spintronics and quantum information processing applications.

5.2.2 Exciton-energy splittings in $Mo_{0.7}W_{0.3}Se_2$

Two-dimensional TMDCs have attracted intense interest due to their direct optical bandgap, large SO splittings, coupled spin-valley states and strong light-matter interaction dominated by robust excitons. As explained in chapter 2.3.4, TMDC materials vary in the optical accessibility of their excitonic ground state, leading to different temperature dependences of their PL intensities. The optoelectronic properties of TMDCs

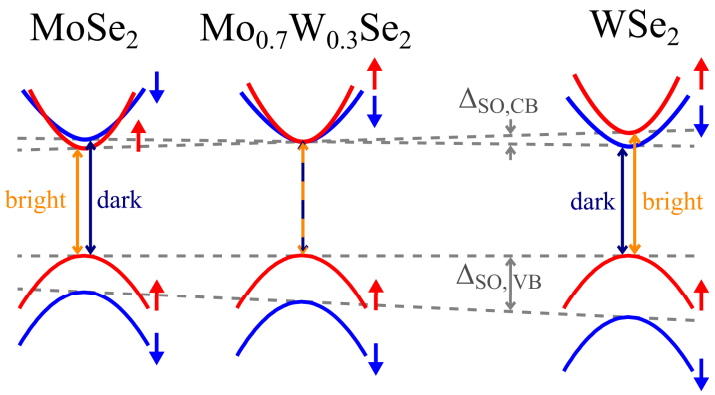

Figure 5-12: Band structure in the K_+ valley of the alloy $Mo_{(1-x)}W_xSe_2$ changing from $MoSe_2$ ($x = 0$) via $Mo_{0.7}W_{0.3}Se_2$ ($x = 0.3$) to WSe_2 ($x = 1$). After Fig. 1 (a) in [498].

may be modified using **alloying**: it provides a versatile and precise **way to tailor the band structures** of TMDCs by adjusting the composition of either the transition metal or chalcogen elements. The continuous tuning between the characteristic bandgaps of the two constituting binary compounds is useful for optoelectronic applications [498, 499]. In addition, alloying TMDCs allows one to **engineer the SO coupling** between the CBs and the VBs, advancing the spin and valley control in these materials. Hence, in such a ternary alloy, a wide range of efficient optical emission is achievable, while alloying also leads to an effective suppression of deep defect levels [500].
Here, the alloy $Mo_{(1-x)}W_xSe_2$ is tuned by varying the relative TM concentration x from the bright $MoSe_2$ ML ($x = 0$) to the dark WSe_2 ML ($x = 1$), see figure 5-12. Note that the SO splittings may change nonlinearly with concentration x, differently than pictured, which may lead to bandgap bowing [501]. In the range from $x = 0.3$ to 0.4, changes of the exciton energies, valley polarization and SO splittings indicate a shift from the bright to dark exciton ground state [498]. Hence, a tungsten composition of $x = 0.3$ is chosen, leading to a **negligible CB spin splitting**, compare figure 5-12. The almost absent splitting allows for a direct coupling of light to the electron spin states of both CBs. Interestingly, large effective exciton g-factors were determined in $Mo_{0.7}W_{0.3}Se_2$ placed on hBN. The effective g-factors of the excitonic complexes are about $g = -6$ to $g = -7.3$, and thus substantially larger than typical effective excitonic g-factors of $g \approx -4$ in binary TMDC MLs [138, 142, 176, 423, 440, 502, 503].

In this thesis, the **effective *g*-factors of the different excitonic complexes** of $Mo_{0.7}W_{0.3}Se_2$ on hBN are studied using magneto-PL. The PL of this ternary alloy is presented in figure 5-13 (a), in comparison to the PL of both binary TMDC MLs $MoSe_2$ and WSe_2. Thereby, $Mo_{0.7}W_{0.3}Se_2$ obtains PL energies of about $E_X = 1.64\,\text{eV}$ and $E_T = 1.61\,\text{eV}$, resembling the PL energies of the binary materials, $E_X = 1.708\,\text{eV}$ and $E_T = 1.684\,\text{eV}$ (WSe_2) and $E_T = 1.604\,\text{eV}$ ($MoSe_2$). The exciton emission energy is energetically closer to that of $MoSe_2$, as expected for the low tungsten concentration of $x = 0.3$ [499]. However, typically the PL of $Mo_{(1-x)}W_xSe_2$ first red-shifts and then blue-shifts with increasing x, with a minimum for $x = 0.3$ [501], so that the PL emission should actually be energetically lower compared to $MoSe_2$. Yet, the different ML environments, e.g., due to hBN-encapsulation, bottom or top hBN layer, and different hBN thicknesses, influence the overall PL position and lead to a shift in the PL energies. The polarization-resolved PL spectra in figure 5-13 (a) show neutral and charged excitons. The exciton peak is the energetically highest peak, while the trion peak is the most intense peak. This indicates a high resident electron concentration in the ML. In between these peaks, the biexciton (XX) and the intervalley exciton (IVX) peaks are

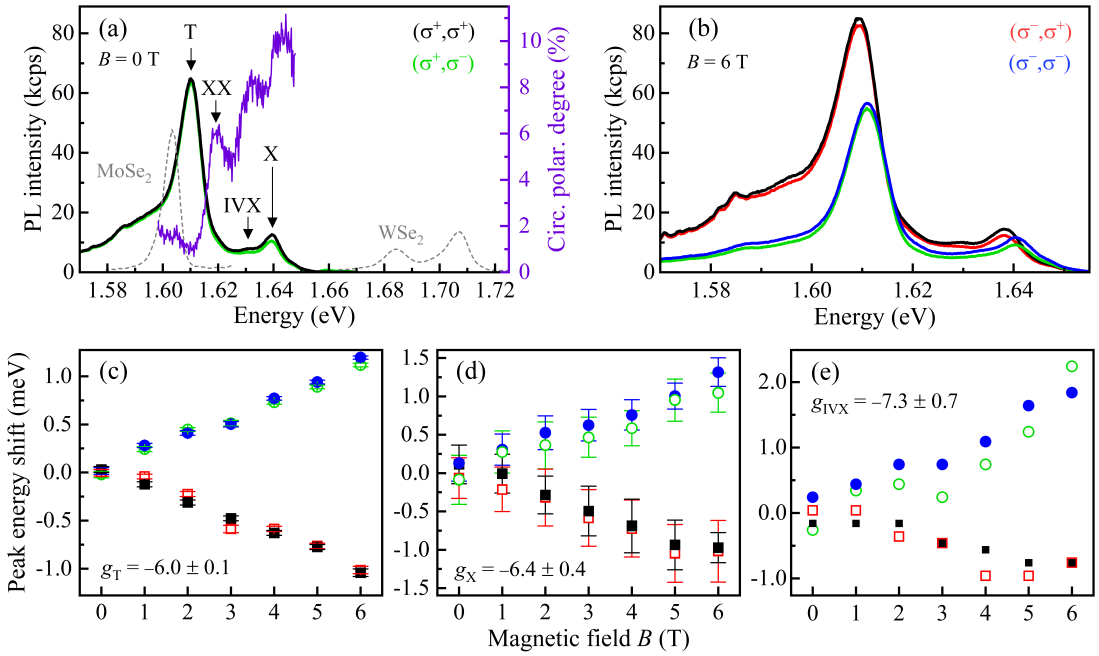

Figure 5-13: (a) Polarization-resolved PL spectra of $Mo_{0.7}W_{0.3}Se_2$ excited with σ^+-polarized light at $T = 6\,\mathrm{K}$ and $B = 0\,\mathrm{T}$, in comparison to the PL of $MoSe_2$ and WSe_2 MLs. The CPD of the excitonic complexes is shown by the purple curve (right scale). (b) Polarization-resolved PL spectra at $B = 6\,\mathrm{T}$. (c-e) Polarization-resolved peak energy shifts as a function of the magnetic field strength, for the different excitonic complexes.

observable, supported by changes in the circular polarization degree (CPD). The CPD of the PL is calculated by $P^+_{\mathrm{circ}} = (I_{\mathrm{co}} - I_{\mathrm{cross}})/(I_{\mathrm{co}} + I_{\mathrm{cross}})$ for σ^+-polarized excitation, as in section 5.1.1. The **intervalley dark exciton** is observed as a peak in the PL at $E_{\mathrm{IVX}} = 1.63\,\mathrm{eV}$, corresponding to an energy difference of about 10 meV to the intravalley bright exciton. Considering only weak energetic differences between the K_+ and K_- valley states, as will be discussed later, this energy difference is proposed to display the binding energy of the momentum-dark (intervalley) exciton. This indirect exciton is optically observed due to phonon assistance [428, 504]. The **biexciton** is observed as a peak in the CPD at $E_{\mathrm{XX}} = 1.62\,\mathrm{eV}$, shifted by about 20 meV from the bright X, which corresponds to the binding energy of the neutral biexciton in TMDC MLs [423, 505]. The exciton PL demonstrates a slightly positive CPD, while the other excitonic complexes possess a lower CPD, e.g., the trion PL is practically unpolarized. The **low CPD of the excitonic complexes** likely originates from the strong coupling to the energetically close spin-dark exciton, and, correspondingly, to the mixing of the electron spin states. The preference of the σ^+-polarized light under non-resonant excitation indicates nevertheless that the corresponding spin-up CB is slightly lower in energy compared to the spin-down CB. The low CPD may also result from a polarization-nonconserving scattering with phonons or a scattering by defects induced by local crystal disorder. The latter is present in the ternary alloys and has considerable impact on the optical and transport properties of excitons [506]. Correspondingly, the other excitonic complexes demonstrate similar polarization behavior. In particular the negligibly weak CPD of the negative trion PL underlines that the **defect scattering** is a potential source of the depolarization.
With increasing magnetic field, the differently polarized PL lines of the excitonic com-

plexes separate in energy; the magneto-PL spectra shown in figure 5-13 (b) display clear differences in PL intensity and energy for the different polarization configurations. The σ^+-polarized PL peaks shift to lower energies while gaining a higher intensity. The σ^--polarized peaks shift to higher energies and decrease in intensity. The change in the intensity may be explained by the Boltzmann factor; the energetically lower lying σ^+ states are more strongly occupied than the states with opposite polarization. From the magnetic field-dependent shifts in the peak positions, as shown in figure 5-13 (c)-(e), the effective g-factors of the different excitonic complexes are obtained according to equation (2.20). Since the σ^- polarized states are shifted to higher energies, the ***g*-factors are negative** by definition. The calculated g-factors are $g_{\mathrm{X}} = -6.4 \pm 0.4$ for the bright exciton, $g_{\mathrm{T}} = -6.0 \pm 0.1$ for the trion and $g_{\mathrm{IVX}} = -7.3 \pm 0.7$ for the intervalley exciton. The effective g-factors may be **contributed by the spin splitting as well as valley Zeeman splitting**. Note that the orbital contribution may be neglected, since the CBs are composed mainly of electrons in d-orbitals with $m_l = 0$. In accordance with literature, the g-factor for both neutral and charged excitons shall then lie within the range of 5 [507]. The discrepancy between that value and the **large effective *g*-factors** for the different exciton complexes may be attributed to the **resident electron concentration** which is able to impact the magnetic field dependence of the excitonic states in TMDC MLs. A high number of resident electrons may affect the excitonic binding energy due to a state-filling effect, in particular in a nonzero magnetic field [507, 508], which enhances the Zeeman splitting. Alternatively, **strong exchange interaction** may contribute to the orbital magnetic moment giving rise to a larger valley g-factor. The interaction strength may increase due to spin-valley degeneracy [507]. While the definite reason for these enhancements of the Zeeman splittings is unclear, large g-factors have already been obtained for dark excitons ($g = -9.75$ [423] and $g = -9.3$ [440]) and for interlayer excitons ($g = -16, g = 6.7$ [509]).

The behavior of the PL peak intensities as function of the magnetic field is displayed in detail in figures 5-14 (a) for the trion and (b) for the exciton. Based on the ratio of the PL peak intensities, the magnetic field-induced circular polarization degree $\rho_{\mathrm{c}}^{\sigma}$ and the degree of optical orientation $\rho_{\mathrm{o}}^{\sigma}$ are calculated using $\rho_{\mathrm{c}}^{\sigma} = \frac{P_{\mathrm{circ}}^{+} + P_{\mathrm{circ}}^{-}}{2} = \frac{1}{2}\left(\frac{I_{+}^{+} - I_{-}^{+}}{I_{+}^{+} + I_{-}^{+}} + \frac{I_{+}^{-} - I_{-}^{-}}{I_{+}^{-} + I_{-}^{-}}\right)$ and $\rho_{\mathrm{o}}^{\sigma} = \frac{P_{\mathrm{circ}}^{+} - P_{\mathrm{circ}}^{-}}{2}$ [510]. The CPD $\rho_{\mathrm{c}}^{\sigma}$ increases for both the exciton and the trion, as shown in figure 5-14 (c). For the exciton (trion), it rises with about 2.4 %/T (4.5 %/T), leading to a **magnetic field-induced valley polarization**. The polarization increase with magnetic field indicates that it arises from magnetic field-induced changes in the exciton and trion populations [511]. The CPD increases faster for the (intervalley) trion than for the exciton due to the high number of resident electrons in the ML, which may lead to an intervalley charge transfer [508]. Contrastingly, the **optical orientation** $\rho_{\mathrm{o}}^{\sigma}$ remains about **constant** for both complexes, see figure 5-14 (d). It is about 10 % for the exciton and about 2 % for the trion. Accordingly, the polarization (helicity) of the exciting laser light is only weakly conserved by the exciton and trion complexes. As the optical orientation degrees only weakly depend on magnetic field induced changes in the level splittings, the optical orientation degree is likely coined by the **electrons scattered by the defect states** which is not impacted by an external magnetic field. The electron scattering rate remains the same at low and high B-fields so that the depolarization of the exciton and trion is significant, independent of the magnetic field strength. Typically, the optical orientation degree is low in bright TMDC MLs and decreases with increasing

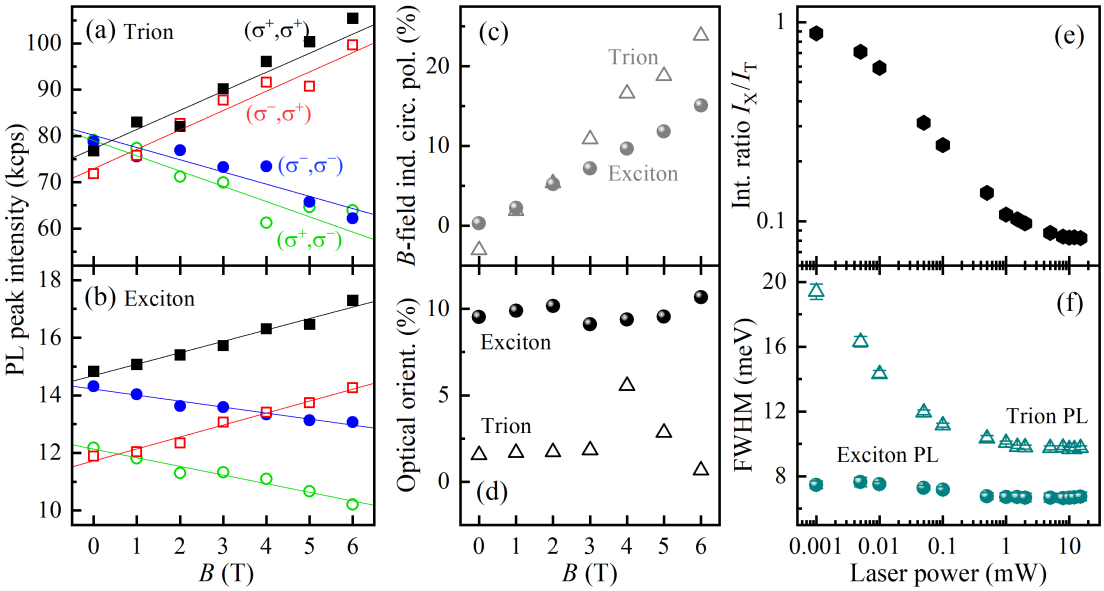

Figure 5-14: (a, b) Polarization-resolved magnetic-field dependence of the (a) trion and (b) exciton PL peak intensities. (c) Magnetic field-induced circular polarization degree and (d) optical orientation degree for exciton and trion. (e, f) Dependence on the laser power for the (e) exciton-to-trion intensity ratio and (f) FWHM of the exciton and trion PL peaks.

excitation energy [512].

The power dependence of the PL reveals a strong change of the ratio between exciton and trion peak intensities. At low power, $P = 1\,\mu W$, the exciton and the trion PL are about equal, $I_X/I_T \approx 1$, see figure 5-14 (e). With increasing laser power, the trion PL increases and the ratio decreases down to $I_X/I_T \to 0.08$. Thus, the trion PL intensity substantially increases in comparison to the exciton PL for increasing laser power. At $P \geq 1\,mW$, both PL intensities behave similarly and the ratio saturates. Overall, the intensity ratio of exciton PL to trion PL decreases by a factor of 10 with increasing power. A higher laser excitation power increases the density of photoexcited charge carriers, leading to an overall signal increase [273]. The increase of the negative trion PL indicates a rise of the electron density with power, so that the **probability of forming trions rather than excitons increases** due to an increase in the number of photogenerated electrons. The saturation of the ratio denotes the point where the probability does not increase further. This might hint at either an increase in free electrons or a more likely **formation of higher excitonic complexes** like neutral and negatively charged biexcitons. The FWHM of the peaks also changes with increasing laser power, see figure 5-14 (f). The exciton PL width decreases only slightly by about 10 %. The trion PL width decreases by about half from 20 meV down to 10 meV. Both widths saturate at about $P \geq 1\,mW$, like the intensity ratio. The **linewidth narrowing** of the negative trion is attributed to a reduction in or a **screening from local electric field fluctuations** due to the high number of nonresonantly generated electrons in the CB [513].

The study of a $Mo_{0.7}W_{0.3}Se_2$ ML via polarization-resolved magneto-PL spectroscopy reveals much larger effective exciton g-factors than in binary TMDC MLs. The enhanced g-factors of the trion, bright intravalley and momentum-dark intervalley exciton, which are about $|g| \approx 6-7.3$, may result from strong exchange interactions. They provide additional contributions to the orbital magnetic moment and thus to an increase of the valley

Zeeman splitting added to the spin Zeeman splitting. The about constant optical orientation degree underlines that the **defect scattering induced by the local disorder** in the $Mo_{0.7}W_{0.3}Se_2$ alloy plays a relevant role in the properties of the excitonic complexes. The PL line narrowing moreover indicates that the laser power shall be varied to further study the magneto-optical features of this ternary alloy in the future. On the whole, these findings on linear and nonlinear magneto-optical responses of excitonic complexes being susceptible to external magnetic and light fields highlight that the studies of the electronic and optical properties of 2D quantum materials are worth to be continued.

5.3 Conclusion and outlook

In the second part of this thesis, different TMDC ML samples have been studied using PL, UPC PL and PLE spectroscopy. The MLs were mechanically exfoliated from CVT-grown bulk crystals and placed on or encapsulated in hBN layers with different thicknesses. TMDCs may be divided into bright (Mo-based) and dark (W-based) materials, according to the optical access of the excitonic ground state. In the first section, the optically dark WSe_2 has been studied using polarization-resolved PL and PLE spectroscopy. Here, the **interlayer electron-phonon coupling** is examined: The intensity of the emission from the WSe_2 monolayer is strongly increased due to a **double resonance**, where the laser excitation is in resonance with the 2s A exciton, while the energy of the combined phonon mode ZO (hBN) + A'$_1$ (WSe_2) is equal to the energy separation between the 2s and 1s exciton states, and the outgoing photon is hence in resonance with the 1s A exciton in WSe_2. A remarkable impact of the interlayer electron-phonon coupling on the preservation of the exciting light helicity in the emission of the neutral and charged excitons and biexcitons is found. The highest value of the circular polarization degree of up to 60 % is detected for the emission of the neutral biexciton and the negative triplet trion. These results highlight a further detail in the exciton-phonon coupling in TMDCs and present a way of enhancing the circular polarization degree of excitonic emissions. Moreover, at the exciton as well as trion resonance energies not only the Raman line is strongly enhanced in its intensity, also the line energies are shifted in a significant way which is characteristic for two **polariton** branches (**anticrossing**). Thus, signatures of phonon-polaritons (phonoritons) in the PLE spectra of WSe_2 are detected. Furthermore, the integrated **upconversion PL discloses exciton-electron and exciton-phonon interactions**. Thereby, the intravalley exciton PL is upconverted by an intervalley exciton via resident electrons, or, less likely, by chiral optical phonons. An elevated temperature and a moderate concentration of resident electrons are necessary for observing upconversion resonances. These results describe a hitherto unexplored interaction process between inter- and intravalley excitons, providing further evidence for the plethora of exciting novel phenomena arising from the strong exciton-phonon interactions in TMDCs.

In the second section, the optically bright MoS_2 and the alloy $Mo_{0.7}W_{0.3}Se_2$ have been studied using polarization-resolved magneto-PL spectroscopy. For MoS_2, the existence of two trion peaks suggests that the MoS_2 monolayer has a dark excitonic ground state, despite having a 'bright' single-particle arrangement of spin-polarized CBs. The effective excitonic ***g*-factor** significantly depends on the **electron concentration** and reaches the lowest value of -2.47 for hBN-encapsulated structures, which reveals a nearly neutral doping regime. In the uncapped structures, the excitonic g-factor varies from -1.15 to

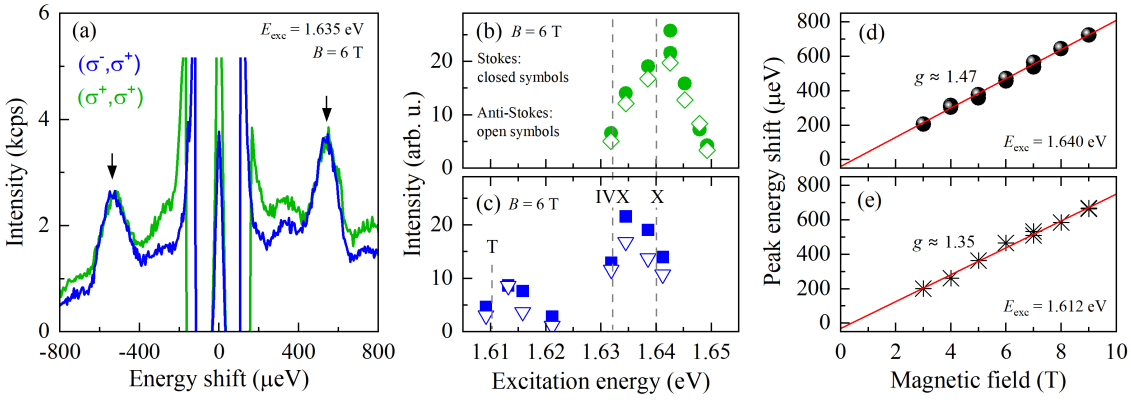

Figure 5-15: (a) Laser-light scattering spectra for resonant excitation for $E_{\mathrm{exc}} = 1.635\,\mathrm{eV}$ in co- and cross-circular polarization, at $B = 6\,\mathrm{T}$ in Voigt geometry. (b, c) Excitation energy dependence of the scattering spectra for (b) co- and (c) cross-circular polarization. The dashed lines indicate the PL peak positions of T, IVX, and X. (d, e) Magnetic field dependences of the spectral positions of the scattered peaks for (d) resonant X excitation, $E_{\mathrm{exc}} = 1.640\,\mathrm{eV}$, and (e) resonant T excitation, $E_{\mathrm{exc}} = 1.612\,\mathrm{eV}$.

-1.60 depending on the **thickness of the bottom hBN layer**, and decreases as a function of rising temperature. In the ternary alloy, enhanced effective g-factors of the exciton, trion and intervalley exciton are found. They are possibly assigned to **large exchange interaction effects**. Furthermore, the polarization characteristics of the PL lines indicate the presence of defect scattering induced by local disorder which is present particularly in the $MoWSe_2$ alloy. These findings present a further step towards understanding the fine structures and interactions of excitonic complexes in TMDCs.

Despite the remarkable advances in the study of excitonic complexes and their interactions with phonons in TMDCs, questions about magneto-optical properties and exciton scattering processes related to the different valleys are still unanswered. In that context, the outlook presents an **intervalley cross-scattering mechanism** studied in the non-encapsulated $Mo_{0.7}W_{0.3}Se_2$/hBN heterostructure by laser-light scattering spectroscopy. In figure 5-15 (a) exemplary laser-light scattering spectra are shown, obtained in cross- and co-circularly polarized configurations. The peaks at the Stokes and anti-Stokes side have energy shifts of 530 μeV, for $B = 6\,\mathrm{T}$, while the linewidths amount to about 100 μeV. The linewidths are somewhat larger compared to spin-flip scattering linewidths of electrons in QDs [248] and QWs [98]. This may hint at contributions from local strain [514] or disorder-induced effects from compositional fluctuations [506], leading to linewidth broadening. Interestingly, the peaks obey **distinct polarization selection rules** measured in Voigt geometry. As demonstrated in figures 5-15 (b) and (c), at the high-energy flank of the exciton PL (above $E = 1.642\,\mathrm{eV}$) the peaks are only visible in the co-polarized configuration, e.g. (σ^+, σ^+), for both Stokes as well as anti-Stokes scattering. For excitation energies between the neutral intravalley exciton X and the trion T, the resonance profiles indicate that the line is visible in every circular polarization setting. Here, the intervalley exciton is probed. At a resonant excitation of about $E_{\mathrm{exc}} = 1.615\,\mathrm{eV}$, probing the negative trion, the scattering line is only obtained for the cross-polarized configuration, e.g. (σ^-, σ^+). While the polarization characteristics of the scattering lines are changed with E_{exc}, their spectral position remains at $(530 \pm 50)\,\mu\mathrm{eV}$ when tuning the excitation energy through the different exciton complexes. Besides these resonance profiles, also the magnetic field dependence of the peak energies is studied. The results

depicted in figures 5-15 (d) and (e) show that the scattering signal is shifted linearly with increasing magnetic field strength. For resonant addressing the intravalley exciton X, the shift is described by a g-factor of about 1.47, while at the trion resonance the g-factor is approximately 1.35.
The g-factors correspond well with the **valley *g*-factor** g_V reported in Ref. [176]. In perpendicular (Voigt, $B_\perp > 0$) magnetic field geometry, the valley splitting which is an orbital effect is pronounced [515, 516]. Hereby, the spin-up and spin-down levels of the CB at the K_+ valley and at the K_- **valley demonstrate a linear Zeeman splitting** with increasing $B_\perp$ which may be described by $g_V \mu_B B_\perp$ in analogy to the spin Zeeman splitting. Hence, it is proposed that in average $g_V \approx 1.41 \pm 0.06$ at both the exciton and the trion resonance. This assignment is in agreement with (i) the observation that the energy shifts of the peaks observed in the spectra are practically independent of the exciton complex excited resonantly and (ii) the g-factor obtained from the PL of the intervalley exciton IVX exceeds the g-factor of the intravalley exciton X by the value of ≥ 1. Note that the g-factor obtained from the PL also includes the valley and orbital angular momentum contributions of the VB [517]. Here, g_V displays the difference in the CB states at the different K valleys. The measurement of the valley Zeeman splitting requires a scattering process in which both valleys are involved. For probing the exciton, we propose a valley-cross scattering, where the hole stays at its initial valley, while the **electron is scattered to the opposite *K*-valley** under spin conservation. The momentum-dark intermediate state is supported by the interaction with a phonon so that the electron recombines with the hole, leading to the scattering line observed in co-polarized configuration. Since, for the studied ternary alloy $MoWSe_2$, the spin-up and spin-down CB levels are quite similar in energy at the K_+ and K_- valley (they are mixed), it can be said that they are distinguished energetically by the valley g-factor in Voigt geometry. The **mixing between the electron spin states** explains the observation of both the Stokes as well as anti-Stokes scattering lines, in the same circular polarization configuration. In case of probing the negative trion and to explain the crossed polarization selection rule, the electrons remain at their states, while the hole has to switch the valley under reversal of its spin (from $-1/2$ to $+1/2$) prior to the final annihilation of the trion. The valley states may possess a slightly different valley splitting which would explain the weak discrepancy in the obtained g-factors.
The relaxed polarization selection rules for exciting the intervalley exciton are right now still puzzling; moreover, the resonant addressing of this momentum-forbidden state which may be assisted by an **electron-phonon-scattering** process shall be studied in future. Here, time-resolved photoluminescence may provide answers how spin and momentum dark excitons contribute to the dynamics of the bright excitons. The high resolution of the inelastic laser-light (spin-flip) scattering could additionally help to reveal the energetic hierarchy of the excitonic levels and may be proven as versatile tool to describe the spin and valley states in 2D materials.

Bibliography

[1] D. Suter and J. Stolze, Quantum computing - A short course from theory to experiment, Wiley-Vch Verlag, Weinheim (2004).

[2] M. T. Bohr and Y. A. El-Mansy, Technology for advanced high-performance microprocessors, IEEE Transactions on Electron Devices **45**, 620 (1998).

[3] F. Montanarella and M. V. Kovalenko, Three millennia of nanocrystals, ACS Nano **16**, 5085 (2022).

[4] F. Pelayo García de Arquer, D. V. Talapin, V. I. Klimov, Y. Arakawa, M. Bayer, and E. H. Sargent, Semiconductor quantum dots: technological progress and future challenges, Science **373**, eaaz8541 (2021).

[5] C. F. Klingshirn, Semiconductor optics, Third Edition, Springer-Verlag, Berlin (2007).

[6] K. S. Novoselov, A. K. Geim, S. V. Morozov, D. Jiang, Y. Zhang, S. V. Dubonos, I. V. Grigorieva, and A. A. Firsov, Electric field effect in atomically thin carbon films, Science **306**, 666 (2004).

[7] K. F. Mak, C. Lee, J. C. Hone, J. Shan, and T. F. Heinz, Atomically thin MoS_2: A new direct-gap semiconductor, Phys. Rev. Lett. **105**, 136805 (2010).

[8] G. Wang, A. Chernikov, M. M. Glazov, T. F. Heinz, X. Marie, T. Amand, and B. Urbaszek, *Colloquium*: Excitons in atomically thin transition metal dichalcogenides, Rev. Mod. Phys. **90**, 021001 (2018).

[9] L. E. Brus, Electron-electron and electron-hole interactions in small semiconductor crystallites: the size dependence of the lowest excited electronic state, J. Chem. Phys. **80**, 4403 (1984).

[10] A. I. Ekimov, Al. L. Efros, and A. A. Onushchenko, Quantum size effect in semiconductor microcrystals, Solid State Communications **56**, 921 (1985).

[11] V. Cerletti, W. A. Coish, O. Gywat, and D. Loss, Recipes for spin-based quantum computing, Nanotechnology **16**, R27 (2005).

[12] V. G. Plekhanov (Ed.), Chapter 6 - Exciton-phonon interaction, In: Isotope Effects in Solid State Physics, Vol. 68 of Semiconductors and Semimetals, Elsevier, Amsterdam (2001).

[13] G. Antonius and S. G. Louie, Theory of exciton-phonon coupling, Phys. Rev. B **105**, 085111 (2022).

[14] J. H. Quilter, A. J. Brash, F. Liu, M. Glässl, A. M. Barth, V. M. Axt, A. J. Ramsay, M. S. Skolnick, and A. M. Fox, Phonon-assisted population inversion of a single InGaAs/GaAs quantum dot by pulsed laser excitation, Phys. Rev. Lett. **114**, 137401 (2015).

[15] J. Jadczak, M. M. Glazov, J. Kutrowska-Girzycka, J. J. Schindler, J. Debus, C.-H. Ho, K. Watanabe, T. Taniguchi, M. Bayer, and L. Bryja, Upconversion of light into bright intravalley excitons via dark intervalley excitons in hBN-encapsulated WSe_2 monolayers, ACS Nano **15**, 19165 (2021).

[16] J. Debus, T. S. Shamirzaev, D. Dunker, V. F. Sapega, E. L. Ivchenko, D. R. Yakovlev, A. I. Toropov, and M. Bayer, Spin-flip Raman scattering of the Γ-X mixed exciton in indirect band gap (In,Al)As/AlAs quantum dots, Phys. Rev. B **90**, 125431 (2014).

[17] V. L. Korenev, M. Salewski, I. A. Akimov, V. F. Sapega, L. Langer, I. V. Kalitukha, J. Debus, R. I. Dzhioev, D. R. Yakovlev, D. Müller, C. Schröder, H. Hövel, G. Karczewski, M. Wiater, T. Wojtowicz, Yu. G. Kusrayev, and M. Bayer, Long-range p-d exchange interaction in a ferromagnet-semiconductor hybrid structure, Nat. Phys. **12**, 85 (2016).

[18] J. V. Jäger, A. V. Scherbakov, B. A. Glavin, A. S. Salasyuk, R. P. Campion, A. W. Rushforth, D. R. Yakovlev, A. V. Akimov, and M. Bayer, Resonant driving of magnetization precession in a ferromagnetic layer by coherent monochromatic phonons, Phys. Rev. B **92**, 020404(R) (2015).

[19] S. Sanguinetti, M. Guzzi, and M. Gurioli, Chapter 6 - Accessing structural and electronic properties of semiconductor nanostructures via photoluminescence, In: C. Lamberti (Ed.), Characterization of semiconductor heterostructures and nanostructures, Elsevier, Amsterdam (2008).

[20] D. Wolverson, Chapter 8 - Raman spectroscopy, In: C. Lamberti (Ed.), Characterization of semiconductor heterostructures and nanostructures, Elsevier, Amsterdam (2008).

[21] R. Koole, E. Groeneveld, D. Vanmaekelbergh, A. Meijerink, and C. de Mello Donegá, Chapter 2: Size effects on semiconductor nanoparticles, In: C. de Mello Donegá (Ed.), Nanoparticles - Workhorses of nanoscience, Springer-Verlag, Berlin (2014).

[22] M. Grundmann, Physics of semiconductors, Vol. 11, Springer-Verlag, Berlin (2010).

[23] P. Y. Yu and M. Cardona, Fundamentals of semiconductors: physics and materials properties, Fourth Edition, Springer-Verlag, Berlin (2010).

[24] O. Gywat, H. J. Krenner, and J. Berezovsky, Spins in optically active quantum dots: concepts and methods, Wiley-Vch Verlag, Weinheim (2010).

[25] F. Meier and B. P. Zakharchenya (Eds.), Optical orientation, Modern problems in condensed matter sciences, Vol. 8, Elsevier, Amsterdam (1984).

[26] M. I. Dyakonov (Ed.), Spin physics in semiconductors, Springer-Verlag, Berlin (2008).

[27] C. Hermann and C. Weisbuch, $\vec{k} \cdot \vec{p}$ perturbation theory in III-V compounds and alloys: a reexamination, Phys. Rev. B **15**, 823 (1977).

[28] M. Cardona, N. E. Christensen, and G. Fasol, Relativistic band structure and spin-orbit splitting of zinc-blende-type semiconductors, Phys. Rev. B **38**, 1806 (1988).

[29] Y. P. Varshni, Temperature dependence of the energy gap in semiconductors, Physica **34**, 149 (1967).

[30] J. Á. Silva-Guillén, P. San-Jose, and R. Roldán, Electronic band structure of transition metal dichalcogenides from ab initio and Slater-Koster tight-binding model, Appl. Sci. **6**, 284 (2016).

[31] M. S. Dresselhaus, G. Dresselhaus, and A. Jorio, Group theory: application to the physics of condensed matter, Springer-Verlag, Berlin (2007).

[32] J. Debus, Spin-flip Raman scattering in low-dimensional semiconductors, Dissertation, TU Dortmund University, Sierke Verlag, Göttingen (2012).

[33] R. C. Ashoori, Electrons in artificial atoms, Nature **379**, 413 (1996).

[34] K. W. Böer and U. W. Pohl, Semiconductor physics, Springer-Verlag, Berlin (2018).

[35] L. Quiroga, D. R. Ardila, and N. F. Johnson, Spatial correlation of quantum dot electrons in a magnetic field, Solid State Commun. **86**, 775 (1993).

[36] M. Holtkemper, D. E. Reiter, and T. Kuhn, Influence of the quantum dot geometry on p-shell transitions in differently charged quantum dots, Phys. Rev. B **97**, 075308 (2018).

[37] G. Bastard and J. A. Brum, Electronic states in semiconductor heterostructures, IEEE J. Quantum Electron. **22**, 1625 (1986).

[38] U. Woggon, Optical properties of semiconductor quantum dots, Springer-Verlag, Berlin (1997).

[39] A. D. Yoffe, Low-dimensional systems: quantum size effects and electronic properties of semiconductor microcrystallites (zero-dimensional systems) and some quasi-two-dimensional systems, Adv. Phys. **42**, 173 (1993).

[40] G. W. Bryant, Excitons in quantum boxes: correlation effects and quantum confinement, Phys. Rev. B **37**, 8763 (1988).

[41] Al. L. Efros and M. Rosen, The electronic structure of semiconductor nanocrystals, Annu. Rev. Mater. Sci. **30**, 475 (2000).

[42] O. Stier, M. Grundmann, and D. Bimberg, Electronic and optical properties of strained quantum dots modeled by 8-band k·p theory, Phys. Rev. B **59**, 5688 (1999).

[43] E. L. Ivchenko, Optical spectroscopy of semiconductor nanostructures, Alpha Science International, Harrow (2005).

[44] A. Wójs and P. Hawrylak, Negatively charged magnetoexcitons in quantum dots, Phys. Rev. B **51**, 10880 (1995).

[45] C. Kittel, Introduction to solid state physics, Vol. 8, John Wiley & Sons, Hoboken (2005).

[46] G. Bester and A. Zunger, Cylindrically shaped zinc-blende semiconductor quantum dots do not have cylindrical symmetry: atomistic symmetry, atomic relaxation, and piezoelectric effects, Phys. Rev. B **71**, 045318 (2005).

[47] H. H. Landolt and R. Börnstein, Numerical Data and Functional Relationships in Science and Technology, Vol. 41, Subvolume B of *New Series*, Springer-Verlag, Berlin (1999).

[48] R. Gross and A. Marx, Festkörperphysik, Oldenbourg Verlag, München (2012).

[49] H. Tahara, Y. Ogawa, and F. Minami, Anisotropic optical properties of excitons in strain-controlled InAs quantum dots, Phys. Rev. B **87**, 035304 (2013).

[50] A. Wójs, P. Hawrylak, S. Fafard, and L. Jacak, Electronic structure and magneto-optics of self-assembled quantum dots, Phys. Rev. B **54**, 5604 (1996).

[51] G. E. Pikus and F. G. Pikus, The mechanism of heavy and light hole mixing in GaAs/AlAs superlattices, Solid State Commun. **89**, 319 (1994).

[52] J. Debus, V. F. Sapega, D. Dunker, D. R. Yakovlev, D. Reuter, A. D. Wieck, and M. Bayer, Spin-flip Raman scattering of the resident electron in singly charged (In,Ga)As/GaAs quantum dot ensembles, Phys. Rev. B **90**, 235404 (2014).

[53] A. Splendiani, L. Sun, Y. Zhang, T. Li, J. Kim, C.-Y. Chim, G. Galli, and F. Wang, Emerging photoluminescence in monolayer MoS_2, Nano Lett. **10**, 1271 (2010).

[54] D. M. Guzman and A. Strachan, Role of strain on electronic and mechanical response of semiconducting transition-metal dichalcogenide monolayers: an *ab-initio* study, J. Appl. Phys. **115**, 243701 (2014).

[55] D. Xiao, G.-B. Liu, W. Feng, X. Xu, and W. Yao, Coupled spin and valley physics in monolayers of MoS_2 and other group-VI dichalcogenides, Phys. Rev. Lett. **108**, 196802 (2012).

[56] M. M. Glazov, E. L. Ivchenko, G. Wang, T. Amand, X. Marie, B. Urbaszek, and B. L. Liu, Spin and valley dynamics of excitons in transition metal dichalcogenide monolayers, Phys. stat. sol. (b) **252**, 2349 (2015).

[57] A. K. Geim and I. V. Grigorieva, Van der Waals heterostructures, Nature **499**, 419 (2013).

[58] E. K. Sichel, R. E. Miller, M. S. Abrahams, and C. J. Buiocchi, Heat capacity and thermal conductivity of hexagonal pyrolytic boron nitride, Phys. Rev. B **13**, 4607 (1976).

[59] K. Watanabe, T. Taniguchi, and H. Kanda, Direct-bandgap properties and evidence for ultraviolet lasing of hexagonal boron nitride single crystal, Nat. Mater. **3**, 404 (2004).

[60] Y. Yu. Illarionov, T. Knobloch, M. Jech, M. Lanza, D. Akinwande, M. I. Vexler, T. Mueller, M. C. Lemme, G. Fiori, F. Schwierz, and T. Grasser, Insulators for 2D nanoelectronics: the gap to bridge, Nat. Commun. **11**, 3385 (2020).

[61] Y. Hoshi, T. Kuroda, M. Okada, R. Moriya, S. Masubuchi, K. Watanabe, T. Taniguchi, R. Kitaura, and T. Machida, Suppression of exciton-exciton annihilation in tungsten disulfide monolayers encapsulated by hexagonal boron nitrides, Phys. Rev. B **95**, 241403(R) (2017).

[62] G.-H. Lee, X. Cui, Y. D. Kim, G. Arefe, X. Zhang, C.-H. Lee, F. Ye, K. Watanabe, T. Taniguchi, P. Kim, and J. C. Hone, Highly stable, dual-gated MoS_2 transistors encapsulated by hexagonal boron nitride with gate-controllable contact, resistance, and threshold voltage, ACS Nano **9**, 7019 (2015).

[63] K. S. Novoselov, A. Mishchenko, A. Carvalho, and A. H. Castro Neto, 2D materials and van der Waals heterostructures, Science **353**, aac9439 (2016).

[64] M. I. Petrescu and M.-G. Balint, Structure and properties modifications in boron nitride. Part I: Direct polymorphic transformations mechanisms, UPB Sci. Bull., Series B **69**, 35 (2007).

[65] K. F. Mak and J. Shan, Photonics and optoelectronics of 2D semiconductor transition metal dichalcogenides, Nat. Photon. **10**, 216 (2016).

[66] A. Chaves, J. G. Azadani, H. Alsalman, D. R. da Costa, R. Frisenda, A. J. Chaves, S. H. Song, Y. D. Kim, D. He, J. Zhou, A. Castellanos-Gomez, F. M. Peeters, Z. Liu, C. L. Hinkle, S.-H. Oh, P. D. Ye, S. J. Koester, Y. H. Lee, Ph. Avouris, X. Wang, and T. Low, Bandgap engineering of two-dimensional semiconductor materials, npj 2D Mater. Appl. **4**, 29 (2020).

[67] A. V. Stier, N. P. Wilson, G. Clark, X. Xu, and S. A. Crooker, Probing the influence of dielectric environment on excitons in monolayer WSe_2: insight from high magnetic fields, Nano Lett. **16**, 7054 (2016).

[68] J. Gao, B. Li, J. Tan, P. Chow, T.-M. Lu, and N. Koratkar, Aging of transition metal dichalcogenide monolayers, ACS Nano **10**, 2628 (2016).

[69] L. Huang, A. Krasnok, A. Alú, Y. Yu, D. Neshev, and A. E. Miroshnichenko, Enhanced light-matter interaction in two-dimensional transition metal dichalcogenides, Rep. Prog. Phys. **85**, 046401 (2022).

[70] L. M. Schneider, S. Lippert, J. Kuhnert, O. A. Ajayi, D. Renaud, S. Firoozabadi, Q. Ngo, R. Guo, Y. D. Kim, W. Heimbrodt, J. C. Hone, and A. Rahimi-Iman, The influence of the environment on monolayer tungsten diselenide photoluminescence, Nano-Structures & Nano-Objects **15**, 84 (2018).

[71] K. Zollner, P. E. Faria Junior, and J. Fabian, Strain-tunable orbital, spin-orbit, and optical properties of monolayer transition-metal dichalcogenides, Phys. Rev. B **100**, 195126 (2019).

[72] O. A. Ajayi, J. V. Ardelean, G. D. Shepard, J. Wang, A. Antony, T. Taniguchi, K. Watanabe, T. F. Heinz, S. Strauf, X.-Y. Zhu, and J. C. Hone, Approaching the intrinsic photoluminescence linewidth in transition metal dichalcogenide monolayers, 2D Materials **4**, 031011 (2017).

[73] F. Cadiz, E. Courtade, C. Robert, G. Wang, Y. Shen, H. Cai, T. Taniguchi, K. Watanabe, H. Carrere, D. Lagarde, M. Manca, T. Amand, P. Renucci, S. Tongay, X. Marie, and B. Urbaszek, Excitonic linewidth approaching the homogeneous limit in MoS_2-based van der Waals heterostructures, Phys. Rev. X **7**, 021026 (2017).

[74] Y. Yu, Y. Yu, C. Xu, Y.-Q. Cai, L. Su, Y. Zhang, Y.-W. Zhang, K. Gundogdu, and L. Cao, Engineering substrate interactions for high luminescence efficiency of transition-metal dichalcogenide monolayers, Adv. Funct. Mater. **26**, 4733 (2016).

[75] A. Chernikov, T. C. Berkelbach, H. M. Hill, A. Rigosi, Y. Li, B. Aslan, D. R. Reichman, M. S. Hybertsen, and T. F. Heinz, Exciton binding energy and nonhydrogenic Rydberg series in monolayer WS_2, Phys. Rev. Lett. **113**, 076802 (2014).

[76] M. Selig, G. Berghäuser, A. Raja, P. Nagler, C. Schüller, T. F. Heinz, T. Korn, A. Chernikov, E. Malic, and A. Knorr, Excitonic linewidth and coherence lifetime in monolayer transition metal dichalcogenides, Nat. Commun. **7**, 13279 (2016).

[77] F. Katsch, M. Selig, A. Carmele, and A. Knorr, Theory of exciton-exciton interactions in monolayer transition metal dichalcogenides, Phys. stat. sol. (b) **255**, 1800185 (2018).

[78] S. Rodt, R. Heitz, A. Schliwa, R. L. Sellin, F. Guffarth, and D. Bimberg, Repulsive exciton-exciton interaction in quantum dots, Phys. Rev. B **68**, 035331 (2003).

[79] Y. Masumoto and T. Takagahara (Eds.), Semiconductor quantum dots: physics, spectroscopy and applications, Springer-Verlag, Berlin (2002).

[80] Al. L. Efros and A. L. Efros, Interband absorption of light in a semiconductor sphere, Sov. Phys. Semicond. **16**, 772 (1982).

[81] Y. Chen, B. Gil, P. Lefebvre, and H. Mathieu, Exchange effects on excitons in quantum wells, Phys. Rev. B **37**, 6429 (1988).

[82] M. Holtkemper, G. F. Quinteiro, D. E. Reiter, and T. Kuhn, Selection rules for the excitation of quantum dots by spatially structured light beams: application to the reconstruction of higher excited exciton wave functions, Phys. Rev. B **102**, 165315 (2020).

[83] G. Czycholl, Theoretische Festkörperphysik: von den klassischen Modellen zu modernen Forschungsthemen, 3. Auflage, Springer-Verlag, Berlin (2008).

[84] M. Bayer, S. N. Walck, T. L. Reinecke, and A. Forchel, Exciton binding energies and diamagnetic shifts in semiconductor quantum wires and quantum dots, Phys. Rev. B **57**, 6584 (1998).

[85] R. L. Greene, K. K. Bajaj, and D. E. Phelps, Energy levels of Wannier excitons in GaAs-$Ga_{1-x}Al_xAs$ quantum-well structures, Phys. Rev. B **29**, 1807 (1984).

[86] M. M. Glazov, F. Dirnberger, V. M. Menon, T. Taniguchi, K. Watanabe, D. Bougeard, J. D. Ziegler, and A. Chernikov, Exciton fine structure splitting and linearly polarized emission in strained transition-metal dichalcogenide monolayers, Phys. Rev. B **106**, 125303 (2022).

[87] S. Rodt, R. Heitz, R. L. Sellin, A. Schliwa, K. Pötschke, and D. Bimberg, Biexcitons in self-organized InAs/GaAs quantum dots: an optical probe for structural properties, Physica E **21**, 1065 (2004).

[88] D. Bimberg (Ed.), Semiconductor nanostructures, Springer-Verlag, Berlin (2008).

[89] M. Van der Donck, M. Zarenia, and F. M. Peeters, Excitons and trions in monolayer transition metal dichalcogenides: a comparative study between the multiband model and the quadratic single-band model, Phys. Rev. B **96**, 035131 (2017).

[90] S. Glutsch, Excitons in low-dimensional semiconductors: theory, numerical methods, applications, Springer-Verlag, Berlin (2004).

[91] S. Stobbe, T. W. Schlereth, S. Höfling, A. Forchel, J. M. Hvam, and P. Lodahl, Large quantum dots with small oscillator strength, Phys. Rev. B **82**, 233302 (2010).

[92] J.-W. Luo, G. Bester, and A. Zunger, Long- and short-range electron-hole exchange interaction in different types of quantum dots, New J. Phys. **11**, 123024 (2009).

[93] I. E. Kozin, V. G. Davydov, I. V. Ignatiev, A. V. Kavokin, K. V. Kavokin, G. Malpuech, H.-W. Ren, M. Sugisaki, S. Sugou, and Y. Masumoto, Zero-field spin quantum beats in charged quantum dots, Phys. Rev. B **65**, 241312(R) (2002).

[94] E. Malic, M. Selig, M. Feierabend, S. Brem, D. Christiansen, F. Wendler, A. Knorr, and G. Berghäuser, Dark excitons in transition metal dichalcogenides, Phys. Rev. Mat. **2**, 014002 (2018).

[95] H. W. van Kesteren, E. C. Cosman, W. A. J. A. van der Poel, and C. T. Foxon, Fine structure of excitons in type-II GaAs/AlAs quantum wells, Phys. Rev. B **41**, 5283 (1990).

[96] M. Bayer, G. Ortner, O. Stern, A. Kuther, A. A. Gorbunov, A. Forchel, P. Hawrylak, S. Fafard, K. Hinzer, T. L. Reinecke, S. N. Walck, J. P. Reithmaier, F. Klopf, and F. Schäfer, Fine structure of neutral and charged excitons in self-assembled In(Ga)As/(Al)GaAs quantum dots, Phys. Rev. B **65**, 195315 (2002).

[97] B. Urbaszek, R. J. Warburton, K. Karrai, B. D. Gerardot, P. M. Petroff, and J. M. Garcia, Fine structure of highly charged excitons in semiconductor quantum dots, Phys. Rev. Lett. **90**, 247403 (2003).

[98] J. Debus, D. Dunker, V. F. Sapega, D. R. Yakovlev, G. Karczewski, T. Wojtowicz, J. Kossut, and M. Bayer, Spin-flip Raman scattering of the neutral and charged excitons confined in a CdTe/(Cd,Mg)Te quantum well, Phys. Rev. B **87**, 205316 (2013).

[99] K. V. Kavokin, Anisotropic exchange interaction of localized conduction-band electrons in semiconductors, Phys. Rev. B **64**, 075305 (2001).

[100] K. V. Kavokin, Symmetry of anisotropic exchange interactions in semiconductor nanostructures, Phys. Rev. B **69**, 075302 (2004).

[101] D. Gammon, E. S. Snow, B. V. Shanabrook, D. S. Katzer, and D. Park, Fine structure splitting in the optical spectra of single GaAs quantum dots, Phys. Rev. Lett. **76**, 3005 (1996).

[102] T. Takagahara, Effects of dielectric confinement and electron-hole exchange interaction on excitonic states in semiconductor quantum dots, Phys. Rev. B **47**, 4569 (1993).

[103] L. M. Schneider, S. S. Esdaille, D. A. Rhodes, K. Barmak, J. C. Hone, and A. Rahimi-Iman, Optical dispersion of valley-hybridised coherent excitons with momentum-dependent valley polarisation in monolayer semiconductor, 2D Materials **8**, 015009 (2020).

[104] C. Robert, B. Han, P. Kapuściński, A. Delhomme, C. Faugeras, T. Amand, M. R. Molas, M. Bartos, K. Watanabe, T. Taniguchi, B. Urbaszek, M. Potemski, and X. Marie, Measurement of the spin-forbidden dark excitons in MoS_2 and $MoSe_2$ monolayers, Nat. Commun. **11**, 4037 (2020).

[105] S. A. Crooker, T. Barrick, J. A. Hollingsworth, and V. I. Klimov, Multiple temperature regimes of radiative decay in CdSe nanocrystal quantum dots: intrinsic limits to the dark-exciton lifetime, Appl. Phys. Lett. **82**, 2793 (2003).

[106] E. Courtade, M. A. Semina, M. Manca, M. M. Glazov, C. Robert, F. Cadiz, G. Wang, T. Taniguchi, K. Watanabe, M. Pierre, W. Escoffier, E. L. Ivchenko, P. Renucci, X. Marie, T. Amand, and B. Urbaszek, Charged excitons in monolayer WSe_2: experiment and theory, Phys. Rev. B **96**, 085302 (2017).

[107] H. Fu, L.-W. Wang, and A. Zunger, Excitonic exchange splitting in bulk semiconductors, Phys. Rev. B **59**, 5568 (1999).

[108] P. Offermans, P. M. Koenraad, J. H. Wolter, K. Pierz, M. Roy, and P. A. Maksym, Atomic-scale structure and photoluminescence of InAs quantum dots in GaAs and AlAs, Phys. Rev. B **72**, 165332 (2005).

[109] P. P. Paskov, P. O. Holtz, B. Monemar, J. M. Garcia, W. V. Schoenfeld, and P. M. Petroff, Magnetoluminescence of highly excited InAs/GaAs self-assembled quantum dots, Phys. Rev. B **62**, 7344 (2000).

[110] H. H. Landolt and R. Börnstein, Numerical Data and Functional Relationships in Science and Technology, Vol. 22, Subvolume A of *New Series*, Springer-Verlag, Berlin (1997).

[111] R. Heitz, O. Stier, I. Mukhametzhanov, A. Madhukar, and D. Bimberg, Quantum size effect in self-organized InAs/GaAs quantum dots, Phys. Rev. B **62**, 11017 (2000).

[112] Y. M. Niquet, Electronic and optical properties of InAs/GaAs nanowire superlattices, Phys. Rev. B **74**, 155304 (2006).

[113] A. J. Williamson, L.-W. Wang, and A. Zunger, Theoretical interpretation of the experimental electronic structure of lens-shaped self-assembled InAs/GaAs quantum dots, Phys. Rev. B **62**, 12963 (2000).

[114] G. Wang, I. C. Gerber, L. Bouet, D. Lagarde, A. Balocchi, M. Vidal, T. Amand, X. Marie, and B. Urbaszek, Exciton states in monolayer $MoSe_2$: impact on interband transitions, 2D Materials **2**, 045005 (2015).

[115] J. Xiao, M. Zhao, Y. Wang, and X. Zhang, Excitons in atomically thin 2D semiconductors and their applications, Nanophotonics **6**, 1309 (2017).

[116] A. Raja, A. Chaves, J. Yu, G. Arefe, H. M. Hill, A. F. Rigosi, T. C. Berkelbach, P. Nagler, C. Schüller, T. Korn, C. Nuckolls, J. C. Hone, L. E. Brus, T. F. Heinz, D. R. Reichman, and A. Chernikov, Coulomb engineering of the bandgap and excitons in two-dimensional materials, Nat. Commun. **8**, 15251 (2017).

[117] A. Laturia, M. L. Van de Put, and W. G. Vandenberghe, Dielectric properties of hexagonal boron nitride and transition metal dichalcogenides: from monolayer to bulk, npj 2D Mater. Appl. **2**, 6 (2018).

[118] X. Xu, W. Yao, D. Xiao, and T. F. Heinz, Spin and pseudospins in layered transition metal dichalcogenides, Nat. Phys. **10**, 343 (2014).

[119] M. Trushin and J. Schliemann, Pseudospin in optical and transport properties of graphene, Phys. Rev. Lett. **107**, 156801 (2011).

[120] A. H. Castro Neto, F. Guinea, N. M. R. Peres, K. S. Novoselov, and A. K. Geim, The electronic properties of graphene, Rev. Mod. Phys. **81**, 109 (2009).

[121] R. Winkler and U. Zülicke, Time reversal of pseudo-spin 1/2 degrees of freedom, Phys. Lett. A **374**, 4003 (2010).

[122] C. L. Kane and E. J. Mele, Quantum spin Hall effect in graphene, Phys. Rev. Lett. **95**, 226801 (2005).

[123] D. Xiao, W. Yao, and Q. Niu, Valley-contrasting physics in graphene: magnetic moment and topological transport, Phys. Rev. Lett. **99**, 236809 (2007).

[124] G. Aivazian, Z. Gong, A. M. Jones, R.-L. Chu, J. Yan, D. G. Mandrus, C. Zhang, D. Cobden, W. Yao, and X. Xu, Magnetic control of valley pseudospin in monolayer WSe_2, Nat. Phys. **11**, 148 (2015).

[125] A. V. Khaetskii and Y. V. Nazarov, Spin relaxation in semiconductor quantum dots, Phys. Rev. B **61**, 12639 (2000).

[126] Z. Y. Zhu, Y. C. Cheng, and U. Schwingenschlögl, Giant spin-orbit-induced spin splitting in two-dimensional transition-metal dichalcogenide semiconductors, Phys. Rev. B **84**, 153402 (2011).

[127] A. V. Khaetskii and Y. V. Nazarov, Spin-flip transitions between Zeeman sublevels in semiconductor quantum dots, Phys. Rev. B **64**, 125316 (2001).

[128] M. Bayer, V. B. Timofeev, T. Gutbrod, A. Forchel, R. Steffen, and J. Oshinowo, Enhancement of spin splitting due to spatial confinement in In_x $Ga_{1-x}As$ quantum dots, Phys. Rev. B **52**, R11623(R) (1995).

[129] D. Erkensten, S. Brem, and E. Malic, Exciton-exciton interaction in transition metal dichalcogenide monolayers and van der Waals heterostructures, Phys. Rev. B **103**, 045426 (2021).

[130] J. Horng, T. Stroucken, L. Zhang, E. Y. Paik, H. Deng, and S. W. Koch, Observation of interlayer excitons in $MoSe_2$ single crystals, Phys. Rev. B **97**, 241404(R) (2018).

[131] X. Ling, W. Fang, Y.-H. Lee, P. T. Araujo, X. Zhang, J. F. Rodriguez-Nieva, Y. Lin, J. Zhang, J. Kong, and M. S. Dresselhaus, Raman enhancement effect on two-dimensional layered materials: graphene, h-BN and MoS_2, Nano Lett. **14**, 3033 (2014).

[132] I. D. Avdeev and D. S. Smirnov, Hyperfine interaction in atomically thin transition metal dichalcogenides, Nanoscale Adv. **1**, 2624 (2019).

[133] Y. Wu, Q. Tong, G. B. Liu, H. Yu, and W. Yao, Spin-valley qubit in nanostructures of monolayer semiconductors: optical control and hyperfine interaction, Phys. Rev. B **93**, 045313 (2016).

[134] D. T. Cong and H. R. Crane, Precision measurement of the g factor of the free electron, Phys. Rev. **130**, 852 (1998).

[135] H. M. G. A. Tholen, J. S. Wildmann, A. Rastelli, R. Trotta, C. E. Pryor, E. Zallo, O. G. Schmidt, P. M. Koenraad, and A. Yu. Silov, Strain-induced g-factor tuning in single InGaAs/GaAs quantum dots, Phys. Rev. B **94**, 245301 (2016).

[136] S. N. Walck and T. L. Reinecke, Exciton diamagnetic shift in semiconductor nanostructures, Phys. Rev. B **57**, 9088 (1998).

[137] K. Cong, G. T. Noe, and J. Kono, Excitons in Magnetic Fields, In: Encyclopedia of Modern Optics, Second Edition, Elsevier, Oxford (2018).

[138] A. V. Stier, K. M. McCreary, B. T. Jonker, J. Kono, and S. A. Crooker, Exciton diamagnetic shifts and valley Zeeman effects in monolayer WS_2 and MoS_2 to 65 Tesla, Nat. Commun. **7**, 10643 (2016).

[139] L. M. Roth, B. Lax, and S. Zwerdling, Theory of optical magneto-absorption effects in semiconductors, Phys. Rev. **114**, 90 (1959).

[140] C. Weisbuch and C. Hermann, Optical detection of conduction-electron spin resonance in GaAs, $Ga_{1-x}In_xAs$, and $Ga_{1-x}Al_xAs$, Phys. Rev. B **15**, 816 (1977).

[141] T. Deilmann, P. Krüger, and M. Rohlfing, *Ab initio* studies of exciton g factors: monolayer transition metal dichalcogenides in magnetic fields, Phys. Rev. Lett. **124**, 226402 (2020).

[142] A. A. Mitioglu, K. Galkowski, A. Surrente, L. Klopotowski, D. Dumcenco, A. Kis, P. Plochocka, and D. K. Maude, Magnetoexcitons in large area CVD-grown monolayer MoS_2 and $MoSe_2$ on sapphire, Phys. Rev. B **93**, 165412 (2016).

[143] C. Robert, H. Dery, L. Ren, D. Van Tuan, E. Courtade, M. Yang, B. Urbaszek, D. Lagarde, K. Watanabe, T. Taniguchi, T. Amand, and X. Marie, Measurement of conduction and valence bands g-factors in a transition metal dichalcogenide monolayer, Phys. Rev. Lett. **126**, 067403 (2021).

[144] H. Kosaka, A. A. Kiselev, F. A. Baron, K. W. Kim, and E. Yablonovitch, Electron g-factor engineering in III-V semiconductors for quantum communications, Electron. Lett. **37**, 464 (2001).

[145] I. A. Yugova, A. Greilich, D. R. Yakovlev, A. A. Kiselev, M. Bayer, V. V. Petrov, Yu. K. Dolgikh, D. Reuter, and A. D. Wieck, Universal behavior of the electron g factor in GaAs/Al_xGa_{1-x}As quantum wells, Phys. Rev. B **75**, 245302 (2007).

[146] V. V. Belykh, D. R. Yakovlev, J. J. Schindler, E. A. Zhukov, M. A. Semina, M. Yacob, J. P. Reithmaier, M. Benyoucef, and M. Bayer, Large anisotropy of electron and hole g factors in infrared-emitting InAs/InAlGaAs self-assembled quantum dots, Phys. Rev. B **93**, 125302 (2016).

[147] S. A. Crooker, J. Brandt, C. Sandfort, A. Greilich, D. R. Yakovlev, D. Reuter, A. D. Wieck, and M. Bayer, Spin noise of electrons and holes in self-assembled quantum dots, Phys. Rev. Lett. **104**, 036601 (2010).

[148] V. V. Belykh, D. R. Yakovlev, J. J. Schindler, J. van Bree, P. M. Koenraad, N. S. Averkiev, M. Bayer, and A. Yu. Silov, Dispersion of the electron g factor anisotropy in InAs/InP self-assembled quantum dots, J. Appl. Phys. **120**, 084301 (2016).

[149] L. F. Chibotaru, A. Ceulemans, and H. Bolvin, Unique definition of the Zeeman-splitting g tensor of a Kramers doublet, Phys. Rev. Lett. **101**, 033003 (2008).

[150] A. Schwan, B.-M. Meiners, A. Greilich, D. R. Yakovlev, M. Bayer, A. D. B. Maia, A. A. Quivy, and A. B. Henriques, Anisotropy of electron and hole g-factors in (In,Ga)As quantum dots, Appl. Phys. Lett. **99**, 221914 (2011).

[151] T. P. Mayer Alegre, F. G. G. Hernández, A. L. C. Pereira, and G. Medeiros-Ribeiro, Landé g tensor in semiconductor nanostructures, Phys. Rev. Lett. **97**, 236402 (2006).

[152] N. J. Traynor, R. T. Harley, and R. J. Warburton, Zeeman splitting and g factor of heavy-hole excitons in In_xGa_{1-x}As/GaAs quantum wells, Phys. Rev. B **51**, 7361(R) (1995).

[153] G. L. Bir and G. E. Pikus, Symmetry and strain-induced effects in semiconductors, Wiley/Halsted Press, New York (1974).

[154] V. F. Sapega, M. Cardona, K. Ploog, E. L. Ivchenko, and D. N. Mirlin, Spin-flip Raman scattering in GaAs/Al_xGa_{1-x}As multiple quantum wells, Phys. Rev. B **45**, 4320 (1992).

[155] X. Marie, T. Amand, P. Le Jeune, M. Paillard, P. Renucci, L. E. Golub, V. D. Dymnikov, and E. L. Ivchenko, Hole spin quantum beats in quantum-well structures, Phys. Rev. B **60**, 5811 (1999).

[156] A. V. Koudinov, I. A. Akimov, Yu. G. Kusrayev, and F. Henneberger, Optical and magnetic anisotropies of the hole states in Stranski-Krastanov quantum dots, Phys. Rev. B **70**, 241305(R) (2004).

[157] G. Bester, S. Nair, and A. Zunger, Pseudopotential calculation of the excitonic fine structure of million-atom self-assembled $In_{1-x}Ga_x$As/GaAs quantum dots, Phys. Rev. B **67**, 161306(R) (2003).

[158] R. Seguin, A. Schliwa, S. Rodt, K. Pötschke, U. W. Pohl, and D. Bimberg, Size-dependent fine-structure splitting in self-organized InAs/GaAs quantum dots, Phys. Rev. Lett. **95**, 257402 (2005).

[159] J. Puls, M. Rabe, H.-J. Wünsche, and F. Henneberger, Magneto-optical study of the exciton fine structure in self-assembled CdSe quantum dots, Phys. Rev. B **60**, R16303(R) (1999).

[160] I. A. Yugova, A. Greilich, E. A. Zhukov, D. R. Yakovlev, M. Bayer, D. Reuter, and A. D. Wieck, Exciton fine structure in InGaAs/GaAs quantum dots revisited by pump-probe Faraday rotation, Phys. Rev. B **75**, 195325 (2007).

[161] J. G. Tischler, A. S. Bracker, D. Gammon, and D. Park, Fine structure of trions and excitons in single GaAs quantum dots, Phys. Rev. B **66**, 081310(R) (2002).

[162] Z. Lu, D. Rhodes, Z. Li, D. Van Tuan, Y. Jiang, J. Ludwig, Z. Jiang, Z. Lian, S.-F. Shi, J. C. Hone, H. Dery, and D. Smirnov, Magnetic field mixing and splitting of bright and dark excitons in monolayer $MoSe_2$, 2D Materials **7**, 015017 (2019).

[163] D. W. Latzke, W. Zhang, A. Suslu, T.-R. Chang, H. Lin, H.-T. Jeng, S. Tongay, J. Wu, A. Bansil, and A. Lanzara, Electronic structure, spin-orbit coupling, and interlayer interaction in bulk MoS_2 and WS_2, Phys. Rev. B **91**, 235202 (2015).

[164] K. Kośmider, J. W. González, and J. Fernández-Rossier, Large spin splitting in the conduction band of transition metal dichalcogenide monolayers, Phys. Rev. B **88**, 245436 (2013).

[165] A. Kormányos, V. Zólyomi, N. D. Drummond, and G. Burkard, Spin-orbit coupling, quantum dots, and qubits in monolayer transition metal dichalcogenides, Phys. Rev. X **4**, 011034 (2014).

[166] A. Kormányos, G. Burkard, M. Gmitra, J. Fabian, V. Zólyomi, N. D. Drummond, and V. I. Fal'ko, k·p theory for two-dimensional transition metal dichalcogenide semiconductors, 2D Materials **2**, 022001 (2015).

[167] G.-B. Liu, W.-Y. Shan, Y. Yao, W. Yao, and D. Xiao, Three-band tight-binding model for monolayers of group-VIB transition metal dichalcogenides, Phys. Rev. B **88**, 085433 (2013).

[168] J. Jadczak, J. Kutrowska-Girzycka, M. Bieniek, T. Kazimierczuk, P. Kossacki, J. J. Schindler, J. Debus, K. Watanabe, T. Taniguchi, C.-H. Ho, A. Wójs, P. Hawrylak, and L. Bryja, Probing negatively charged and neutral excitons in MoS_2/hBN and hBN/MoS_2/hBN van der Waals heterostructures, Nanotechnology **32**, 145717 (2021).

[169] X.-X. Zhang, Y. You, S. Y. F. Zhao, and T. F. Heinz, Experimental evidence for dark excitons in monolayer WSe_2, Phys. Rev. Lett. **115**, 257403 (2015).

[170] G.-h. Peng, P.-Y. Lo, W.-H. Li, Y.-C. Huang, Y.-H. Chen, C.-H. Lee, C.-K. Yang, and S.-J. Cheng, Distinctive signatures of the spin- and momentum-forbidden dark exciton states in the photoluminescence of strained WSe_2 monolayers under thermalization, Nano Lett. **19**, 2299 (2019).

[171] J. P. Echeverry, B. Urbaszek, T. Amand, X. Marie, and I. C. Gerber, Splitting between bright and dark excitons in transition metal dichalcogenide monolayers, Phys. Rev. B **93**, 121107(R) (2016).

[172] S. Park and B.-J. Yang, Phonon angular momentum Hall effect, Nano Lett.**20**, 7694 (2020).

[173] M. R. Molas, A. O. Slobodeniuk, T. Kazimierczuk, K. Nogajewski, M. Bartos, P. Kapuściński, K. Oreszczuk, K. Watanabe, T. Taniguchi, C. Faugeras, P. Kossacki, D. M. Basko, and M. Potemski, Probing and manipulating valley coherence of dark excitons in monolayer WSe_2, Phys. Rev. Lett. **123**, 096803 (2019).

[174] M. Zinkiewicz, A. O. Slobodeniuk, T. Kazimierczuk, P. Kapuściński, K. Oreszczuk, M. Grzeszczyk, M. Bartos, K. Nogajewski, K. Watanabe, T. Taniguchi, C. Faugeras, P. Kossacki, M. Potemski, A. Babiński, and M. R. Molas, Neutral and charged dark excitons in monolayer WS_2, Nanoscale **12**, 18153 (2020).

[175] Z. Li, T. Wang, S. Miao, Z. Lian, and S.-F. Shi, Fine structures of valley-polarized excitonic states in monolayer transitional metal dichalcogenides, Nanophotonics **9**, 1811 (2020).

[176] M. Koperski, M. R. Molas, A. Arora, K. Nogajewski, M. Bartos, J. Wyzula, D. Vaclavkova, P. Kossacki, and M. Potemski, Orbital, spin and valley contributions to Zeeman splitting of excitonic resonances in $MoSe_2$, WSe_2 and WS_2 monolayers, 2D Materials **6**, 015001 (2018).

[177] G. Plechinger, P. Nagler, A. Arora, A. Granados del Águila, M. V. Ballottin, T. Frank, P. Steinleitner, M. Gmitra, J. Fabian, P. C. M. Christianen, R. Bratschitsch, C. Schüller, and T. Korn, Excitonic valley effects in monolayer WS_2 under high magnetic fields, Nano Lett. **16**, 7899 (2016).

[178] A. A. Mitioglu, P. Plochocka, A. Granados del Águila, P. C. M. Christianen, G. Deligeorgis, S. Anghel, L. Kulyuk, and D. K. Maude, Optical investigation of monolayer and bulk tungsten diselenide (WSe_2) in high magnetic fields, Nano Lett. **15**, 4387 (2015).

[179] X.-X. Zhang, T. Cao, Z. Lu, Y.-C. Lin, F. Zhang, Y. Wang, Z. Li, J. C. Hone, J. A. Robinson, D. Smirnov, S. G. Louie, and T. F. Heinz, Magnetic brightening and control of dark excitons in monolayer WSe_2, Nat. Nanotechnol. **12**, 883 (2017).

[180] W. Yao, D. Xiao, and Q. Niu, Valley-dependent optoelectronics from inversion symmetry breaking, Phys. Rev. B **77**, 235406 (2008).

[181] J. Xiao, Z. Ye, Y. Wang, H. Zhu, Y. Wang, and X. Zhang, Nonlinear optical selection rule based on valley-exciton locking in monolayer WS_2, Light Sci. Appl. **4**, e366 (2015).

[182] P. Gong, H. Yu, Y. Wang, and W. Yao, Optical selection rules for excitonic Rydberg series in the massive Dirac cones of hexagonal two-dimensional materials, Phys. Rev. B **95**, 125420 (2017).

[183] H. J. Simon and N. Bloembergen, Second-harmonic light generation in crystals with natural optical activity, Phys. Rev. **171**, 1104 (1968).

[184] T. Cao, G. Wang, W. Han, H. Ye, C. Zhu, J. Shi, Q. Niu, P. Tan, E. Wang, B. Liu, and J. Feng, Valley-selective circular dichroism of monolayer molybdenum disulphide, Nat. Commun. **3**, 887 (2012).

[185] Z. Ye, T. Cao, K. O'Brien, H. Zhu, X. Yin, Y. Wang, S. G. Louie, and X. Zhang, Probing excitonic dark states in single-layer tungsten disulphide, Nature **513**, 214 (2014).

[186] J.-P. Leburton, J. Pascual, and C. S. Torres (Eds.), Phonons in semiconductor nanostructures, In: Series E: Applied Sciences - Vol. 236, Springer-Verlag, Berlin (1993).

[187] U. Rössler, Solid state theory: an introduction, Springer-Verlag, Berlin (2004).

[188] J. B. J. Chapman, Improving the functional control of ferroelectrics using insights from atomistic modelling, Dissertation, University College London, London (2018).

[189] T. Czerniuk, Picosecond ultrasonics for the modulation and nanoscopy of semiconductor lasers, Dissertation, TU Dortmund University, Dortmund (2017).

[190] R. C. Fivaz, Dimensionality and the electron-phonon interaction in layer structures, Nuovo Cimento **63 B**, 10 (1969).

[191] T. Deng, G. Wu, W. Shi, Z. M. Wong, J.-S. Wang, and S.-W. Yang, *Ab initio* dipolar electron-phonon interactions in two-dimensional materials, Phys. Rev. B **103**, 075410 (2021).

[192] K. Kaasbjerg, K. S. Thygesen, and A.-P. Jauho, Acoustic phonon limited mobility in two-dimensional semiconductors: deformation potential and piezoelectric scattering in monolayer MoS_2 from first principles, Phys. Rev. B **87**, 235312 (2013).

[193] R. Heitz, M. Grundmann, N. N. Ledentsov, L. Eckey, M. Veit, D. Bimberg, V. M. Ustinov, A. Yu. Egorov, A. E. Zhukov, P. S. Kop'ev, and Zh. I. Alferov, Multiphonon-relaxation processes in self-organized InAs/GaAs quantum dots, Appl. Phys. Lett. **68**, 361 (1996).

[194] I. Favero, G. Cassabois, R. Ferreira, D. Darson, C. Voisin, J. Tignon, C. Delalande, G. Bastard, Ph. Roussignol, and J.-M. Gérard, Acoustic phonon sidebands in the emission line of single InAs/GaAs quantum dots, Phys. Rev. B **68**, 233301 (2003).

[195] A. K.. Arora, M. Rajalakshmi, T. R. Ravindran, and V. Sivasubramanian, Raman spectroscopy of optical phonon confinement in nanostructured materials, J. Raman Spectrosc. **38**, 604 (2007).

[196] P. Han and G. Bester, Confinement effects on the vibrational properties of III-V and II-VI nanoclusters, Phys. Rev. B **85**, 041306(R) (2012).

[197] C. Trallero-Giner, A. Debernardi, M. Cardona, E. Menéndez-Proupín, and A. I. Ekimov, Optical vibrons in CdSe dots and dispersion relation of the bulk material, Phys. Rev. B **57**, 4664 (1998).

[198] U. Woggon, F. Gindele, O. Wind, and C. F. Klingshirn, Exchange interaction and phonon confinement in CdSe quantum dots, Phys. Rev. B **54**, 1506 (1996).

[199] D. M. Sagar, R. R. Cooney, S. L. Sewall, E. A. Dias, M. M. Barsan, I. S. Butler, and P. Kambhampati, Size dependent, state-resolved studies of exciton-phonon couplings in strongly confined semiconductor quantum dots, Phys. Rev. B **77**, 235321 (2008).

[200] D. E. Reiter, T. Kuhn, and V. M. Axt, Distinctive characteristics of carrier-phonon interactions in optically driven semiconductor quantum dots, Adv. Phys.: X **4**, 1655478 (2019).

[201] L. J. Challis (Ed.), Electron-phonon interactions in low-dimensional structures, Oxford University Press, Oxford (2003).

[202] B. Krummheuer, V. M. Axt, and T. Kuhn, Theory of pure dephasing and the resulting absorption line shape in semiconductor quantum dots, Phys. Rev. B **65**, 195313 (2002).

[203] L. M. Woods, T. L. Reinecke, and Y. Lyanda-Geller, Spin relaxation in quantum dots, Phys. Rev. B **66**, 161318(R) (2002).

[204] P. A. Knipp and T. L. Reinecke, Coupling between electrons and acoustic phonons in semiconductor nanostructures, Phys. Rev. B **52**, 5923 (1995).

[205] A. M. Marvin, V. Bortolani, and F. Nizzoli, Surface Brillouin scattering from acoustic phonons, I. General theory. J. Phys. C: Solid State Phys. **13**, 299 (1980).

[206] P. A. Knipp and T. L. Reinecke, Electron scattering from acoustic phonons in quantum dots and other nanostructures, Solid-State Electronics **40**, 343 (1996).

[207] S. Mishra and R. Bray, Surface-ripple mechanism for Brillouin scattering of reflected light from bulk acoustic waves, Phys. Rev. Lett. **39**, 222 (1977).

[208] L. Chu, A. Zrenner, M. Bichler, G. Böhm, and G. Abstreiter, Raman spectroscopy of In(Ga)As/GaAs quantum dots, Appl. Phys. Lett. **77**, 3944 (2000).

[209] B. Miller, J. Lindlau, M. Bommert, A. Neumann, H. Yamaguchi, A. W. Holleitner, A. Högele, and U. Wurstbauer, Tuning the Fröhlich exciton-phonon scattering in monolayer MoS_2, Nat. Commun. **10**, 807 (2019).

[210] K. Kaasbjerg, K. S. Thygesen, and K. W. Jacobsen, Phonon-limited mobility in n-type single-layer MoS_2 from first principles, Phys. Rev. B **85**, 115317 (2012).

[211] S.-Y. Chen, C. Zheng, M. S. Fuhrer, and J. Yan, Helicity-resolved Raman scattering of MoS_2, $MoSe_2$, WS_2, and WSe_2 atomic layers, Nano Lett. **15**, 2526 (2015).

[212] X. Zhang, X. F. Qiao, W. Shi, J.-B. Wu, D.-S. Jiang, and P.-H. Tan, Phonon and Raman scattering of two-dimensional transition metal dichalcogenides from monolayer, multilayer to bulk material, Chem. Soc. Rev. **44**, 2757 (2015).

[213] Y. Zhao, S. Zhang, Y. Shi, Y. Zhang, R. Saito, J. Zhang, and L. Tong, Characterization of excitonic nature in Raman spectra using circularly polarized light, ACS Nano **14**, 10527 (2020).

[214] J. Su, Z.-T. Liu, L.-P. Feng, and N. Li, Effect of temperature on thermal properties of monolayer MoS_2 sheet, J. Alloys Compd., **622**, 777 (2015).

[215] T. Sohier, M. Gibertini, M. Calandra, F. Mauri, and N. Marzari, Breakdown of optical phonons' splitting in two-dimensional materials, Nano Lett. **17**, 3758 (2017).

[216] X. Gu and R. Yang, Phonon transport in single-layer transition metal dichalcogenides: a first-principles study, Appl. Phys. Lett. **105**, 131903 (2014).

[217] H. Zhu, J. Yi, M.-Y. Li, J. Xiao, L. Zhang, C.-W. Yang, R. A. Kaindl, L.-J. Li, Y. Wang, and X. Zhang, Observation of chiral phonons, Science **359**, 579 (2018).

[218] R. Saito, Y. Tatsumi, S. Huang, X. Ling, and M. S. Dresselhaus, Raman spectroscopy of transition metal dichalcogenides, J. Phys.: Condens. Matter **28**, 353002 (2016).

[219] C. H. Lui, Z. Ye, C. Ji, K.-C. Chiu, C.-T. Chou, T. I. Andersen, C. Means-Shively, H. Anderson, J.-M. Wu, T. Kidd, Y.-H. Lee, and R. He, Observation of interlayer phonon modes in van der Waals heterostructures, Phys. Rev. B **91**, 165403 (2015).

[220] C. Jin, J. Kim, J. Suh, Z. Shi, B. Chen, X. Fan, M. Kam, K. Watanabe, T. Taniguchi, S. Tongay, A. Zettl, J. Wu, and F. Wang, Interlayer electron-phonon coupling in WSe_2/hBN heterostructures, Nat. Phys. **13**, 127 (2017).

[221] C. M. Chow, H. Yu, A. M. Jones, J. Yan, D. G. Mandrus, T. Taniguchi, K. Watanabe, W. Yao, and X. Xu, Unusual exciton-phonon interactions at van der Waals engineered interfaces, Nano Lett. **17**, 1194 (2017).

[222] U. Wurstbauer, B. Miller, E. Parzinger, and A. W. Holleitner, Light-matter interaction in transition metal dichalcogenides and their heterostructures, J. Phys. D: Appl. Phys. **50**, 173001 (2017).

[223] F. Leonardi, Self-assembled monolayers (SAMs) in organic field-effect transistors, Dissertation, University of Bologna, Bologna (2014).

[224] P. Vogl, Microscopic theory of electron-phonon interaction in insulators or semiconductors, Phys. Rev. B **13**, 694 (1976).

[225] K. Kaasbjerg, K. S. Bhargavi, and S. S. Kubakaddi, Hot-electron cooling by acoustic and optical phonons in monolayers of MoS_2 and other transition-metal dichalcogenides, Phys. Rev. B **90**, 165436 (2014).

[226] G. D. Mahan, Condensed matter in a nutshell, Princeton University Press, Princeton (2011).

[227] T. Takagahara, Electron-phonon interactions and excitonic dephasing in semiconductor nanocrystals, Phys. Rev. Lett. **71**, 3577 (1993).

[228] V. Nadtochenko, N. Denisov, A. Aybush, F. Gostev, I. Shelaev, A. Titov, S. Umanskiy, and D. Cherepanov, Ultrafast spectroscopy of Fano-like resonance between optical phonon and excitons in CdSe quantum dots: dependence of coherent vibrational wave-packet dynamics on pump fluence, Nanomaterials **7**, 371 (2017).

[229] T. Takagahara, Theory of exciton dephasing in semiconductor quantum dots, Phys. Rev. B **60**, 2638 (1999).

[230] S. Krishnamurthy, A. Sher, A.-B. Chen, Deformation potential and intervalley scattering: Hot-electron transistor analysis, Appl. Phys. Lett. **53**, 1853 (1988).

[231] A. N. Das, J. Konior, and D. K. Ray, Hole-phonon interaction in a strongly correlated Hubbard system, Physica C: Superconductivity **170**, 215 (1990).

[232] L. M. Woods, T. L. Reinecke, and R. Kotlyar, Hole spin relaxation in quantum dots, Phys. Rev. B **69**, 125330 (2004).

[233] S. Lüker, T. Kuhn, and D. E. Reiter, Phonon impact on optical control schemes of quantum dots: role of quantum dot geometry and symmetry, Phys. Rev. B **96**, 245306 (2017).

[234] J. Bardeen and W. Shockley, Deformation potentials and mobilities in non-polar crystals, Phys. Rev. **80**, 72 (1950).

[235] F. H. Pollak and M. Cardona, Piezo-Electroreflectance in Ge, GaAs, and Si, Phys. Rev. **172**, 816 (1968).

[236] T. B. Bahder, Eight-band k·p model of strained zinc-blende crystals, Phys. Rev. B **41**, 11992 (1990).

[237] J. Wiktor and A. Pasquarello, Absolute deformation potentials of two-dimensional materials, Phys. Rev. B **94**, 245411 (2016).

[238] I. Vurgaftman, J. R. Meyer, and L. R. Ram-Mohan, Band parameters for III-V compound semiconductors and their alloys, J. Appl. Phys. **89**, 5815 (2001).

[239] S.-H. Wei and A. Zunger, Predicted band-gap pressure coefficients of all diamond and zinc-blende semiconductors: chemical trends, Phys. Rev. B **60**, 5404 (1999).

[240] P. Stepanov, M. Elzo-Aizarna, J. Bleuse, N. S. Malik, Y. Curé, E. Gautier, V. Favre-Nicolin, J.-M. Gérard, and J. Claudon, Large and uniform optical emission shifts in quantum dots strained along their growth axis, Nano Lett. **16**, 3215 (2016).

[241] Z. Guo, X. Wu, T. Zhu, X. Zhu, and L. Huang, Electron-phonon scattering in atomically thin 2D perovskites, ACS Nano **10**, 9992 (2016).

[242] M. Usman, Y.-H. M. Tan, H. Ryu, S. S. Ahmed, H. J. Krenner, T. B. Boykin, and G. Klimeck, Quantitative excited state spectroscopy of a single InGaAs quantum dot molecule through multi-million-atom electronic structure calculations, Nanotechnology **22**, 315709 (2011).

[243] T. Kaldewey, S. Lüker, A. V. Kuhlmann, S. R. Valentin, J.-M. Chauveau, A. Ludwig, A. D. Wieck, D. E. Reiter, T. Kuhn, and R. J. Warburton, Demonstrating the decoupling regime of the electron-phonon interaction in a quantum dot using chirped optical excitation, Phys. Rev. B **95**, 241306(R) (2017).

[244] T. E. Hodgson, L. Viola, and I. D'Amico, Decoherence-protected storage of exciton qubits through ultrafast multipulse control, Phys. Rev. B **78**, 165311 (2008).

[245] S. Rudin, T. L. Reinecke, and B. Segall, Temperature-dependent exciton linewidths in semiconductors, Phys. Rev. B **42**, 11218 (1990).

[246] M. M. Alyörük, Y. Aierken, D. Çakır, F. M. Peeters, and C. Sevik, Promising piezoelectric performance of single layer transition-metal dichalcogenides and dioxides, J. Phys. Chem. C **119**, 23231 (2015).

[247] M. A. Brummell, R. J. Nicholas, M. A. Hopkins, J. J. Harris, and C. T. Foxon, Modification of the electron-phonon interactions in GaAs-GaAIAs heterojunctions, Phys. Rev. Lett. **58**, 77 (1987).

[248] J. Debus, D. Kudlacik, P. Waldkirch, V. F. Sapega, S. Scholz, A. Ludwig, A. D. Wieck, and M. Bayer, Efficiency enhancement of the coherent electron spin-flip Raman scattering through thermal phonons in (In,Ga)As/GaAs quantum dots, Phys. Rev. B **95**, 201303(R) (2017).

[249] J. Jadczak, L. Bryja, J. Kutrowska-Girzycka, P. Kapuściński, M. Bieniek, Y.-S. Huang, and P. Hawrylak, Room temperature multi-phonon upconversion photoluminescence in monolayer semiconductor WS_2, Nat. Commun. **10**, 107 (2019).

[250] P. Dey, J. Paul, Z. Wang, C. E. Stevens, C. Liu, A. H. Romero, J. Shan, D. J. Hilton, and D. Karaiskaj, Optical coherence in atomic-monolayer transition-metal dichalcogenides limited by electron-phonon interactions, Phys. Rev. Lett. **116**, 127402 (2016).

[251] J. Debus, D. Kudlacik, V. F. Sapega, T. S. Shamirzaev, D. R. Yakovlev, D. Reuter, A. D. Wieck, A. Waag, and M. Bayer, Basic requirements of spin-flip Raman scattering on excitonic resonances and its modulation through additional high-energy illumination in semiconductor heterostructures, Phys. Solid State **60**, 1611 (2018).

[252] T. M. Hsu, Y. S. Lan, W.-H. Chang, N. T. Yeh, and J.-I. Chyi, Tuning the energy levels of self-assembled InAs quantum dots by rapid thermal annealing, Appl. Phys. Lett. **76**, 691 (2000).

[253] A. O. Kosogov, P. Werner, U. Gösele, N. N. Ledentsov, D. Bimberg, V. M. Ustinov, A. Yu. Egorov, A. E. Zhukov, P. S. Kop'ev, N. A. Bert, Zh. I. Alferov, Structural and optical properties of InAs-GaAs quantum dots subjected to high temperature annealing, Appl. Phys. Lett. **69**, 3072 (1996).

[254] J. Jadczak, J. Kutrowska-Girzycka, J. J. Schindler, J. Debus, K. Watanabe, T. Taniguchi, C.-H. Ho, and L. Bryja, Investigations of electron-electron and interlayer electron-phonon coupling in van der Waals hBN/WSe_2/hBN heterostructures by photoluminescence excitation experiments, Materials **14**, 399 (2021).

[255] S. Sanguinetti, D. Colombo, M. Guzzi, E. Grilli, M. Gurioli, L. Seravalli, P. Frigeri, and S. Franchi, Carrier thermodynamics in InAs/$In_xGa_{1-x}As$ quantum dots, Phys. Rev. B **74**, 205302 (2006).

[256] M. Cardona, Infrared dielectric constant and ultraviolet optical properties of solids with diamond, zinc blende, wurtzite, and rocksalt structure, J. Appl. Phys. **36**, 2181 (1965).

[257] L. Pavesi and M. Guzzi, Photoluminescence of $Al_xGa_{1-x}As$ alloys, J. Appl. Phys. **75**, 4779 (1994).

[258] F. Withers, O. Del Pozo-Zamudio, A. Mishchenko, A. P. Rooney, A. Gholinia, K. Watanabe, T. Taniguchi, S. J. Haigh, A. K. Geim, A. I. Tartakovskii, and K. S. Novoselov, Light-emitting diodes by band-structure engineering in van der Waals heterostructures, Nat. Mater. **14**, 301 (2015).

[259] T. Aoki, Photoluminescence spectroscopy, In: E. N. Kaufmann (Ed.), Characterization of materials, Second Edition, John Wiley & Sons, Hoboken (2012).

[260] G. Mie, Beiträge zur Optik trüber Medien speziell kolloidaler Metallösungen, Ann. Phys. **330**, 377(1908).

[261] M. Born and E. Wolf, Principles of optics, 7th anniversary edition, Cambridge University Press, Cambridge (2019).

[262] P. Laven, Simulation of rainbows, coronas and glories using Mie theory and the Debye series, J. Quant. Spectrosc. Radiat. Transf. **89**, 257 (2004).

[263] L. Brillouin, Diffusion of light and X-rays by a transparent homogeneous body - The influence of thermal agitation, Ann. Phys. **9**, 88 (1922).

[264] G. S. Landsberg and L. I. Mandelstam, Über die Lichtzerstreuung in Kristallen, Zs. Phys. **50**, 769 (1928).

[265] C. V. Raman and K. S. Krishnan, A new class of spectra due to secondary radiation - Part I, Indian J. Phys. **2**, 399 (1928).

[266] M. Cardona, G. Güntherodt, and R. Merlin (Eds.), Book IX: Novel materials and techniques, Series: Light Scattering in Solids, In: Topics in Applied Physics, Springer-Verlag, Berlin (1975-2007).

[267] W. Heitler, The quantum theory of radiation, Third Edition, Dover Publications, New York (1984).

[268] V. F. Sapega, T. Ruf, and M. Cardona, Spin-flip Raman study of exchange interactions in bulk GaAs:Mn, Phys. stat. sol. (b) **226**, 339 (2001).

[269] A. A. Sirenko, V. I. Belitsky, T. Ruf, M. Cardona, A. I. Ekimov, and C. Trallero-Giner, Spin-flip and acoustic-phonon Raman scattering in CdS nanocrystals, Phys. Rev. B **58**, 2077 (1998).

[270] V. F. Sapega, T. Ruf, M. Cardona, K. Ploog, E. L. Ivchenko, and D. N. Mirlin, Resonant Raman scattering due to bound-carrier spin flip in GaAs/$Al_xGa_{1-x}As$ quantum wells, Phys. Rev. B **50**, 2510 (1994).

[271] M. Nawrocki, R. Planel, G. Fishman, and R. Galazka, Exchange-induced spin-flip Raman scattering in a semimagnetic semiconductor, Phys. Rev. Lett. **46**, 735 (1981).

[272] J. Debus, D. Kudlacik, V. F. Sapega, D. Dunker, P. Bohn, F. Paßmann, D. Braukmann, J. Rautert, D. R. Yakovlev, D. Reuter, A. D. Wieck, and M. Bayer, Nuclear spin polarization in the electron spin-flip Raman scattering of singly charged (In,Ga)As/GaAs quantum dots, Phys. Rev. B **92**, 195421 (2015).

[273] D. Kudlacik, K. V. Kavokin, C. Lüders, K. Barthelmi, J. J. Schindler, H. Moldenhauer, P. Waldkirch, V. F. Sapega, D. R. Yakovlev, A. Waag, M. Bayer, and J. Debus, Asymmetric spin transitions of nonthermalized Mn^{2+} ions in (Zn,Mn)Se-based quantum wells, Phys. Rev. B **101**, 155432 (2020).

[274] M. Sugawara, Magnetic-field-induced enhancement of exciton oscillator strength in $In_{0.53}Ga_{0.47}As$/InP quantum wells, Phys. Rev. B **45**, 11423(R) (1992).

[275] G. F. Koster, J. O. Dimmock, R. G. Wheeler, and H. Statz, Properties of the thirty-two point groups, M.I.T. Press, Cambridge (1963).

[276] J. P. Eisenstein, H. L. Störmer, V. Narayanamurti, A. C. Gossard, and W. Wiegmann, Effect of inversion symmetry on the band structure of semiconductor heterostructures, Phys. Rev. Lett. **53**, 2579 (1984).

[277] Y. Song and H. Dery, Transport theory of monolayer transition-metal dichalcogenides through symmetry, Phys. Rev. Lett. **111**, 026601 (2013).

[278] Al. L. Efros, Luminescence polarization of CdSe microcrystals, Phys. Rev. B **46**, 7448 (1992).

[279] M. Beye, F. Hennies, M. Deppe, E. Suljoti, M. Nagasono, W. Wurth, and A. Föhlisch, Dynamics of electron-phonon scattering: crystal- and angular-momentum transfer probed by resonant inelastic X-ray scattering, Phys. Rev. Lett. **103**, 237401 (2009).

[280] R. Ruppin, Thermal fluctuations and Raman scattering in small spherical crystals, J. Phys. C: Solid State Phys. **8**, 1969 (1975).

[281] D. G. Thomas and J. J. Hopfield, Spin-flip Raman scattering in cadmium sulfide, Phys. Rev. **175**, 1021 (1968).

[282] M. Grundmann, J. Christen, N. N. Ledentsov, J. Böhrer, D. Bimberg, S. S. Ruvimov, P. Werner, U. Richter, U. Gösele, J. Heydenreich, V. M. Ustinov, A. Yu. Egorov, A. E. Zhukov, P. S. Kop'ev, and Zh. I. Alferov, Ultranarrow luminescence lines from single quantum dots, Phys. Rev. Lett. **74**, 4043 (1995).

[283] J. Toporski, T. Dieing, and O. Hollricher (Eds.), Confocal Raman microscopy, Second Edition, In: Springer Series in Surface Sciences, Vol. 66, Springer-Verlag, Berlin (2018).

[284] C. Trallero-Giner, T. Ruf, and M. Cardona, Theory of one-phonon resonant Raman scattering in a magnetic field, Phys. Rev. B **41**, 3028 (1990).

[285] A. V. Koudinov, Yu. G. Kusrayev, D. Wolverson, L. C. Smith, J. J. Davies, G. Karczewski, and T. Wojtowicz, Giant modulation of resonance Raman scattering from (Cd,Mn)Te quantum wells by secondary illumination, Phys. Rev. B **79**, 241310(R) (2009).

[286] G. Ambrazevičius, S. Marcinkevičius, T. Lideikis, and K. Naudžius, Oscillatory photoluminescence excitation in InGaAs/GaAs strained-layer quantum well structures, Semicond. Sci. Technol. **6**, 41 (1991).

[287] J. Eichler and H. J. Eichler, Laser - Bauformen, Strahlführung, Anwendungen, 6. Auflage, Springer-Verlag, Berlin (2006).

[288] D. Kudlacik, Characterization of semiconductor nanostructures by spin-flip Raman spectroscopy, Dissertation, TU Dortmund University, Dortmund (2018).

[289] A. K. Zvezdin and V. A. Kotov, Modern magnetooptics and magnetooptical materials, Institute of Physics Publishing, Bristol (1997).

[290] D. Braukmann, V. P. Popov, E. R. Glaser, T. A. Kennedy, M. Bayer, and J. Debus, Anisotropies in the linear polarization of vacancy photoluminescence in diamond induced by crystal rotations and strong magnetic fields, Phys. Rev. B **97**, 125426 (2018).

[291] T. C. Damen, S. P. S. Porto, and B. Tell, Raman effect in zinc oxide, Phys. Rev. **142**, 570 (1966).

[292] H. E. Johns and J. O. Wilhelm, The refractive indices of liquid helium I and helium II, Can. J. Research **16a**, 131 (1938).

[293] TriVista System Manual - Version 1.A, Princeton Instruments, Trenton (2005).

[294] R. Petit (Ed.), Electromagnetic theory of gratings, In: Topics in current physics, Vol. 22, Springer-Verlag, Berlin (1980).

[295] Technical Manual - Ramanor U1000 Monochromator, Version 3, Jobin Yvon (1988).

[296] M. Grundmann, O. Stier, and D. Bimberg, InAs/GaAs pyramidal quantum dots: strain distribution, optical phonons, and electronic structure, Phys. Rev. B **52**, 11969 (1995).

[297] K. S. Novoselov, D. Jiang, F. Schedin, and A. K. Geim, Two-dimensional atomic crystals, Proc. Natl. Acad. Sci. USA **102**, 10451 (2005).

[298] K. S. Novoselov and A. K. Geim, The rise of graphene, Nat. Mater. **6**, 183 (2007).

[299] S. M. Poh, S. J. R. Tan, X. Zhao, Z. Chen, I. Abdelwahab, D. Fu, H. Xu, Y. Bao, W. Zhou, and K. P. Loh, Large area synthesis of 1D-$MoSe_2$ using molecular beam epitaxy, Adv. Mater. **29**, 1605641 (2017).

[300] Y.-H. Lee, X.-Q. Zhang, W. Zhang, M.-T. Chang, C.-T. Lin, K.-D. Chang, Y.-C. Yu, J. T.-W. Wang, C.-S. Chang, L.-J. Li, and T.-W. Lin, Synthesis of large-area MoS_2 atomic layers with chemical vapor deposition, Adv. Mater. **24**, 2320 (2012).

[301] A. Castellanos-Gomez, M. Buscema, R. Molenaar, V. Singh, L. Janssen, H. S. J. van der Zant, and G. A. Steele, Deterministic transfer of two-dimensional materials by all-dry viscoelastic stamping, 2D Materials **1**, 011002 (2014).

[302] M. Bayer, Bridging two worlds: colloidal versus epitaxial quantum dots, Ann. Phys. **531**, 1900039 (2019).

[303] S. M. Reimann and M. Manninen, Electronic structure of quantum dots, Rev. Mod. Phys. **74**, 1283 (2002).

[304] R. Hanson, L. P. Kouwenhoven, J. R. Petta, S. Tarucha, and L. M. K. Vandersypen, Spins in few-electron quantum dots, Rev. Mod. Phys. **79**, 1217 (2007).

[305] S. A. Wolf, D. D. Awschalom, R. A. Buhrman, J. M. Daughton, S. von Molnár, M. L. Roukes, A. Yu. Chtchelkanova, and D. M. Treger, Spintronics: a spin-based electronics vision for the future, Science **294**, 1488 (2001).

[306] I. Žutić, J. Fabian, and S. Das Sarma, Spintronics: fundamentals and applications, Rev. Mod. Phys. **76**, 323 (2004).

[307] A. Greilich, D. R. Yakovlev, A. Shabaev, Al. L. Efros, I. A. Yugova, R. Oulton, V. Stavarache, D. Reuter, A. Wieck, and M. Bayer, Mode locking of electron spin coherences in singly charged quantum dots, Science **313**, 341 (2006).

[308] A. Greilich, S. E. Economou, S. Spatzek, D. R. Yakovlev, D. Reuter, A. Wieck, T. L. Reinecke, and M. Bayer, Ultrafast optical rotations of electron spins in quantum dots, Nat. Phys. **5**, 262 (2009).

[309] J. McFarlane, P. A. Dalgarno, B. D. Gerardot, R. H. Hadfield, R. J. Warburton, K. Karrai, A. Badolato, and P. M. Petroff, Gigahertz bandwidth electrical control over a dark exciton-based memory bit in a single quantum dot, Appl. Phys. Lett. **94**, 093113 (2009).

[310] E. Poem, Y. Kodriano, C. Tradonsky, N. H. Lindner, B. D. Gerardot, P. M. Petroff, and D. Gershoni, Accessing the dark exciton with light, Nat. Phys. **6**, 993 (2010).

[311] M. Nirmal, D. J. Norris, M. Kuno, M. G. Bawendi, Al. L. Efros, and M. Rosen, Observation of the "dark exciton" in CdSe quantum dots, Phys. Rev. Lett. **75**, 3728 (1995).

[312] T. Smoleński, T. Kazimierczuk, M. Goryca, T. Jakubczyk, Ł. Kłopotowski, Ł. Cywiński, P. Wojnar, A. Golnik, and P. Kossacki, In-plane radiative recombination channel of a dark exciton in self-assembled quantum dots, Phys. Rev. B **86**, 241305(R) (2012).

[313] S. Lüker, T. Kuhn, and D. E. Reiter, Direct optical state preparation of the dark exciton in a quantum dot, Phys. Rev. B **92**, 201305(R) (2015).

[314] L. Gantz, E. R. Schmidgall, I. Schwartz, Y. Don, E. Waks, G. Bahir, and D. Gershoni, Controlling the dark exciton spin eigenstates by external magnetic field, Phys. Rev. B **94**, 045426 (2016).

[315] M. F. Limonov, M. V. Rybin, A. N. Poddubny, and Y. S. Kivshar, Fano resonances in photonics, Nat. Photon. **11**, 543 (2017).

[316] G. Breit and E. Wigner, Capture of slow neutrons, Phys. Rev. **49**, 519 (1936).

[317] U. Fano, Effects of configuration interaction on intensities and phase shifts, Phys. Rev. **124**, 1866 (1961).

[318] F. Bechstedt and K. Peuker, Theory of interference between electronic and phonon Raman scattering, Phys. stat. sol. (b) **72**, 743 (1975).

[319] D. L. Rousseau and S. P. S. Porto, Auger-like resonant interference in Raman scattering from one- and two-phonon states of $BaTiO_3$, Phys. Rev. Lett. **20**, 1354 (1968).

[320] M. Kroner, A. O. Govorov, S. Remi, B. Biedermann, S. Seidl, A. Badolato, P. M. Petroff, W. Zhang, R. Barbour, B. D. Gerardot, R. J. Warburton, and K. Karrai, The nonlinear Fano effect, Nature **451**, 311 (2008).

[321] E. H. Hasdeo, A. R. T. Nugraha, M. S. Dresselhaus, and R. Saito, Breit-Wigner-Fano line shapes in Raman spectra of graphene, Phys. Rev. B **90**, 245140 (2014).

[322] J. F. Song, Y. Ochiai, and J. P. Bird, Fano resonances in open quantum dots and their application as spin filters, Appl. Phys. Lett. **82**, 4561 (2003).

[323] I. A. Shelykh and N. G. Galkin, Fano and Breit-Wigner resonances in carrier transport through Datta and Das spin modulators, Phys. Rev. B **70**, 205328 (2004).

[324] M. L. Kerfoot, A. O. Govorov, C. Czarnocki, D. Lu, Y. N. Gad, A. S. Bracker, D. Gammon, and M. Scheibner, Optophononics with coupled quantum dots, Nat. Commun. **5**, 3299 (2014).

[325] S. Schippers, Analytical expression for the convolution of a Fano line profile with a gaussian, J. Quant. Spectrosc. Radiat. Transf. **219**, 33 (2018).

[326] B. Georgeot and D. L. Shepelyansky, Breit-Wigner width and inverse participation ratio in finite interacting Fermi systems, Phys. Rev. Lett. **79**, 4365 (1997).

[327] S. Schippers, S. Kieslich, A. Müller, G. Gwinner, A. Schnell, A. Wolf, A. Covington, M. E. Bannister, and L.-B. Zhao, Interference effects in the photorecombination of argonlike Sc^{3+} ions: storage-ring experiment and theory, Phys. Rev. A **65**, 042723 (2002).

[328] B. Eble, P. Desfonds, F. Fras, F. Bernardot, C. Testelin, M. Chamarro, A. Miard, and A. Lemaître, Hole and trion spin dynamics in quantum dots under excitation by a train of circularly polarized pulses, Phys. Rev. B **81**, 045322 (2010).

[329] A. Franceschetti, L. W. Wang, H. Fu, and A. Zunger, Short-range versus long-range electron-hole exchange interactions in semiconductor quantum dots, Phys. Rev. B **58**, R13367(R) (1998).

[330] T. Smoleński, T. Kazimierczuk, M. Goryca, P. Wojnar, and P. Kossacki, Mechanism and dynamics of biexciton formation from a long-lived dark exciton in a CdTe quantum dot, Phys. Rev. B **91**, 155430 (2015).

[331] A. S. Bracker, D. Gammon, and V. L. Korenev, Fine structure and optical pumping of spins in individual semiconductor quantum dots, Semicond. Sci. Technol. **23**, 114004 (2008).

[332] D. Gammon, Al. L. Efros, T. A. Kennedy, M. Rosen, D. S. Katzer, D. Park, S. W. Brown, V. L. Korenev, and I. A. Merkulov, Electron and nuclear spin interactions in the optical spectra of single GaAs quantum dots, Phys. Rev. Lett. **86**, 5176 (2001).

[333] M. Zieliński, Dark-bright excitons mixing in alloyed InGaAs self-assembled quantum dots, Phys. Rev. B **103**, 155418 (2021).

[334] R. M. Stevenson, R. J. Young, P. See, D. G. Gevaux, K. Cooper, P. Atkinson, I. Farrer, D. A. Ritchie, and A. J. Shields, Magnetic-field-induced reduction of the exciton polarization splitting in InAs quantum dots, Phys. Rev. B **73**, 033306 (2006).

[335] P. Kapuściński, A. Delhomme, D. Vaclavkova, A. O. Slobodeniuk, M. Grzeszczyk, M. Bartos, K. Watanabe, T. Taniguchi, C. Faugeras, and M. Potemski, Rydberg series of dark excitons and the conduction band spin-orbit splitting in monolayer WSe_2, Commun. Phys. **4**, 186 (2021).

[336] M. Dyksik, H. Duim, D. K. Maude, M. Baranowski, M. A. Loi, and P. Plochocka, Brightening of dark excitons in 2D perovskites, Sci. Adv. **7**, eabk0904 (2021).

[337] M. Krzykowski, K. Gawarecki, and P. Machnikowski, Hole spin-flip transitions in a self-assembled quantum dot, Phys. Rev. B **102**, 205301 (2020).

[338] A. Mielnik-Pyszczorski, K. Gawarecki, M. Gawełczyk, and P. Machnikowski, Dominant role of the shear strain induced admixture in spin-flip processes in self-assembled quantum dots, Phys. Rev. B **97**, 245313 (2018).

[339] J. F. Scott, Hybrid phonons and anharmonic interactions in $AlPO_4$, Phys. Rev. Lett. **24**, 1107 (1970).

[340] H. S. Nikoghosyan, V. F. Manukyan, S. L. Harutyunyan, and G. Nikoghosyan, Fano resonance model for the processes of photoionization of two-well heterostructures in a transverse electric field, Physica E **128**, 114587 (2021).

[341] R. A. Cowley, The lattice dynamics of an anharmonic crystal, Adv. Phys. **12**, 421 (1963).

[342] A. Kaldun, C. Ott, A. Blättermann, M. Laux, K. Meyer, T. Ding, A. Fischer, and T. Pfeifer, Extracting phase and amplitude modifications of laser-coupled Fano resonances, Phys. Rev. Lett. **112**, 103001 (2014).

[343] D. A. Garanin and E. M. Chudnovsky, Angular momentum in spin-phonon processes, Phys. Rev. B **92**, 024421 (2015).

[344] L. Zhang and Q. Niu, Chiral phonons at high-symmetry points in monolayer hexagonal lattices, Phys. Rev. Lett. **115**, 115502 (2015).

[345] D. M. Juraschek and N. A. Spaldin, Orbital magnetic moments of phonons, Phys. Rev. Mat. **3**, 064405 (2019).

[346] S. Lüker, T. Kuhn, and D. E. Reiter, Phonon-assisted dark exciton preparation in a quantum dot, Phys. Rev. B **95**, 195305 (2017).

[347] V. N. Stavrou and X. Hu, Electron relaxation in a double quantum dot through two-phonon processes, Phys. Rev. B **73**, 205313 (2006).

[348] K. Roszak, V. M. Axt, T. Kuhn, and T. Machnikowski, Exciton spin decay in quantum dots to bright and dark states, Phys. Rev. B **76**, 195324 (2007).

[349] A. Schliwa, M. Winkelnkemper, and D. Bimberg, Impact of size, shape, and composition on piezoelectric effects and electronic properties of In(Ga)As/GaAs quantum dots, Phys. Rev. B **76**, 205324 (2007).

[350] D. Sarkar, H. P. van der Meulen, J. M. Calleja, J. M. Meyer, R. J. Haug, and K. Pierz, Piezoelectric exciton acoustic-phonon coupling in single quantum dots, Phys. Rev. B **78**, 241305(R) (2008).

[351] A. Anedda and G. Bongiovanni, Anharmonic mixing between two phonons in red mercury iodide, Phys. Rev. B. **38**, 13343 (1988).

[352] K. Brennan and K. Hess, High field transport in GaAs, InP and InAs, Solid-State Electronics **27**, 347 (1984).

[353] D. Gerlich, Elastic constants of single-crystal indium arsenide, J. Appl. Phys. **34**, 2915 (1963).

[354] R. I. Cottam and G. A. Saunders, The elastic constants of GaAs from 2 K to 320 K, J. Phys. C Solid State Phys. **6**, 2105 (1973).

[355] D. P. S. McCutcheon and A. Nazir, Quantum dot Rabi rotations beyond the weak exciton-phonon coupling regime, New J. Phys. **12**, 113042 (2010).

[356] A. J. Ramsay, T. M. Godden, S. J. Boyle, E. M. Gauger, A. Nazir, B. W. Lovett, A. M. Fox, and M. S. Skolnick, Phonon-induced Rabi-frequency renormalization of optically driven single InGaAs/GaAs quantum dots, Phys. Rev. Lett. **105**, 177402 (2010).

[357] M. Reppert, A. Kell, T. Pruitt, and R. Jankowiak, Comments on the optical lineshape function: application to transient hole-burned spectra of bacterial reaction centers, J. Chem. Phys. **142**, 094111 (2015).

[358] A. Svizhenko, A. Balandin, S. Bandyopadhyay, and M. A. Stroscio, Electron interaction with confined acoustic phonons in quantum wires subjected to a magnetic field, Phys. Rev. B **57**, 4687 (1998).

[359] M. A. Stroscio, M. Dutta, S. Rufo, and J. Yang, Dispersion and damping of acoustic phonons in quantum dots, IEEE Trans. Nanotechnol. **3**, 32 (2004).

[360] V. P. Kunets, M. D. Teodoro, V. G. Dorogan, P. M. Lytvyn, G. G. Tarasov, R. Sleezer, M. E. Ware, Yu. I. Mazur, J. S. Krasinski, and G. J. Salamo, Interface roughness scattering in laterally coupled InGaAs quantum wires, Appl. Phys. Lett. **97**, 262103 (2010).

[361] T. Sugaya, J. P. Bird, D. K. Ferry, T. Shimizu, K. Y. Jang, M. Ogura, Y. Sugiyama, and K. Yonei, Electron-phonon scattering in an etched InGaAs quantum wire, Physica B **314**, 99 (2002).

[362] B. Krummheuer, V. M. Axt, and T. Kuhn, Coupled polarization and acoustic-phonon dynamics after optical excitation of quantum dots near surfaces, Phys. Rev. B **72**, 245336 (2005).

[363] H. Lamb, On the vibrations of an elastic sphere, Proc. London Math. Soc. **13**, 189 (1882).

[364] F. Grosse and R. Zimmermann, Electron-phonon interaction in embedded semiconductor nanostructures, Phys. Rev. B **75**, 235320 (2007).

[365] D. Palaniappan, A general solution of equations of equilibrium in linear elasticity, Applied Mathematical Modelling **35**, 5494 (2011).

[366] A. N. Norris, An inequality for longitudinal and transverse wave attenuation coefficients, J. Acoust. Soc. Am. **141**, 475 (2017).

[367] F. Comas and N. Studart, Electron-phonon interaction in quantum-dot/quantum-well semiconductor heterostructures, Phys. Rev. B **69**, 235321 (2004).

[368] M. Montagna and R. Dusi, Raman scattering from small spherical particles, Phys. Rev. B **52**, 10080 (1995).

[369] F. Werschler, C. Hinz, F. Froning, P. Gumbsheimer, J. Haase, C. Negele, T. de Roo, S. Mecking, A. Leitenstorfer, and D. V. Seletskiy, Coupling of excitons and discrete acoustic phonons in vibrationally isolated quantum emitters, Nano Lett. **16**, 5861 (2016).

[370] L. Saviot and D. B. Murray, Longitudinal versus transverse spheroidal vibrational modes of an elastic sphere, Phys. Rev. B **72**, 205433 (2005).

[371] D. Zhou and A. Lorke, Wave functions of elliptical quantum dots in a magnetic field, Am. J. Phys. **83**, 205 (2015).

[372] M. Zieliński, Including strain in atomistic tight-binding Hamiltonians: an application to self-assembled InAs/GaAs and InAs/InP quantum dots, Phys. Rev. B **86**, 115424 (2012).

[373] G. Bester, A. Zunger, X. Wu, and D. Vanderbilt, Effects of linear and nonlinear piezoelectricity on the electronic properties of InAs/GaAs quantum dots, Phys. Rev. B **74**, 081305(R) (2006).

[374] A. Rückriegel, S. Streib, G. E. W. Bauer, and R. A. Duine, Angular momentum conservation and phonon spin in magnetic insulators, Phys. Rev. B **101**, 104402 (2020).

[375] E. P. Pokatilov, D. L. Nika, and A. A. Balandin, Confined electron-confined phonon scattering rates in wurtzite AlN/GaN/AlN heterostructures, J. Appl. Phys. **95**, 5626 (2004).

[376] P. Merkl, C.-K. Yong, M. Liebich, I. Hofmeister, G. Berghäuser, E. Malic, and R. Huber, Proximity control of interlayer exciton-phonon hybridization in van der Waals heterostructures, Nat. Commun. **12**, 1719 (2021).

[377] A. E. Miroshnichenko, S. Flach, and Yu. S. Kivshar, Fano resonances in nanoscale structures, Rev. Mod. Phys. **82**, 2257 (2010).

[378] A. Schwan, B.-M. Meiners, A. B. Henriques, A. D. B. Maia, A. A. Quivy, S. Spatzek, S. Varwig, D. R. Yakovlev, and M. Bayer, Dispersion of electron g-factor with optical transition energy in (In,Ga)As/GaAs self-assembled quantum dots, Appl. Phys. Lett. **98**, 233102 (2011).

[379] G. Sallen, A. Tribu, T. Aichele, R. André, L. Besombes, C. Bougerol, M. Richard, S. Tatarenko, K. Kheng, and J.-Ph. Poizat, Subnanosecond spectral diffusion measurement using photon correlation, Nat. Photon. **4**, 696 (2010).

[380] F. Basso Basset, S. Bietti, A. Tuktamyshev, S. Vichi, E. Bonera, and S. Sanguinetti, Spectral broadening in self-assembled GaAs quantum dots with narrow size distribution, J. Appl. Phys. **126**, 024301 (2019).

[381] G. Marx and R. Kummel, Electronic structure and jumping magnetization of quantum wells in tilted magnetic fields, J. Phys.: Condens. Matter **3**, 8237 (1991).

[382] D. Cialla-May, M. Schmitt, and J. Popp, Theoretical principles of Raman spectroscopy, Phys. Sci. Rev. **4**, 20170040 (2019).

[383] M. Dyakonov, X. Marie, T. Amand, P. Le Jeune, D. Robart, M. Brousseau, and J. Barrau, Coherent spin dynamics of excitons in quantum wells, Phys. Rev. B **56**, 10412 (1997).

[384] L. Besombes, K. Kheng, L. Marsal, and H. Mariette, Acoustic phonon broadening mechanism in single quantum dot emission, Phys. Rev. B **63**, 155307 (2001).

[385] K. H. Madsen, P. Kaer, A. Kreiner-Møller, S. Stobbe, A. Nysteen, J. Mørk, and P. Lodahl, Measuring the effective phonon density of states of a quantum dot in cavity quantum electrodynamics, Phys. Rev. B **88**, 045316 (2013).

[386] C. B. Duke and G. D. Mahan, Phonon-broadened impurity spectra. I. Density of states, Phys. Rev. **139**, A1965 (1965).

[387] T. Suzuki, R. Singh, G. Moody, M.-A. Aßmann, M. Bayer, A. Ludwig, A. D. Wieck, and S. T. Cundiff, Dephasing of InAs quantum dot p-shell excitons studied using two-dimensional coherent spectroscopy, Phys. Rev. B **98**, 195304 (2018).

[388] C. de Mello Donegá, M. Bode, and A. Meijerink, Size- and temperature-dependence of exciton lifetimes in CdSe quantum dots, Phys. Rev. B **74**, 085320 (2006).

[389] S. Arrhenius, Über die Dissociationswärme und den Einfluss der Temperatur auf den Dissociationsgrad der Elektrolyte, Z. Phys. Chem. **4**, 96 (1889).

[390] G. McArdle and I. V. Lerner, Electron-phonon decoupling in two dimensions, Sci. Rep. **11**, 24293 (2021).

[391] P. Borri, W. Langbein, U. Woggon, V. Stavarache, D. Reuter, and A. D. Wieck, Exciton dephasing via phonon interactions in InAs quantum dots: dependence on quantum confinement, Phys. Rev. B **71**, 115328 (2005).

[392] P. Holewa, M. Burakowski, A. Musiał, N. Srocka, D. Quandt, A. Strittmatter, S. Rodt, S. Reitzenstein, and G. Sęk, Thermal stability of emission from single InGaAs/GaAs quantum dots at the telecom O-band, Sci. Rep. **10**, 21816 (2020).

[393] P. Tamarat, L. Hou, J.-B. Trebbia, A. Swarnkar, L. Biadala, Y. Louyer, M. Y. Bodnarchuk, M. V. Kovalenko, J. Even, and B. Lounis, The dark exciton ground state promotes photon-pair emission in individual perovskite nanocrystals, Nat. Commun. **11**, 6001 (2020).

[394] Y. Louyer, L. Biadala, Ph. Tamarat, and B. Lounis, Spectroscopy of neutral and charged exciton states in single CdSe/ZnS nanocrystals, Appl. Phys. Lett. **96**, 203111 (2010).

[395] L. Biadala, Y. Louyer, Ph. Tamarat, and B. Lounis, Direct observation of the two lowest exciton zero-phonon lines in single CdSe/ZnS nanocrystals, Phys. Rev. Lett. **103**, 037404 (2009).

[396] A. Vagov, V. M. Axt, and T. Kuhn, Impact of pure dephasing on the nonlinear optical response of single quantum dots and dot ensembles, Phys. Rev. B **67**, 115338 (2003).

[397] J. G. Dil, Brillouin scattering in condensed matter, Rep. Prog. Phys. **45**, 285 (1982).

[398] S. Adachi, Optical dispersion relations for GaP, GaAs, GaSb, InP, InAs, InSb, $Al_xGa_{1-x}As$, and $In_{1-x}Ga_xAs_yP_{1-y}$, J. Appl. Phys. **66**, 6030 (1989).

[399] D. H. Park and K. F. Brennan, Theory of electronic transport in two-dimensional $Ga_{0.85}In_{0.15}As/Al_{0.15}Ga_{0.85}As$ pseudomorphic structures, J. Appl. Phys. **65**, 1615 (1989).

[400] J. A. Lock and P. Laven, Co-polarized and cross-polarized scattering of an off-axis focused Gaussian beam by a spherical particle, In: Special Issue on Laser-light and Interactions with Particles, J. Quant. Spectrosc. Radiat. Transf. **221**, 260 (2018).

[401] S. V. Gupalov and I. A. Merkulov, Theory of Raman light scattering by nanocrystal acoustic vibrations, Phys. Solid State **41**, 1349 (1999).

[402] L. Brillouin, The scattering cross section of spheres for electromagnetic waves, J. Appl. Phys. **20**, 1110 (1949).

[403] J. I. Climente, A. Bertoni, G. Goldoni, and E. Molinari, Directionality of acoustic-phonon emission in weakly confined semiconductor quantum dots, Phys. Rev. B **75**, 245330 (2007).

[404] S. A. Sørngård, M. Førre, and J. P. Hansen, Angular resolved phonon emission from excited quantum dots, New J. Phys. **14**, 013035 (2012).

[405] A. Chatterjee and S. Mukhopadhyay, Polaronic effects in quantum dots, Acta Phys. Pol. B **32**, 473 (2001).

[406] S. Mukhopadhyay and A. Chatterjee, Suppression of Zeeman splitting in a GaAs quantum dot, Phys. Rev. B **59**, R7833(R) (1999).

[407] K. Deng, F. A. Calderon-Vargas, N. J. Mayhall, and E. Barnes, Negative exchange interactions in coupled few-electron quantum dots, Phys. Rev. B **97**, 245301 (2018).

[408] M. Bayer, A. Forchel, P. Hawrylak, S. Fafard, and G. A. Narvaez, Excitonic states in In(Ga)As self-assembled quantum dots, Phys. stat. sol. (b) **224**, 331 (2001).

[409] J. Manalo, M. Cygorek, A. Altintas, and P. Hawrylak, Electronic and magnetic properties of many-electron complexes in charged $InAs_xP_{1-x}$ quantum dots in InP nanowires, Phys. Rev. B **104**, 125402 (2021).

[410] E. A. Zibik, T. Grange, B. A. Carpenter, R. Ferreira, G. Bastard, N. Q. Vinh, P. J. Phillips, M. J. Steer, M. Hopkinson, J. W. Cockburn, M. S. Skolnick, and L. R. Wilson, Intersublevel polaron dephasing in self-assembled quantum dots, Phys. Rev. B **77**, 041307(R) (2008).

[411] G. A. Narvaez and A. Zunger, Nominally forbidden transitions in the interband optical spectrum of quantum dots, Phys. Rev. Lett. **74**, 045316 (2006).

[412] T. Smoleński, T. Kazimierczuk, M. Goryca, P. Wojnar, and P. Kossacki, Fine structure of a resonantly excited p-shell exciton in a CdTe quantum dot, Phys. Rev. B **93**, 195311 (2016).

[413] A. K. Geim, Graphene: status and prospects, Science **324**, 1530 (2009).

[414] K. S. Novoselov, V. I. Fal'ko, L. Colombo, P. R. Gellert, M. G. Schwab, and K. Kim, A roadmap for graphene, Nature **490**, 192 (2012).

[415] K. F. Mak, D. Xiao, and J. Shan, Light-valley interactions in 2D semiconductors, Nat. Photon. **12**, 451 (2018).

[416] G. Sallen, L. Bouet, X. Marie, G. Wang, C. R. Zhu, W. P. Han, Y. Lu, P. H. Tan, T. Amand, B. L. Liu, and B. Urbaszek, Robust optical emission polarization in MoS_2 monolayers through selective valley excitation, Phys. Rev. B **86**, 081301(R) (2012).

[417] K. F. Mak, K. He, J. Shan, and T. F. Heinz, Control of valley polarization in monolayer MoS_2 by optical helicity, Nat. Nanotechnol. **7**, 494 (2012).

[418] M. Bieniek, L. Szulakowska, and P. Hawrylak, Band nesting and exciton spectrum in monolayer MoS_2, Phys. Rev. B **101**, 125423 (2020).

[419] D. Y. Qiu, F. H. da Jornada, and S. G. Louie, Optical Spectrum of MoS_2: Many-Body Effects and Diversity of Exciton States, Phys. Rev. Lett. **111**, 216805 (2013).

[420] R. Dingle, W. Wiegmann, and C. H. Henry, Quantum states of confined carriers in very thin $Al_xGa_{1-x}As$-GaAs-$Al_xGa_{1-x}As$ heterostructures, Phys. Rev. Lett. **33**, 827 (1974).

[421] J. Jadczak, L. Bryja, A. Wójs, and M. Potemski, Optically induced charge conversion of coexistent free and bound excitonic complexes in two-beam magnetophotoluminescence of two-dimensional quantum structures, Phys. Rev. B **85**, 195108 (2012).

[422] S. Shree, M. Semina, C. Robert, B. Han, T. Amand, A. Balocchi, M. Manca, E. Courtade, X. Marie, T. Taniguchi, K. Watanabe, M. M. Glazov, and B. Urbaszek, Observation of exciton-phonon coupling in MoSe: 2 monolayers, Phys. Rev. B **98**, 035302 (2018).

[423] Z. Li, T. Wang, Z. Lu, C. Jin, Y. Chen, Y. Meng, Z. Lian, T. Taniguchi, K. Watanabe, S. Zhang, D. Smirnov, and S.-F. Shi, Revealing the biexciton and trion-exciton complexes in BN encapsulated WSe_2, Nat. Commun. **9**, 3719 (2018).

[424] M. Barbone, A. R.-P. Montblanch, D. M. Kara, C. Palacios-Berraquero, A. R. Cadore, D. De Fazio, B. Pingault, E. Mostaani, H. Li, B. Chen, K. Watanabe, T. Taniguchi, S. Tongay, G. Wang, A. C. Ferrari, and M. Atatüre, Charge-tuneable biexciton complexes in monolayer WSe_2, Nat. Commun. **9**, 3721 (2018).

[425] K. F. Mak, K. He, C. Lee, G. H. Lee, J. C. Hone, T. F. Heinz, and J. Shan, Tightly bound trions in monolayer MoS_2, Nat. Mater. **12**, 207 (2013).

[426] J. Jadczak, J. Kutrowska-Girzycka, P. Kapuściński, Y.-S. Huang, A. Wójs, and L. Bryja, Probing of free and localized excitons and trions in atomically thin WSe_2, WS_2, $MoSe_2$ and MoS_2 in photoluminescence and reflectivity experiments, Nanotechnology **28**, 395702 (2017).

[427] J. Jadczak, A. Delgado, L. Bryja, Y. S. Huang, and P. Hawrylak, Robust high-temperature trion emission in monolayers of $Mo(S_ySe_{1-y})_2$ alloys, Phys. Rev. B **95**, 195427 (2017).

[428] S. Brem, A. Ekman, D. Christiansen, F. Katsch, M. Selig, C. Robert, X. Marie, B. Urbaszek, A. Knorr, and E. Malic, Phonon-assisted photoluminescence from indirect excitons in monolayers of transition-metal dichalcogenides, Nano Lett. **20**, 2849 (2020).

[429] M. Danovich, V. Zólyomi, and V. I. Fal'ko, Dark trions and biexcitons in WS_2 and WSe_2 made bright by e-e scattering, Sci. Rep. **7**, 45998 (2017).

[430] A. Arora, N. K. Wessling, T. Deilmann, T. Reichenauer, P. Steeger, P. Kossacki, M. Potemski, S. Michaelis de Vasconcellos, M. Rohlfing, and R. Bratschitsch, Dark trions govern the temperature-dependent optical absorption and emission of doped atomically thin semiconductors, Phys. Rev. B **101**, 241413(R) (2020).

[431] E. Liu, J. van Baren, C.-T. Liang, T. Taniguchi, K. Watanabe, N. M. Gabor, Y.-C. Chang, and C. H. Lui, Multipath optical recombination of intervalley dark excitons and trions in monolayer WSe_2, Phys. Rev. Lett. **124**, 196802 (2020).

[432] G. Bartsch, M. Gerbracht, D. R. Yakovlev, J. H. Blokland, P. C. M. Christianen, E. A. Zhukov, A. B. Dzyubenko, G. Karczewski, T. Wojtowicz, J. Kossut, J. C. Maan, and M. Bayer, Positively versus negatively charged excitons: a high magnetic field study of $CdTe/Cd_{1-x}Mg_xTe$ quantum wells, Phys. Rev. B **83**, 235317 (2011).

[433] J. Jadczak, M. Kubisa, K. Ryczko, L. Bryja, and M. Potemski, High magnetic field spin splitting of excitons in asymmetric GaAs quantum wells, Phys. Rev. B **86**, 245401 (2012).

[434] A. Arora, M. Koperski, K. Nogajewski, J. Marcus, C. Faugeras, and M. Potemski, Excitonic resonances in thin films of WSe_2: from monolayer to bulk material, Nanoscale **7**, 10421 (2015).

[435] M. Manca, M. M. Glazov, C. Robert, F. Cadiz, T. Taniguchi, K. Watanabe, E. Courtade, T. Amand, P. Renucci, X. Marie, G. Wang, and B. Urbaszek, Enabling valley selective exciton scattering in monolayer WSe_2 through upconversion, Nat. Commun. **8**, 14927 (2017).

[436] D. Vaclavkova, J. Wyzula, K. Nogajewski, M. Bartos, A. O. Slobodeniuk, C. Faugeras, M. Potemski, and M. R. Molas, Singlet and triplet trions in WS_2 monolayer encapsulated in hexagonal boron nitride, Nanotechnology **29**, 325705 (2018).

[437] G. Plechinger, P. Nagler, A. Arora, R. Schmidt, A. Chernikov, A. Granados del Águila, P. C. M. Christianen, R. Bratschitsch, C. Schüller, and T. Korn, Trion fine structure and coupled spin-valley dynamics in monolayer tungsten disulfide, Nat. Commun. **7**, 12715 (2016).

[438] A. M. Jones, H. Yu, J. R. Schaibley, J. Yan, D. G. Mandrus, T. Taniguchi, K. Watanabe, H. Dery, W. Yao, and X. Xu, Excitonic luminescence upconversion in a two-dimensional semiconductor, Nat. Phys. **12**, 323 (2016).

[439] G. Wang, C. Robert, M. M. Glazov, F. Cadiz, E. Courtade, T. Amand, D. Lagarde, T. Taniguchi, K. Watanabe, B. Urbaszek, and X. Marie, In-plane propagation of light in transition metal dichalcogenide monolayers: optical selection rules, Phys. Rev. Lett. **119**, 047401 (2017).

[440] Z. Li, T. Wang, C. Jin, Z. Lu, Z. Lian, Y. Meng, M. Blei, S. Gao, T. Taniguchi, K. Watanabe, T. Ren, S. Tongay, L. Yang, D. Smirnov, T. Cao, and S.-F. Shi, Emerging photoluminescence from the dark-exciton phonon replica in monolayer WSe_2, Nat. Commun. **10**, 2469 (2018).

[441] L. Sun, J. Yan, D. Zhan, L. Liu, H. Hu, H. Li, B. K. Tay, J.-L. Kuo, C.-C. Huang, D. W. Hewak, P. S. Lee, and Z. X. Shen, Spin-orbit splitting in single-layer MoS_2 revealed by triply resonant Raman scattering, Phys. Rev. Lett. **111**, 126801 (2013).

[442] E. del Corro, H. Terrones, A. Elias, C. Fantini, S. Feng, M. A. T. Nguyen, T. E. Mallouk, M. Terrones, and M. A. Pimenta, Excited excitonic states in 1L, 2L, 3L, and bulk WSe_2 observed by resonant Raman spectroscopy, ACS Nano **8**, 9629 (2014).

[443] S.-Y. Chen, T. Goldstein, T. Taniguchi, K. Watanabe, and J. Yan, Coulomb-bound four- and five-particle intervalley states in an atomically-thin semiconductor, Nat. Commun. **9**, 3717 (2018).

[444] A. Singh, K. Tran, M. Kolarczik, J. Seifert, Y. Wang, K. Hao, D. Pleskot, N. M. Gabor, S. Helmrich, N. Owschimikow, U. Woggon, and X. Li, Long-lived valley polarization of intravalley trions in monolayer WSe_2, Phys. Rev. Lett. **117**, 257402 (2016).

[445] P. Li, C. Robert, D. Van Tuan, L. Ren, M. Yang, X. Marie, and H. Dery, Intervalley electron-hole exchange interaction and impurity-assisted recombination of indirect excitons in WS_2 and WSe_2 monolayers, Phys. Rev. B **106**, 085414 (2022).

[446] S. Park, S. Arscott, T. Taniguchi, K. Watanabe, F. Sirotti, and F. Cadiz, Efficient valley polarization of charged excitons and resident carriers in molybdenum disulfide monolayers by optical pumping, Commun. Phys. **5**, 73 (2022).

[447] J. Serrano, A. Bosak, R. Arenal, M. Krisch, K. Watanabe, T. Taniguchi, H. Kanda, A. Rubio, and L. Wirtz, Vibrational properties of hexagonal boron nitride: inelastic X-ray scattering and *Ab Initio* calculations, Phys. Rev. Lett. **98**, 095503 (2007).

[448] J. J. Hopfield, Theory of the contribution of excitons to the complex dielectric constant of crystals, Phys. Rev. **112**, 1555 (1958).

[449] C. Weisbuch, M. Nishioka, A. Ishikawa, and Y. Arakawa, Observation of the coupled exciton-photon mode splitting in a semiconductor quantum microcavity, Phys. Rev. B **69**, 3314 (1992).

[450] M. S. Skolnick, T. A. Fisher, and D. M. Whittaker, Strong coupling phenomena in quantum microcavity structures, Semicond. Sci. Technol. **13**, 645 (1998).

[451] A. Canales, D. G. Baranov, T. J. Antosiewicz, and T. Shegai, Abundance of cavity-free polaritonic states in resonant materials and nanostructures, J. Chem. Phys. **154**, 024701 (2021).

[452] P. A. Thomas, K. S. Menghrajani, and W. L. Barnes, Cavity-free ultrastrong light-matter coupling, J. Phys. Chem. Lett. **12**, 6914 (2021).

[453] D. G. Baranov, M. Wersäll, J. Cuadra, T. J. Antosiewicz, and T. Shegai, Novel nanostructures and materials for strong light-matter interactions, ACS Photonics **5**, 1, (2018).

[454] D. Fröhlich, A. Kulik, B. Uebbing, A. Mysyrowicz, V. Langer, H. Stolz, and W. von der Osten, Coherent propagation and quantum beats of quadrupole polaritons in Cu_2O, Phys. Rev. Lett. **67**, 2343 (1991).

[455] J. Schmutzler, M.-A. Aßmann, T. Czerniuk, M. Kamp, C. Schneider, S. Höfling, and M. Bayer, Nonlinear spectroscopy of exciton-polaritons in a GaAs-based microcavity, Phys. Rev. B **90**, 075103 (2014).

[456] H. M. Gibbs, G. Khitrova, and S. W. Koch, Exciton-polariton light-semiconductor coupling effects, Nat. Photon. **5**, 273 (2011).

[457] X. Guo, W. Lyu, T. Chen, Y. Luo, C. Wu, B. Yang, Z. Sun, F. J. García de Abajo, X. Yang, Q. Dai, Polaritons in van der Waals heterostructures, Adv. Mater. **35**, 2201856 (2022).

[458] D. N. Basov , M. M. Fogler, and F. J. García de Abajo, Polaritons in van der Waals materials, Science **354**, aag1992 (2016).

[459] S. Dufferwiel, S. Schwarz, F. Withers, A. A. P. Trichet, F. Li, M. Sich, O. Del Pozo-Zamudio, C. Clark, A. Nalitov, D. D. Solnyshkov, G. Malpuech, K. S. Novoselov, J. M. Smith, M. S. Skolnick, D. N. Krizhanovskii, and A. I. Tartakovskii, Exciton-polaritons in van der Waals heterostructures embedded in tunable microcavities, Nat. Commun. **6**, 8579 (2015).

[460] X. Liu, T. Galfsky, Z. Sun, F. Xia, E.-C. Lin, Y.-H. Lee, S. Kéna-Cohen, and V. M. Menon, Strong light-matter coupling in two-dimensional atomic crystals, Nat. Photon. **9**, 30 (2015).

[461] N. Jia, N. Schine, A. Georgakopoulos, A. Ryou, L. W. Clark, A. Sommer, and J. Simon, A strongly interacting polaritonic quantum dot, Nat. Phys. **14**, 550 (2018).

[462] P. Törmä and W. L. Barnes, Strong coupling between surface plasmon polaritons and emitters: a review, Rep. Prog. Phys. **78**, 013901 (2015).

[463] R. Liu, Z.-K. Zhou, Y.-C. Yu, T. Zhang, H. Wang, G. Liu, Y. Wei, H. Chen, and X.-H. Wang, Strong light-matter interactions in single open plasmonic nanocavities at the quantum optics limit, Phys. Rev. Lett. **118**, 237401 (2017).

[464] B. Munkhbat, D. G. Baranov, M. Stührenberg, M. Wersäll, A. Bisht, and T. Shegai, Self-hybridized exciton-polaritons in multilayers of transition metal dichalcogenides for efficient light absorption, ACS Photonics **6**, 139 (2019).

[465] Q. Wang, L. Sun, B. Zhang, C. Chen, X. Shen, and W. Lu, Direct observation of strong light-exciton coupling in thin WS_2 flakes, Optics Express **24**, 7151 (2016).

[466] K. Chaudhary, M. Tamagnone, M. Rezaee, D. K. Bediako, A. Ambrosio, P. Kim, and F. Capasso, Engineering phonon polaritons in van der Waals heterostructures to enhance in-plane optical anisotropy, Sci. Adv. **5**, eaau7171 (2019).

[467] S. Dai, Z. Fei, Q. Ma, A. S. Rodin, M. Wagner, A. S. McLeod, M. K. Liu, W. Gannett, W. Regan, K. Watanabe, T. Taniguchi, M. Thiemens, G. Dominguez, A. H. Castro Neto, A. Zettl, F. Keilmann, P. Jarillo-Herrero, M. M. Fogler, and D. N. Basov, Tunable phonon polaritons in atomically thin van der Waals crystals of Boron Nitride, Science **343**, 1125 (2014).

[468] L. Hanke, D. Fröhlich, A. L. Ivanov, P. B. Littlewood, and H. Stolz, LA phonoritons in Cu_2O, Phys. Rev. Lett. **83**, 4365 (1999).

[469] B. S. Wang and J. L. Birman, Theory of phonoritons and experiments to determine phonoriton dispersion and spectrum, Phys. Rev. B **42**, 9609 (1990).

[470] S. Latini, U. De Giovannini, E. J. Sie, N. Gedik, H. Hübener, and A. Rubio, Phonoritons as hybridized exciton-photon-phonon excitations in a monolayer h-BN optical cavity, Phys. Rev. Lett. **126**, 227401 (2021).

[471] M. Wurdack, E. Estrecho, S. Todd, T. Yun, M. Pieczarka, S. K. Earl, J. A. Davis, C. Schneider, A. G. Truscott, and E. A. Ostrovskaya, Motional narrowing, ballistic transport, and trapping of room-temperature exciton polaritons in an atomically-thin semiconductor, Nat. Commun. **12**, 5366 (2021).

[472] A. Raja, L. Waldecker, J. Zipfel, Y. Cho, S. Brem, J. D. Ziegler, M. Kulig, T. Taniguchi, K. Watanabe, E. Malic, T. F. Heinz, T. C. Berkelbach, and A. Chernikov, Dielectric disorder in two-dimensional materials, Nat. Nanotechnol. **14**, 832 (2019).

[473] D. M. Whittaker, P. Kinsler, T. A. Fisher, M. S. Skolnick, A. Armitage, A. M. Afshar, M. D. Sturge, and J. S. Roberts, Motional narrowing in semiconductor microcavities, Phys. Rev. Lett. **77**, 4792 (1996).

[474] G. Zengin, M. Wersäll, S. Nilsson, T. J. Antosiewicz, M. Käll, and T. Shegai, Realizing strong light-matter interactions between single-nanoparticle plasmons and molecular excitons at ambient conditions, Phys. Rev. Lett. **114**, 157401 (2015).

[475] E. T. Jaynes and F. W. Cummings, Comparison of quantum and semiclassical radiation theories with application to the beam maser, Proc. IEEE. **51**, 89 (1963).

[476] V. M. Agranovich, M. Litinskaia, and D. G. Lidzey, Cavity polaritons in microcavities containing disordered organic semiconductors, Phys. Rev. B **67**, 085311 (2003).

[477] Y. Li, A. Chernikov, X. Zhang, A. Rigosi, H. M. Hill, A. M. van der Zande, D. A. Chenet, E.-M. Shih, J. C. Hone, and T . F. Heinz, Measurement of the optical dielectric function of monolayer transition-metal dichalcogenides: MoS_2, $MoSe_2$, WS_2, and WSe_2, Phys. Rev. B **90**, 205422 (2014).

[478] N. Lundt, P. Nagler, A. Nalitov, S. Klembt, M. Wurdack, S. Stoll, T. H. Harder, S. Betzold, V. Baumann, A. V. Kavokin, C. Schüller, T. Korn, S. Höfling, and C. Schneider, Valley polarized relaxation and upconversion luminescence from Tamm-plasmon trion-polaritons with a $MoSe_2$ monolayer, 2D Materials **4**, 025096 (2017).

[479] S. Dufferwiel, T. P. Lyons, D. D. Solnyshkov, A. A. P. Trichet, F. Withers, S. Schwarz, G. Malpuech, J. M. Smith, K. S. Novoselov, M. S. Skolnick, D. N. Krizhanovskii, and A. I. Tartakovskii, Valley-addressable polaritons in atomically thin semiconductors, Nat. Photon. **11**, 497 (2017).

[480] Z. Ye, L. Waldecker, E. Y. Ma, D. Rhodes, A. Antony, B. Kim, X.-X. Zhang, M. Deng, Y. Jiang, Z. Lu, D. Smirnov, K. Watanabe, T. Taniguchi, J. C. Hone, and T. F. Heinz, Nat. Commun. **9**, 3718 (2018).

[481] B. Han, C. Robert, E. Courtade, M. Manca, S. Shree, T. Amand, P. Renucci, T. Taniguchi, K. Watanabe, X. Marie, L. E. Golub, M. M. Glazov, and B. Urbaszek, Exciton states in monolayer $MoSe_2$ and $MoTe_2$ probed by upconversion spectroscopy, Phys. Rev. X **8**, 031073 (2018).

[482] M. He, P. Rivera, D. Van Tuan, N. P. Wilson, M. Yang, T. Taniguchi, K. Watanabe, J. Yan, D. G. Mandrus, H. Yu, H. Dery, W. Yao, and X. Xu, Valley phonons and exciton complexes in a monolayer semiconductor, Nat. Commun. **11**, 618 (2020).

[483] S. Ayari, S. Jaziri, R. Ferreira, and G. Bastard, Phonon-assisted exciton/trion conversion efficiency in transition metal dichalcogenides, Phys. Rev. B **102**, 125410 (2020).

[484] Z. Jin, X. Li, J. T. Mullen, and K. W. Kim, Intrinsic transport properties of electrons and holes in monolayer transition-metal dichalcogenides, Phys. Rev. B **90**, 045422 (2014).

[485] I. Paradisanos, G. Wang, E. M. Alexeev, A. R. Cadore, X. Marie, A. C. Ferrari, M. M. Glazov, and B. Urbaszek, Efficient phonon cascades in WSe_2 monolayers, Nat. Commun. **12**, 538 (2021).

[486] J. Madéo, M. K. L. Man, C. Sahoo, M. Campbell, V. Pareek, E. Laine Wong, A. Al-Mahboob, N. S. Chan, A. Karmakar, B. M. K. Mariserla, X. Li, T. F. Heinz, T. Cao, and K. M. Dani, Directly visualizing the momentum-forbidden dark excitons and their dynamics in atomically thin semiconductors, Science **370**, 1199 (2020).

[487] Z. A. Iakovlev and M. M. Glazov, Fermi polaron fine structure in strained van der Waals heterostructures, 2D Materials **10**, 035034 (2023).

[488] E. S. Kadantsev and P. Hawrylak, Electronic structure of a single MoS_2 monolayer, Solid State Commun. **152**, 909 (2012).

[489] J. G. Roch, G. Froehlicher, N. Leisgang, P. Makk, K. Watanabe, T. Taniguchi, and R. J. Warburton, Spin-polarized electrons in monolayer MoS_2, Nat. Nanotechnol. **14**, 432 (2019).

[490] T. P. Lyons, S. Dufferwiel, M. Brooks, F. Withers, T. Taniguchi, K. Watanabe, K. S. Novoselov, G. Burkard, and A. I. Tartakovskii, The valley Zeeman effect in inter- and intra-valley trions in monolayer WSe_2, Nat. Commun. **10**, 2330 (2019).

[491] M. Goryca, J. Li, A. V. Stier, T. Taniguchi, K. Watanabe, E. Courtade, S. Shree, C. Robert, B. Urbaszek, X. Marie, and S. A. Crooker, Revealing exciton masses and dielectric properties of monolayer semiconductors with high magnetic fields, Nat. Commun. **10**, 4172 (2019).

[492] R. Pisoni, A. Kormányos, M. Brooks, Z. Lei, P. Back, M. Eich, H. Overweg, Y. Lee, P. Rickhaus, K. Watanabe, T. Taniguchi, A. Imamoğlu, G. Burkard, T. Ihn, and K. Ensslin, Interactions and magnetotransport through spin-valley coupled landau levels in monolayer MoS_2, Phys. Rev. Lett. **121**, 247701 (2018).

[493] P. Hawrylak, Optical properties of a two-dimensional electron gas: Evolution of spectra from excitons to Fermi-edge singularities, Phys. Rev. B **44**, 3821 (1991).

[494] D. K. Efimkin and A. H. MacDonald, Many-body theory of trion absorption features in two-dimensional semiconductors, Phys. Rev. B **95**, 035417 (2017).

[495] Y. Ferreiros and A. Cortijo, Large conduction band and Fermi velocity spin splitting due to Coulomb interactions in single-layer MoS_2, Phys. Rev. B **90**, 195426 (2014).

[496] M. M. Glazov, M. A. Semina, C. Robert, B. Urbaszek, T. Amand, and X. Marie, Intervalley polaron in atomically thin transition metal dichalcogenides, Phys. Rev. B **100**, 041301(R) (2019).

[497] C. Robert, M. A. Semina, F. Cadiz, M. Manca, E. Courtade, T. Taniguchi, K. Watanabe, H. Cai, S. Tongay, B. Lassagne, P. Renucci, T. Amand, X. Marie, M. M. Glazov, and B. Urbaszek, Optical spectroscopy of excited exciton states in MoS_2 monolayers in van der Waals heterostructures, Phys. Rev. Materials **2**, 011001(R) 2018.

[498] G. Wang, C. Robert, A. Suslu, B. Chen, S. Yang, S. Alamdari, I. C. Gerber, T. Amand, X. Marie, S. Tongay, and B. Urbaszek, Spin-orbit engineering in transition metal dichalcogenide alloy monolayers, Nat. Commun. **6**, 10110 (2015).

[499] M. Zhang,J. Wu, Y. Zhu, D. O. Dumcenco, J. Hong, N. Mao, S. Deng, Y. Chen, Y. Yang, C. Jin, S. H. Chaki, Y.-S. Huang, J. Zhang, and L. Xie, Two-dimensional molybdenum tungsten diselenide alloys: photoluminescence, Raman scattering, and electrical transport, ACS Nano **8**, 7130 (2014).

[500] B. Huang, M. Yoon, B. G. Sumpter, S.-H. Wei, and F. Liu, Alloy engineering of defect properties in semiconductors: suppression of deep Levels in transition-metal dichalcogenides, Phys. Rev. Lett. **115**, 126806 (2015).

[501] Y. Chen, J. Xi, D. O. Dumcenco, Z. Liu, K. Suenaga, D. Wang, Z. Shuai, Y.-S. Huang, and L. Xie, Tunable band gap photoluminescence from atomically thin transition-metal dichalcogenide alloys, ACS Nano **7**, 4610 (2013).

[502] J. Förste, N. V. Tepliakov, S. Yu. Kruchinin, J. Lindlau, V. Funk, M. Förg, K. Watanabe, T. Taniguchi, A. S. Baimuratov, and A. Högele, Exciton g-factors in monolayer and bilayer WSe_2 from experiment and theory, Nat. Commun. **11**, 4539 (2020).

[503] G. Wang, L. Bouet, M. M. Glazov, T. Amand, E. L. Ivchenko, E. Palleau, X. Marie and B. Urbaszek, Magneto-optics in transition metal diselenide monolayers, 2D Materials **2**, 034002 (2015).

[504] Z. Li, T. Wang, C. Jin, Z. Lu, Z. Lian, Y. Meng, M. Blei, M. Gao, T. Taniguchi, K. Watanabe, T. Ren, T. Cao, S. Tongay, D. Smirnov, L. Zhang, and S.-F. Shi, Momentum-dark intervalley exciton in monolayer tungsten diselenide brightened *via* chiral phonon, ACS Nano **13**, 14107 (2019).

[505] K. Hao, J. F. Specht, P. Nagler, L. Xu, K. Tran, A. Singh, C. K. Dass, C. Schüller, T. Korn, M. Richter, A. Knorr, X. Li, and G. Moody, Neutral and charged inter-valley biexcitons in monolayer $MoSe_2$, Nat. Commun. **8**, 15552 (2017).

[506] H. Masenda, L. M. Schneider, M. Adel Aly, S. J. Machchhar, A. Usman, K. Meerholz, F. Gebhard, S. D. Baranovskii, and M. Koch, Energy scaling of compositional disorder in ternary transition-metal dichalcogenide monolayers, Adv. Electron. Mater. **7**, 2100196 (2021).

[507] L. Wu, C. Cong, W. Yang, Y. Chen, Y. Shao, T. Thu Ha Do, W. Wen, S. Feng, C. Zou, H. Zhang, B. Du, B. Cao, J. Shang, Q. Xiong, K. Ping Loh, and T. Yu, Observation of strong valley magnetic response in monolayer transition metal dichalcogenide alloys of $Mo_{0.5}W_{0.5}Se_2$ and $Mo_{0.5}W_{0.5}Se_2/WS_2$ heterostructures, ACS Nano **5**, 8397 (2021).

[508] Y. Li, J. Ludwig, T. Low, A. Chernikov, X. Cui, G. Arefe, Y. D. Kim, A. M. van der Zande, A. Rigosi, H. M. Hill, S. H. Kim, J. C. Hone, Z. Li, D. Smirnov, and T. F. Heinz, Valley splitting and polarization by the Zeeman effect in monolayer $MoSe_2$, Phys. Rev. Lett. **113**, 266804 (2014).

[509] K. L. Seyler, P. Rivera, H. Yu, N. P. Wilson, E. L. Ray, D. G. Mandrus, J. Yan, W. Yao, and X. Xu, Signatures of moiré-trapped valley excitons in $MoSe_2/WSe_2$ heterobilayers, Nature **567**, 66 (2019).

[510] D. Braukmann, E. R. Glaser, T. A. Kennedy, M. Bayer, and J. Debus, Circularly polarized zero-phonon transitions of vacancies in diamond at high magnetic fields, Phys. Rev. B **97**, 195448 (2018).

[511] D. MacNeill, C. Heikes, K. F. Mak, Z. Anderson, A. Kormányos, V. Zólyomi, J. Park, and D. C. Ralph, Breaking of valley degeneracy by magnetic field in monolayer $MoSe_2$, Phys. Rev. Lett. **114**, 037401 (2015).

[512] M. Koperski, M. R. Molas, A. Arora, K. Nogajewski, A. O. Slobodeniuk, C. Faugeras, and M. Potemski, Optical properties of atomically thin transition metal dichalcogenides: observations and puzzles, Nanophotonics **6**, 1289 (2017).

[513] J. Wierzbowski, J. Klein, F. Sigger, C. Straubinger, M. Kremser, T. Taniguchi, K. Watanabe, U. Wurstbauer, A. W. Holleitner, M. Kaniber, K. Müller, and J. J. Finley, Direct exciton emission from atomically thin transition metal dichalcogenide heterostructures near the lifetime limit, Sci. Rep. **7**, 12383 (2017).

[514] Z. Khatibi, M. Feierabend, M. Selig, S. Brem, C. Linderälv, P. Erhart, and E. Malic, Impact of strain on the excitonic linewidth in transition metal dichalcogenides, 2D Materials **6**, 015015 (2019).

[515] Y. Lee, A. Knothe, H. Overweg, M. Eich, C. Gold, A. Kurzmann, V. Klasovika, T. Taniguchi, K. Wantanabe, V. Fal'ko, T. Ihn, K. Ensslin, and P. Rickhaus, Tunable valley splitting due to topological orbital magnetic moment in bilayer graphene quantum point contacts, Phys. Rev. Lett. **124**, 126802 (2020).

[516] D. Mayer and A. Knothe, Tuning confined states and valley g-factors by quantum dot design in bilayer graphene, Phys. Status Solidi B, not yet published, doi: 10.1002/pssb.202300395.

[517] T. Woźiak, P. E. Faria Junior, G. Seifert, A. Chaves, and J. Kunstmann, Exciton g factors of van der Waals heterostructures from first-principles calculations, Phys. Rev. B **101**, 235408 (2020).

Symbols and Abbreviations

Symbol	Meaning
ac	Acoustic phonon
A-exciton	Excitons involving holes from the upper VB states in TMDCs
Al	Aluminum
AlAs	Aluminum arsenide
As	Arsenic
aSt	anti-Stokes
arb.u.	Arbitrary units
A'$_1$, A$_{1g}$	Out-of-plane phonon mode in TMDCs
A	Amplitude of the Fano profile function and Breit-Wigner function
a	Lattice constant
a_0	Distance between the two atoms inside a primitive unit cell
a_{loc}	Carrier localization length
a_{B}, $a_{\mathrm{B,2D}}$	(Excitonic) Bohr radius, - for a hydrogenic 2D exciton
$a_{\mathrm{ex},i}$	Spin-spin coupling constant of the exchange interaction
a_i	Deformation potential coefficients, with $i = c(v)$ for the CB (VB)
$\hat{a}$, $\hat{a}^\dagger$	Annihilation and creation operators
$\hat{a}_q$, $\hat{a}_q^\dagger$	Annihilation and creation operators for a phonon
α	Polarizability tensor (operator)
α_i, $\Delta\alpha_{cv}$	Valley g-factor with $i = c(v)$ for the CB (VB), and $\Delta\alpha_{cv} = \alpha_c - \alpha_v$
α_{d}	Diamagnetic shift coefficient
$\alpha_{\mathrm{d,2D/QD}}$	Diamagnetic shift coefficient in a 2D ML / in a QD
$\alpha_{\mathrm{p},0}$	Equilibrium polarizability
$\frac{\partial^2 \alpha_{\mathrm{p}}}{\partial t^2}$	Polarizability gradient
B	Boron
B-exciton	Excitons involving holes from the lower VB states in TMDCs
BS	Beamsplitter (cube)
bcc	Body-centered cubic crystal system
B	Magnetic field
$B_{x/y/z}$	Magnetic field along $x/y/z$-axis
$\vec{B}$	Magnetic field (vector)
$b_{\mathrm{ex},i}$	Spin-spin coupling constant of the exchange interaction
β	Index for electrons ($\beta = e$) or holes ($\beta = h$)
CB	Conduction band
CCD	Charge-coupled device
Ch	Chalcogen
CM	Center of mass
CPD	Circular polarization degree
CS	Cross slit
cw	Continuous-wave
C_n	Crystallographic point group for cyclic symmetries with n-fold rotation axes, $n = 1, 2, 3, 4, 6$
C_{2v}	Point group of lens-shaped self-assembled QDs
C_{3h}	Point group of ML TMDCs at the K-points

c	Speed of light in vacuum, 2.9979×10^8 m/s
$\chi_{n,l}$	Zeros or roots of the Bessel function
DCM	4-(Dicyanmethylen)-6-(4-dimethylaminostyryl)-2-methyl-4H-pyran
DMSO	Dimethyl Sulfoxide
DP	Deformation potential
$\mathrm{d}_{x^2-y^2}$, d_{xy}, d_{z^2}	Atomic d-orbitals of TMDCs in different directions
D	Diameter
D_n	Crystallographic point group for dihedral (two-sided) symmetries with n-fold rotation axis plus and additional n twofold axes perpendicular to that axis, $n = 1, 2, 3, 4, 6$
D_{2d}	Point group of two-dimensional QWs
D_{3h}	Point group of ML TMDCs
D_{6h}	Point group of bulk TMDCs
d	Additional mirror symmetry
d_{im}	Dimension
$\Delta(E)$, $\delta(E)$	Generic splitting (of an energy), Energy shift
ΔE	Upconversion energy gain
ΔE_{st}	Energy shift under strain
Δ_{bd}	Exchange splitting between bright and dark exciton states with short- and long-range e-h Coulomb exchange contribution
$\Delta_{\text{hh-lh}}$	Energy splitting between the hh and lh subbands
Δ_{SO}	Energy splitting of the split-off subband
Δ_{Z}	Valley-dependent Zeeman shift of the optical resonances
δ-function	Dirac delta distribution
δ_{b}	Exchange splitting between bright exciton states
δ_{bd}	Exchange splitting between bright and dark exciton states from the short-range e-h Coulomb exchange contribution, also δ_0
$\delta_{\mathrm{corr,X}}$	Energy correction of the exciton governed by the self-polarization energies of the electron and hole
δ_{d}	Exchange splitting between dark exciton states
δ_{t}	Detuning in the semi-classical coupled oscillator model
δ_0	Splitting between the bright and dark exciton states, Electron-hole exchange energy, also δ_{bd}
∂	Partial derivative, derivative of a function of several variables with respect to one of those variables
e	Electron
e-h	Electron-hole (pair)
E', $\mathrm{E}^1_{2\mathrm{g}}$	In-plane phonon mode in TMDCs
$\mathrm{e}^{i\vec{k}\vec{r}}$	Plane wave
eV	Electron volt (unit), 1.6022×10^{-19} J
E	Energy, Energy eigenvalues of a Hamilton operator; also Spectral position
$E(\vec{k})$	Energy in dependence of the wavevector
E_{ac}	Energy of acoustic phonons
E_{B}, $E_{\mathrm{B,QW/QD}}$	Binding energy, - of an exciton in a QW or ML / in a QD
E_{bd}, $E_{\mathrm{bd}+/-}$	Bright-dark-exciton energy difference, - at the Stokes (+) / anti-Stokes (-) side
E_c	Low-energy (cut-off) bound of the phonon spectral density
E_{conf}	Confinement energy
E_{deac}	Thermal deactivation energy
E_{DP}	Dominant energy term of the deformation potential coupling
$E_{\mathrm{e/h}}$	Confinement energy of the electron/hole

E_{exc}	Excitation energy
E_{Fano}	Resonant energy of the Fano-type quantum interference
E_{g}	Bandgap (energy)
E_{harm}	Energy of the harmonic oscillator
E_{kin}	Kinetic energy
$E_{n',m}$	In-plane eigenenergies of a harmonic oscillator
$E^{\beta}_{n_x,n_y}$	Energy of an e-h pair in an anisotropic parabolic potential
E_{op}	Energy of optical phonons
E_{p}	Kane energy
E_{PE}	Electrostatic potential or piezoelectric field
E_{ph}	Energy eigenvalue of the the two-phonon continuum
E_{phn}	Energy of a phonon
E_{piezo}	Piezoelectric coupling energy
E_{PL}	Energy of the PL maximum
E_{pol}, $E_{\mathrm{pol,e/h}}$	Self-polarization energy, - of electron/hole
E_{QD}	Energy in a QD potential
E_{QW}	Energy in a QW potential
$E_{\vec{R}_{\mathrm{CM}}}$	Energy of the CM coordinate
E_{res}	Resonant energy of a Fano resonance
$E_{\vec{r}_{\mathrm{r}}}$	Energy of the relative coordinate
E_{signal}	Energy of the measured signal
E_{X}	Energy of an exciton
$E_{\mathrm{X},\pm1/\pm2}$	Energy of an exciton with $j_z = \pm1$ (bright) / $j_z = \pm2$ (dark)
E_{Z}, $E_{\mathrm{Z},i}$	Zeeman energy
$E_{\pm}$	Eigenenergies in the semi-classical coupled oscillator model
$E_{\uparrow/\downarrow}$	Energy of spin-split spin basis eigenstates
E_i	Electric field amplitude
E_0	Electric field amplitude
E_{10}	Energy of the longitudinal phonon mode with $n = 1, l = 0$ from Brillouin scattering
$E(t)$	Periodic varying electric field, Electromagnetic field
e	Elementary charge, 1.6022×10^{-19} C
e_{m}	Electromechanical tensor
e_{PE}	Piezoelectric tensor
η_s	Scattering efficiency
ϵ	Reduced energy variable
ϵ_{st}	Strain tensor
ε	Dielectric constant or relative permittivity
$\varepsilon_{\mathrm{air/encaps}}$	Dielectric constant of air / the encapsulating material
$\varepsilon_{\mathrm{ML/bulk}}$	Dielectric constant of a ML/bulk
ε_0	Dielectric constant of vacuum
$\varepsilon_{\perp/\parallel}$	Dielectric constant perpendicular/parallel to a ML
$\varepsilon_{texteff}$	Effective dielectric constant
FI	Insertion for neutral density filters (experimental details chapter)
FI	Fröhlich interaction (theory chapter)
fcc	Face-centered cubic crystal system
F	Shift of the resonance position with respect to the discrete state in the Fano-type quantum interference
$\hat{F}$	Total angular momentum operator of an atom, $\hat{F} = \hat{J} + \hat{I}$
f	Focal length, focus
f_1, f_2, f_3	WSe_2 samples in section 5.1.3
f_{fi}, f_{X}	Oscillator strength, - of the exciton in the bulk
$f(q,\epsilon)$	Breit-Wigner function

Φ	Electrostatic potential
$\Phi(E)$	Efficiency dependence of the CCD camera
Φ_{env}	Envelope wavefunction
Φ_{LO}	Coulomb potential from a LO phonon
Φ_{m}	Minimal spot diameter of the laser beam on the sample surface
$\Phi_{\mathrm{m,L/S}}$	Laser spot size or Diameter of the laser spot / of the observed sample position
Φ_{PE}	Piezoelectric field
ϕ	Azimuthal coordinate
$\Phi_{\vec{R}}$	Wannier functions
$\varphi\measuredangle(\vec{k}_{\mathrm{exc}}, \vec{k}_{\mathrm{det}})$	Angle between the wavevector of the excited and detected light
Ga	Gallium
GaAs	Gallium arsenide
Group II	Chemical elements in group 12 of the periodic table
Group III	Chemical elements in group 13 of the periodic table (Boron group)
Group IV	Chemical elements in group 14 of the periodic table (Carbon group)
Group V	Chemical elements in group 15 of the periodic table (Nitrogen group)
Group VI	Chemical elements in group 16 of the periodic table (Oxygen group)
GT	Glan-Taylor prism
g	Landé factor or electron g-factor: splitting of degenerate energy states in a magnetic field due to different magnetic moments
g_{c}	Coupling rate in the semi-classical coupled oscillator model
$g_{\mathrm{e/h/hh/X/T/IVX}}$	(Effective) g-factor of the electron/hole/heavy hole/exciton/trion/intervalley exciton
g_L	Orbital g-factor
g_S	Spin g-factor
$g_{S,0}$	Free electron spin g-factor in vacuum, $g_{S,0} \approx 2.0023$
g_{V}	Valley g-factor
$g_{\mathrm{e/hh},x}$	In-plane g-factor of the electron/heavy hole
$g_{\mathrm{e/hh},z}$	Longitudinal g-factor of the electron/heavy hole
$g_{xx/yy/zz}$	Diagonal elements of the g-factor tensor along $x/y/z$-axis
$g_{\parallel}$	Longitudinal g-factor, equal to g_z/g_{zz}
$g_{\perp}$	Transverse g-factor, equal to g_{xx} and g_{yy}
$g_{\mathrm{e/hh},\perp}$	Transverse g-factor of the electron/heavy hole
Γ	Width (of the resonance)
$\Gamma_{\mathrm{G/L}}$	Full width at half maximum of the Gaussian/Lorentzian function
Γ-point	High-symmetry point of the unit cell at the center of the Brillouin zone
Γ_{sr}	Spectral resolution
γ	Gyromagnetic ratio
$\gamma(t)$	Time-varying coupling
γ_{phn}	Phonon linewidth
γ_{pol}	Polariton linewidth
γ_t	Time dependent coupling term
γ_{X}	Exciton linewidth
γ_0	Constant coupling term, coupling constant
h	Hole
hh	Heavy hole
hBN	Hexagonal boron nitride
hcp	Hexagonal close-packed crystal system
$\|H\rangle$	Horizontal linear polarization state of a transverse acoustic phonon
$\hat{H}$	Hamilton operator or Hamiltonian: an operator corresponding to the total energy of a system

$\hat{H}_0$	Unperturbed Hamiltonian
$\hat{H}_\mathrm{c}$	Hamiltonian of a crystal
$\hat{H}_\mathrm{DP}$	Deformation potential interaction Hamiltonian
$\hat{H}_\mathrm{e}$	Hamiltonian of the electron
$\hat{H}_\mathrm{e\text{-}ph}$	Electron-phonon interaction operator/Hamiltonian
$\hat{H}_\mathrm{ex}$	Hamiltonian of the e-h exchange interaction
$\hat{H}_\mathrm{FI}$	Fröhlich interaction Hamiltonian
$\hat{H}_\mathrm{harm}$	Hamiltonian of the harmonic oscillator
$\hat{H}_\mathrm{ion}$	Hamiltonian of the atoms, ions or nuclei
$\hat{H}_\mathrm{nZ}$	Magnetic coupling of a hole to a magnetic field described by a non-Zeeman interaction
$\hat{H}_\mathrm{PE}$	Piezoelectric interaction Hamiltonian
$\hat{H}_\mathrm{ph}$	Phonon Hamiltonian
$\hat{H}_\mathrm{sf}$	Electron spin-flip Hamiltonian
$\hat{H}_\mathrm{SO}$	Hamiltonian of the spin-orbit coupling
$\hat{H}_\mathrm{Z}$	Zeeman Hamiltonian for an electron in a magnetic field
h	Additional mirror symmetry
$\hbar$	Reduced Planck constant, $\hbar = \frac{h}{2\pi} \approx 6.5821 \times 10^{-16}$ eVs
$\hbar\vec{q}$	Crystal impulse
$\hbar\omega_\mathrm{exc}$	Energy of the exciting photon
$\hbar\omega_\mathrm{f}$	Energy of the final photon
$\hbar\Omega$	Rabi-splitting energy
$\hbar\Omega_K$	Energy of the intervalley chiral phonon ($K_+ \to K_-$)
$\hbar\omega_q$	Modulation energy
$\hbar\omega_0$	Intershell spacing
ID	Iris diaphragms
In	Indium
InAs, InGaAs	Indium arsenide, Indium gallium arsenide
(In,Ga)As	Gallium arsenide with a small inflow of indium arsenide
IVS	Intervalley scattering
IVX	Intervalley exciton
I_back	Background intensity
I_co	PL intensity in the co-polarized configuration
I_cross	PL intensity in the cross-polarized configuration
I_i	Intensity of the incident light
I_L	(Gathered) Light intensity
I_S	Scattered light intensity
I_SF	Intensity of a spin-flip signal
$I_{+/-}^{-/+}$	Intensity of the $\sigma^{+/-}$-polarized PL under $\sigma^{-/+}$-polarized excitation
$\hat{I}$	Nuclear angular momentum quantum number, Nuclear spin
i	Imaginary number, $i^2 = -1$
i, ij, ijk	Indices for the spatial coordinates x, y, or z
J_ac	Acoustic phonon spectral density
J_eh	Direct Coulomb integral of the e-h pair
J_ex	Exchange splitting between the spins
J_ph	Phonon spectral density
$\vec{J}_\mathrm{e/h/X}$	Total angular momentum of electron/hole/exciton
$\hat{J}$, also $\vec{J}$	Total angular momentum operator, $\vec{J} = \vec{L} + \vec{S}$
$\hat{J}_{\mathrm{h},i}$	Total angular momentum projection operator of the hole
j	Total angular momentum quantum number

$\bar{j}$	Average total angular momentum
$j_{\mathrm{e/hh/X}}$	Total angular momentum of the electron/heavy hole/exciton
$j_{\mathrm{e/hh/X},z}$	Total angular momentum projection quantum number along z-axis of the electron/heavy hole/exciton
$j_{i/s}$	Total angular momentum of the incident/scattered photon
j_m	Total angular momentum of the local system
$j_{x/y}$	Total angular momentum projection quantum number along x/y-axis
j_z, also m_j	Total angular momentum projection quantum number along z-axis
$j_l(k_n r)$	First-order spherical Bessel functions
K-point	High-symmetry point of a hexagonal unit cell at the middle of an edge joining two rectangular faces
K_+, K_-	Inequivalent points or valleys in the Brillouin zone of TMDCs, also denoted with plus and minus sign before or after the letter, or as subscript or superscript or as K and K'
$\vec{K}$	Reciprocal lattice vector
$\vec{K}_{\mathrm{X}}$	Exciton wavevector
k_{B}	Boltzmann constant, $8.6173 \times 10^{-5}\,\mathrm{eV/K}$
k_n	Quantized phonon wavevector
k_z	Wavevector in z-direction
$\vec{k}$ or k-vector, $\vec{k}_{\mathrm{e/h}}$	Wavevector, - of the electron/hole
$\vec{k}_{\mathrm{exc/det}}$	Wavevector of the excited/detected light
$\vec{k}_{i/s}$	Wavevector of the incident/scattered photon
$\vec{k}\cdot\vec{p}$ theory	Perturbation theory: semi-empirical approach for calculating the band structure
κ	Parameter of the Faddeeva function
LA	Longitudinal acoustic phonon mode
LFOC	Long focus
LO, $\mathrm{LO_{ph}}$	Longitudinal optical phonon mode
LP	Longpass filter
$\mathrm{L_C}$	Lens collimating the emitted light of the sample
$\mathrm{L_L}$	Final focusing lens of the excitation path
$\mathrm{L_N}$	Collimating lens inside the VTI of the cryostat
$\mathrm{L_S}$	Final focusing lens in front of the spectrometer
lh	Light hole
L-point	High-symmetry point of a fcc unit cell at the center of the big hexagonal face
$\hat{L}$, also $\vec{L}$	Orbital angular momentum operator
l	Orbital angular momentum or azimuthal quantum number, also orbital quantum momentum
l_{pht}	Orbital angular momentum of a photon
l_{X}	Orbital angular momentum of the exciton
l_z	Orbital angular momentum projection quantum number along z-axis, also m_l
Λ-point	High-symmetry point of a hexagonal unit cell between center and edge of the Brillouin zone in the ML crystal
λ	Wavelength
λ_{B}	de Broglie-wavelength
λ_{L}	Lamé coefficient
λ_{SO}	Splitting constant for nearly isotropic spin-orbit coupling
$\lambda/2$, $\lambda/4$	Half-wave plate, Quarter-wave plate

M	Mirror
Mo	Molybdenum
MoX_2:	Molybdenum-chalcogenide compounds: Molybdenumdisulphide, Molybdenumdiselenide
MoS_2, $MoSe_2$	
$Mo_{1-x}W_xSe_2$	Molybdenumdiselenide with different compositions x of molybdenum and tungsten
MO	Microscope objective
ML	Monolayer, a very thin quantum well
M_{fi}	Transition matrix element
$\lvert M_{\mathrm{fi}}\rvert^2$	Transition probability
M_{X}	Exciton mass
M-point	High-symmetry point of a hexagonal unit cell at the center of a rectangular face
m	Mass
m_{eff}	Effective mass
$m_{\mathrm{eff,e/h/hh/lh}}$	Effective mass of the electron/hole/heavy hole/light hole
$m_{0,\mathrm{e}}$	Free electron mass, 9.1094×10^{-31} kg
m_l (or l_z)	Orbital angular momentum projection quantum number along z-axis, magnetic quantum number, azimuthal quantization number
m'	Quantum number of the angular momentum component corresponding to the number of nodes ($2\lvert m'\rvert$) seen in moving circumferentially around the QD center
m_τ	Magnetic moment of the valley
μ_{B}	Bohr magneton, 5.7884×10^{-5} eV/T
μ_{L}	Lamé coefficient
μ_{X}	Reduced mass of the exciton
$\vec{\mu}$	Magnetic moment
$\vec{\mu_J}$	Total angular momentum magnetic moment
$\vec{\mu_S}$	Spin magnetic moment
N	Nitrogen
NE	Noise eater
N	Number
$N(E,T)$	Thermal occupation number
N_A	Numerical aperture
N_F-number	Nominal focal ratio, f-number
n	Radial, main, or principal quantum number, also discrete value of the band index
$n=1, l=0$	Ground state, s-like state
$n=1, l=\pm1$	First excited state, p-like state
$n_{x/y}$	Integers enumerating the eigenstates of a 1D oscillator
n_ρ	Radial quantum number corresponding to the number of nodes in the wavefunction as one moves radially out from the center
∇	Nabla or Del operator: a vector of partial derivative operators with meanings gradient of a scalar field (∇f), divergence of a vector field ($\nabla \cdot \vec{v}$), and curl (rotation) of a vector field ($\nabla \times \vec{v}$)
∇^2	Laplace operator or Laplacian: a vector differential operator given by the divergence of the gradient of a scalar function
ν	Refractive index
op	Optical phonon
ω	Frequency
ω_{c}	Cyclotron frequency
ω_{co}	Cut-off frequency

$\omega_{i/s}$	Frequency of the incident/scattered photon
ω_{L}	Laser frequency
ω_q	Frequency of the generated or annihilated elementary excitation, specifically phonon frequency
ω_β	Frequency describing the strength of the confinement
ω_0	Resonance frequency, (Harmonic) Oscillator characteristic frequency
PE	Piezoelectric interactions
PL, PLE, PL(E)	Photoluminescence, Photoluminescence excitation, both
PLA	Polylactic acid, plastic filament
PMT	Photomultiplier tube
PZT	Lead-zirconate-titanate ceramics
p_x, p_y, p_z	Atomic p-wavefunctions (triply degenerate)
P	(Excitation) Laser power; or eigenvalues of parity operator, parity quantum number
$P_{\mathrm{circ}}^{+/-}$	Degree of circular polarization for $\sigma^{+/-}$-polarized light excitation
P_{exc}	Excitation power
P_i	Dielectric polarization
$P(t)$	Electric dipole oscillator
$\hat{P}$	Parity transformation or reflection or inversion operator
p_d	Power density
p_v	Pressure
$\vec{p}$	Vector of momentum operators, $\vec{p} = (\hat{p}_x, \hat{p}_y, \hat{p}_z)^T$
$\hat{p}$	Momentum operator: operator associated with linear momentum
$\hat{p}_z$	z-component of the momentum operator
π	Ratio of the circumference of a circle to its diameter
Ψ, $\Psi(\vec{r})$	Wavefunction (of the electron)
$\lvert\Psi\rangle = \lvert n, l, m_l, s\rangle$	Arbitrary quantum state (with full spherical symmetry)
$\lvert\Psi_{\mathrm{b}}\rangle$, $\lvert\pm1\rangle$	Wavefunction of the bright exciton state in bra-ket notation
$\lvert\Psi_{\mathrm{d}}\rangle$, $\lvert\pm2\rangle$	Wavefunction of the dark exciton state in bra-ket notation
$\Psi_{\mathrm{d},0}$	Unperturbed dark exciton state
$\Psi_{\mathrm{e,s/p}}$	Wavefunction of the s/p-shell electron
$\Psi_{\mathrm{e},\pm}$	Wavefunction of the electron in dependence of the tilting angle
$\Psi_{i/f}$	Wavefunction of the initial/final state
$\Psi_{l,m}(k_n r)$	Phonon wavefunction
Ψ_{ph}	Wavefunction of the two-phonon continuum
$\Psi(\theta, \phi)$	Wavefunction as a product of spherical harmonics
$\Psi_{00}(k_1 r)$	Wavefunction of the lowest-energy (fundamental) phonon mode with $n = 1$, $l = 0$
$\Psi_{10}(k_1 r)$	Wavefunction of the first-excited phonon mode with $n = 1$, $l = 1$
$\lvert\Psi_{lm}\rvert^2$	Probability densitiy of a phonon wavefunction
QD, QW	Quantum dot, quantum well
Q_c	Electric charge
Q-point	High-symmetry point of a hexagonal unit cell between center and edge of the Brillouin zone in the bulk crystal
q	Asymmetry factor
q_{bd}, $q_{\mathrm{bd}+/-}$	Asymmetry factor of the bright-dark-exciton transition, - at the Stokes (+) / anti-Stokes (-) side
$\vec{q}$	Wavevector of the generated or annihilated elementary excitation, specifically phonon wavevector
RTA	Rapid thermal annealing
R	Spatial distance

R_z	Distance in z-direction
$\vec{R}_{\mathrm{CM}}$	CM coordinate
ΔR	Atomic displacements
$R(r)$	Radial Bessel function
$\vec{R}$	Lattice vector
r	Position
r_{ad}	Radius
$\vec{r}_{\mathrm{r}}$	Relative coordinate
r_s	Stray-light rejection ratio
$\vec{r}$, $\vec{r}_{\mathrm{e/h}}$	Coordinate or position vector, - of the electron/hole
ρ	Mass density
$\rho_{\mathrm{c}}^{\sigma}$	Magnetic-field induced circular polarization degree
$\rho_{\mathrm{o}}^{\sigma}$	Optical orientation degree
S	Sulfur
Se	Selenium
SFOC	Short focus
SFS, SFRS	Spin-flip (Raman) scattering
Si	Silicon
SiO_2	Silicondioxide
SO	Spin-orbit
SP	Shortpass filter
St	Stokes
sp^2	Orbital hybridization, strong covalent bonding with two single and one double bond
s-, p-, d-, f-shells	Energy shells (levels or orbitals) of a QD
$\hat{S}$, also $\vec{S}$	Spin angular momentum operator
$\hat{S}_z$	Spin projection operator along z-axis
$\hat{S}_{\mathrm{e},i}$	Spin projection operator of the electron
s	Spin angular momentum quantum number, in short: spin
$s_{\mathrm{e/h}}$	Spin of the electron/hole
$s_{x/y}$	Spin projection quantum number along x/y-axis
s_z, also m_s	Spin projection or magnetic spin quantum number along z-axis
$s_z = +1/2$, $\uparrow$	Spin basis eigenstate: spin-up
$s_z = -1/2$, $\downarrow$	Spin basis eigenstate: spin-down
σ, $\hat{\sigma}$	Pauli spin matrix, - operator
σ_i	Pauli spin matrix along $i = x/y/z$-axis
$\sigma^{+/-}$	Right/left-handed circular polarization, also $\sigma^{\pm}$
TA	Transverse acoustic phonon mode
TM	Transition metal
TMDC	Transition metal dichalcogenide, also TMD
TO	Transverse optical phonon mode
T	Temperature
T_d	Crystallographic point group for tetrahedral symmetries, tetragonal point group
T_{RTA}	Annealing temperature
$\hat{T}$	Kinetic energy operator
$\hat{T}_{\mathrm{Fano}}$	Transition operator of the Fano-type quantum interference
t	Time
τ, $\tau_{\mathrm{e/h}}$	Valley index, - of electron/hole
τ_{L}, $\tau_{\mathrm{L,X}}$	Lifetime, - of the exciton
$\tau_{\mathrm{L},j/\bar{j}}$	Lifetime of the excited carrier or carrier complex with total angular momentum

$\tau_{\mathrm{L},v}$	Lifetime of the virtual state
θ	Tilting angle, angle between magnetic field and growth axis: $\theta \measuredangle (\vec{B}, \vec{z})$; also azimuthal coordinate
ϑ	Half-angle of the light-cone
2D	Two-dimensional
2H	Two layers in hexagonal symmetry
UPC	Upconversion photoluminescence spectroscopy
UV range	Ultraviolet range (below 400 nm)
u	Generic periodic function
$u_{n\vec{k}}$	Wavefunction close to the cores of the lattice atoms, Bloch waves
$\boldsymbol{u}_{l,n}$	Acoustic-phonon displacement field
$\boldsymbol{u}_{\mathrm{LO}}$	Longitudinal optical-phonon displacement field
VB	Valence band
vdW	van der Waals
VTI	Variable temperature insert
V, $V(r)$, $V(\vec{r})$	Potential energy term
$\lvert V\rangle$	Vertical linear polarization state of a transverse acoustic phonon
$V_{\mathrm{e/h}}$	Confinement potential of the electron/hole
V_{eff}	Effective potential energy of a crystal
V_{el}	Electric potential
v_{g}	Group velocity, speed of sound, propagation speed of an acoustic mode
V_{harm}	Potential energy of the harmonic oscillator
V_{ol}	Volume of the crystal, equivalent to the number of primitive unit cells
$\Delta V_{ol}/V_{ol}$	Relative volume change under strain
$\hat{V}$	Potential energy operator
v	Additional mirror symmetry
$\lvert v\rangle$, $\lvert v'\rangle$, $\lvert v''\rangle$	Virtual intermediate scattering states
v_{g}	Group velocity, propagation speed of an acoustic mode, speed of sound in the lattice, Sound velocity of a material
$v_{\mathrm{L/T}}$	Sound velocity of the longitudinal/transverse acoustic phonons
W	Tungsten
WD	Working distance
WX_2: WS_2, WSe_2	Tungsten-chalcogenide compounds: Tungstendisulphide, Tungstendiselenide
WP	Wave plate or retardation plate
W	Transition rate (between unperturbed dark exciton state and two-phonon continuum)
$W_{\mathrm{abs/em}}$	Probability rate for photon absorption/emission
W_{SF}	Spin-flip transition probability rate
w	Linewidth
$w(\kappa)$	Faddeeva function, a scaled complex error function
X	Exciton
$\mathrm{X_D}$	Dark exciton
$\mathrm{X_G}$	Gray exciton
XX	Biexciton
$\mathrm{XX^-}$	Charged biexciton
X-point	High-symmetry point of a fcc unit cell for the point in x-direction on the small square face
x	Spatial coordinate; or variable (unkown); or content, composition
$\hat{x}$	Position operator: operator corresponding to the position observable of a particle

$Y_{l,m}(\theta, \phi)$	Vector potential involving spherical harmonics
y	Spatial coordinate
ZO	Out-of-plane transversal phonon mode
z	Spatial coordinate
z-axis	Quantization axis, optical axis of a setup, growth direction of a nanostructure
z/z'	Light propagation directions of the incident/scattered light
$z(\sigma^{\pm}, \sigma^{\pm})z'$	Light polarization configuration of the incident (z) and scattered (z') light
$\vec{z} = (0, 0, 1)^T$	Vector of z-axis
ζ	Phase shift of the continuum
0D	Zero-dimensional

List of Figures

List of Tables

List of Publications

(1) V. V. Belykh, D. R. Yakovlev, J. J. Schindler, E. A. Zhukov, M. A. Semina, M. Yacob, J. P. Reithmaier, M. Benyoucef, and M. Bayer, Large anisotropy of electron and hole g factors in infrared-emitting InAs/InAlGaAs self-assembled quantum dots, Phys. Rev. B **93**, 125302 (2016).

(2) V. V. Belykh, D. R. Yakovlev, J. J. Schindler, J. van Bree, P. M. Koenraad, N. S. Averkiev, M. Bayer, and A. Yu. Silov, Dispersion of the electron g factor anisotropy in InAs/InP self-assembled quantum dots, J. Appl. Phys. **120**, 084301 (2016).

(3) J. Debus, J. J. Schindler, P. Waldkirch, S. Goeke, A. Brümmer, D. Biermann, and M. Bayer, Indication of worn WC/C surface locations of a dry-running twin-screw rotor by the oxygen incorporation in tungsten-related Raman modes, Appl. Phys. Lett. **109**, 171601 (2016).

(4) D. Kudlacik, K. V. Kavokin, C. Lüders, K. Barthelmi, J. J. Schindler, H. Moldenhauer, P. Waldkirch, V. F. Sapega, D. R. Yakovlev, A. Waag, M. Bayer and J. Debus, Asymmetric spin transitions of nonthermalized Mn^{2+} ions in (Zn,Mn)Se-based quantum wells, Phys. Rev. B **101**, 155432 (2020).

(5) D. Kudlacik, V. Yu. Ivanov, D. R. Yakovlev, V. F. Sapega, J. J. Schindler, J. Debus, M. Bayer and R. V. Pisarev, Exciton and exciton-magnon photoluminescence in the antiferromagnet CuB_2O_4, Phys. Rev. B **102**, 035128 (2020).

(6) J. Jadczak, J. Kutrowska-Girzycka, J. J. Schindler, J. Debus, K. Watanabe, T. Taniguchi, C.-H. Ho, and L. Bryja, Investigations of electron-electron and interlayer electron-phonon coupling in van der Waals hBN/WSe_2/hBN heterostructures by photoluminescence excitation experiments, Materials **14**, 399 (2021).

(7) J. Jadczak, J. Kutrowska-Girzycka, M. Bieniek, T. Kazimierczuk, P. Kossacki, J. J. Schindler, J. Debus, K. Watanabe, T. Taniguchi, C.-H. Ho, A. Wójs, P. Hawrylak, and L. Bryja, Probing negatively charged and neutral excitons in MoS_2/hBN and hBN/MoS_2/hBN van der Waals heterostructures, Nanotechnology **32**, 145717 (2021).

(8) J. Jadczak, M. Glazov, J. Kutrowska-Girzycka, J. J. Schindler, J. Debus, C.-H. Ho, K. Watanabe, T. Taniguchi, M. Bayer, and L. Bryja, Upconversion of light into bright intravalley excitons via dark intervalley excitons in hBN-encapsulated WSe_2 monolayers, ACS Nano **15**, 19165 (2021).

(9) J. J. Schindler, K. Barthelmi, J. Kaspari, D. Reiter, C. Sgroi, S. Scholz, A. Ludwig, A. D. Wieck, and J. Debus, Optically probing dark excitons via Fano resonances, in preparation for submission to Nat. Commun.

(10) J. J. Schindler, J. Jadczak, J. Kutrowska-Girzycka, L. Bryja, and J. Debus, Magnetic field dependence of exciton-energy splittings in $Mo_{0.7}W_{0.3}Se_2$ monolayers, in preparation.

Acknowledgments

I thank all the people who supported, helped and encouraged me to finish this thesis. First of all, I acknowledge Prof. Dr. Manfred Bayer for providing me the opportunity to work at the E2 chair and for his multifarious support, e.g., the possibility to work with cutting edge equipment and various measurement techniques. The E2 chair offers excellent scientific conditions, a great working atmosphere and many opportunities to learn, travel and have fun, which I highly appreciate. Most of all, I thank my group leader and mentor Dr. Jörg Debus for supervising my studies, introducing me to these interesting topics, sharing knowledge and invaluable guidance in the lab and beyond. Thank you for answering all my questions, for valuable advice and the great time! Additionally, I am very grateful to Prof. Dr. Marc-Alexander Aßmann and Prof. Dr. Mirko Cinchetti for reviewing my thesis. Many thanks to Dr. Dennis Kudlacik for introducing me to the spin-flip setup and great willingness to help, as well as Dr. Dion Braukmann, Dr. Vasilii V. Belykh, and Dr. Steffen Varwig.
Furthermore, I express my gratitude to Dr. A. Ludwig, Prof. Dr. A. D. Wieck and their chair members from Ruhr-Universität Bochum for the growth of the excellent quantum dot samples. Further, I am thankful to Dr. Vitaly Yu. Ivanov from Institute of Physics in Warsaw, Poland, Prof. Dr. Victor F. Sapega from Ioffe Institue in St. Petersburg, Russia, and Dr. hab. inż. Joanna Jadczak and Prof. Dr. Leszek Bryja from Wrocław University of Science and Technology in Wrocław, Poland, for their cooperation, their outstanding support and fruitful discussions during my research visits. In addition, I thank Dr. Joanna Kutrowska-Girzycka for sharing her office with me and for the supply of high-quality monolayer samples. I highly appreciate the time and effort you put in these!

All our experiments were not possible without the constant supply of helium and nitrogen from Daniel Tüttmann and Klaus Wiegers, the mechanical skills from Lars Wieschollek, and the electrical troubleshooting from Thomas Stöhr. Further gratitude goes to Michaela Wäscher, Nina Sesemann (previously Collette), and Katharina Goldack (previously Sparka), who took quick care of all administrative tasks with competence and patience. Thank you all!

I thank all E2 members for the pleasant atmosphere and lots of fun. Specifically, I always had a great time with my CP-01-190 office colleagues Eiko Evers, Henning Moldenhauer and Janina Rautert, my Lab C colleagues, my master student Katja Barthelmi, and the unofficial E2 women club members, as well as further colleagues from other chairs. I will keep this time in very good memory!

Great thanks to all my friends, especially the Botox vs. Feenstaub group, Hans Tholen, and my football team, Tus Eichlinghofen Damen (I), who offered welcome distraction from writing my thesis and made me think about other stuff than physics. Moreover, I am extraordinarily grateful for the evidently endless backing and patience of my family, and for their continuous support during my whole academic career. Finally, I thank Jörg Debus with all my heart for being the person that you are and supporting me as the person that I am. I'd say Okay again :)